

Open Research Online

The Open University's repository of research publications
and other research outputs

A Hybrid Similarity Measure Framework for Multimodal Medical Image Registration

Thesis

How to cite:

Reel, Parminder Singh (2016). A Hybrid Similarity Measure Framework for Multimodal Medical Image Registration. PhD thesis The Open University.

For guidance on citations see [FAQs](#).

© 2016 Parminder Reel

Version: Version of Record

Copyright and Moral Rights for the articles on this site are retained by the individual authors and/or other copyright owners. For more information on Open Research Online's data [policy](#) on reuse of materials please consult the policies page.

oro.open.ac.uk

A Hybrid Similarity Measure Framework for Multimodal Medical Image Registration

Parminder Singh Reel

B.Eng, M.Sc

A thesis submitted in partial fulfilment of the requirements for the
degree of

Doctor of Philosophy



Department of Computing and Communications

Faculty of Mathematics, Computing and Technology

The Open University

Milton Keynes, United Kingdom

Submitted on 28th August 2015

I dedicate this work to ...

My Parents, and I hope that this achievement will complete the dream that you had for me all those many years ago when you chose to give me the best education you could.

My Wife, whose loyalty to our best interests and willing sacrifices have been such great factors in the completion of this work. Without her patience, understanding, support and most of all love, this work would have not been possible.

My Sister, for her love, care and support at all times.

Acknowledgements

Looking back at the PhD journey, I have to agree with my supervisor, Prof. Laurence S. Dooley, who at the beginning told me that what I have started, would be at times both an intellectually and emotionally challenging journey, that would indeed require a lot of personal motivation on my part. I am deeply grateful for his endless support, guidance and wisdom. His constant academic and moral support gave me the confidence to succeed which I needed during the various highs and lows in this journey. I would also like to express my sincere gratitude to Dr. Patrick Wong for always providing me very useful comments and excellent guidance. Discussions with him have always helped me to improve the quality of my work. I am also thankful to my external supervisor Dr.-Ing. Anko Börner at German Aerospace Center (DLR), Berlin for his constant support, encouragement and insightful discussions despite his busy schedule. I especially thank him for the hospitality and personal effort in accommodating me at DLR during my three annual visits. I will forever be grateful, and could not have completed this thesis without you all.

I am thankful to my mini viva examiners Dr. David Chapman and Dr. Allan Jones for their suggestions and feedback during the early stages of this thesis work. I also owe my thanks to Dr. Asanobu KITAMOTO at National Institute of Informatics (NII), Tokyo, for giving me the opportunity to work in his laboratory during my internship at NII. I also wish to thank Dr. Adrian S. Poulton and Dr. Soraya Kouadri Mostéfaoui for their valuable feedback, as well as all the current and alumni members of *neXt Generation Multimedia Technologies* (XGMT) research group for their supportive and interesting technical discussions. I am also grateful to Hartwig Hetzheim, Eugen Funk and other colleagues at DLR for providing me valuable ideas as well as a friendly environment to work. I am also thankful to Thomas Fähsing for his support and efforts during my visits to Berlin. I would also like to thank all the co-travellers of doctoral journey in Room S1005, for providing me a friendly as well as focused environment. I am thankful to Advait, Alam, Mobolaji and Faisal for taking out time from their busy schedules to go through my thesis draft.

Finally, I would like to thank The Open University, Research Degrees Office, Faculty of MCT and its Computing and Communications Department for offering me the funding and an opportunity to pursue this PhD study.

Abstract

Medical imaging is widely used today to facilitate both disease diagnosis and treatment planning practice, with a key prerequisite being the systematic process of *medical image registration* (MIR) to align either mono or multimodal images of different anatomical parts of the human body. MIR utilises a *similarity measure* (SM) to quantify the level of spatial alignment and is particularly demanding due to the presence of inherent modality characteristics like *intensity non-uniformities* (INU) in magnetic resonance images and large homogeneous non-vascular regions in retinal images. While various *intensity* and *feature*-based SMs exist for MIR, *mutual information* (MI) has become established because of its computational efficiency and ability to register multimodal images. It is however, very sensitive to interpolation artefacts in the presence of INU with noise and can be compromised when overlapping areas are small. Recently MI-based *hybrid* variants which combine regional features with intensity have emerged, though these incur high dimensionality and large computational overheads.

To address these challenges and secure accurate, efficient and robust registration of images containing high INU, noise and large homogeneous regions, this thesis presents a new *hybrid* SM framework for 2D multimodal rigid MIR. The framework consistently provides superior quantitative and qualitative performance, while offering a uniquely flexible design trade-off between registration accuracy and computational time. It makes three significant technical contributions to the field: i) An *expectation maximisation-based principal component analysis with mutual information* (EMPCA-MI) framework incorporating neighbourhood feature information; ii) Two innovative enhancements to reduce information redundancy and improve MI computational efficiency; and iii) an *adaptive* algorithm to select the most significant principal components for feature selection.

The thesis findings conclusively confirm the *hybrid* SM framework offers an accurate and robust 2D registration solution for challenging multimodal medical imaging datasets, while its inherent flexibility means it can also be extended to the 3D registration domain.

Declaration

The work presented in this thesis is an original contribution of the author. Parts of this thesis have appeared in the following:

Peer-Reviewed Publications:

1. **Reel, P. S.**, Dooley, L. S., and Wong, K. C. P. (2012b). A new mutual information based similarity measure for medical image registration. In *IET Conference on Image Processing (IPR 2012)*, pages 1-6, London, UK.
doi : 10.1049/cp.2012.0424
2. **Reel, P. S.**, Dooley, L. S., and Wong, K. C. P. (2012a). Efficient Image Registration using Fast Principal Component Analysis. In *19th IEEE International Conference on Image Processing (ICIP 2012)*, pages 1661-1664, Lake Buena Vista, Orlando, Florida, USA.
doi : 10.1109/ICIP.2012.6467196
3. **Reel, P. S.**, Dooley, L., Wong, K., and Borner, A. (2013c). Robust retinal image registration using expectation maximisation with mutual information. In *38th IEEE International Conference on Acoustics, Speech and Signal Processing (ICASSP 2013)*, pages 1118-1122, Vancouver, BC, Canada.
doi : 10.1109/ICASSP.2013.6637824
4. **Reel, P. S.**, Dooley, L., Wong, K., and Borner, A. (2013b). Multimodal retinal image registration using a fast principal component analysis hybrid-based similarity measure. In *20th IEEE International Conference on Image Processing (ICIP 2013)*, pages 1428-1432, Melbourne, Australia.
doi : 10.1109/ICIP.2013.6738293

5. **Reel, P. S.**, Dooley, L. S., Wong, K. C. P., and Börner, A. (2013a). Fast EM Principal Component Analysis Image Registration Using Neighbourhood Pixel Connectivity. In Wilson, R., Hancock, E., Bors, A., and Smith, W., editors, *Computer Analysis of Images and Patterns*, volume 8047 in *Lecture Notes in Computer Science*, pages 270-277. Springer Berlin Heidelberg.
doi : 10.1007/978-3-642-40261-6_32
6. **Reel, P. S.**, Dooley, L. S., Wong, K., and Borner, A. (2014a). Enhanced retinal image registration accuracy using expectation maximisation and variable bin-sized mutual information. In *39th IEEE International Conference on Acoustics, Speech and Signal Processing (ICASSP 2014)*, pages 6632-6636, Florence, Italy.
doi : 10.1109/ICASSP.2014.6854883
7. **Reel, P. S.**, Dooley, L. S., Wong, K. C. P., and Börner, A. (2014b). Robust Image Registration using Adaptive Expectation Maximisation based PCA. In *IEEE Visual Communications and Image Processing Conference (VCIP 2014)*, pages 105-108, Valletta, Malta.
doi : 10.1109/VCIP.2014.7051515

Research Prize:

IET Engineering Prize Award sponsored by ABB Group at IET Midlands Power Network Engineering Prize Award Evening Event (in association with industry), Coventry University, UK, Mar 18, 2014.

doi : 10.6084/m9.figshare.1004109

Parminder Singh Reel

Submitted on 28th August 2015

Contents

Contents	vi
List of Figures	xii
List of Tables	xxviii
List of Abbreviations	xxix
List of Symbols	xxxix
1 Introduction	1
1.1 Overview	1
1.2 Mutual Information-based Multimodal MIR	4
1.3 Research Motivation	6
1.4 Research Question and Objectives	9
1.5 Contributions	12
1.6 Thesis Structure	14
1.7 Summary	16

2	Medical Image Registration: A Review	17
2.1	Introduction	17
2.2	Brief History of Medical Imaging	18
2.3	Medical Image Registration	25
2.3.1	Transformation	26
2.3.2	Interpolation	29
2.3.3	Similarity Measure	32
2.3.4	Optimisation	37
2.4	MI and its variants for multimodal MIR	41
2.5	Discussion	54
2.6	Summary	57
3	Research Methodology	58
3.1	Introduction	58
3.2	Research Methodology and Test-bed	59
3.3	Generic MIR Model Setup	61
3.4	Image Datasets	63
3.4.1	Mono and Multimodal BrainWeb Dataset	63

3.4.2	Mono and Multimodal Retinal Datasets	64
3.5	Robustness Scenarios	67
3.5.1	Initial Misregistration	68
3.5.2	INU and Gaussian Noise	69
3.5.3	Low Contrast and Homogeneous Regions	71
3.6	Performance Metrics	73
3.6.1	Quantitative Assessment	73
3.6.2	Perceptual Assessment	74
3.6.3	Computational Cost	75
3.7	Simulation Platform	76
3.8	Software Code Validation	77
3.9	Summary	80
4	EMPCA-MI for Medical Image Registration	81
4.1	Introduction	81
4.2	EMPCA-MI	83
4.2.1	<i>Step I</i> : Image Neighbourhood Rearrangement	83
4.2.2	<i>Step II</i> : EMPCA-based feature extraction	86

4.2.3	<i>Step III: Finding MI for Registration</i>	88
4.3	Choosing interpolation and neighbourhood radius for EMPCA-MI	93
4.3.1	Choice of Interpolation Technique	94
4.3.2	Choice of neighbourhood radius	102
4.4	Summary	111
5	EMPCA-MI-based Registration Results	113
5.1	Introduction	113
5.2	Experimental Setup	114
5.3	Experimental Results Discussion	116
5.3.1	<i>Set 1: BrainWeb</i> Dataset-based Experiments	116
5.3.2	<i>Set 2: DRIVE</i> and <i>Brno-Multi</i> Dataset Experiments	127
5.3.3	EMPCA-MI Framework Robustness	137
5.4	Summary	141
6	EMPCA-MI Framework Enhancements	142
6.1	Introduction	142
6.2	EMPCA-MI Framework <i>Enhancement 1</i>	144
6.2.1	Neighbourhood Region Selection	146

6.2.2	Experiment Setup	147
6.2.3	Experimental Results Discussion	148
6.3	EMPCA-MI Framework <i>Enhancement 2</i>	154
6.3.1	Number of bins for MI computation	155
6.3.2	Experimental Setup	159
6.3.3	Experimental Results and Discussion	159
6.4	Summary	164
7	Adaptive EMPCA-MI Framework	166
7.1	Introduction	166
7.2	<i>Adaptive</i> EMPCA-MI framework	167
7.2.1	Stopping Rules for PCA	168
7.2.2	Adaptively choosing P in the EMPCA-MI framework	169
7.3	Experimental Setup	170
7.4	Experimental Results Discussion	172
7.4.1	<i>Set 1: BrainWeb</i> Dataset Registration Experiments	172
7.4.2	<i>Set 2: DRIVE</i> and <i>Brno-Multi</i> Dataset Experiments	178
7.4.3	Computational Cost of <i>Adaptive</i> EMPCA-MI Framework	185

7.5 Summary	187
8 Future Work	188
9 Conclusion	191
References	194
Appendices	242
A Initial Misregistration Scenarios	243
B EMPCA-MI Results for Interpolation	246
C EMPCA-MI Results for Neighbourhood Radius	253
D Supplementary Results for <i>Chapter 5</i>	260
E Supplementary Results for <i>Chapter 6</i>	269
F Supplementary Results for <i>Chapter 7</i>	272

List of Figures

1.1	Layout of the framework objectives in this thesis.	10
2.1	Brief historical timeline of medical imaging.	19
2.2	showing (a) the first published human Fundus photography apparatus (T. Jackman and J.D. Webster, 1886), (b) the first Fundus retinal image taken from it, with top white area as the optic disc and the lower, light area as an artefact (Saine, 1993), (c) the first ever X-ray image of A. B. Röntgen’s hand taken in 1895 (Kevles, 1997).	20
2.3	showing (a) the first fluorescein angiogram (H. R. Novotny and D. L. Alvis, 1961) and (b) the first brain CT scan in 1971 with 80×80 pixels resolution (Beckmann, 2006).	21
2.4	Various medical imaging modalities for (a & b) human brain, (c & d) eye retina from (Montreal Neurological Institute and Hospital, nd) and (Kolar et al., 2013; Kolar and Tasevsky, 2010).	22
2.5	Generic MIR model.	27
2.6	Rigid registration followed by non-rigid registration.	29

2.7	(a) Nearest neighbour, (b) Bilinear and (c) Bicubic Interpolation Methods.	31
2.8	Bifurcation structure comprising of a master bifurcation point and its three connected neighbours. Figure reproduced from (Chen et al., 2015).	36
3.1	Block diagram of the research methodology including the simulation test bed.	60
3.2	Example <i>BrainWeb</i> images of brain MRI (a) T1, (b) T2 and (c) PD from (Montreal Neurological Institute and Hospital, nd).	65
3.3	Example retinal images (a) and (b) of monomodal colour Fundus retinal images from the <i>DRIVE</i> dataset (Image Sciences Institute, nd) and (c) colour Fundus, (d) SLO from <i>Brno-Multi</i> dataset (Kolar et al., 2013; Kolar and Tasevsky, 2010).	66
3.4	Example <i>BrainWeb</i> image of (a) uncorrupted brain MRI T1 u , (b) multiplicative 20% INU α , (c) additive Gaussian noise β and (d) measured T1 image a (Collins et al., 1998; Montreal Neurological Institute and Hospital, nd; Razlighi et al., 2013).	70
3.5	Example <i>BrainWeb</i> images of misregistered brain MRI (a) $T1+\alpha_{40}+\beta$, (b) $T2+\alpha_{40}+\beta$ and (c) $PD+\alpha_{40}+\beta$ from (Montreal Neurological Institute and Hospital, nd).	71

3.6	Example retinal images from <i>Brno-Mono</i> dataset (a) colour Fundus and (b) only its green channel (shown in <i>grayscale</i> colour) from (Kolar et al., 2013; Kolar and Tasevsky, 2010).	72
3.7	Visual quality assessment of (a) multimodal $T1+\alpha_{40}+\beta/T2$ pair registration using <i>Canny edge detection</i> overlay (with inset showing zoomed in region) and (b) monomodal retinal registration zoomed-in view using <i>checkerboard</i> overlay (reproduced from (Gharabaghi et al., 2013)).	76
3.8	<i>Shepp-Logan</i> head phantom image (Guo and Huang, 2008; Haideker, 2011)	80
4.1	The neighbourhood region selection for feature extraction in EMPCA-MI, showing the dimensionality d with radius (a) $r=1$, (b) $r=2$ and (c) $r=3$ pixels.	85
4.2	Illustration showing EMPCA-MI computation steps on reference I_R and interpolated sensed I_S^* images.	90
4.3	EMPCA-MI Traces with nearest neighbour, bilinear and bicubic interpolation for x and y axis translation for monomodal $T2/T2$ image pairs (a & b) $T2+\alpha_{20}/T2$, (c & d) $T2+\beta/T2$ with inset showing zoomed-in view.	96
4.4	EMPCA-MI Traces with nearest neighbour, bilinear and bicubic interpolation for x and y axis translation for multimodal $PD/T1$ image pairs (a & b) $PD+\alpha_{20}/T1$, (c & d) $PD+\beta/T1$	97

4.5	ART performance of EMPCA-MI using nearest neighbour, bilinear and bicubic interpolation methods for monomodal T2/T2 and multimodal PD/T1 image pairs.	98
4.6	RE versus iterations plots for nearest neighbour, bilinear and bicubic interpolation with EMPCA-MI-based monomodal T2/T2 registration using (a) 1 st initial misregistration scenario and (b) 20 th initial misregistration scenario, multimodal PD/T1 registration using (c) 1 st initial misregistration scenario and (d) 20 th initial misregistration scenario.	100
4.7	RE summary boxplot of (a) monomodal T2/T2 registration and (b) multimodal PD/T1 registration using nearest neighbour, bilinear and bicubic interpolation with EMPCA-MI for all 20 initial misregistration scenarios. The <i>mean</i> and <i>outliers</i> are denoted by \blacklozenge and $+$ shapes. The numbers on top of the plots refer to the number of <i>out-of-range</i> outliers with RE higher than 9 and 14 pixels respectively.	102
4.8	EMPCA-MI Traces with different radius values for x and y axis translation for monomodal T2/T2 image pairs (a & b) T2+ α_{20} /T2, (c & d) T2+ β /T2.	103
4.9	EMPCA-MI Traces with different radius values for x and y axis translation for multimodal PD/T1 image pairs (a & b) PD+ α_{20} /T1, (c & d) PD+ β /T1.	104

4.10	Number of samples (q) with respect to different neighbourhood radii for the variety of datasets.	106
4.11	ART performances for EMPCA-MI and conventional PCA-MI with respect to different neighbourhood radii.	107
4.12	RE versus iterations plots for EMPCA-MI with varying neighbourhood radius for monomodal (a) $T2+\alpha_{20}/T2$ pair (using 12 th initial misregistration scenario) and (b) $T2+\beta/T2$ pair (using 16 th initial misregistration scenario). Multimodal (c) $PD+\alpha_{20}/T1$ pair (using 3 rd initial misregistration scenario) and (d) $PD+\beta/T1$ pair (using 17 th initial misregistration scenario).	108
4.13	RE summary boxplot of (a) monomodal $T2/T2$ registration and (b) multimodal $PD/T1$ registration using varying neighbourhood radius with EMPCA-MI for all 20 initial misregistration scenarios. The <i>mean</i> and <i>outliers</i> are denoted by \blacklozenge and $+$ shapes. The numbers on top of the plots refer to the number of <i>out-of-range</i> outliers with RE higher than 140 and 200 pixels respectively.	110
5.1	RE versus iteration plots for MI, GMI, RMI and EMPCA-MI using 18 th initial misregistration scenario for monomodal registration of (a) $T1/T1$, (b) $T1+\alpha_{20}/T1$, (c) $T1+\alpha_{40}/T1$, (d) $T1+\beta/T1$ and (e) $T1+\alpha_{40}+\beta/T1$ pairs.	117

5.2	Qualitative results of monomodal $T1+\alpha_{40}+\beta/T1$ pair using 18 th initial misregistration scenario showing (a) initial misregistration, (b) ground truth and (c) MI, (d) GMI, (e) RMI, (f) EMPCA-MI output with inset showing zoomed-in central lobes.	119
5.3	RE versus iterations plots for MI, GMI, RMI and EMPCA-MI using 15 th initial misregistration scenario for multimodal registration of (a) $T1+\alpha_{40}+\beta/T2$ pair.	121
5.4	Qualitative results of multimodal $T1+\alpha_{40}+\beta/T2$ pair using 15 th initial misregistration scenario showing (a) initial misregistration, (b) ground truth and (c) MI, (d) GMI, (e) RMI, (f) EMPCA-MI output with inset showing zoomed-in central lobes.	122
5.5	RE summary boxplot of (a) monomodal $T1/T1$ pair and (b) multimodal $T1/T2$ pair using MI, GMI, RMI and EMPCA-MI for all 20 initial misregistration scenarios. The <i>mean</i> and <i>outliers</i> are denoted by \blacklozenge and $+$ shapes. The numbers on top of the plots refer to the number of <i>out-of-range</i> outliers with RE higher than 65 and 85 pixels respectively.	124
5.6	ART performance of various similarity measures for <i>Set 1: Brain-Web</i> Dataset-based mono and multimodal registration experiments.	126
5.7	RE summary bar graph of 20 monomodal Fundus retinal image pairs using GFM and EMPCA-MI for 3 rd initial misregistration scenario. <i>N.B.</i> Bar graph does not show GFM result for Image Pair 9 since the registration fails for the particular image pair.	128

- 5.8 Qualitative results of monomodal Fundus retinal *Image Pair 5* using 3^{rd} initial misregistration scenario, showing (a) initial misregistration, (b) ground truth, (c) GFM and (d) EMPCA-MI output. Also (e) shows the zoomed-in regions of ground truth (1^{st} row), GFM (2^{nd} row) and EMPCA-MI output (3^{rd} row) respectively. 130
- 5.9 Qualitative results of monomodal Fundus retinal *Image Pair 9* using 3^{rd} initial misregistration scenario, showing (a) initial misregistration, (b) ground truth, (c) EMPCA-MI output, with (d) zoomed-in ground truth and (e) EMPCA-MI regions. *N.B. GFM failed to register this image pair.* 131
- 5.10 RE summary boxplot of 20 monomodal Fundus retinal image pairs using GFM and EMPCA-MI for all 4 initial misregistration scenarios. The *mean* and *outliers* are denoted by \blacklozenge and $+$ shapes. The numbers on top of the plot refer to the number of *out-of-range* outliers with RE higher than 18 pixels. *N.B. GFM results for scenario no. 4 were unavailable.* 132
- 5.11 RE summary bar graph of 10 multimodal Fundus/SLO retinal image pairs using RIR-BS and EMPCA-MI for 2^{nd} initial misregistration scenario. 133

- 5.12 Qualitative results of multimodal Fundus/SLO retinal *Image Pair 3* using 2^{nd} initial misregistration scenario, showing (a) initial misregistration, (b) ground truth, (c) RIR-BS and (d) EMPCA-MI output. Also (e) shows the zoomed-in regions of ground truth (1^{st} row), RIR-BS (2^{nd} row) and EMPCA-MI output (3^{rd} row) respectively. . 135
- 5.13 RE summary boxplot of 10 multimodal Fundus/SLO retinal image pairs using RIR-BS and EMPCA-MI for all 3 initial misregistration scenarios. The *mean* and *outliers* are denoted by \blacklozenge and $+$ shapes. The numbers on top of the plot refer to the number of *out-of-range* outliers with RE higher than 190 pixels. 136
- 5.14 Qualitative results of multimodal $T1+\alpha_{40}+\beta/T1$ pair using 11^{th} initial misregistration scenario showing (a) initial misregistration with (b) ground truth and (c) EMPCA-MI output with inset showing zoomed-in central lobes. 138
- 5.15 Qualitative results of multimodal Fundus/SLO retinal *Image Pair 4* using 3^{rd} initial misregistration scenario, showing (a) EMPCA-MI output (with $P=2$) and (b) RIR-BS output. Also (c) shows the three zoomed-in regions of EMPCA-MI output (with $P=2$) (1^{st} row) and RIR-BS (2^{nd} row) respectively. 140
- 6.1 Schematic showing (a) the original EMPCA-MI framework and the various approaches investigated as enhancements in (b) *Step I* and (c) *Step III* respectively. 143

6.2	Illustration of the original EMPCA-MI framework with 1 st order (<i>8-pixel</i>) and the proposed 2 nd order (<i>8-pixel</i> and <i>4-pixel</i>) region connectivity-based pre-processing in <i>Step I</i> , for an image pair with size of 10×10 pixels.	145
6.3	RE summary boxplot of (a) monomodal T1/T1 pair and (b) multimodal T1/T2 pair using 1 st order (<i>8-pixel</i>), 2 nd order (<i>8-pixel</i>) and 2 nd order (<i>4-pixel</i>) neighbourhood region connectivity in EMPCA-MI framework for all 20 initial misregistration scenarios. The <i>mean</i> and <i>outliers</i> are denoted by \blacklozenge and $+$ shapes. The numbers on top of the plots refer to the number of <i>out-of-range</i> outliers with RE higher than 14 and 20 pixels respectively.	149
6.4	ART performance for using original EMPCA-MI (1 st order (<i>8-pixel</i>)) followed by 2 nd order (<i>8-pixel</i>) and 2 nd order (<i>4-pixel</i>) neighbourhood region connectivity in the EMPCA-MI framework for <i>Brain-Web</i> dataset-based mono and multimodal registration experiments.	151
6.5	Qualitative results of monomodal T1+ $\alpha_{40}+\beta$ /T1 pair using 11 th initial misregistration scenario showing (a) initial misregistration and (b) ground truth followed results for (c) original EMPCA-MI framework (1 st order (<i>8-pixel</i>)), then EMPCA-MI framework with (d) 2 nd order (<i>8-pixel</i>) and (e) 2 nd order (<i>4-pixel</i>) neighbourhood region connectivity enhancements (with inset showing the zoomed-in central lobes).	153

- 6.6 RE summary boxplot for EMPCA-MI framework using different number of bins selection strategies for monomodal *Brno-Mono* retinal dataset registration. *Blue* and *red* colour represent the fixed and adaptive number of bins selection approaches, while *mean* and *outliers* are denoted by \blacklozenge and $+$ shapes. 160
- 6.7 ART summary bar graph for EMPCA-MI framework for monomodal *Brno-Mono* retinal dataset registration using different number of bins selection strategies. *Blue* and *red* colour represent the *fixed* and *adaptive* number of bins approaches. 162
- 6.8 Qualitative results of monomodal Fundus retinal *Image Pair 22*, showing (a) initial misregistration, (b) ground truth and (c) the zoomed-in regions of ground truth and different *fixed* and *adaptive* number of bins selection strategies with EMPCA-MI framework. . . 163
- 7.1 Flowchart for the *adaptive* EMPCA-MI framework. 169
- 7.2 RE summary boxplot of (a) monomodal T1/T1 pair and (b) multimodal T1/T2 pair using EMPCA-MI $\{1\}$ and *adaptive* EMPCA-MI $\{P\}$ for all 20 initial misregistration scenarios. The *mean* and *outliers* are denoted by \blacklozenge and $+$ shapes. The numbers on top of the plots refer to the number of *out-of-range* outliers with RE higher than *10* and *20* pixels respectively. 174

- 7.3 Qualitative results of monomodal $T1+\alpha_{40}+\beta/T1$ pair using 14^{th} initial misregistration scenario showing (a) initial misregistration, (b) ground truth and (c) EMPCA-MI $\{1\}$ and (d) *adaptive* EMPCA-MI $\{3\}$ output (with inset showing the zoomed-in central lobes). . . . 176
- 7.4 Qualitative results of multimodal $T1+\alpha_{40}+\beta/T2$ pair using 13^{th} initial misregistration scenario showing (a) initial misregistration, (b) ground truth and (c) EMPCA-MI $\{1\}$ and (d) *adaptive* EMPCA-MI $\{2\}$ output (with inset showing the zoomed-in central lobes). . . . 177
- 7.5 RE summary bar graph of 20 monomodal Fundus retinal image pairs using EMPCA-MI $\{1\}$ and *adaptive* EMPCA-MI $\{P\}$ for 3^{rd} initial misregistration scenario. 178
- 7.6 Qualitative results of monomodal Fundus retinal *Image Pair 20* using the 3^{rd} initial misregistration scenario, showing (a) initial misregistration, (b) ground truth, (c) EMPCA-MI $\{1\}$ and (d) *adaptive* EMPCA-MI $\{3\}$ output. Also (e) shows the zoomed-in regions of ground truth (1^{st} row), EMPCA-MI $\{1\}$ (2^{nd} row) and *adaptive* EMPCA-MI $\{3\}$ (3^{rd} row). 180
- 7.7 RE summary boxplot of 20 monomodal Fundus retinal image pairs using EMPCA-MI $\{1\}$ and *adaptive* EMPCA-MI $\{P\}$ for all 4 initial misregistration scenarios. The *mean* and *outliers* are denoted by \blacklozenge and $+$ shapes. The numbers on top of the plot refer to the number of *out-of-range* outliers with RE higher than 18 pixels. 181

7.8	RE summary bar graph of 10 multimodal Fundus/SLO retinal image pairs using EMPCA-MI $\{1\}$ and <i>adaptive</i> EMPCA-MI $\{P\}$ for the 2^{nd} initial misregistration scenario.	182
7.9	Qualitative results of multimodal Fundus/SLO retinal <i>Image Pair 6</i> using the 2^{nd} initial misregistration scenario, showing (a) initial misregistration, (b) ground truth, (c) EMPCA-MI $\{1\}$ and (d) <i>adaptive</i> EMPCA-MI $\{2\}$ output. Also (e) shows the zoomed-in regions of ground truth (1^{st} row), EMPCA-MI $\{1\}$ (2^{nd} row) and <i>adaptive</i> EMPCA-MI $\{2\}$ (3^{rd} row).	183
7.10	RE summary boxplot of 10 multimodal Fundus/SLO retinal image pairs using EMPCA-MI $\{1\}$ and <i>adaptive</i> EMPCA-MI $\{P\}$ for all 3 initial misregistration scenarios. The <i>mean</i> and <i>outliers</i> are denoted by \blacklozenge and $+$ shapes. The numbers on top of the plot refer to the number of <i>out-of-range</i> outliers with RE higher than 150 pixels. . .	184
7.11	ART performance for EMPCA-MI $\{1\}$ and <i>adaptive</i> EMPCA-MI $\{P\}$ frameworks for <i>Set 1</i> and <i>Set 2</i> registration experiments. . . .	186
B.1	EMPCA-MI Traces for monomodal T1/T1, T1+ α_{20} /T1, T1+ α_{40} /T1, T1+ β /T1 and T1+ α_{40} + β /T1 image pairs for x , y translation and θ rotation.	247
B.2	EMPCA-MI Traces for monomodal T2/T2, T2+ α_{20} /T2, T2+ α_{40} /T2, T2+ β /T2 and T2+ α_{40} + β /T2 image pairs for x , y translation and θ rotation.	248

B.3	EMPCA-MI Traces for monomodal PD/PD, PD+ α_{20} /PD, PD+ α_{40} /PD, PD+ β /PD and PD+ $\alpha_{40}+\beta$ /PD image pairs for x, y translation and θ rotation.	249
B.4	EMPCA-MI Traces for multimodal T1/T2, T1+ α_{20} /T2, T1+ α_{40} /T2, T1+ β /T2 and T1+ $\alpha_{40}+\beta$ /T2 image pairs for x, y translation and θ rotation.	250
B.5	EMPCA-MI Traces for multimodal T2/PD, T2+ α_{20} /PD, T2+ α_{40} /PD, T2+ β /PD and T2+ $\alpha_{40}+\beta$ /PD image pairs for x, y translation and θ rotation.	251
B.6	EMPCA-MI Traces for multimodal PD/T1, PD+ α_{20} /T1, PD+ α_{40} /T1, PD+ β /T1 and PD+ $\alpha_{40}+\beta$ /T1 image pairs for x, y translation and θ rotation.	252
C.1	EMPCA-MI Traces for monomodal T1/T1, T1+ α_{20} /T1, T1+ α_{40} /T1, T1+ β /T1 and T1+ $\alpha_{40}+\beta$ /T1 image pairs for x, y translation and θ rotation.	254
C.2	EMPCA-MI Traces for monomodal T2/T2, T2+ α_{20} /T2, T2+ α_{40} /T2, T2+ β /T2 and T2+ $\alpha_{40}+\beta$ /T2 image pairs for x, y translation and θ rotation.	255
C.3	EMPCA-MI Traces for monomodal PD/PD, PD+ α_{20} /PD, PD+ α_{40} /PD, PD+ β /PD and PD+ $\alpha_{40}+\beta$ /PD image pairs for x, y translation and θ rotation.	256

C.4	EMPCA-MI Traces for multimodal T1/T2, T1+ α_{20} /T2, T1+ α_{40} /T2, T1+ β /T2 and T1+ $\alpha_{40}+\beta$ /T2 image pairs for x , y translation and θ rotation.	257
C.5	EMPCA-MI Traces for multimodal T2/PD, T2+ α_{20} /PD, T2+ α_{40} /PD, T2+ β /PD and T2+ $\alpha_{40}+\beta$ /PD image pairs for x , y translation and θ rotation.	258
C.6	EMPCA-MI Traces for multimodal PD/T1, PD+ α_{20} /T1, PD+ α_{40} /T1, PD+ β /T1 and PD+ $\alpha_{40}+\beta$ /T1 image pairs for x , y translation and θ rotation.	259
D.1	RE versus iterations plots for MI, GMI, RMI and EMPCA-MI using 18 th initial misregistration scenario for monomodal registration of (a) T2+ $\alpha_{40}+\beta$ /T2 and (b) PD+ $\alpha_{40}+\beta$ /PD pairs.	261
D.2	Qualitative results for T2+ $\alpha_{40}+\beta$ /T2 with inset showing zoomed-in central lobes for 18 th initial misregistration scenario.	262
D.3	Qualitative results for PD+ $\alpha_{40}+\beta$ /PD with inset showing zoomed-in central lobes for 18 th initial misregistration scenario.	263
D.4	RE versus iterations plots for MI, GMI, RMI and EMPCA-MI using 15 th initial misregistration scenario for multimodal registration of (a) T1/T2, (b) T1+ α_{20} /T2, (c) T1+ α_{40} /T2 and (d) T1+ β /T2 (e) T2+ $\alpha_{40}+\beta$ /PD and (f) PD+ $\alpha_{40}+\beta$ /T1 pairs.	264

D.5	Qualitative results for $T2+\alpha_{40}+\beta/PD$ with inset showing zoomed-in central lobes for 15^{th} initial misregistration scenario.	265
D.6	Qualitative results for $PD+\alpha_{40}+\beta/T1$ with inset showing zoomed-in central lobes for 15^{th} initial misregistration scenario.	266
D.7	RE summary boxplot of monomodal (a) $T2/T2$ and (b) PD/PD pairs using MI, GMI, RMI and EMPCA-MI for all 20 initial misregistration scenarios. The <i>mean</i> and <i>outliers</i> are denoted by \blacklozenge and $+$ shapes. The numbers on top of the plots refer to the number of <i>out-of-range</i> outliers with RE higher than 65 and 85 pixels respectively.	267
D.8	RE summary boxplot of multimodal (a) $T2/PD$ and (b) $PD/T1$ pairs using MI, GMI, RMI and EMPCA-MI for all 20 initial misregistration scenarios. The <i>mean</i> and <i>outliers</i> are denoted by \blacklozenge and $+$ shapes. The numbers on top of the plots refer to the number of <i>out-of-range</i> outliers with RE higher than 60 and 95 pixels respectively.	268
E.1	RE summary boxplot of monomodal (a) $T2/T2$ and (b) PD/PD pairs using 1^{st} order (<i>8-pixel</i>), 2^{nd} order (<i>8-pixel</i>) and 2^{nd} order (<i>4-pixel</i>) neighbourhood region connectivity in EMPCA-MI framework for all 20 initial misregistration scenarios. The <i>mean</i> and <i>outliers</i> are denoted by \blacklozenge and $+$ shapes. The numbers on top of the plots refer to the number of <i>out-of-range</i> outliers with RE higher than 35 and 15 pixels respectively.	270

- E.2 RE summary boxplot of multimodal (a) T2/PD and (b) PD/T1 pairs using 1st order (*8-pixel*), 2nd order (*8-pixel*) and 2nd order (*4-pixel*) neighbourhood region connectivity in EMPCA-MI framework for all 20 initial misregistration scenarios. The *mean* and *outliers* are denoted by \blacklozenge and $+$ shapes. The numbers on top of the plots refer to the number of *out-of-range* outliers with RE higher than 21 and 16 pixels respectively. 271
- F.1 RE summary boxplot of monomodal (a) T2/T2 and (b) PD/PD pairs using the EMPCA-MI {1} and *adaptive* EMPCA-MI {P} for all 20 initial misregistration scenarios. The *mean* and *outliers* are denoted by \blacklozenge and $+$ shapes. The numbers on top of the plots refer to the number of *out-of-range* outliers with RE higher than 11 and 15 pixels respectively. 273
- F.2 RE summary boxplot of multimodal (a) T2/PD and (b) PD/T1 pairs using the EMPCA-MI {1} and *adaptive* EMPCA-MI {P} for all 20 initial misregistration scenarios. The *mean* and *outliers* are denoted by \blacklozenge and $+$ shapes. The numbers on top of the plots refer to the number of *out-of-range* outliers with RE higher than 17 and 16 pixels respectively. 274

List of Tables

2.1	Comparative summary of major existing similarity measures.	56
3.1	Parameter settings for the generic MIR model.	63
3.2	Various clinical image dataset details (Kolar et al., 2013; Kolar and Tasevsky, 2010; Montreal Neurological Institute and Hospital, 2000, nd).	64
3.3	Simulation platform specifications and their details.	78
5.1	Parameter settings for EMPCA-MI framework.	114
5.2	Experiments and their relevant parameter details.	115
7.1	The different parameter selections for the <i>adaptive</i> EMPCA-MI framework.	171
A.1	Initial misregistration scenarios for the <i>BrainWeb</i> (Collins et al., 1998) dataset as in (Kotsas and Dodd, 2011).	244
A.2	Initial misregistration scenarios for the retinal datasets as in (Gharabaghi et al., 2013).	245

List of Abbreviations

ART	Average Runtimes
CC	Correlation Coefficient
cMI	conditional Mutual Information
CR	Correlation Ratio
CT	Computed Tomography
DB-ICP	Dual-bootstrap Iterative Closest Point
DE	Difference Image
DRIVE	Digital Retinal Images for Vessel Extraction
EMPCA	Expectation Maximisation for Principal Component Analysis
EMPCA-MI	EMPCA with MI
FNMI	Feature Neighbourhood MI
GC	Gradient Correlation
GD	Gradient Difference
GFM	Geometrical Features Method
GMI	Gradient MI
GPVE	Generalised Partial Volume joint histogram Estimation
HO-MI	Higher-order MI
INU	Intensity Non-Uniformities
LBP	Local Binary Pattern
LC	Local correlation
MC-MI	Multi-channel MI

MF-MI	Multi-feature MI
MI	Mutual Information
MIR	Medical Image Registration
MRI	Magnetic Resonance Imaging
MRI-PD	Proton Density weighted MRI
MRI-T2	T2 relaxation time weighted MRI
NCC	Normalised Correlation Coefficient
NHS	National Health Service
NMI	Normalised MI
NMR	Nuclear Magnetic Resonance
OF-MI	Organ Focused MI
PC	Personal Computer
PCA	Principal Component Analysis
PCA-MI	Conventional PCA with MI
PI	Pattern Intensity
PVI	Partial Volume Interpolation
RE	Registration Error
RIR-BS	Vascular Bifurcation Structures Method
RIU	Ratio Image Uniformity
RMI	Regional MI
SAD	Sum of Absolute Difference
SE-MI	Spatially Encoded MI
SLO	Scanning Laser Ophthalmoscopy
SSD	Sum of Squared Difference
WC	Woods Criterion

List of Symbols

\triangleq	Is equal by definition to
\triangleapprox	Approximately equal to
\in	Is an element of
\notin	Is not an element of
$ $	Such that
$\sim \mathcal{N}(\mu, \sigma^2)$	Normal distribution
$\nabla x(\psi)$	Gradient vector at point x of scale ψ in GMI
α_{20}	20% INU
α_{40}	40% INU
β	Gaussian noise
γ_k	Unit vector in the x_k -coordinate direction
ϵ	Tolerance threshold for Powell optimisation
θ	Rotational angle in xy plane
$\theta_{initial}$	Initial rotational angle in xy plane
κ	Weighting function of GMI
$\lambda_P, \lambda_{P'}$	Eigenvalue of P and P'
μ	Mean
μ_{MN}	Central moment of order $(M + N)$ of binary 2D region
\mathcal{O}	Computational complexity
σ	Standard deviation
σ^2	Variance

τ	Transformation parameters
τ_{final}	Final registration transformation parameters
$\tau_{initial}$	Initial misregistration transformation parameters
$\phi_{x,x'}(\psi)$	Angle between the gradient vectors for given ψ in GMI
ψ	Scale of Gaussian kernel in GMI
Λ	Bifurcation structure vector for RIR-BS
Σ_d	Covariance matrix of d -dimensional normal distribution
γ_i	Branch angle for RIR-BS
Φ	Transforming variable
Φ^{new}	Updated value of Φ
Φ^T	Transpose of Φ
Ω_S	Unknown states
Ω_S^T	Transpose of Ω_S
a	Measured MRI image
b	Number of bins
B	Sliding window with radius r
B^*	Processed column vector using 2^{nd} order connectivity
c	Neighbourhood region connectivity
d	Dimensional Subspace
det	Determinant
D_∞	<i>Chebyshev</i> distance
e	<i>Euler's</i> number constant (≈ 2.71828)
$f(x)$	Sample function for Powell optimisation
g	Center pixel of the neighbourhood sliding window
G	Gradient term in GMI

h	Pixel location within the sliding window
H_g	Entropy term in RMI
$H(I_R), H(I_S)$	Marginal entropy of I_R and I_S respectively
$H(I_R, I_S)$	Joint entropy between I_R and I_S
$H(X_R), H(X_S)$	Marginal entropy of X_R and X_S respectively
$H(X_R, X_S)$	Joint entropy between X_R and X_S
i	Number of rows to be scanned by the sliding window
I	Sample image
I_R	Reference image
I_S	Sensed image
I_S^*	Interpolated sensed image
I^*	Interpolated sample image
$I_{11}-I_{44}$	coordinates of sample image I
I_1-I_4	First four affine moment invariant descriptors for GFM
j	Number of columns to be scanned by the sliding window
k	Natural number having value $1 < k < q$
K	<i>kurtosis</i>
l_i	Normalised branch length for RIR-BS
l_k	Starting vector of Powell optimisation with index k
m	Number of columns in the image
n	Number of rows in the image
\mathbb{N}	Set of natural numbers
P, P'	Number of principal components
p	Probability function

q	Number of observed data vectors
Q_R, Q_S	Processed I_R and I_S^* respectively using r
r	Neighbourhood radius
R	Range of Z
S_k	Generalised column vector s
s	Column vector
S	Uniform scaling in xy plane
$S_{initial}$	Initial uniform scaling in xy plane
\mathcal{SM}	Similarity measure
t_x	Translation in x axis direction
t_y	Translation in y axis direction
u	uncorrupted MRI image
U	Count of possibilities for computing probability
v	Normally distributed Gaussian noise
V	Covariance Matrix
w	Number of elements in Z
W	Design variables for Powell optimisation
x	x axis
x_0	Initial starting point of Powell optimisation
$x_{initial}$	Initial translation in x axis
(x, y)	original pixel location in a image
(x', y')	transformed pixel location in a image
(\bar{x}, \bar{y})	pixel location of center of gravity in binary 2D image
X_R, X_S	EMPCA output for Q_R and Q_S respectively
y	y axis

$y_{initial}$	Initial translation in y axis direction
z	Latent variable
Z	Sample data for selecting number of bins
\bar{Z}	Mean of Z

Chapter 1

Introduction

1.1 Overview

Medical imaging is a technical process to create visual representations of the interior of a body for medical inspection. In 1895, Röntgen firstly discovered that X-rays could identify bone structures (Kevles, 1997) and since then they have been widely used for the detection of pathology of the skeletal system. In the past decades, they have also been used to identify diseases such as pneumonia, lung cancer and kidney stones, though somewhat less useful in the imaging of soft tissues like the brain or muscle (Sherrow, 2006). Recent advancements in medical physics have led to the development of generic medical imaging modalities/technologies such as *Computed Tomography* (CT), *Magnetic Resonance Imaging* (MRI) (Analoui et al., 2012) as well as application-specific technologies such as mammography, angiography and fluoroscopy (Paragios et al., 2015) which can be used to image almost the whole human anatomy.

According to the National Health Service (NHS), in England, a total of 37.9 million imaging tests were conducted during the year ending March 2014, with an increase of more than 5% compared to the previous year (NHS England Analytical Services, 2014). Medical imaging has thus become one of the most indispensable components of healthcare technology by providing complementary anatomic and functional information which helps the physician in detecting and diagnosing diseases and health conditions (Bourland, 2012).

The medical images acquired using the imaging technologies need to be aligned amongst themselves as this allows the physician to examine the advancement of a disease over a period of time or to compare the pre/post-surgery condition of a patient (Gunderman, 2013). Similarly retinal scans for a patient over a course of time will inevitably have been taken using different orientations, resolutions and/or magnification settings, and these will need to be physically aligned to help facilitate the physician perform clinical analysis (Holz and Spaide, 2010). Most of the advanced medical applications such as image guided therapy/surgery require the acquired images to be in alignment (Khalifa et al., 2011).

The process of geometrically transforming a source medical image in order to attain the best physical alignment with a reference medical image is called *medical image registration* (MIR) (Modersitzki, 2004). It uses an optimisation method to maximise a similarity measure with known transformations between the two images. It is usually considered to be a mathematical optimisation problem with the similarity measure playing a critical role in its successful convergence (Hajnal and Hill, 2001). This process is termed monomodal or multimodal depending on whether the images to be aligned are from the same or different modalities.

Medical image registration can be broadly classified into *feature* and *intensity* techniques (Zitová and Flusser, 2003). For example, feature-based approaches for registering the retinal images primarily use optical disc, fovea (Xu et al., 2007) and vascular structural details (Lowe, 2004; Sofka and Stewart, 2006), while brain images use edge detection and surface extraction followed by the least mean square of extracted features (Hsu and Loew, 2001). Although feature-based approaches are fast, their performance is very dependent on the segmentation quality and degree of overlap of the extracted features. This is especially evident in the case of challenging retinal Fundus and *Scanning Laser Ophthalmoscopy* (SLO) images which normally have inherently low contrast and large homogeneous non-vascular region characteristics, which can undermine their registration performance.

In contrast, intensity-based registration employs pixel intensity information by means of similarity measures such as normalised correlation coefficient (NCC) (Rogelj and Kovačič, 2003), phase correlation (Kolar et al., 2013), Fourier-based methods (Maintz and Viergever, 1998) and *mutual information* (MI) (Pluim et al., 2003). Although all these similarity measures are commonly used for monomodal registration, MI has been proven to be popular because of its ability to perform multimodal image registration of various parts of human anatomy (Tagare and Rao, 2015).

Multimodal registration is considered more demanding in comparison to the monomodal registration since it aligns different modalities having structural and functional imaging information effectively which is not always complementary in nature (Analoui et al., 2012). Multimodal registration also acts as a prerequisite for applications such as multimodal image fusion and its visualisation.

For example, MI has been used to perform multimodal registration between MRI, CT as well as *positron emission tomography* and *single photon emission computed tomography* images (Studholme et al., 1996a; Yin et al., 2010; Zhu and Cochoff, 2002) which enable the physician to provide an accurate diagnosis. Furthermore, in comparison to feature and other intensity-based similarity measures, MI does not require any prior segmentation or pre-processing steps. It is for these reasons that MI has been readily adopted for a variety of registration problems in the fields of microscopy, histology, computer vision and remote sensing (Paragios et al., 2015). In the last decade, few variants of MI-based similarity measures have emerged and offer solutions to the multimodal MIR problem (Fernandez-de Manuel et al., 2014).

1.2 Mutual Information-based Multimodal MIR

MI establishes a statistical relationship between the intensity values of the images to quantify the level of alignment between a source and reference image by utilising the underlying fundamental concepts of information theory (Hartley, 1928). However during MIR, it is sensitive to the interpolation artefacts, and its performance can be severely compromised when the overlap region between the images is small (Pluim et al., 2000b). While *normalised* MI (NMI) has been shown to successfully register partially overlapping images (Loi et al., 2008), it along with MI is unable to consistently and accurately register images containing *intensity non-uniformities* (INU) which are an omnipresent feature in MRI images. INU is a smooth intensity variation caused by factors such as radio frequency excitation field inhomogeneity, non-uniform reception coil sensitivity and eddy currents (Zhuang et al., 2011).

Furthermore, a degraded registration performance is also observed for retinal images having innately challenging characteristics such as low contrast and large homogeneous regions (Kubecka and Jan, 2004). This has led to the recent development of *hybrid* approaches which combine different aspects of the aforesaid *feature* and *intensity* methods (Holden et al., 2004; Legg et al., 2008; Studholme et al., 1996b). *Higher-order* MI (HO-MI) (Rueckert et al., 2000) and *gradient* MI (GMI) (Pluim et al., 2000a) for instance, help align images even at lower sampling resolutions, achieving better global maxima with low interpolation induced local minima. However, their performance degrades as noise is introduced.

On the other hand, methods such as *regional* MI (RMI) and its variants incorporate neighbourhood features within MI by segmenting the image into several regions for feature extraction to reduce the influence of INU and noise in the case of MRI images. Similarly for retinal images, the extracted vascular structures with spatial information are used for RMI and *feature neighbourhood* MI to improve the registration performance (Russakoff et al., 2004). In computing the associated entropies, these MI-based approaches employ a covariance matrix instead of high-dimensional histograms to reduce data complexity, though as the size of a neighbourhood grows, the computation overheads also increase correspondingly.

As will be discussed in *Chapter 2*, the current literature highlights the presence of inherent artefacts and noise in medical images as one of the major challenges in both rigid and non-rigid registration (Argyriou et al., 2015; Wilson and Laxminarayan, 2007). The two key examples are INU and noise in MRI images (Zhuang et al., 2011) and large homogeneous region with low contrast in retinal images (Legg et al., 2015), which make their registration especially challenging.

Since patterns of INU fields vary in different MRI images, the inconsistency of intensity values of same tissue region in two images lead to large errors when existing techniques are used (Razlighi et al., 2013). Similarly for retinal images, the quality of images is further compromised by the presence of different pathologies like haemorrhages and retinal scars caused by laser treatment (Holz and Spaide, 2010; Saine and Tyler, 2002).

Previous contributions (Butz and Thiran, 2001; Chappelow and Madabhushi, 2010; Kang et al., 2011; Luan et al., 2008; Yang et al., 2006; Yi and Soatto, 2011; Zhang et al., 2011; Zheng, 2010; Zouqi et al., 2010) have also combined spatial information in different ways for these challenging cases but the computation overhead remains high. This provided the key motivation for this research as there exists the clear prospect to exploit these opportunities and develop a new hybrid similarity measure which is able to provide better accuracy and robustness in the registration performance alongside lower computational costs.

1.3 Research Motivation

The inclusion of spatial features along with MI for multimodal MIR similarity measure has been considered as a promising solution (Fernandez-de Manuel et al., 2014; Woo et al., 2015) because it provides better robustness and performance. Although it can significantly improve the registration process, there are still many underlying challenges to resolve in realising a robust and flexible hybrid similarity measure for MIR.

Some of the main challenges to be addressed include:

- In the presence of inherent artefacts in particular medical modalities, rigid and non-rigid registration processes can be difficult, and convergence is not always guaranteed. For example, in case of MRI and retinal Fundus images, having high INU and large homogeneous non-vascular regions, respectively.
- Local features used along with information-theoretic similarity measures help in registering the medical images with the aforementioned characteristics by utilising higher order dimensionality, but incur high data and computational complexity. Conversely using the fast but rough approximating dimensionality reduction techniques underperform, especially in the presence of artefacts and noise.
- While dimensionality reduction for feature selection is possible, the stopping rule is a challenging problem in machine learning (Cangelosi and Goriely, 2007; Jackson, 1993; Villacampa, 2015) and can lead to performance degradation.
- Although the similarity measure plays a critical role in the image registration process, inappropriate choice of interpolation technique for a given transformation and optimisation can degrade the convergence rate of the registration process.
- For information theoretic similarity measures such as MI, there are various choice of parameters which impact significantly on the probability distribution estimation, especially when the medical images have varying image intensity characteristics.

These challenges and the general aim of improving the robustness and performance of multimodal MIR without increasing the computational costs were the main motivations behind this research. These are important requirements both in terms of being able to register challenging multimodal images and practical computational costs.

As mentioned in *Section 1.2*, the performance of both rigid and non-rigid registration is known to be compromised in the presence of inherent artefacts in medical images. Commonly, rigid registration is performed prior to non-rigid registration being undertaken for two reasons (Holden, 2008; Rueckert et al., 2000). Firstly, it helps in ascertaining the global correspondences between the images, and secondly, it reduces the computation time needed for the non-rigid registration stage. Hence, it is essential in addressing the aforementioned challenges for the rigid registration scenario to be considered in order to reduce the likelihood of the propagation of errors within the subsequent non-rigid registration step (Argyriou et al., 2015; Modersitzki, 2004; Zhao and Jia, 2015).

For these reasons, this thesis will only focus on rigid image registration. Furthermore, while multimodal registration is the primary objective of this research, without loss of generality both mono and multimodal rigid registration techniques will be considered and critically investigated. This all serves to provide the context for the overarching thesis research question and the related objectives which are discussed in the next section.

1.4 Research Question and Objectives

From the above discussion, the following research question was framed:

How can the multimodal medical images be efficiently and accurately registered?

After a detailed review of the existing methods and a critical evaluation of prospective techniques, a strategy combining local regional features with MI for a robust and flexible similarity measure was identified as a particularly promising area for investigation as it has considerable potential to achieve superior rigid registration performance on challenging mono and multimodal medical images. Such a strategy would not only enable the integration of image features within an entropy-based approach, but also offer greater flexibility in terms of both computational cost and registration performance by employing effective dimensionality reduction.

A set of three research objectives was framed to underpin the above overarching research question, and these are shown in Figure 1.1. The objectives are specifically:

1. *To develop and critically evaluate a hybrid similarity measure framework which utilises regional spatial features for efficient registration performance of multimodal datasets.*

Justification: The objective is to develop a new similarity measure, which utilises dimensionality reduction to not only extract spatial features but to lower the computational overheads with minimal impact on the registration

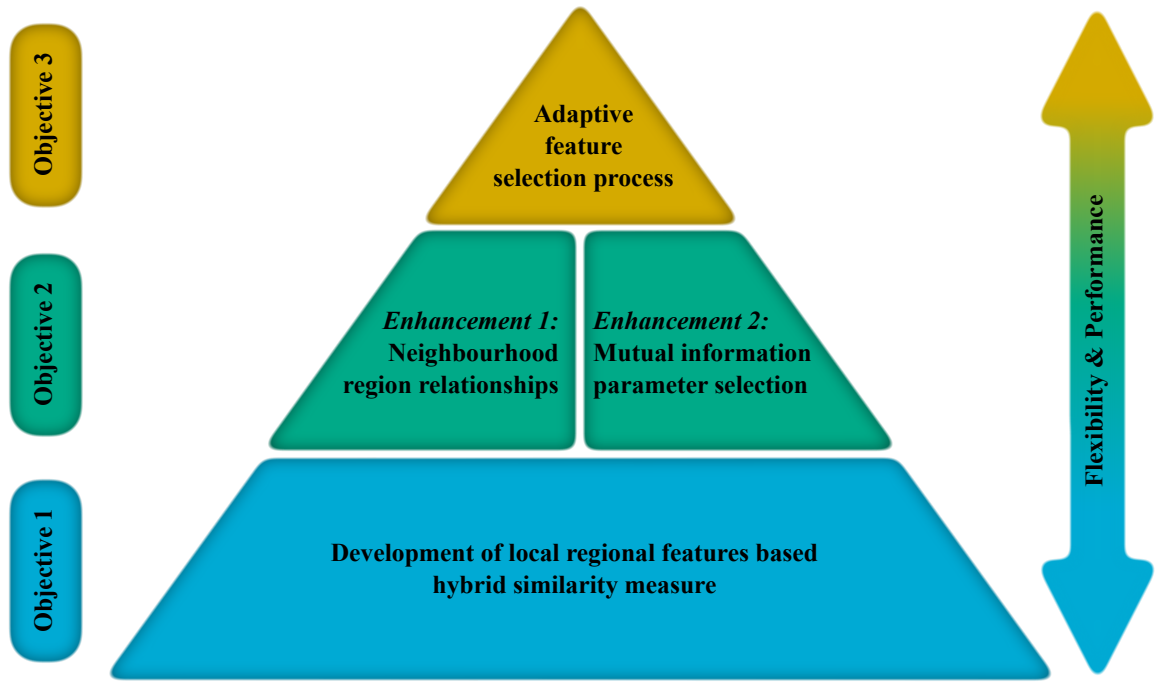


Figure 1.1: Layout of the framework objectives in this thesis.

performance. It will address the potential problem of degraded registration performance of medical images having inherent characteristics such as INU and non-vascular regions. The use of spatial regions for the dominant feature selection from the image dataset is followed by MI computation. The assumption to choose only the most significant features aims to lower the computational cost, while observing the corresponding impact upon the quality of the registration. Furthermore, by investigating appropriate spatial radius selection and interpolation techniques for the new similarity measure, faster convergence will be feasible.

2. *To critically analyse key neighbourhood region relationships and framework parameter choices.*

Justification: This objective seeks to enhance the capability of the new hybrid similarity measure framework by relaxing both the spatial region relationships and fixed parameter selection assumptions made in *Objective 1*, while still using only the most significant features. Since the neighbourhood region represents these features, it is essential that an accurate representation is used. A neighbourhood region scheme needs to be developed and incorporated into the similarity measure to achieve this. Similarly, choosing the best parameters for the MI computation will allow more accurate registration. Figure 1.1 shows these two enhancements which offer a refined and more flexible similarity measure while for computational efficiency, using only the most significant features.

3. *To develop and critically evaluate a mechanism to improve robustness by adaptively selecting the best number of features, based on image characteristics.*

Justification: Many existing hybrid similarity measures use high-dimensional representation of the spatial features and consequently experience high computational cost (Russakoff et al., 2004; Zhuang et al., 2011). Reducing the computation by estimating the similarity measure generally leads to poorer registration performance especially for images with artefacts (Legg et al., 2009). Hence, there is a need to develop new mechanisms which provide the flexibility to incorporate a varying number of features, based upon the dataset characteristics. As shown in Figure 1.1, this objective will enable the framework to have the flexibility to trade different levels of granularity for different mono and multimodal registration scenarios, as well as a corresponding trade-off with the computational cost incurred.

In summary, the overall aim is to develop a flexible similarity measure framework which provides consistently robust performance with lower computational overheads by utilising the hybrid combination of spatial features with MI for multimodal MIR of challenging image datasets. The new hybrid similarity measure achieves this aim by successfully fulfilling *Objectives 2* and *3*, which build upon the basis of new similarity measure framework developed as an outcome of *Objective 1*.

1.5 Contributions

To accomplish the aforementioned three objectives, this thesis presents a new robust hybrid *Expectation Maximisation for Principal Component Analysis with MI* (EMPCA-MI) *similarity measure framework*, which combines the neighbourhood feature information with MI. Initially the framework is developed with a series of underlying assumptions, which are subsequently relaxed to provide some important framework enhancements. It explores the impact of neighbourhood region relationships and parameter selection for MI computation and integrates an adaptive mechanism to select the most appropriate number of features for the EMPCA-MI similarity measure framework during the registration process. Each of these enhancements increases the flexibility of the framework as well as increasing its robustness to registering multimodal medical images.

The three original scientific contributions made in this thesis to the multimodal MIR domain are as follows:

1. A new EMPCA-MI similarity measure framework which utilises local regional features is introduced and analysed to address the challenge of multimodal image registration in the presence of modality artefacts. It involves a three step process: firstly, local regional features are identified and processed by employing neighbourhood region connectivity. Secondly, an iterative *Expectation Maximisation for Principal Component Analysis* (EMPCA) technique is applied to extract the most dominant features. Finally, the spatial alignment is quantified using MI. The appropriate selection of the interpolation technique and neighbourhood radius is determined, and the registration performance and computational efficiency of the new framework are benchmarked against existing comparative similarity measures.
2. Two novel enhancements are subsequently integrated into the EMPCA-MI framework designed in contribution 1. Firstly, higher-order neighbourhood region connectivity is exploited and, secondly, parameter selection strategies for MI are analysed. Higher-order neighbourhood region connectivity preserves the intensity relationships and so better represents the features, especially, for example, in MRI images which contain artefacts. Similarly, the new, variable parameter strategies are able to accommodate low contrast and large homogeneous regions present in many retinal image datasets.
3. Finally, an *adaptive* EMPCA-MI similarity measure framework is developed which can automatically determine the most significant features, based on the image characteristics to achieve further improvements in the registration performance. Furthermore, it affords a flexible trade-off mechanism between overall registration quality and the computational time involved.

1.6 Thesis Structure

The rest of the thesis is organised as following:

- *Chapter 2* presents a historical background for medical imaging, before a thorough literature review of the different components of MIR algorithms is presented. It also focuses on the strengths and weaknesses of existing MI-based similarity measures and their associated variants which are used for MIR.
- *Chapter 3* discusses the research methodology deployed, including the description of MIR test-bed and its parameters settings. It also presents the various testing scenarios employed, together with details on the clinical datasets, performance metrics and software validation methods used.
- *Chapter 4* details the formulation of the new EMPCA-MI similarity measure framework for MIR. It also provides an empirical evaluation for the choice of interpolation technique and neighbourhood radius. Work from this chapter has been published in (Reel et al., 2012b) and (Reel et al., 2012a).
- *Chapter 5* rigorously assesses the performance of the EMPCA-MI similarity measure framework presented in *Chapter 4*. Using various test clinical images under different scenarios, a critical evaluation is undertaken in terms of both the registration quality and computational efficiency against existing similarity measures. Work from this chapter has been published in (Reel et al., 2013c) and (Reel et al., 2013b).
- *Chapter 6* leverages from the key findings of *Chapter 5* to boost the EMPCA-

MI similarity measure framework with two enhancements. *Enhancement 1* extends the idea of neighbourhood region connectivity to a higher order in the pre-processing stage, while *Enhancement 2* investigates the impact of introducing different fixed and parameter selection strategies for the MI computation. Both these enhancements enable the EMPCA-MI similarity measure framework to provide improved registration performance in comparison with the original framework proposed in *Chapter 4*. Work from this chapter has been published in (Reel et al., 2013a) and (Reel et al., 2014a).

- *Chapter 7* formulates the *adaptive* EMPCA-MI similarity measure framework which has the ability to choose the best number of features instead of empirically choosing the most significant features as in *Chapter 4* and integrating the two enhancements in *Chapter 6*. It provides the flexibility in terms of robust registration performance and corresponding trade-off in computational cost. Work from this chapter has been published in (Reel et al., 2014b).
- *Chapter 8* presents potential future directions for the new EMPCA-MI similarity measure framework in the MIR domain.
- Finally, *Chapter 9* summarises the main findings and contributions emanating from this research.

1.7 Summary

In this chapter, the overarching research question and three principal research objectives have been framed to address some of the key challenges in multimodal MIR, particularly in the presence of artefacts in clinical images and the correspondingly high computational overheads incurred by existing techniques. The next chapter will provide a deeper context for this by presenting an overview of medical imaging history and a critique of MIR literature.

Chapter 2

Medical Image Registration: A Review

2.1 Introduction

Imaging is one of the fundamental tools used in the modern medical science. Today, imaging technologies are used by physicians to detect cancerous lesions, diagnose broken bones as well as perform image guided surgeries and track the progression of a disease (Paragios et al., 2015). For instance, diabetic retinopathy is the first cause of blindness in the working age population in the United Kingdom and had led to the recently announced NHS diabetic eye screening programme which will extensively employ retinal imaging to diagnose diabetic retinopathy and will be offered annually to all people with any type of diabetes aged 12 or over (Keenan et al., 2013; Martín-Merino et al., 2014).

Different medical imaging technologies are used to create different pictures of the human anatomy. While these modalities generally provide different information, there are few similarities. For example the external contour of two different modalities images can be similar, while the information they contain can be complementary. The integration of this imaging information from different modalities creates a compilation, which can be used to improve diagnosis and treatment of the subject. Hence, image registration is used to spatially align the medical images from the same or different modalities and is one of the key tasks in the medical image processing domain (Goshtasby, 2012).

While MIR is a vital and commonly used process, no one technique or method is known to work efficiently for all applications. Also as mentioned in *Chapter 1*, the clinical images with INU and large homogeneous non-vascular regions present a challenge for registration. This chapter discusses the historical background of medical imaging in brief and the need of image registration in medical imaging and its current challenges. The goal of this chapter is to provide a broad overview of the MIR literature and a detailed discussion on existing MI-based similarity measures highlighting their limitations.

2.2 Brief History of Medical Imaging

Medical imaging is a technical process which is used to create images of the human body for clinical purposes. This ability of looking into the human body is an essential diagnostic tool in the field of medical science and prime topic of research in healthcare technology (Damas et al., 2011b; Liu et al., 2008).

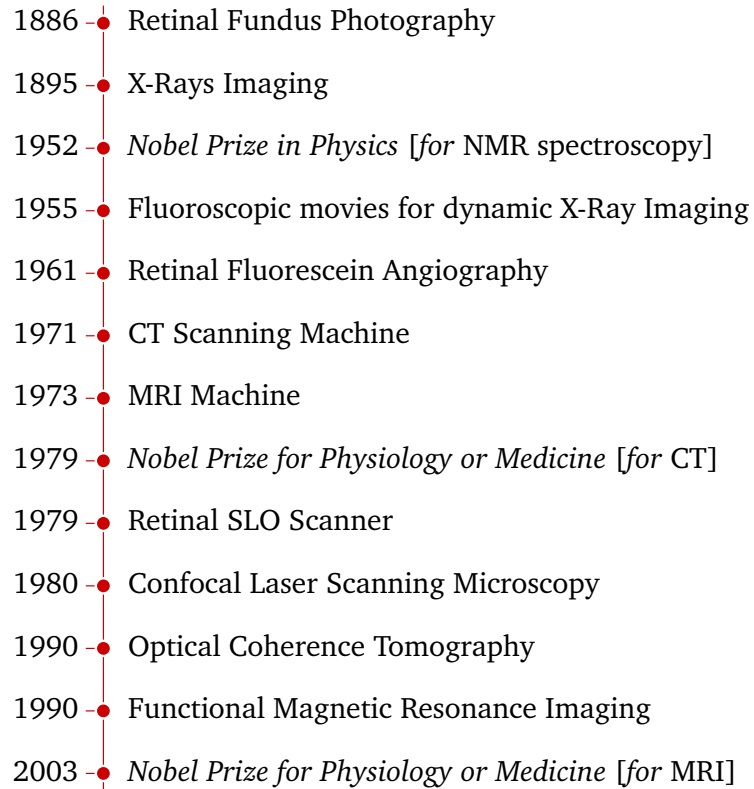


Figure 2.1: Brief historical timeline of medical imaging.

Medical imaging technologies have improved significantly since the late nineteenth century, since many different imaging modalities have been developed and are in practical use clinically. All these modalities are based on different physics principles and are usually more or less suitable for different part of the human anatomy (Hendee and Ritenour, 2002; Hobbie, 2001). Figure 2.1 shows the major technologies discovered and invented for imaging of human brain and eye retina. This timeline summarises the various modalities and is not exhaustive since new techniques are added every few years (Brooks, 2001; Cherry, 2009). Although the research and development of imaging the various anatomy parts (such as heart, lungs and abdomen) has progressed considerably, this section addresses the focus of this thesis which is related to modalities containing INU and large homogeneous non-vascular regions.

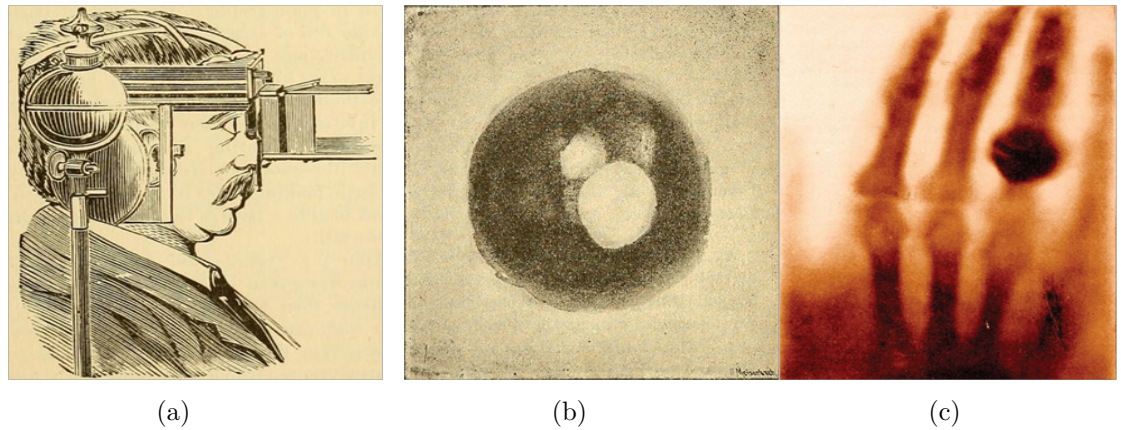


Figure 2.2: showing (a) the first published human Fundus photography apparatus (T. Jackman and J.D. Webster, 1886), (b) the first Fundus retinal image taken from it, with top white area as the optic disc and the lower, light area as an artefact (Saine, 1993), (c) the first ever X-ray image of A. B. Röntgen's hand taken in 1895 (Kevles, 1997).

The first published account of in-vivo human retinal Fundus photography is from 1886 (T. Jackman and J.D. Webster, 1886), which used the novel apparatus of albo-carbon burner shown in Figure 2.2(a) and with an exposure of $2\frac{1}{2}$ minutes, it was used to photograph the first very fair image of large blood vessels of the living human retina. As observed in Figure 2.2(b) the image obtained was blurry and needed more advancement in the instrumentation and acquisition techniques before the high quality Fundus photography could become a routine procedure (Saine, 1993). In 1895, the first X-ray picture was taken by the German physicist W. C. Röntgen, showing the skeletal composition of his wife's hand, as shown in Figure 2.2(c) (Kevles, 1997). Initially, X-rays were a novelty but by the end of the year they were used by physicians around the world (Linton, 1995).

Around half century later in 1946, F. Bloch and E. Purcell developed the concept of using magnets for taking pictures of a living being, which led to the nuclear magnetic resonance (NMR) spectroscopy (Gunderman, 2013) and they were awarded the Nobel Prize in Physics in 1952.

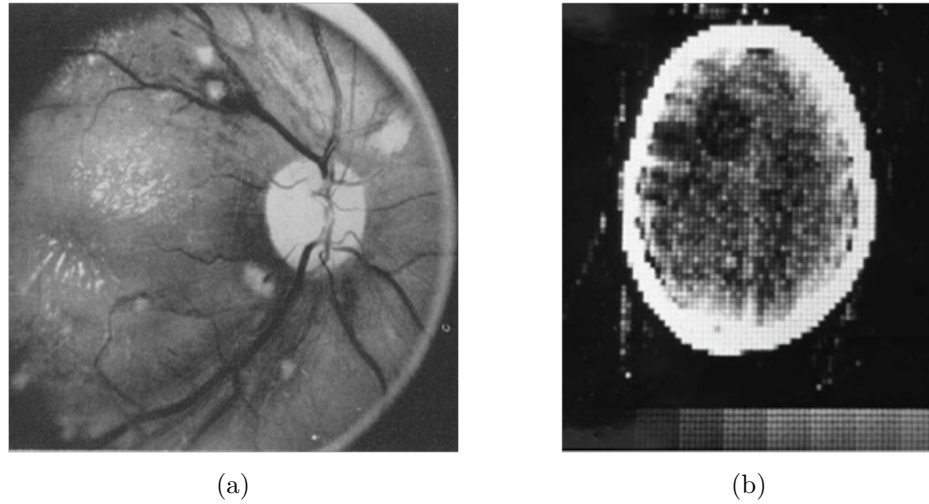


Figure 2.3: showing (a) the first fluorescein angiogram (H. R. Novotny and D. L. Alvis, 1961) and (b) the first brain CT scan in 1971 with 80×80 pixels resolution (Beckmann, 2006).

Furthermore in 1961, Novotny and Alvis published the first successful retinal fluorescein angiogram (H. R. Novotny and D. L. Alvis, 1961) which showed the vascular pattern and blood flow in a human retina as shown in Figure 2.3(a). Ten years later, the CT scanning machine was invented by G. Hounsfield and A. Cormack (Analoui et al., 2012). Figure 2.3(b) shows the first brain CT scan taken by them (Beckmann, 2006).

In the next four years, MRI was invented by P. Lauterbur and E. Mandfield for which they were awarded the Nobel Prize for Physiology or Medicine in 2003 (Bushong and Clarke, 2013). The MRI in particular, is considered to be a special modality since using different pulse sequences, the modality produces different images. For example, consider two contrasts e.g. proton density weighted MRI (MRI-PD) and T2 relaxation time weighted MRI (MRI-T2). A proton density sequence used in MRI detects the proton density of the subject while the T2 relaxation time sequence in MRI detects the transverse relaxation time of a proton in its environment.

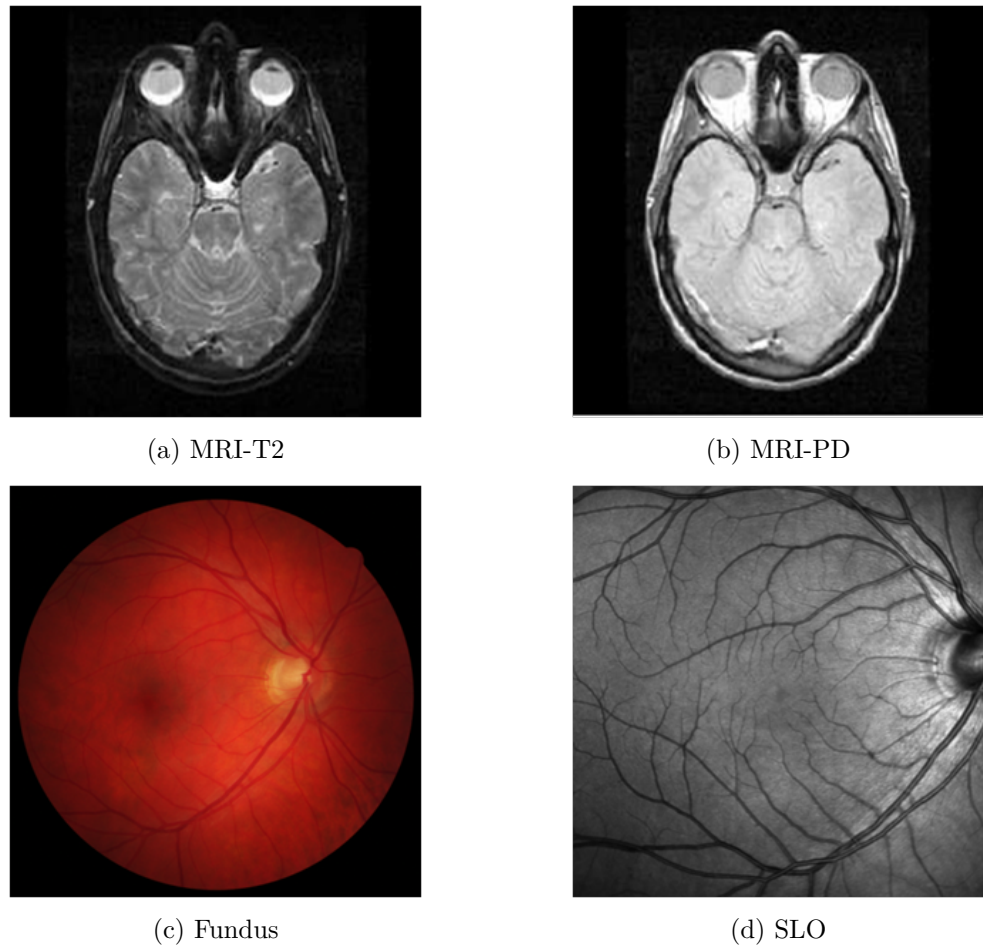


Figure 2.4: Various medical imaging modalities for (a & b) human brain, (c & d) eye retina from (Montreal Neurological Institute and Hospital, nd) and (Kolar et al., 2013; Kolar and Tasevsky, 2010).

Figures 2.4(a) and (b) show the trans-axial brain images of MRI-T2 and MRI-PD respectively. Here, MRI-PD image displays the dense tissues but shows very little detail of the brain tissue, while MRI-T2 image on the other hand, displays brain tissue details more clearly (Ackerman, 1998). However, MRI is known to be prone to non-anatomic INU variations due to radio frequency non-uniformities and static field inhomogeneity. INU along with the Gaussian noise causes the corruption of tissue images leading to their poorer visual quality (Simmons et al., 1994; Sled and Pike, 1998).

In 1979, G. Hounsfield and A. Cormack shared the Nobel Prize for Physiology or Medicine for their part in developing the computer assisted tomography (Beckmann, 2006). In the meantime, the retinal diagnosis also progressed considerably with the development of better quality Fundus imaging and the invention of SLO and Optical Coherence Tomography (Saine and Tyler, 2002).

Figures 2.4(c) and (d) show the Fundus and SLO image, respectively, of the same human retina. These retinal imaging methods have specific clinical applications for identifying eye conditions and diseases like myopia, glaucoma and diabetic retinopathy (Saine and Tyler, 2002; Sanchez-Galeana et al., 2001). They provide complementary information with the colour Fundus image showing the boundary of the optic nerve head, while the SLO images reveal deep layer reflectivity and surface topology of both the optic nerve head and retina. However, retinal images exhibit the inherent characteristics of low contrasted intensity distributions, as well as having large homogeneous non-vascular regions (Holz and Spaide, 2010).

Some of imaging modalities in the literature can be classified as structural or functional imaging systems. For example, the MRI and CT provide high-resolution information about the structure and anatomy, while functional MRI imaging gives the functional information (Cherry, 2009). Furthermore, they have been prominently used for both clinical and industrial research. Many derivative medical imaging modalities also exist such as magnetic resonance angiography from magnetic resonance imaging, computed tomography angiography from computed tomography and digital subtraction angiography from X-rays (Schneider et al., 2005).

The imaging activity conducted by NHS, England from February 2014 to February 2015 comprises of X-rays having the biggest share of all tests performed followed by Ultrasound, CT, MRI and others (NHS England Analytical Services, 2015). In the past decade, research and development trends in medical imaging have also been significant with the utilisation of methods/techniques such as biomarkers and gene expression along with the use of big data mining and informatics for the new cellular and molecular level imaging methods (Analoui et al., 2012; Gunderman, 2013). Hence, they give the unprecedented ability to detect, diagnose and monitor the various pathological as well as physiological conditions.

Most of these medical imaging modalities broadly deploy at least one of the key image processing tasks namely segmentation, registration and visualisation (Stytz et al., 1991). While medical image segmentation is usually performed as a pre-processing step to define a region of interest, on the other hand, medical image visualisation acts as a visual aid to see the medical images from different perspective and angles in order to facilitate in the diagnosis process (Brock, 2013). But, in order to fuse and visualise more than one image it is important that a correspondence is drawn among them using MIR (George, 2011; Wang et al., 2008). It can also be further used to study the time series information of mono or multimodal images, which can help to evaluate the growth rates in the region of interest (Alberto, 2011).

As mentioned in *Chapter 1*, the focus of this thesis is MIR in particular. The next section gives a detailed literature review of the MIR process.

2.3 Medical Image Registration

Broadly, the process of MIR utilises the feature or intensity-based information for various parts of human anatomy (Hill et al., 2001). The feature-based registration typically requires some features to be extracted or identified before the registration process. For example for retinal images, these features can be edges, contours, surfaces, statistical features, control points or high level structural descriptors (Khalifa et al., 2011). On the other hand, intensity-based methods do not require any feature extraction or segmentation. Hence, raw pixel values are used straight forwardly for registration process, as in case of brain images (Maintz and Viergever, 1998). Overall, intensity-based registration has particularly gained popularity, due to its ability to register multimodal images more effectively in comparison to the feature-based registration (Pluim et al., 2003).

Usually, two images are used in the generic image registration process (or more in case of group-wise registration (Paragios et al., 2015)), where one of the medical images is considered as reference image I_R while the other image as sensed image I_S . Image registration is usually considered to be an optimisation problem with the prime goal of finding the spatial mapping which enables the alignment of I_S with respect to image I_R . The generic MIR model is a multi-step, iterative process (Zitová and Flusser, 2003) which involves:

1. Transforming the coordinates of the sensed image I_S with known transformation parameters τ in a given reference space (*transformation step*).
2. Generating a new interpolated sensed image I_S^* in the reference space (*interpolation step*).

3. Comparing I_S^* with the reference medical image I_R using a similarity measure (*compute similarity measure step*).
4. Optimising the transformation parameters iteratively to achieve the best possible alignment at τ_{final} , where its similarity measure value is maximum between the images (*optimisation step*).
5. This value of final transformation is saved.

This process of registration can be generalised as a maximisation problem:

$$\tau_{final} = \arg \max_{\tau} \mathcal{SM}(I_R, \tau(I_S)) \quad (2.1)$$

where \mathcal{SM} denotes the similarity measure used and τ is the class of allowed *affine* and *similarity* transformations.

The aforementioned steps for a generic MIR model are shown in Figure 2.5 and discussed in detail as follows:

2.3.1 Transformation

In order to determine the position of corresponding points in reference and sensed images, a combination of translation, rotation and scaling parameters is considered. Image registration methods employ transformations such as rigid, affine and elastic (non-rigid) transformations (Zitová and Flusser, 2003). The rigid transformation considers t_x and t_y translations along the x and y axes, and a rotational angle θ for the registration process (Brown, 1992). It assumes that the subject in the image

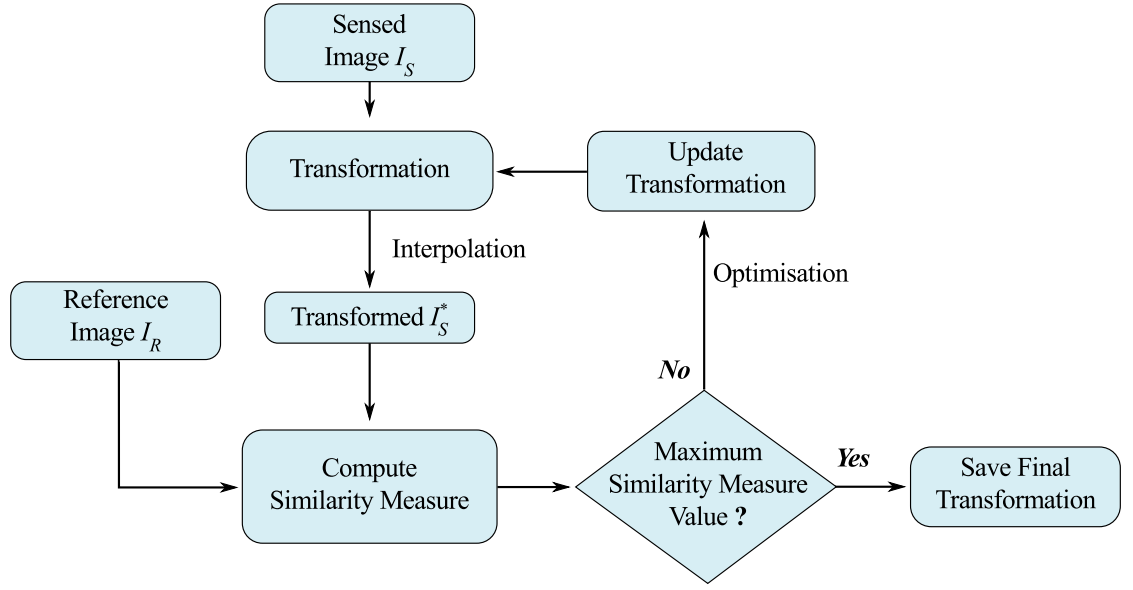


Figure 2.5: Generic MIR model.

maintain its shape and size (Yu, 2005). Affine transformations offer a high degree of flexibility in accommodating linear distortions by allowing scaling and shearing in addition to translation and rotation (Jenkinson and Smith, 2001).

The choice of using a particular transformation model for registration depends on the anatomy parts and their characteristics. For example, in the case of retinal images, the *similarity* transformation as in (Gharabaghi et al., 2013; Legg et al., 2008, 2009) is popularly used because it allows the magnification changes either due to the use of different optical instrument for image acquisition or the changes due to the motion in the direction of the optical axis (Ryan et al., 2004), represented as a uniform scaling S . It is a special form of global affine transform which includes S along with t_x , t_y and θ parameters. Hence, the similarity transformation can be defined as:

$$\begin{bmatrix} x' \\ y' \end{bmatrix} = \begin{bmatrix} t_x & S \cos \theta & S \sin \theta \\ t_y & -S \sin \theta & S \cos \theta \end{bmatrix} \begin{bmatrix} 1 \\ x \\ y \end{bmatrix} \quad (2.2)$$

Here, (x, y) and (x', y') are the original and transformed pixel positions, respectively, and (2.2) becomes a rigid transformation when $S=1$.

Elastic transformations provide more degrees of freedom as compared to rigid and affine transformations. It is also called non-rigid transformation due to its non-linear nature. Non-rigid transformations can be broadly classified on the basis of physical models or basis function expansion. While linear elasticity (Moshfeghi, 1991), viscous fluid flow (Christensen et al., 1997) and optical flow (Horn and Schunck, 1981) are examples of physical model-based transformations, radial basis functions (Fornet et al., 2001), multiquadrics (Zhang et al., 2002), thin-plate splines (Bookstein, 1989), B-spline (Denton et al., 1999), wavelets (Wu et al., 2000) and piecewise affine transforms (Crum, 2004) are some of basis function expansion transformations.

Various surveys on transformation are conducted in the past and it is considered very difficult to robustly conclude which transformation is the most accurate or best suited to a particular application (Crum, 2004; Holden, 2008; Klein et al., 2009). Although physical models are considered to have an advantage in non-rigid registration since they offer realistic solutions, some of their properties hinder the registration. For example, linear elasticity can only accurately model small deformations, which is a limitation because often soft tissues exhibit large deformation. Fluid flow offers a solution for this and can ensure that the topology is preserved.

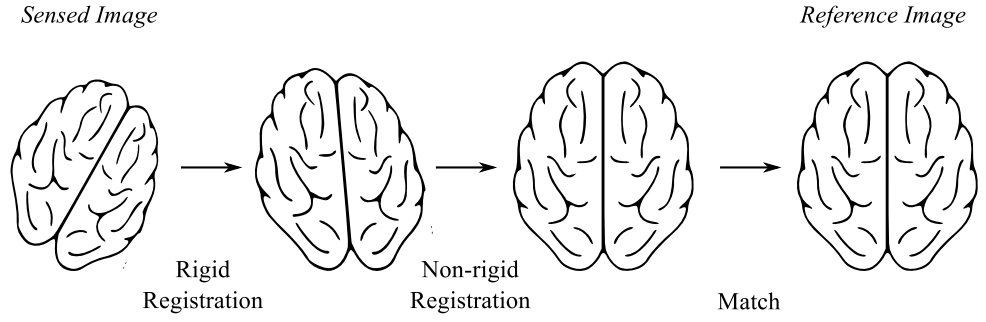


Figure 2.6: Rigid registration followed by non-rigid registration.

However, it cannot model the elastic component of the tissue deformation.

In reality, tissue exhibits a complex behaviour, which in certain conditions considered as elastic or visco-elastic. Demons (Crum, 2004; Thirion, 1998) is one of the most popular optical flow models, but it also has no constraints on the displacement and does not necessarily preserve the tissue structure.

In practice, most of the time, non-rigid registrations are not performed directly (Zhao and Jia, 2015). Rigid registration is used as a pre-processing step to non-rigid registration, in order to compute the global transformation parameters and then later non-rigid registration is performed to analyse the local deformation of the subject (Holden, 2008; Rueckert et al., 2000, 1999) as shown in Figure 2.6. The primary focus of this thesis is on the rigid registration stage.

2.3.2 Interpolation

Interpolation is one of the important techniques used in medical image processing in a variety of different applications (Lehmann et al., 1999; Thevenaz et al., 2000). During registration the mapping of corresponding points as per transformation model requires them to be mapped to a non-grid position. Interpolation interpol-

ates the position of the points with respect to the grid. Intensity values can be estimated in the mapped position using a particular interpolation method (Ibanez et al., 2003). There are various types of interpolation methods used for medical image processing. They can be broadly classified as either filter or function-based. Mean, Gaussian, B-spline and median (Maeland, 1988) based interpolation methods are filter-based interpolation, while nearest neighbour, bilinear, bicubic, Lagrange and splines (quadratic, cubic, B-spline) (Grevera et al., 1999; Lehmann et al., 1999; Shi and Reichenbach, 2006) interpolations are based on functions.

Figure 2.7 shows the most commonly used interpolation methods namely, nearest neighbour, bilinear and bicubic. It shows the new pixel value assigned at position $I^*(x, y)$ using pixel values from image I . Both nearest neighbour and bilinear interpolations are less computationally intensive but offer poorer sub-pixel accuracy. Bicubic interpolation is more popular due to its higher accuracy in comparison to nearest neighbour and bilinear as well as being less computationally complex than spline interpolation (Wang et al., 2008). Spline interpolation (Pan et al., 2012), which represents the image intensity using a spline function, but incur higher computational cost. While higher-order spline functions are smoother, providing considerable accuracy in some cases, if however they are generalised, they can lead to overfitting. Meanwhile Fourier analysis-based windowed *sinc* interpolation (Meijering et al., 1999), is formed by multiplying a sampled *sinc* function (Olver et al., 2010) by a windowing function. This produces very high accuracy, but is not chosen for an iterative registration process since it involves a high computational overhead. It is used later, once the optimal transformation values are achieved, to re-sample the final registered image (Ibanez et al., 2003).

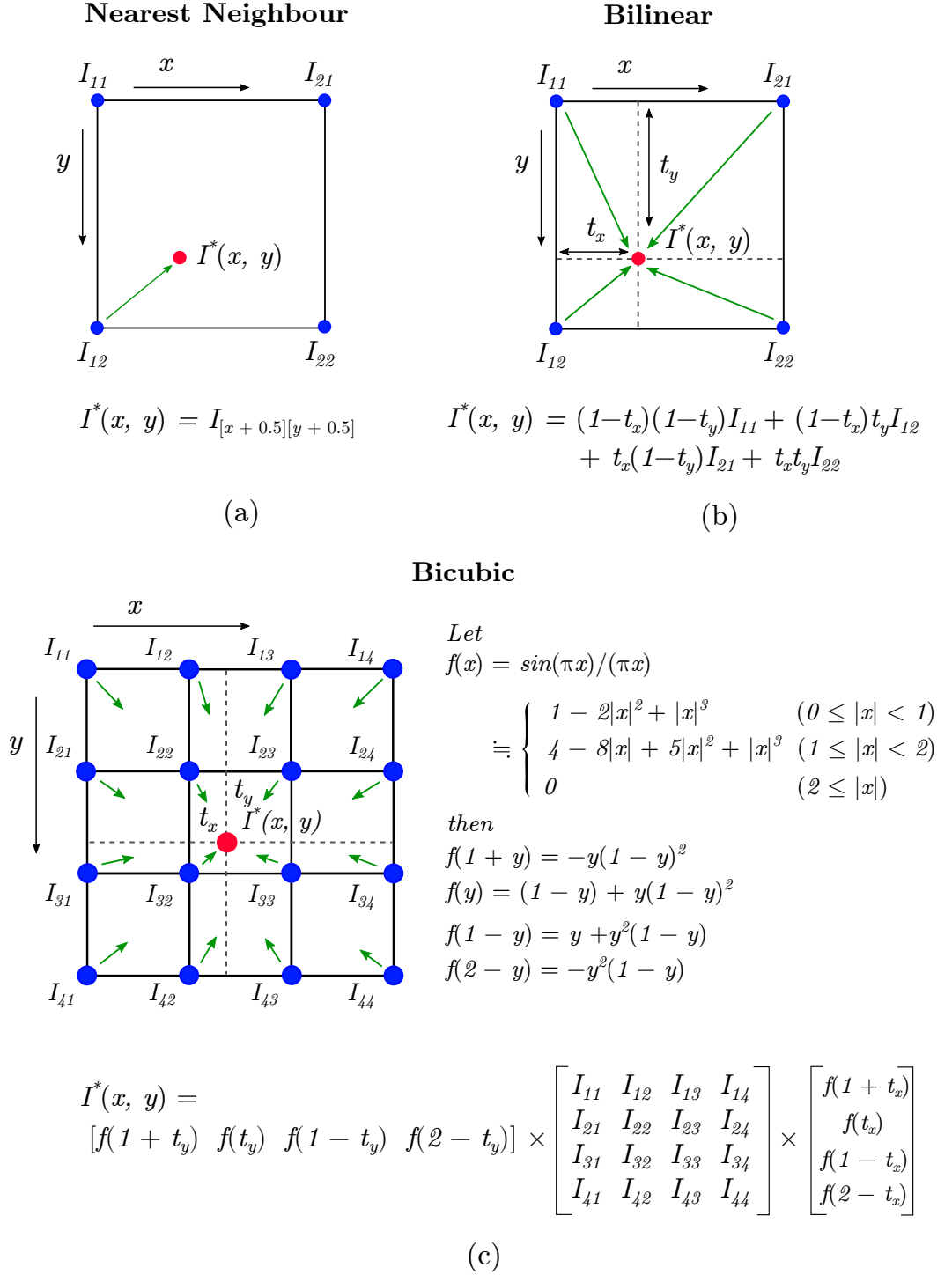


Figure 2.7: (a) Nearest neighbour, (b) Bilinear and (c) Bicubic Interpolation Methods.

While all the above mentioned interpolation methods, especially higher order methods, introduce new intensity values for the interpolated image, partial volume interpolation (PVI) (Maes et al., 1997) ensures that no new intensity values are

generated. In fact in traditional sense, it does not qualify as an interpolation method, since it directly updates the joint histogram, without creating any new pixel values at non grid positions. While PVI also results in abrupt changes in the joint histogram dispersion and, hence, has a serious influence on registration process. Later generalised partial volume joint histogram estimation (GPVE) was proposed (mei Chen and Varshney, 2003), which reduced the abrupt changes using B-spline instead of linear interpolation in processing GPVE, reducing the local optima effectively (Jacquet et al., 2010). Recently, Gaussian, cubic spline and notch general partial volume interpolation are proposed and their perform is better than others in its class (Pan et al., 2012). Although most of the medical registration applications are software-based, many have been implemented in hardware due to their high computational cost (Lehmann et al., 1999; Moses et al., 2011).

2.3.3 Similarity Measure

A similarity measure gives the ability to determine the level of global correspondence between two images. During the registration process the parameters of a given transformation model are changed, based on the optimisation technique until the similarity measure reaches a maximum value (Wilson and Laxminarayan, 2007). Hence the choice of similarity measure along with optimisation method plays a crucial role for a successful outcome of a registration process. In all, similarity measure quantifies the spatial alignment between two images. Various intensity-based similarity measures such as sum of squared difference (SSD) (Friston et al., 1995), sum of absolute difference (SAD) (Lemieux et al., 1994), correlation coefficient (CC) (Cideciyan, 1995), NCC (Rogelj and Kovačič, 2003) and ratio image

uniformity (RIU) (Holden et al., 2000) have been proposed for monomodal registration processes. These measures do not perform well in all cases. While SSD is highly sensitive to Gaussian noise, SAD is less sensitive to outliers on the subject boundaries. CC, NCC and RIU perform well in these conditions, but are highly sensitive to non uniform illumination in the images. Other similarity measures are entropy of difference image (DE), pattern intensity (PI), gradient correlation (GC) (Wu et al., 2009) and gradient difference (GD) (Penney et al., 1998). While DE and PI are robust against large difference of intensity values between monomodal images, GC and GD are highly sensitive to thin line structures.

Most of the these similarity measures have been prominently used for monomodal images and are known for their inability to perform multimodal registration (Gao et al., 2008). This is due to the fact that all of them assume a linear relationship between the intensity values of the two images. This is mostly the case when both the images belong to the same modality and a monomodal registration is undertaken. On the other hand, multimodal images do not share any global linear relationship between each other in terms of intensity values. However, predominant relationships can be established between the intensity values of smaller neighbourhoods of the images. This makes local correlation (LC) (Netsch et al., 2001) and correlation ratio (CR) (Roche et al., 1998) suitable for multimodal registration, but they suffer from expensive computations. Meanwhile, feature-based approaches instead of using the pixel intensity information, extract key structures like optic disc (Li and Chutatape, 2004) and vascular structural features (Lowe, 2004; Sofka and Stewart, 2006) from the retinal images. Bifurcation point matching approaches such as dual-bootstrap iterative closest point (DB-ICP) (Stewart

et al., 2003) and its variant (Pereira et al., 2012) accomplish registration by using vascular features to grow a bootstrap region. While these methods are computationally fast, their performance is very dependent on the segmentation quality and degree of overlap of the extracted features.

The geometrical features method (GFM) (Gharabaghi et al., 2013) is a recent feature-based method for monomodal retinal image registration. It extracts closed-boundary regions from the green channel of retinal fundus image and computes the affine moment invariant descriptors for each of the binary regions in both reference and sensed images. The affine moment invariant descriptors are moment based descriptors of planar shape, which are derived by means of the algebraic invariants theory and are invariant under general affine transformations (Flusser and Suk, 1993). GFM utilises the first four simplest affine moment invariant descriptors denoted as I_1 , I_2 , I_3 and I_4 (Flusser and Suk, 1993), which are defined as:

$$\begin{aligned}
 I_1 &= (\mu_{20}\mu_{02} - \mu_{11}^2)/\mu_{00}^4 \\
 I_2 &= (\mu_{30}^2\mu_{03}^2 - 6\mu_{30}\mu_{21}\mu_{12}\mu_{03} + 4\mu_{03}\mu_{12}^3 + 4\mu_{21}^3\mu_{03} - 3\mu_{21}^2\mu_{12}^2)/\mu_{00}^{10} \\
 I_3 &= (\mu_{20}(\mu_{21}\mu_{03} - \mu_{12}^2) - \mu_{11}(\mu_{30}\mu_{03} - \mu_{21}\mu_{12}) + \mu_{02}(\mu_{30}\mu_{12} - \mu_{21}^2))/\mu_{00}^7 \\
 I_4 &= (\mu_{20}^3\mu_{03}^2 - 6\mu_{20}^2\mu_{11}\mu_{12}\mu_{03} - 6\mu_{20}^2\mu_{02}\mu_{21}\mu_{03} + 9\mu_{20}^2\mu_{02}\mu_{12}^2 \\
 &\quad + 12\mu_{20}\mu_{11}^2\mu_{21}\mu_{03} + 6\mu_{20}\mu_{11}\mu_{02}\mu_{30}\mu_{03} - 18\mu_{20}\mu_{11}\mu_{02}\mu_{21}\mu_{12} \\
 &\quad - 8\mu_{11}^3\mu_{30}\mu_{03} - 6\mu_{20}\mu_{02}^2\mu_{30}\mu_{12} + 9\mu_{20}\mu_{02}^2\mu_{21}^2 + 12\mu_{11}^2\mu_{02}\mu_{30}\mu_{12} \\
 &\quad - 6\mu_{11}\mu_{02}^2\mu_{30}\mu_{12} + \mu_{02}^3\mu_{30}^2)/\mu_{00}^{11}
 \end{aligned} \tag{2.3}$$

Here, the central moment μ_{MN} of order $(M + N)$ of binary 2D region is defined as:

$$\mu_{MN} = \iint_{-\infty}^{\infty} (x - \bar{x})(y - \bar{y})dx dy \quad M, N = 0, 1, 2, \dots \tag{2.4}$$

Here, (\bar{x}, \bar{y}) are the coordinates of the center of gravity of the binary region. For example, the central moment using $M = 1$ and $N = 2$, is denoted as μ_{21} . The complete proof and detailed discussion on the the properties of invariants is discussed in (Maitra, 1979) and (Amanatiadis et al., 2009). Once the affine moment invariant descriptors are computed, region matching is performed using the feature distance (Gharabaghi et al., 2013) between them. The three most likely corresponding regions are then selected and used to estimate the registration parameters between the reference and sensed images. While GFM has inherent computational simplicity, it exhibits poor resilience to noise in images, especially when higher-order invariant descriptors are selected (Rodrigues, 2000).

Similarly, for multimodal retinal image registration - vascular bifurcation structures (RIR-BS) has performed satisfactorily for linear and affine transformation models (Chen et al., 2015, 2011). Unlike other conventional feature point-matching methods, whom largely depend on the branching angles of single bifurcation point, RIR-BS employs a feature structure-matching approach. RIR-BS utilises the bifurcation structure which comprises a master bifurcation point and its three connected neighbours, as shown in Figure 2.8. The characteristic vector of each bifurcation structure consists of the normalized branching angle and length, which is invariant against translation, rotation, scaling, and even modest distortion. The characteristic vector for each bifurcation structure in the reference and sensed image is formulated as:

$$\begin{aligned}\Lambda &= \{lengths, angles\} \\ &= \{l_1, l_2, l_3, \gamma_1, \gamma_2, \gamma_3, \gamma_4, \gamma_5, \gamma_6, \gamma_7, \gamma_8, \gamma_9, \gamma_{10}, \gamma_{11}, \gamma_{12}\}\end{aligned}\tag{2.5}$$

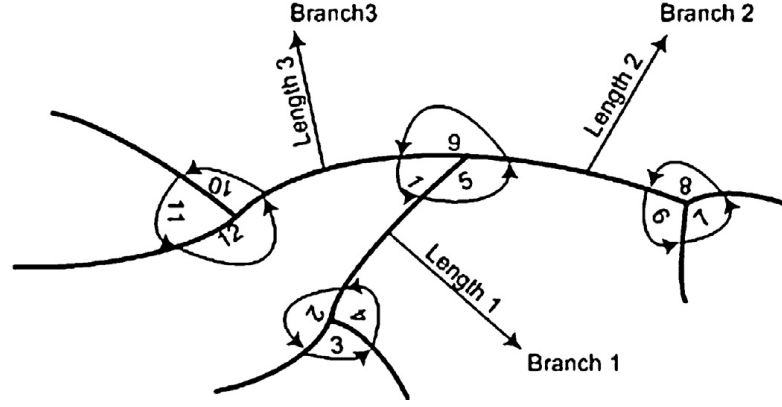


Figure 2.8: Bifurcation structure comprising of a master bifurcation point and its three connected neighbours. Figure reproduced from (Chen et al., 2015).

Here, l_i and \mathcal{V}_i represent the normalised length and angle respectively:

$$l_i = \text{ith branch length} / \text{sum} \{ \text{length1}, \text{length2}, \text{length3} \} \quad (2.6)$$

$$\mathcal{V}_i = \text{ith branch angle in degree} / 360^\circ$$

The corresponding bifurcation structure pairs from reference and sensed image are matched in order to align them. Although, these normalised bifurcation structures can greatly reduce the ill-posed nature of the matching process, this method can only be deployed as long as the vasculature pattern can be segmented reliably.

Various graph measures-based on minimal spanning trees (Hero et al., 2002; Ma et al., 2000; Neemuchwala et al., 2004), have been also proposed, as an alternative to histogram-based measures since they all eliminate the need of estimating the intensity densities of images. They can be extended to registration of more than two images, but require large memory and computing resources compared to histogram-based measures. Since MI and its variants have been extensively used as similarity measures for image registration, especially in the field of medical ima-

ging (Pluim et al., 2003), *Section 2.4* is dedicated to critically discuss them. The next section discusses the role of optimisation in the registration process.

2.3.4 Optimisation

In order to find the maximum value of similarity measure for a given registration process, an optimisation problem is formulated on the basis of number of parameters used for transformation (Hajnal and Hill, 2001). The choice of the transformation is essentially dependent on the application and its geometrical complexity (i.e. degrees of freedom). Although a optimal solution is guaranteed by exhaustive search, its computational expense is proportional to size of the search space as well as the number of parameters used for transformation and, hence, becomes infeasible as they increase (Khalifa et al., 2011). Therefore, this forms the motivation to explore refined search strategies or optimisation methods which can help to find the maximum value for a given similarity measure.

A good optimisation method should be reliable and be capable of finding the best possible transformation quickly (Goshtasby, 2012). The choice of optimisation method hence requires a good understanding of the registration problem along with the constraints that can be applied and a knowledge of numerical analysis. Many optimisation methods have been introduced and adopted for the registration process, on the basis of the transformation parameters, similarity measure, time constrains and required accuracy of registration.

Optimisation methods can be formally classified in terms of function-based, such as Powell (Collignon et al., 1995; Maes et al., 1997), Downhill Simplex

(Meyer et al., 1997) methods or gradient-based, such as simple (Rueckert et al., 1999; Wells III et al., 1996) and conjugate gradient descent (Hayton et al., 1999), stochastic gradient approximation (De Craene et al., 2004; Spall, 1992).

Downhill Simplex performs well in the absence of local distortions and can be used by combining all the transformation parameters in one function (Press et al., 2007). Relaxation Matching (Price, 1985) and Dynamic Programming (Milios, 1988) gives the advantage of handling local distortion along with overall global transformation, in case of non-rigid registration. Various other prominently used methods in the literature, including Newton-Raphson (Miga, 2003), Levenberg-Marquardt (Kabus et al., 2004; Maes et al., 1999; Thevenaz et al., 1995), simulated annealing (Mazur et al., 1993), Monte Carlo (Wong, 2010) and evolutionary computing methods such as particle swarm (Rezaei et al., 2009) and genetic algorithms (Damas et al., 2011a). Hierarchical methods (Bajcsy and Kovačič, 1989; Klein et al., 2007; Lester and Arridge, 1999; Maes et al., 1999; Thevenaz and Unser, 2000) for registration of multi-resolution medical images are also used for registering low resolution versions of the image and then progressed to higher resolution, which helps enhancing the optimisation speed and robustness of registration. Using different filters, e.g. Gaussian (Bajcsy and Kovačič, 1989; Burt and Adelson, 1983; Suárez et al., 2002), Spline (Thevenaz et al., 1995, 1998; Thevenaz and Unser, 1997; Unser et al., 1993) and Wavelet-based pyramids (Allen et al., 1993; Amit, 1994; Deubler and Olivo, 1997; Gefen et al., 2003; Wu et al., 2000) are created for multi-resolution medical images (Jenkinson and Smith, 2001; Rohlfing et al., 2003; Rueckert et al., 1999; Thevenaz et al., 1995; Wirth et al., 2002; Yeung et al., 1998).

As discussed before, since the overall performance of a registration algorithm depends on the effectiveness of the optimisation method. This in turn, depends on the number of iterations needed for the algorithm to converge. Hardware-based implementations of MIR consider the choice of optimisation method on the basis that they are fully or partially parallelise (Cooper et al., 2011; Shams et al., 2010; Tsoi et al., 2009). Various comparative evaluations for the above mentioned optimisation techniques have been conducted in the past (Khalifa et al., 2011) which investigated them on the basis of different factors which impact the performance of the registration such as accuracy, computational cost and number of iterations needed. Amongst them Powell and its variants, which are zero-order methods, have shown a balanced performance and hence been popularly adopted for a variety of registration applications in the medical imaging domain (Rios and Sahinidis, 2012; van der Bom et al., 2011).

Algorithm 2.1 shows the pseudo-code of the Powell optimisation method, considering the maximisation of a sample function $f(x)$ involving W variables. Furthermore, Powell method can be utilise with Brent line search, which combines a parabolic interpolation with the golden section algorithm (Press et al., 2007). Hence together Powell Brent is known to provide an overall fast and accurate local search performance (Pluim et al., 2003; Zitová and Flusser, 2003). In case of MIR, it can iteratively search in a given parameter space such as (t_x, t_y, θ, S) in case of similarity transformation model, to locate the highest value of the similarity measure by individually maximising one parameter at a time. Subsequent iterations then start from the maximum of these four parameters until a predefined tolerance threshold ϵ is met.

Algorithm 2.1 Pseudo Code for Powell optimisation method

Input: Function $f(x)$

Variables: W design variables; x_0 initial starting point; l_k starting vector; k index varying from 1 to W ; ϵ tolerance threshold.

Output: Maximum value of $f(x)$

1: Choose a point x_0 in the design space.

2: Choose the starting vectors l_k , $k = 1, 2, \dots, W$. (the recommended choice is $l_k = \gamma_k$, where γ_k is the unit vector in the x_k -coordinate direction).

3: START

FOR each k

Maximise $f(x)$ along the line through x_{k-1} in the direction of l_k .

Let the maximum point be x_k .

END LOOP

$l_{W+1} \leftarrow x_0 - x_W$

Maximise $f(x)$ along the line through x_0 in the direction of l_{W+1} .

Let the maximum point be x_{W+1} .

IF $|x_{W+1} - x_0| < \epsilon$ THEN

GOTO STEP 4.

END IF

FOR each k

$l_k \leftarrow l_{k+1}$ (l_1 is discarded and the other vectors are reused).

END LOOP.

4: END

Hence, the iterative registration process shown in Figure 2.5 is then concluded by saving the final transformation value τ_{final} using (2.1), at which the reference and sensed image are best registered.

The next section focuses on MI and its variants used as similarity measures in MIR.

2.4 MI and its variants for multimodal MIR

While MI originated in the field of information and communication theory some decades ago, it was first introduced into the field of image registration during the mid 1990s, by two independent research groups (Collignon et al., 1995; Maes et al., 1997) and (Wells III et al., 1996). While both the versions were the same, they were formulated independently and differently. As mentioned earlier, the prime success of MI as a similarity measure is because it makes very few assumptions about the images to be registered. It only assumes statistical dependence between the images, which helps it in enhancing its performance, especially for multimodal registration, where the relationship between the intensity values of two images is non-linear.

Research related to MI began in 1980s with the start of intensity-based registration methods. These methods had an advantage over traditional registration methods, since no prior segmentation or feature extraction was needed. While initial intensity-based methods involved image registration by matching the moments (Flusser and Suk, 1994) and principal axis (Alpert et al., 1990), later correlation-based approaches (Manduchi and Mian, 1993) emerged. However, these techniques were not effective for multimodal image registration because they only used intensity information (van den Elsen et al., 1993).

In 1993, the first similarity measure for multimodal data was proposed and known as the Woods Criterion (WC) (Woods et al., 1992, 1993), which quantified the relationship between the intensity values for corresponding points for a known region. It needed however, the regions of both images to be segmented manually

before registration. This was overcome by an adaptation from (Hill et al., 1993), which used a feature space in the form of a 2D joint histogram. At the correct alignment, the histogram is found to be more focused and dispersed during misaligned positions. Later, Hartley introduced Entropy as a similarity measure (Collignon et al., 1995), which was originally developed in communication theory (Hartley, 1928). Hartley's entropy was extended by Shannon, which did not assume that each symbol was equally likely to occur but could be expressed as a probability distribution (Shannon, 1948). The final phase of this research movement was the independent introduction of MI by (Viola and Wells, 1995) and (Collignon et al., 1995). While Viola and Wells technique used Parzen window density estimation (Wells III et al., 1996), Collignon's formulation used a frequency histogram technique for Kullback-Leiber or Shannon's information (Maes et al., 1997).

Given the reference image I_R and its probability $p_{I_R}(I_R)$, the entropy $H(I_R)$ is defined as:

$$H(I_R) = -\sum_{I_R} p_{I_R}(I_R) \log_2 p_{I_R}(I_R) \quad (2.7)$$

Correspondingly, for sensed image I_S , $H(I_S)$, is defined as:

$$H(I_S) = -\sum_{I_S} p_{I_S}(I_S) \log_2 p_{I_S}(I_S) \quad (2.8)$$

Then, the joint histogram is constructed with the entries $U_{I_R I_S}$ using b number of bins. U is the total count of possibilities, while U_{I_R} and U_{I_S} are count of possibility for I_R and I_S only, respectively. The marginal probability $p_{I_R}(I_R)$ and

$p_{I_S}(I_S)$, and the joint probability $p_{I_R I_S}(I_R, I_S)$ are determined by:

$$p_{I_R}(I_R) = \frac{U_{I_R}}{U} \quad (2.9)$$

$$p_{I_S}(I_S) = \frac{U_{I_S}}{U} \quad (2.10)$$

$$p_{I_R I_S}(I_R, I_S) = \frac{U_{I_R I_S}}{U} \quad (2.11)$$

Correspondingly, the joint entropy $H(I_R, I_S)$ are defined as:

$$H(I_R, I_S) = - \sum_{I_R, I_S} p_{I_R I_S}(I_R, I_S) \log_2 p_{I_R I_S}(I_R, I_S) \quad (2.12)$$

The conditional entropies $H(I_R | I_S)$ and $H(I_S | I_R)$ are defined as:

$$\begin{aligned} H(I_R | I_S) &= - \sum_{I_R, I_S} p_{I_R I_S}(I_R, I_S) \log_2 p_{I_R I_S}(I_R | I_S) \\ &= - \sum_{I_R, I_S} p_{I_R I_S}(I_R, I_S) \log_2 \left\{ \frac{p_{I_R I_S}(I_R, I_S)}{p_{I_S}(I_S)} \right\} \end{aligned} \quad (2.13)$$

$$\begin{aligned} H(I_S | I_R) &= - \sum_{I_R, I_S} p_{I_R I_S}(I_R, I_S) \log_2 p_{I_R I_S}(I_S | I_R) \\ &= - \sum_{I_R, I_S} p_{I_R I_S}(I_R, I_S) \log_2 \left\{ \frac{p_{I_R I_S}(I_R, I_S)}{p_{I_R}(I_R)} \right\} \end{aligned} \quad (2.14)$$

The strength of dependence between I_R and I_S is measured by their MI value

as:

$$\begin{aligned}
MI(I_R, I_S) &= H(I_R) + H(I_S) - H(I_R, I_S) = H(I_R) - H(I_R|I_S) \quad (2.15) \\
&= H(I_S) - H(I_S|I_R) \\
&= - \sum_{I_R, I_S} p_{I_R I_S}(I_R, I_S) \log_2 \left\{ \frac{p_{I_R I_S}(I_R, I_S)}{p_{I_R}(I_R) p_{I_S}(I_S)} \right\}
\end{aligned}$$

To illustrate how to calculate the MI, consider the following scenario of two matrices (representing an image dataset of spatial dimensions 3×3 pixels) I_R and I_S is as follows:

$$\text{Let, } I_R = \begin{bmatrix} 1 & 2 & 3 \\ 3 & 2 & 3 \\ 1 & 1 & 1 \end{bmatrix} \text{ and } I_S = \begin{bmatrix} 3 & 3 & 1 \\ 2 & 2 & 1 \\ 1 & 3 & 1 \end{bmatrix}.$$

Then, the joint probability distribution can be tabulated for one to one correspondence, using $b = 3$ as:

		I_R			
		1	2	3	$p_{I_S}(I_S)$
I_S	1	2/9	0	2/9	4/9
	2	0	1/9	1/9	2/9
	3	2/9	1/9	0	3/9
$p_{I_R}(I_R)$		4/9	2/9	3/9	

Here, the rightmost column and bottom row consists of the marginal probabilities $p_{I_S}(I_S)$ and $p_{I_R}(I_R)$, respectively. Similarly, the first three columns and rows

show the joint probability $p_{I_R I_S}(I_R, I_S)$. For example, the joint probability value in first column and row denotes the one to one correspondence where elements of I_R and I_S are both equal to 1. Moreover, this 2D histogram table shows all the combinations of one to one correspondence possible, with elements equal to 0 highlighting that the particular combination does not exist.

Finally, the calculation of MI using (2.15) is:

$$\begin{aligned}
 MI(I_R, I_S) &= \frac{2}{9} \log_2 \left(\frac{2/9}{16/81} \right) + \frac{2}{9} \log_2 \left(\frac{2/9}{12/81} \right) + \frac{1}{9} \log_2 \left(\frac{1/9}{4/81} \right) + \frac{1}{9} \log_2 \left(\frac{1/9}{6/81} \right) \\
 &\quad + \frac{2}{9} \log_2 \left(\frac{2/9}{12/81} \right) + \frac{1}{9} \log_2 \left(\frac{1/9}{4/81} \right) \\
 &= \frac{2}{9} \log_2 \left(\frac{9}{8} \right) + \frac{2}{9} \log_2 \left(\frac{9}{6} \right) + \frac{1}{9} \log_2 \left(\frac{9}{4} \right) + \frac{1}{9} \log_2 \left(\frac{9}{6} \right) \\
 &\quad + \frac{2}{9} \log_2 \left(\frac{9}{6} \right) + \frac{1}{9} \log_2 \left(\frac{9}{4} \right) \\
 &\approx 0.6227.
 \end{aligned}$$

Here, the MI value quantifies the spatial alignment between I_R and I_S . Now considering the scenario where I_S is rotated $+90^\circ$, while I_R remains unchanged as follows:

$$I_R = \begin{bmatrix} 1 & 2 & 3 \\ 3 & 2 & 3 \\ 1 & 1 & 1 \end{bmatrix} \text{ and } I_S = \begin{bmatrix} 1 & 2 & 3 \\ 3 & 2 & 3 \\ 1 & 1 & 1 \end{bmatrix}.$$

Then, the joint probability distribution can be tabulated as:

		I_R			
		1	2	3	$p_{I_S}(I_S)$
I_S	1	4/9	0	0	4/9
	2	0	2/9	0	2/9
	3	0	0	3/9	3/9
$p_{I_R}(I_R)$		4/9	2/9	3/9	

and

$$\begin{aligned}
MI(I_R, I_S) &= \frac{4}{9} \log_2 \left(\frac{4/9}{16/81} \right) + \frac{2}{9} \log_2 \left(\frac{2/9}{4/81} \right) + \frac{3}{9} \log_2 \left(\frac{3/9}{9/81} \right) \\
&= \frac{4}{9} \log_2 \left(\frac{9}{4} \right) + \frac{2}{9} \log_2 \left(\frac{9}{2} \right) + \frac{3}{9} \log_2 \left(\frac{9}{3} \right) \\
&\approx 1.5305.
\end{aligned}$$

Evidently, the MI value has increased since I_R and I_S are both now spatially registered. Although, the marginal probabilities $p_{I_R}(I_R)$ and $p_{I_S}(I_S)$ are same in both scenarios, the joint probability has decreased in the latter case. This is highlighted in the second scenario by the tabulated distribution being noticeably more concentrated compared with the earlier misaligned registration. Moreover, it is clear MI uses the one-to-one correspondence without assuming any neighbourhood relationships.

Since the original proposals of MI, various researchers have contributed to the performance, robustness, and other relevant issues of MI. Many research groups then demonstrated its properties using different medical imaging data (Gao et al.,

2008; Holden et al., 2000; Studholme et al., 1996b, 1997; West et al., 1997) and clinical applications (HAWKES, 1998; Meyer et al., 1997). While MI has been successfully applied to a range of modalities, there are few cases, when the measure does not provide correct spatial alignment, due to the presence of local or spurious global maxima (Rodriguez-Carranza and Loew, 1998), this is particularly observed when the regions of overlaps are small (Studholme et al., 1998).

Two independent groups (Rodriguez-Carranza and Loew, 1998; Studholme et al., 1998) proposed NMI, which improved the behaviour of MI, by significantly enhancing the overlap invariance of the measure. NMI can be denoted as:

$$NMI(I_R, I_S) = \frac{H(I_R) + H(I_S)}{H(I_R, I_S)} \quad (2.16)$$

Later, multivariate and high dimensional versions of MI and NMI (Gan and Chung, 2005; Meyer et al., 1999; Wang and Shen, 2006; Zhang and Rangarajan, 2005) were proposed, which extended the registration to three or more images and provided a faster convergence and better final accuracy. Although these MI variants have been popular, their performance degrades for some modalities. For example, in case of retinal image registration their performance is degraded due to the presence of innately challenging characteristics (Kubecka and Jan, 2004). These similarity measures had a disadvantage that they ignore the spatial information i.e. if the 2D histograms of registering images are the same, the images were assumed to be matched, which was not true if the intensity values are rearranged in a particular way (Rueckert et al., 2000).

This gave researchers an opportunity to improve the MI by incorporating spatial information in various ways. It was proposed to combine MI with connected region labelling in the past (Studholme et al., 1996a) and then HO-MI, (Rueckert et al., 2000) using co-occurrence information matrices of neighbouring intensities for better registration results.

GMI combined the gradient information with MI (Pluim et al., 2000a) which helps to align images even at lower sampling resolutions, achieving better global maximum and have very low interpolation induced local maxima. For a given 2D reference and sensed image pair I_R and I_S , it computes two partial derivatives for each sample point x and x' in I_R and I_S , forming together the gradient vector, calculated by convolving the image with the appropriate first derivatives of a Gaussian kernel having scale ψ . Thus the angle $\phi_{x,x'}(\psi)$ between the gradient vectors is defined by:

$$\phi_{x,x'}(\psi) = \arccos \frac{\nabla x(\psi) \cdot \nabla x'(\psi)}{|\nabla x(\psi)| |\nabla x'(\psi)|} \quad (2.17)$$

Here, $\nabla x(\psi)$ denotes the gradient vector at point x of scale ψ and $|\cdot|$ denotes the magnitude. Furthermore, since multimodal images can have different gradient value at best aligned position, a weighting function κ is incorporated as follows:

$$\kappa(\phi) = \frac{\cos(2\phi) + 1}{2} \quad (2.18)$$

Thus, GMI between I_R and I_S can be defined as:

$$GMI(I_R, I_S) = G(I_R, I_S) MI(I_R, I_S) \quad (2.19)$$

with the gradient term $G(I_R, I_S)$ as:

$$G(I_R, I_S) = \sum_{(x, x') \in (I_R \cap I_S)} \kappa(\phi_{x, x'}(\psi)) \min(|\nabla x(\psi)|, |\nabla x'(\psi)|) \quad (2.20)$$

The gradient term not only seeks to align locations of high gradient magnitude, but also aims for a similar orientation of the gradients at these locations. Although GMI perform better for low-resolution images and decrease interpolation-induced local minima, it underperforms in the presence of noise. In a similar approach, Holden et al. (Holden et al., 2004) used Gaussian scale space derivatives as local image structure to integrate another channel with MI to propose Multi-channel MI (MC-MI).

Russakoff et al. (Russakoff et al., 2004) proposed a novel extension to MI called RMI, which use local regions to compute MI and considers high dimensional distributions to be normally distributed. RMI takes neighbouring pixels into account to incorporate spatial information. Essentially, for each pixel, a vector of all the local intensities is created for I_R and I_S . It provides much greater relational information for each pixel, it also means that many intensities need to be considered. Therefore, using a joint histogram to represent this information would lead to high computational cost. To overcome this complexity problem, the samples are replaced by a covariance matrix which substantially reduces the amount of data. The covariance matrix represents the relation between the original vector elements by approximating the joint intensities by a normal distribution.

Considering a normally distributed d -dimensional distribution, the entropy H_g can be computed in terms of covariance matrix Σ_d as:

$$H_g(\Sigma_d) = \log((2\pi e)^{\frac{d}{2}} \det(\Sigma_d)^{\frac{1}{2}}) \quad (2.21)$$

This is mathematically equivalent to transforming the points into a new basis, where each dimension is uncorrelated, projecting the data onto each of the d new axes, and summing the entropies of those d independent 1-dimensional distributions (Shannon, 1948). It allows RMI to offer a clear improvement over standard MI, although computing the original matrix can still be computationally demanding. This becomes even more apparent in difficult registration problems where a larger neighbourhood radius is required. Similarly, Tomazevic et al. (Tomazevic et al., 2004) contributed a Multi-feature MI (MF-MI). While they had a common advantage of approximating the distribution as normal, still the calculation burden was computationally expensive.

Various other hybrid approaches also combine different aspects of the afore-said feature and intensity methods, as for example, by using extracted vascular structures (Chanwimaluang et al., 2006) together with spatial information in feature neighbourhood MI (FNMI) (Legg et al., 2008, 2009, 2015). These techniques use covariance matrices to reduce the data complexity instead of high-dimensional histograms, though as the spatial information increases, so commensurately does the corresponding computational cost. Other contributors have combined the spatial information in different ways but still the computation overhead is significant (Butz and Thiran, 2001; Chappelow and Madabhushi, 2010; Kang et al., 2011; Luan et al., 2005, 2008; Woo et al., 2015; Yang et al., 2006; Yi and Soatto, 2011; Zhang et al., 2011; Zheng, 2010; Zouqi et al., 2010).

Although MI variants have found numerous clinical applications, there are still many issues which pose challenges (Pluim et al., 2003). As discussed in *Section 2.2*, the presence of intensity variations due to variety of reasons poses a problem in multimodal imaging, which includes INU and the radio frequency inhomogeneity in MRI imaging. While MI can also be computed locally, i.e within the image by dividing it into sub images and then performing registration, but then the significant problem is that with the decreased image size, the statistical power of MI is reduced drastically. To improve registration in such cases images are registered rigidly using global MI and then locally in sub images using local MI (Maintz et al., 1998) and interpolated finally using Thin-Plate Splines, at the cost of computational complexity. Similar results are also reported using HO-MI (Denton et al., 1999; Rueckert et al., 2000, 1999), and other approaches which improve the MI performance by using varying number of bins, based on image characteristics instead of choosing fixed number of bins (Legg et al., 2007).

MI and its spatial information-based variants have also been used for non-rigid registration, giving the flexibility of local estimation of the joint histogram, by dividing the image into small regions (Garcia-Arteaga and Kybic, 2008; Russakoff et al., 2004; Zhang et al., 2011). However, as the subdivided image parts become too small, the small samples can limit the estimation performance of the local histogram. Several adaptations have been proposed to overcome this. Likar and Pernuš (2001) combined the local and global intensity distribution and Andronache et al. presented a local intensity remapping to allow the use of cross correlation as similarity measure in the smaller sub-images (Andronache et al., 2006, 2008). Weese et al. (1999) argued that, when the image parts are sufficiently small, they

will likely contain not more than two different structures that are rather homogeneous and hence used CC straight away, without any intensity remapping but Studholme et al. (2006) uses total correlation between the intensity joint histogram and a third channel representing a spatial label. Loeckx et al. considered the spatial coordinates of sample points in the reference image as a priori known conditions and proposed conditional MI (cMI) as similarity measure (Loeckx et al., 2007, 2010), however, it is found to be ten times slower than the traditional MI measures.

The generalised weighting scheme for spatial information encoding, was extended by Zhuang et al. which proposed a new registration method called as spatially encoded MI (SE-MI) (Zhuang et al., 2011, 2009, 2010). The weighting scheme is used to vary the contribution of pixels to a set of joint histogram tables, which associate with a spatial variable. Similarly, multidimensional self-similarity-based descriptor (Heinrich et al., 2012) and an organ focused MI (OF-MI) are reported, which need pre-processed segmentation of organ to be registered (Fernandez-de Manuel et al., 2014). Recently, two of the popular MI variants, namely GMI and RMI have been extensively employed for different medical registration applications as reported in (Jin et al., 2013; Yang and Fu, 2012; Yang et al., 2015) and (Chen and Lin, 2011; Ng et al., 2015; Pradhan and Patra, 2013, 2015), respectively.

In the past, many dimensionality reduction techniques have been utilised in the registration process. For example, RMI uses a covariance matrix for the fast computation of entropies instead of a high dimensional histogram to provide a rough estimate but as neighbourhood region size increases it becomes computationally intensive. Conventional Principal Component Analysis (PCA) being a versatile

multivariate analysis tool has also been popularly deployed for faster registration (Leng et al., 2015; Lu and Chen, 2007) due to its ability to linearly compress and preserve the randomness of the higher dimensional space with fewer components. But as the dimensionality increases, its covariance-based computation is also high. This led to the development of other methods which do not involve computation of covariance matrix and can be classed as either power iteration or competitive learning methods (Roweis, 1998). The power iteration method such as Arnoldi (Saad, 2011) iteratively update their eigenvector estimates, through repeated multiplication with the matrix to be diagonalised, while competitive learning methods like Sanger (Hancock et al., 1992) find the principal subspace by setting a learning rate parameter.

EMPCA is another effective approach (Roweis, 1998), which iteratively estimates the dominant principal components using an expectation (*e-step*) and subsequent maximisation step (*m-step*). It avoids the computation of entire covariance matrix and effectively finds PCA components with fewer iterations than power iteration and competitive learning methods (Roweis, 1998).

Another popular approach used with PCA computation involves selecting the best subset of significant principal components instead of using all PCA components. Methods like Scree Graph, Broken-stick and their variants (Cangelosi and Goriely, 2007; Jolliffe, 2002) choose a subset by computing the cumulative variance of all components. In contrast, the *Kaiser Rule* (Jackson, 1993; Jolliffe, 2002) retains only those principal components whose eigenvalues are greater than one. Some surveys on the similarity measures also exist, which discuss and compare them in terms of their strengths and applications (Klein et al., 2009; Penney

et al., 1998; Rogelj, 2001; Rogelj and Kovačič, 2003; Skerl et al., 2006, 2008; Wu et al., 2009). Next section provides a discussion on the existing similarity measures and highlight their limitations.

2.5 Discussion

As discussed in the previous section, the registration performance was shown to clearly be dependent on the appropriate choices made in each step, with a complex interdependency existing between different steps of registration, in addition to other challenging factors such as multimodality, interpolation artefacts and the presence of INU and homogeneous content in clinical images (Woo et al., 2015; Zhuang et al., 2011). It is evident the similarity measure used to quantify the level of alignment is one of the prime factors influencing the overall quality of the registration.

In addition to the popular use of MI and its variants as a similarity measure in multimodal MIR, they have also found applications in many other domains including remote sensing and pattern recognition (Argyriou et al., 2015). Since MI computes the statistical relationship between different modalities, it is an appropriate choice for remote sensing image registration and assessment (Chen et al., 2003).

Recent work also shows the prominence of MI in the remote sensing domain, with (Yao et al., 2010) proposing MI for feature selection in high dimensional hyper-spectral imagery and claiming it performs better than conventional classific-

ation methods. Wang and Jin (2012) has also recently implemented a range of MI variants for analysing post-earthquake building damage using pre-event IKONOS optical images and post-event Radarsat-2 and COSMO-SkyMed synthetic aperture radar images. Similarly, MI has also been applied in the field of pattern recognition and machine learning for dimensionality reduction by feature extraction and selection (Wu and Murphy, 2010).

These aforementioned applications of MI are not exhaustive, but they do showcase its versatility as a statistical measure which is especially relevant to the multimodal image registration challenges this thesis addresses.

Table 2.1 provides a comparative summary, presented in chronological order of existing similarity measures in terms of their appropriateness for mono and multimodal registration, characteristic type and computational efficiency. It highlights their drawbacks particularly reflecting their sensitivity to illumination, segmentation quality, use of spatial information and computational cost.

Broadly, the intensity and feature-based similarity measures are sensitive to both noise and the quality of segmentation, with their performance being further degraded in clinical images containing INU and large homogeneous regions. Although, incorporating local spatial information into intensity-based similarity measures to develop hybrid solutions appears promising for multimodal registration, the associated high dimensionality leads to large computational overheads (Goshtasby, 2012). Clearly, the computational efficiency is further impacted when dealing with datasets which include the aforementioned artefacts leading to slower convergence (Oliveira and Tavares, 2014).

SM Method			Monomodal		Registration
			Multimodal		
			Type (I= <i>Intensity</i> , F= <i>Feature</i> , H= <i>Hybrid</i>)		
			Computational Efficiency		
			Limitation		
WC	✓	✓	I	✓	Need to define ROI
SAD	✓	✗	I	✓	Outliers sensitive
SSD	✓	✗	I	✓	Noise sensitive
CC	✓	✗	I	✓	Non-uniform illumination sensitive
MI	✓	✓	I	✓	Small overlapping sensitive
GD	✓	✗	I	✓	Thin line structure sensitive
CR	✓	✓	I	✓	Computationally expensive
NMI	✓	✓	I	✓	Spatial information not used
RIU	✓	✗	I	✓	Non-uniform illumination sensitive
HO-MI	✓	✓	H	✗	Computationally expensive
GMI	✓	✓	H	✓	Noise sensitive
LC	✓	✓	I	✗	Computationally expensive
NCC	✓	✗	I	✓	Non-uniform illumination sensitive
DB-ICP	✓	✗	F	✓	Need accurate segmentation
MC-MI	✓	✓	H	✓	Noise sensitive
MF-MI	✓	✓	H	✗	Computationally expensive
RMI	✓	✓	H	✗	Computationally expensive
DE, PI, GC	✓	✗	I	✓	Unsuitable for multimodality
cMI	✓	✓	H	✗	Computationally expensive
SE-MI	✓	✓	H	✗	Computationally expensive
RIR-BS	✓	✓	F	✓	Need accurate segmentation
GFM	✓	✗	F	✓	Need accurate segmentation
OF-MI	✓	✓	H	✗	Need accurate segmentation
FNMI	✓	✓	H	✗	Computationally expensive

Table 2.1: Comparative summary of major existing similarity measures.

Overall, these observations conclusively confirm the need for a new hybrid similarity measure which combines local regional features with MI to enable the registration of challenging multimodal clinical images while at the same time incurring low computational cost. Since iterative EMPCA offers speed benefits over conventional dimensionality reduction mechanisms, this was the motivation to investigate whether an efficient hybrid EMPCA-based similarity measure could be

framed without compromising registration performance. This was the context for the overarching research question formulated in *Section 1.4* and from which the new EMPCA-MI similarity measure framework presented in this thesis was developed as detailed in *Chapters 4, 6* and *7*.

Before presenting the constituent components of this framework, the next chapter describes the research methodology adopted.

2.6 Summary

This chapter discussed the historical background and developments in the medical imaging domain in brief. It highlighted the need of multimodal registration and an insight into the various challenges of the process. It also presents an elaborative literature review of the various steps involved in the registration process, which include different transformations, interpolations, similarity measures and optimisation methods. Since MI-based similarity measures have been most popular in the MIR domain, a review of them has been presented. Finally, a comparative summary table is presented for the limitations of major existing similarity measures. The next chapter will focus on the research methodology adopted for this thesis.

Chapter 3

Research Methodology

3.1 Introduction

This chapter presents the research methodology adopted to design, develop as well as test and critically evaluate the new hybrid EMPCA-MI similarity measure framework. The methodology is based on the generic MIR model (Oliveira and Tavares, 2014), to critically analyse the robustness of the framework in a variety of practical scenarios, including different levels of misregistration along with the presence of modality artefacts and noise. This enables an equitable performance comparison of the new framework by assessing its impact both qualitatively and quantitatively for a given reference and sensed medical image pair (Khalifa et al., 2011; Zitová and Flusser, 2003). The research methodology utilises images from a variety of mono and multimodal clinical datasets.

3.2 Research Methodology and Test-bed

Medical image registration is a challenging and computationally intensive problem, which has led to its methodological design and development on both dedicated hardware-based prototype and computer-based simulations (Eklund et al., 2013; Fluck et al., 2011; Neri et al., 2008). As discussed in *Section 2.3*, a software implementation offers greater flexibility of rapid development/verification cycle and is more cost effective in comparison to a hardware-based solution. Hence, a software simulation-based test-bed was adopted for developmental and experimental purposes.

Figure 3.1 shows the high-level block diagram of both the methodology and test bed used. It highlights the generic MIR model which uses various inputs and parameter settings; a set of predefined performance metrics for evaluation and a final registration output of a pair of medical images which are spatially aligned and have a minimum registration error. The various phases of the adopted research methodology are summarised in following steps:

1. Critical review of the MIR literature and narrow the research focus to similarity measure in the registration process.
2. Implement an established generic MIR model which will be used as an underlying building block for the evaluation process.
3. Identify the gaps and limitations of existing similarity measures. Iteratively test and develop new ideas for new hybrid EMPCA-MI similarity measure framework which can close the gap with the objective to improve registration

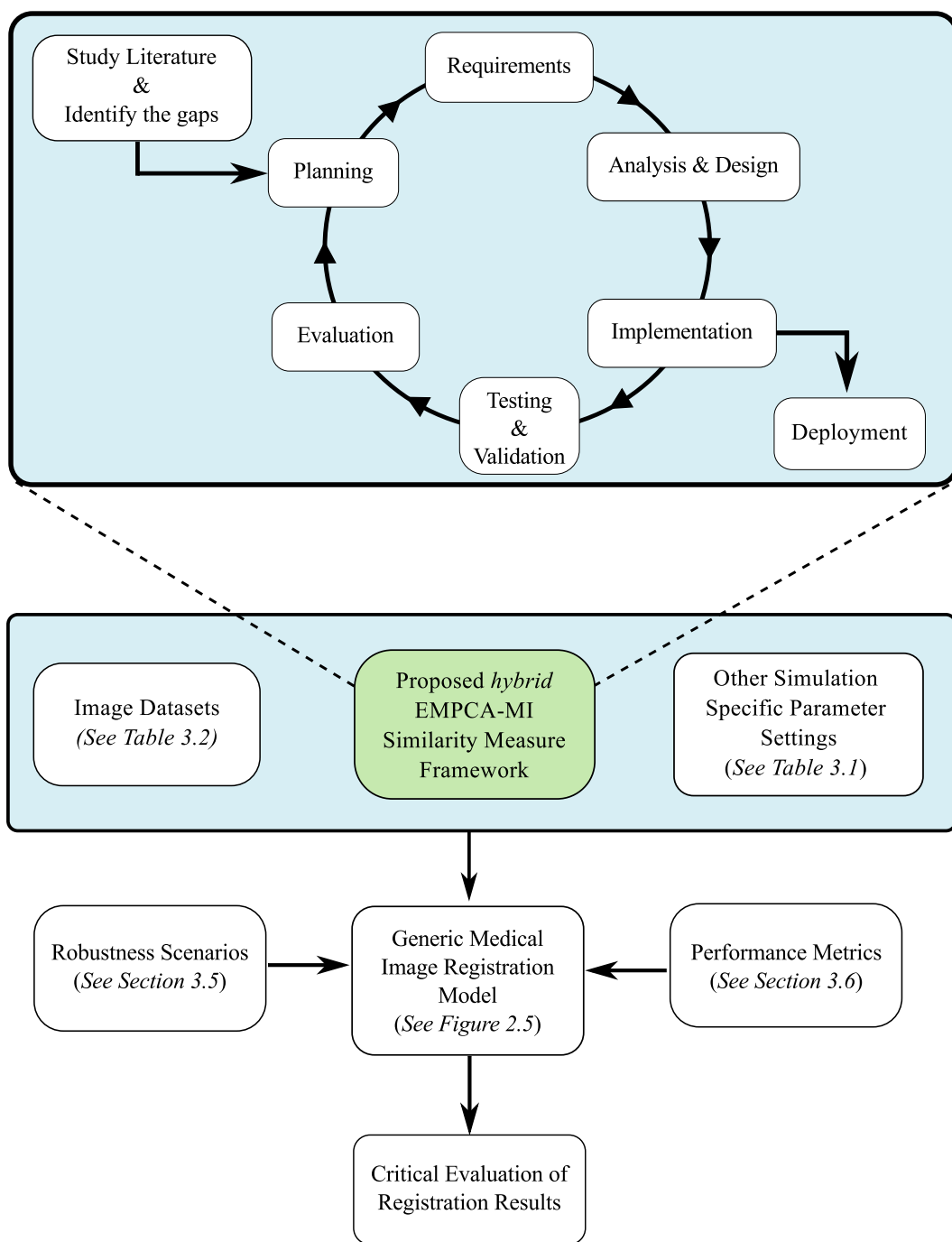


Figure 3.1: Block diagram of the research methodology including the simulation test bed.

performance with respect to the challenging conditions highlighted in *Section 1.3*. This process comprises the development cycle as shown in Figure 3.1, which includes design, development followed by testing and evaluation.

4. Based on the generic MIR model, implement the EMPCA-MI similarity

measure framework (*step 3*) in the simulation environment using a reference and sensed multimodal medical image pair from the image dataset and chosen set of simulation specific parameter settings.

5. Setup a new scenario experiment to validate the level of robustness of the EMPCA-MI similarity measure framework in terms of registration performance for a given level of misregistration and noise artefacts.
6. Perform the registration simulation as in Figure 2.6 and save the final registration results using (2.1).
7. Critically evaluate the registration quality using appropriate performance metrics.
8. Repeat *steps 5-7* until all scenarios have been considered.
9. Analyse the new similarity measure results for a range of scenario experiments and compare with the performance of existing similarity measures.

These steps provide the necessary rigour to critically evaluate the EMPCA-MI similarity measure framework. The next section will consider the registration model set-up.

3.3 Generic MIR Model Setup

As discussed in *Section 2.3*, most of the literature uses a generic registration model for the iterative MIR process which comprises of various steps as shown in Figure 2.5. Since the generic model has been rigorously used in the past for a variety of

medical registration applications (Oliveira and Tavares, 2014), it was considered as the primary choice for the deployment of the new EMPCA-MI similarity measure framework. The transformation assumed for the registration model is *two dimensional rigid* (Brown, 1992) having t_x and t_y translations along the x and y axes, and rotational angle θ for all registrations, except the retinal image datasets, where for the reasons given in *Section 2.3.1*, a *similarity* transformation with uniform scaling S (Gharabaghi et al., 2013; Legg et al., 2008, 2009) is used. For interpolation, in the past various methods have been applied (Zitová and Flusser, 2003) as discussed in *Section 2.3.2*. Of these, bicubic, bilinear and nearest neighbour interpolations were chosen for the generic registration model since they have been shown to produce minimal artefacts compared to other techniques (Acharya and Tsai, 2007; Pluim et al., 2000b) and are computationally faster than higher-order interpolation methods (Thevenaz et al., 2000).

As the behaviour of an interpolator is also dependent on the similarity measure, a rigorous analysis and investigation using these interpolators within the new hybrid EMPCA-MI similarity measure will be undertaken in *Chapter 4*. The most appropriate interpolation method emerging in this analysis will be then used in the subsequent chapters. Furthermore, due to the overall faster and better convergence performance, the *Powell Brent* optimisation (Press et al., 2007) has been adopted for the registration model. Table 3.1 shows the different parameter settings and their empirical selections used in the registration model and these remain fixed throughout the experimental analysis unless otherwise stated.

Generic MIR Model	
<i>Parameter Setting</i>	<i>Selection</i>
Transformation	2D Rigid and Similarity.
Interpolation	Bicubic, Bilinear and Nearest Neighbour
Optimisation	Powell Brent Method
	Tolerance= 10^{-5} (Powell) and 10^{-3} (Brent line search)
	Maximum number of iterations is 10.

Table 3.1: Parameter settings for the generic MIR model.

3.4 Image Datasets

A range of mono and multimodal clinical datasets are chosen for the evaluation of the EMPCA-MI similarity measure framework for the registration experiments. Table 3.2 shows the details of the image datasets.

3.4.1 Mono and Multimodal BrainWeb Dataset

The *BrainWeb* Database (Montreal Neurological Institute and Hospital, nd) comprises multimodal MRI T1, T2 and PD brain images which have been synthesised from a digital phantom (Collins et al., 1998). The *BrainWeb* images are defined at a 1 mm isotropic voxel grid in Talairach space, with dimensions as shown in Table 3.2. They have been used extensively to study the performance of MIR methods (Gholipour et al., 2007; Razlighi et al., 2013) as well as in other applications (Khademi et al., 2014; Nordenskjöld et al., 2014). The main advantages of using this dataset are: i) the ground truth is known a priori, and ii) the imaging parameters can be independently controlled. Since the source for simulation of

Dataset	Modality	Resolution (pixels)	INU(α)	Noise(β)
<i>BrainWeb</i>	MRI T1 (T1)	[181×217×181]	$\alpha_{20}=20\%$ INU, $\alpha_{40}=40\%$ INU	Gaussian ($\mu=0.01$, $\sigma^2=0.01$)
	MRI T2 (T2)			
	MRI PD (PD)			
<i>DRIVE</i>	Fundus	[768 × 584]	INU and noise are not present in these images though they are characterised by having low contrast, non-uniformly illuminated homogeneous regions & different pathologies.	
<i>Brno-Mono</i>	Fundus	[3504 × 2336]		
<i>Brno-Multi</i>	Fundus	[3888 × 2592]		
	SLO	[768 × 768]		

Table 3.2: Various clinical image dataset details (Kolar et al., 2013; Kolar and Tasevsky, 2010; Montreal Neurological Institute and Hospital, 2000, nd).

the functional images is the same digital phantom, one has a systematic means of establishing a gold standard for registration and control over the level of image degradation for all modalities (Collins et al., 1998). For these reasons, this particular database was used for the experimental work and will be referred throughout as *BrainWeb*. Figures 3.2(a) – (c) show a sample set of MRI T1, T2 and PD images of the *BrainWeb* dataset. In order to test the robustness of the EMPCA-MI similarity measure framework, both INU and Gaussian noise-based artefacts were introduced into the *BrainWeb* dataset as will be discussed in *Section 3.5.2*.

3.4.2 Mono and Multimodal Retinal Datasets

As mentioned in *Section 2.2*, retinal images represent very challenging cases for MIR due to the presence of low contrasted homogeneous and non-uniformly illuminated regions. The following two mono and multimodal retinal databases were used for the experimental work:

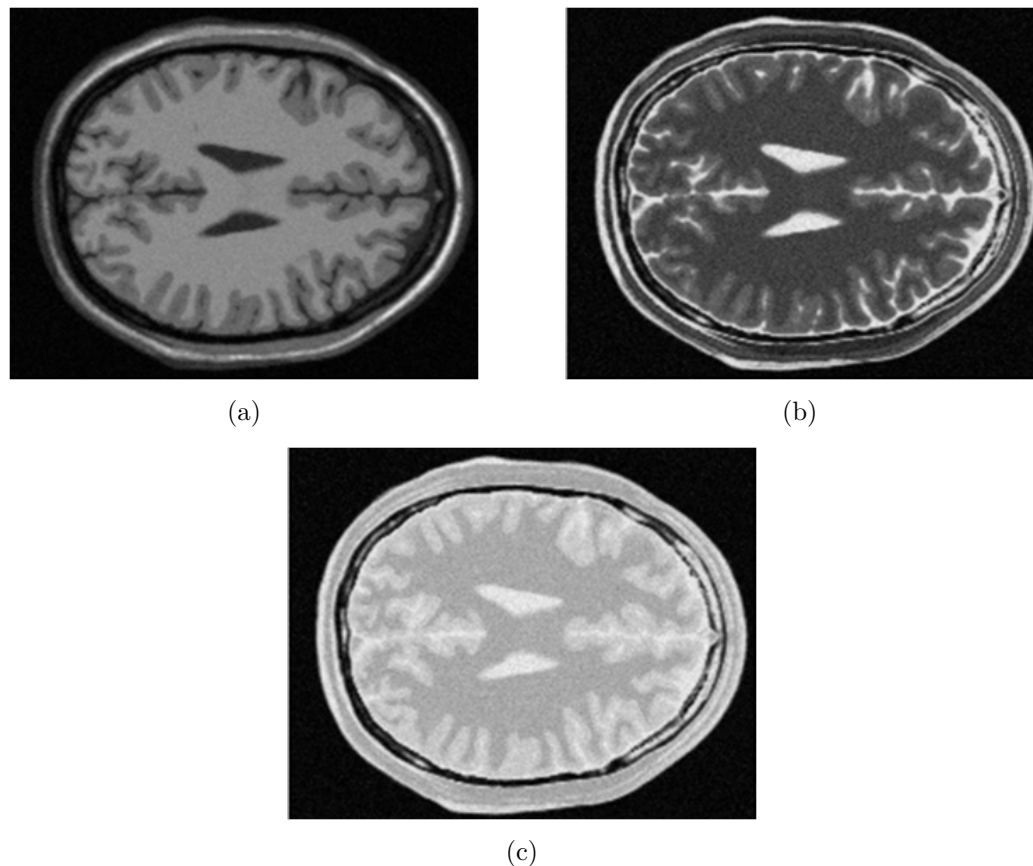


Figure 3.2: Example *BrainWeb* images of brain MRI (a) T1, (b) T2 and (c) PD from (Montreal Neurological Institute and Hospital, nd).

DRIVE Retinal Database

Digital Retinal Images for Vessel Extraction (DRIVE) (Image Sciences Institute, nd) is a clinical database of monomodal retinal images from a diabetic retinopathy screening program in The Netherlands (Staal et al., 2004). This database comprises of twenty colour retinal images acquired with 45° field of view, using a Canon CR5 non-mydratic 3CCD camera. *DRIVE* database was initially established to enable comparative studies on the segmentation of blood vessels in retinal images (Fraz et al., 2012), but has recently been more widely adopted for retinal image registration (Gharabaghi et al., 2013; Patankar and Kulkarni, 2015), due to the lack of publicly accessible retinal datasets (Karnowski et al., 2013; Sim et al.,

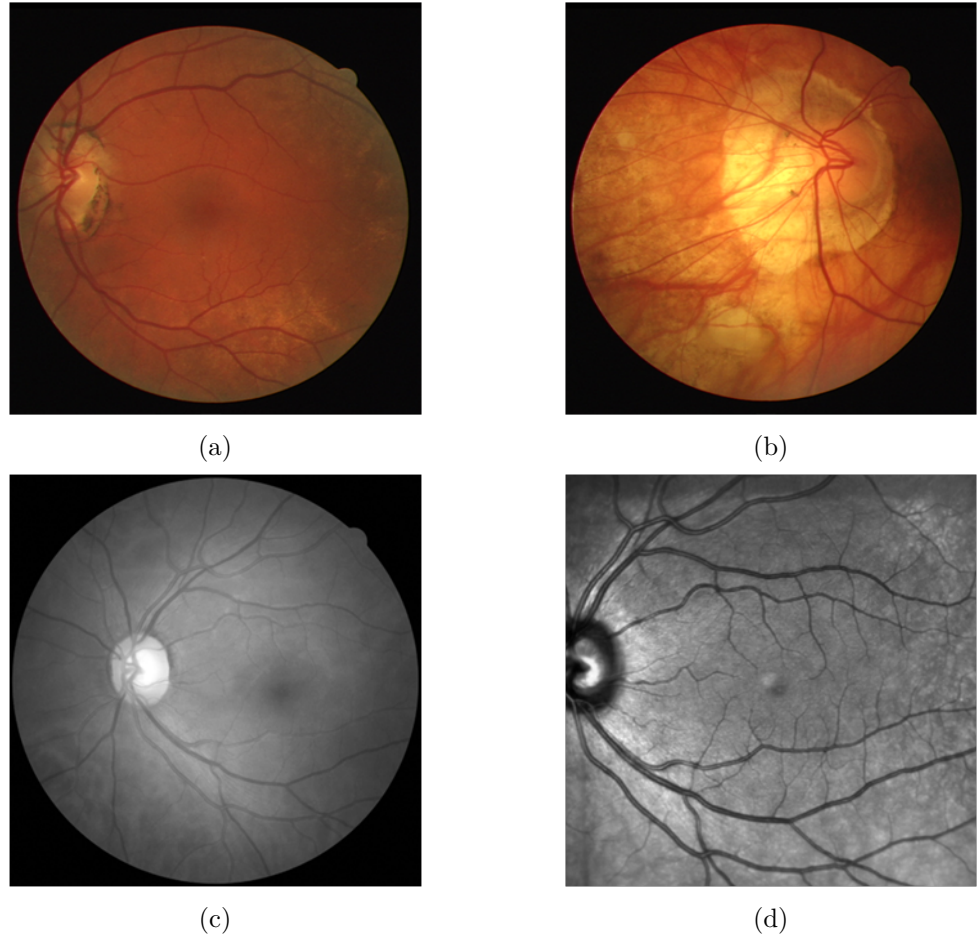


Figure 3.3: Example retinal images (a) and (b) of monomodal colour Fundus retinal images from the *DRIVE* dataset (Image Sciences Institute, nd) and (c) colour Fundus, (d) SLO from *Brno-Multi* dataset (Kolar et al., 2013; Kolar and Tasevsky, 2010).

2015). This database is denoted as the *DRIVE* dataset in this thesis, with Figures 3.3(a) – (b) showing a sample set of retinal images from this dataset.

Brno Retinal Database

This retinal database is maintained by Brno University of Technology and comprises both mono and multimodal retinal datasets (Kolar et al., 2013; Kolar and Tasevsky, 2010), which are denoted throughout this thesis, as *Brno-Mono* and *Brno-Multi* respectively. The *Brno-Mono* dataset comprises 44 colour Fundus im-

age pairs. Each colour Fundus image was acquired with 60° field of view using Canon CF-60UV with digital camera Canon EOS 20D. The *Brno-Multi* dataset comprises 10 pairs of colour Fundus and *grayscale* SLO images. Each colour Fundus image of this dataset was acquired using a Canon CR-1, while the SLO images were obtained from a SLO system from Spectralis, Heidelberg Engineering. This database is not publicly available and was made available upon request. Figures 3.3(c) – (d) show a set of retinal images from the *Brno-Multi* dataset.

3.5 Robustness Scenarios

To validate the robustness of the registration performance for the proposed similarity measure, various scenarios were introduced. Ideally a robust similarity measure must be stable towards perturbations in the condition of input medical images. For example, different level of misalignment and the presence of noise/INU should not significantly affect the final registration, though in practice, such scenarios tend to test the limitations of a similarity measure and the registration model as a whole, depending on its clinical applicability.

Existing scenarios as in (Argyriou et al., 2015; Brock, 2013; Hajnal and Hill, 2001; Zitová and Flusser, 2003), are deployed for testing the robustness of the new EMPCA-MI similarity measure, which include: varying the level of misalignment between the reference and sensed image pair; introducing known artefacts such as INU and noise, and using image pairs which have large homogeneous non-vascular regions. The following sections will discuss each of these scenarios in detail:

3.5.1 Initial Misregistration

The registration process spatially aligns a reference and sensed medical image pair, which are misregistered. The level of misregistration present can depend on various reasons such as the medical imaging equipment, its acquisition times, inter/intra patient imaging and clinical application (Hajnal and Hill, 2001). Ideally, the registration model is supposed to register an image pair having any level of misregistration, but in practice the result is highly dependent on the initial misregistration since this governs the amount of initial overlap between the images (Studholme et al., 1994).

A robust similarity measure should be able to overcome this dependency by consistently providing lower *registration error* (RE) even when the level of misregistration in the image pair is increased (Modersitzki, 2004). For this reason, most literature makes use of a consistent methodology of introducing different levels of random, but known initial misalignment to the reference image I_R before beginning the registration process (Russakoff et al., 2003; Wiest-Daesslé et al., 2007). In the experiments, the initial misregistration transformation parameters are defined as $\tau_{initial}$, and this is used to evaluate and compare the robustness of the new EMPCA-MI similarity measure with existing similarity measures. The $\tau_{initial}$ values for the registration of both *BrainWeb* and retinal image datasets were adopted from (Kotsas and Dodd, 2011) and (Gharabaghi et al., 2013) respectively. Since a known ground truth between I_R and I_S exists, the *initial* RE is then computed as the mean of Euclidean distances between the four corner points of $\tau_{initial}(I_R)$ and I_S in pixels (Beutel, 2000; Hajnal and Hill, 2001).

The twenty initial misregistration scenarios for *BrainWeb* dataset as adopted from (Kotsas and Dodd, 2011) varies with *initial* RE=18.59 pixels (for 1st initial misregistration scenario $(-5.55, 17.74, 0.35^\circ)$) to 109.25 pixels (for 20th initial misregistration scenario $(0.55, 29.63, -44.7^\circ)$). Similarly, five initial misregistration scenarios were used from (Chen et al., 2011) and (Gharabaghi et al., 2013) for the retinal datasets. These different initial misregistration scenarios represent the initial misalignments, which occur in practice. Tables A.1 and A.2 in *Appendix A* show the various $\tau_{initial}$ used throughout this thesis together with the corresponding *initial* RE for the BrainWeb and retinal datasets respectively. A larger value of *initial* RE emphasises that the image pair is more misaligned and will prove to be more challenging for registration.

3.5.2 INU and Gaussian Noise

Another challenging condition which impacts the performance of registration process is the presence of INU in multimodal medical images, as already mentioned in *Section 2.2*. According to the radio frequency mapping theory (Insko and Bolinger, 1993; Stollberger and Wach, 1996), INU can be modelled as a multiplicative process (Ganzetti et al., 2016; Sled, 2015). The majority of previous studies including (Belaroussi et al., 2006; Dawant et al., 1993; Pham and Prince, 1999; Wells et al., 1995), have all formalised the corrupting influence of INU in MRI images as follows:

$$a(x, y) = u(x, y) \alpha(x, y) + \beta(x, y) \quad (3.1)$$

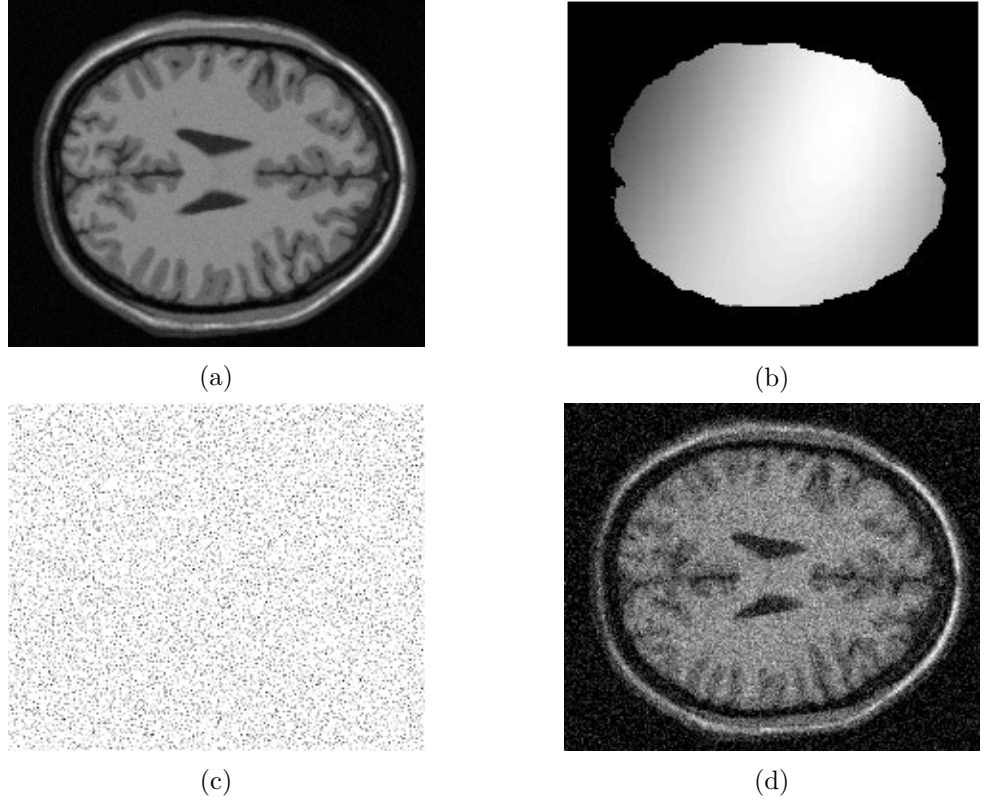


Figure 3.4: Example *BrainWeb* image of (a) uncorrupted brain MRI T1 u , (b) multiplicative 20% INU α , (c) additive Gaussian noise β and (d) measured T1 image a (Collins et al., 1998; Montreal Neurological Institute and Hospital, nd; Razlighi et al., 2013).

Where, a is the measured MRI image as a function of spatial location (x, y) , u is the uncorrupted image, α is the multiplicative artefact, and β is the image noise which is Gaussian distributed and independent of u (Belaroussi et al., 2006; Gudbjartsson and Patz, 1995; Henkelman, 1985). Figures 3.4(a) – (d) shows the uncorrupted MRI T1 image u , corresponding 20% INU α and noise β , and the resultant MRI image a . In order to test the robustness of any new similarity measure against such artefacts, INU is introduced into the MRI image pairs with levels of 20% and 40%, denoted by α_{20} and α_{40} respectively as detailed in (Collins et al., 1998), (Leondes, 2005), (Yi and Soatto, 2011) and (Razlighi et al., 2013). Also Gaussian noise denoted by β having mean μ and variance σ^2 values is used, as shown in Table 3.2.

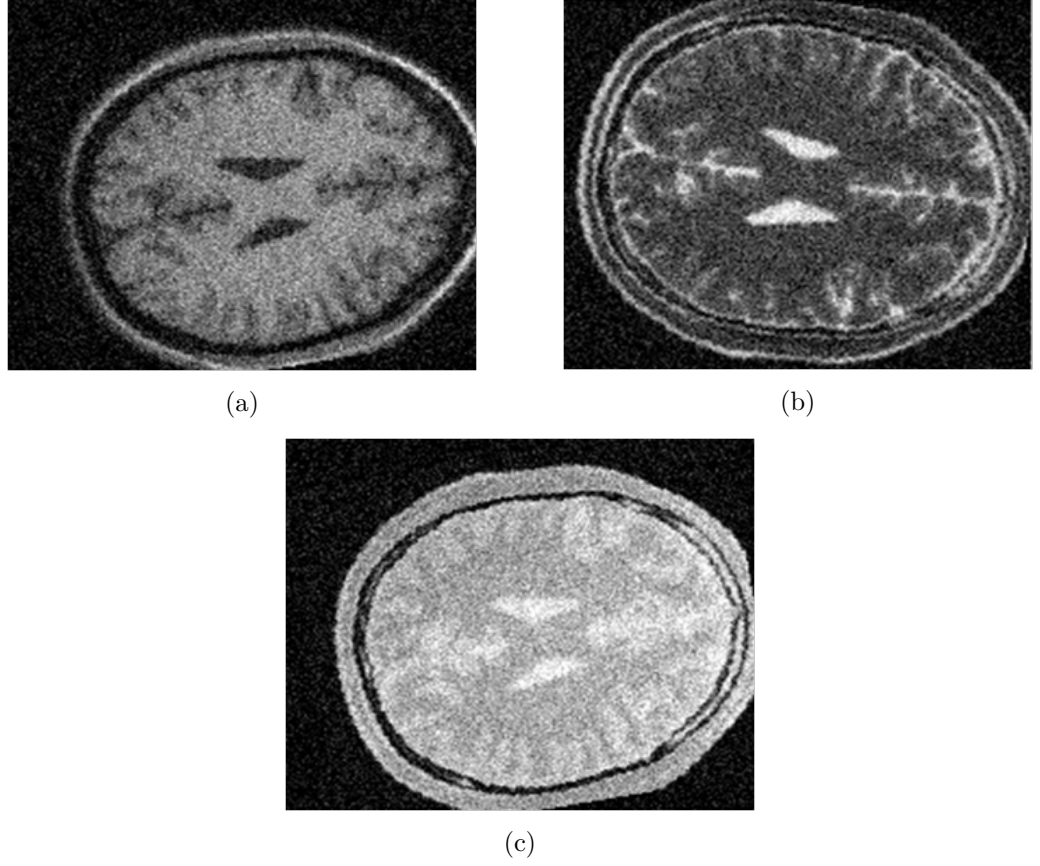


Figure 3.5: Example *BrainWeb* images of misregistered brain MRI (a) $T1+\alpha_{40}+\beta$, (b) $T2+\alpha_{40}+\beta$ and (c) $PD+\alpha_{40}+\beta$ from (Montreal Neurological Institute and Hospital, nd).

To clarify the nomenclature used, $T1+\alpha_{20}$ represents a MRI T1 image with 20% INU. Correspondingly $T2+\alpha_{40}+\beta$ represents a MRI T2 image with 40% INU and Gaussian noise. Figures 3.5(a) – (c) show a selection of misregistered images from the *BrainWeb* dataset, with different levels of INU and Gaussian noise combinations.

3.5.3 Low Contrast and Homogeneous Regions

As highlighted in *Section 2.2*, retinal images are challenging to register due to their innate features (Sanchez-Galeana et al., 2001), especially low-contrast ho-

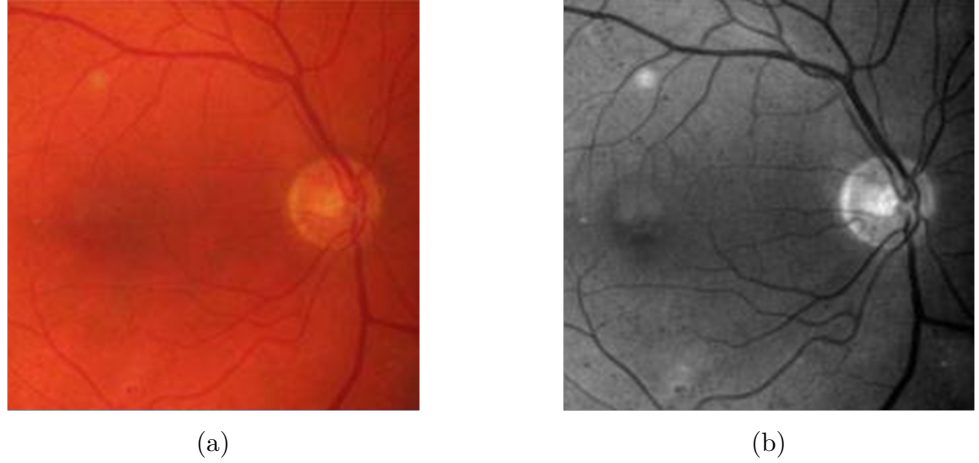


Figure 3.6: Example retinal images from *Brno-Mono* dataset (a) colour Fundus and (b) only its green channel (shown in *grayscale* colour) from (Kolar et al., 2013; Kolar and Tasevsky, 2010).

mogeneous and non-uniformly illuminated regions (Marrugo and Millán, 2011), in addition to different pathological conditions like haemorrhages, retinal scars and clumping of the dark pigment (Saine and Tyler, 2002). All these characteristics are known to cause deterioration of the registration performance in many existing similarity measures (Legg et al., 2009) while some fail totally (Fang et al., 2005). For these reasons, the mono and multimodal retinal images are chosen in order to test the robustness of the hybrid EMPCA-MI similarity measure framework. Furthermore, for retinal images, registration is performed using only the green channel, since it has the highest contrast compared with the red and blue channels, which are saturated and contain acquisition noise (Chanwimaluang et al., 2006; Laliberte et al., 2003; Skokan et al., 2002). Figures 3.6(a) and (b) respectively show a sample retinal image from the *Brno-Mono* dataset of colour Fundus together with its green channel. Clearly the visibility of vascular regions is enhanced when only the green channel is considered, while no INU or Gaussian noise is added to any of the retinal images because these artefacts are not prominent during the acquisition process (Saine and Tyler, 2002).

3.6 Performance Metrics

These are pivotal in the evaluation and validation of an image registration process (Maintz and Viergever, 1998) by measuring the success of a registration outcome along with their computational cost in both a quantitative and qualitative manner. They also provide the insight for analysing the new EMPCA-MI similarity measure framework for experiments with the scenarios in *Section 3.5*. Despite the importance of this comparison, before deploying image registration for clinical use, there are no established criteria or standard methods available (D. Forsberg, 2013). This hiatus and inadequate validation practice has tended to impede the widespread usage of image registration in different clinical workflows. The following sections will review those performance metrics which have previously been used for quantitative and perceptual assessment of the registration process, along with the computational cost.

3.6.1 Quantitative Assessment

Various quantitative methods to evaluate the registration performance, including the target landmarks, embedded fiducial markers, transformation error or Euclidean distance between pair of known points in the reference and sensed images (Klein et al., 2009), (Murphy et al., 2011) and (Rohlfing, 2012). The applicability of these methods depends on different factors such as availability of a ground truth and whether the fiducial markers are surgically implanted prior to image acquisition. Of these, a distance-based numerical error is adopted as the ground truth between the image pair as it is available for all the datasets used in the experiments (Goshtasby, 2012; Hajnal and Hill, 2001).

Once the new hybrid EMPCA-MI similarity measure is maximised in (2.1), the final registration transformation parameters τ_{final} are saved and the *final* RE is computed as the mean of Euclidean distance between the four corner points of $\tau_{initial}(I_R)$ and $\tau_{final}(I_S)$ in pixels (Bernardes et al., 2014; Dame and Marchand, 2010; Legg et al., 2007; Tang et al., 2010; Yin et al., 2010). For any modality, the lower the *final* RE value, the better registered the image pair.

In order to display and critically analyse the *final* RE values for a group of registrations, a box and whisker plot is used. This is a descriptive statistical tool (Klein et al., 2007) chosen because it represents the spread and skewness of the RE by displaying the mean, median, lower and upper quartiles and outliers. RE values outside 1.5 times interquartile range from the lower and upper quartiles are termed as outliers (Brase and Brase, 1999). In addition, the number of outliers having RE values higher than a given limit are shown as *out-of-range* outliers on top of the corresponding box and whisker plot (Murphy et al., 2011).

3.6.2 Perceptual Assessment

The registration process performance is also qualitatively evaluated using visual quality assessment (Woods, 2009). A variety of image overlaying visualisation methods can be used including *contour*, *coloured*, *Canny edge detection* and *checkerboard* overlay (Bourland, 2012). In addition, some software-based dynamic graphic user interfaces use a *sliding window* method to reflect the correspondence between the reference and sensed image pair (Fedorov et al., 2012; Meyer, 2007).

This thesis utilises the *Canny edge detection* and *checkerboard* overlay method for perceptual evaluation of the registration process as they can effectively visualise the qualitative differences and degree of physical misalignment between the registering images.

The *Canny edge detection* overlay method displays the whole image pair after the edge detection process, while the *checkerboard* overlay divides both the image into square regions, with the diagonal squares displaying the regions of the same image. The *checkerboard* overlay specifically suits retinal images since it enables close observation of vascular lines and their continuity (Kolar et al., 2013; Wilson and Laxminarayan, 2007). Figure 3.7(a) shows the result of multimodal $T1+\alpha_{40}+\beta/T2$ pair registration using *Canny edge detection* overlay with an inset of zoomed in region showing the central lobes. This clearly emphasises the level of misregistration between the image pair. Similarly, Figure 3.7(b) shows an example of *checkerboard* overlay after monomodal retinal Fundus registration, highlighting the evident discontinuity in vascular lines at the edges of the square regions (Gharabaghi et al., 2013).

3.6.3 Computational Cost

Another key challenge for MIR besides attaining lower RE, is to minimise the overall computation cost of registration (Eklund et al., 2013; Shekhar et al., 2003; Zitová and Flusser, 2003). This is the total computational time incurred for each registration component as shown earlier in Figure 2.5, which is clearly dependent on the different algorithms comprising the hybrid EMPCA-MI similarity measure

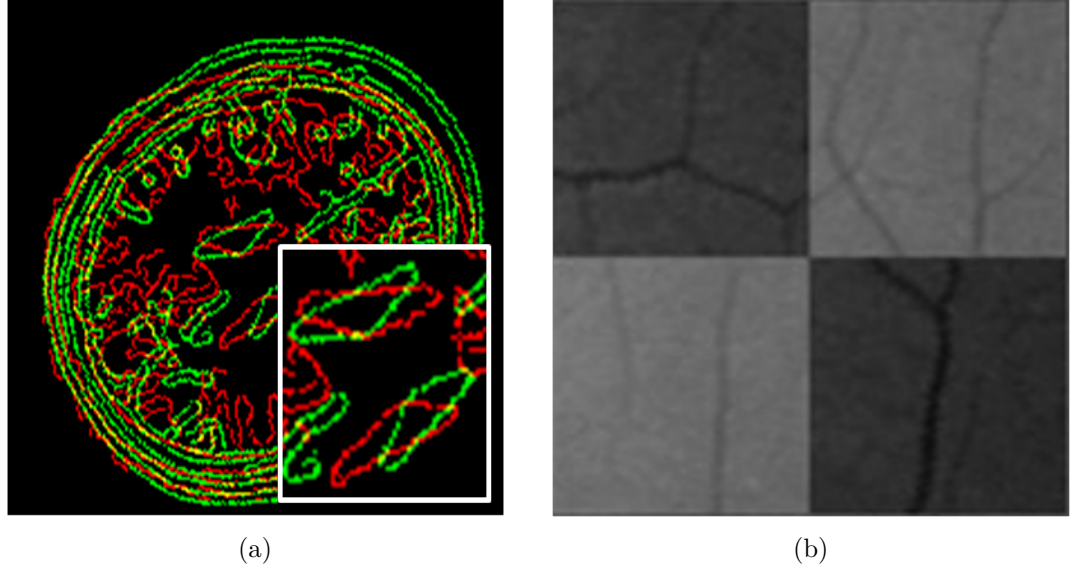


Figure 3.7: Visual quality assessment of (a) multimodal $T1+\alpha_{40}+\beta/T2$ pair registration using *Canny edge detection* overlay (with inset showing zoomed in region) and (b) monomodal retinal registration zoomed-in view using *checkerboard* overlay (reproduced from (Gharabaghi et al., 2013)).

framework. As registration is an iterative process along with, where appropriate, an order of time complexity analysis, the average time to compute one cycle of iteration of the EMPCA-MI framework during registration is also considered as a key performance metric. This is calculated by averaging the computational time for all iterations in each registration and is defined as the *average runtimes* (ART) in *seconds*.

3.7 Simulation Platform

A variety of programming languages and open-source coding platforms are available for designing and developing the MIR model (Goshtasby, 2012; Modersitzki, 2004). High level languages such as *C/C++* (Wang and Lai, 2008) and *Java* (Lyon, 1999) are compiler-based and require development of components and libraries for

each element, which can be time consuming in most cases. In contrast, open-source platforms like *Python* (Chityala and Pudipeddi, 2014) and *ImageJ* (Pascau and Mateos, 2013) have specific libraries for image processing applications.

A popular alternative is MATLAB[®] (Mathworks, nd) which is well accepted by the community because of its rapid prototyping capabilities. Although it is interpreter-based commercial software and has comparatively slower execution times, it comes with rich built-in functions, lucid error reporting and has specifically developed toolboxes for image and signal processing. The slow execution speeds can be compensated by choosing a high-end personal computer (PC). The toolboxes are written and rigorously tested, making them more compact and straightforward to use compared with *C/C++* and *Java* code. Since the main focus is on having a development platform to design, test and evaluate the new hybrid EMPCA-MI similarity measure framework, rather than designing new tools, MATLAB was the pragmatic choice for all experimental work.

The technical specifications for the MATLAB software and high-end PC are detailed in Table 3.3. These were fixed throughout all the experimentation work to ensure consistent and accurate performance comparison of the ART metric.

3.8 Software Code Validation

Various code verification and validation techniques (Oberkamp and Roy, 2010) based on software life cycle model were used throughout the design and implementation of the EMPCA-MI similarity measure framework. These included both

Software Platform	PC Specifications	
MATLAB 7.12 R2011a	<i>Processor</i>	Intel® Core TM 2 Duo E7500 (2.93GHz, 1066MHz FSB, 3MB L2 Cache)
	<i>RAM</i>	3 GB, DDR2, 800MHz
	<i>Hard Disk</i>	160GB, 8MB Cache, 7200 RPM
	<i>Operating System</i>	Ubuntu Release 10.04 (<i>lucid</i>) Kernel Linux 2.6.32-67-generic GNOME 2.30.2

Table 3.3: Simulation platform specifications and their details.

static analysis checks, such as data type, control flow and data use, as well as dynamic checks including running the model with *Shepp-Logan* head phantom test image pair (Haidekker, 2011).

An advantage of using MATLAB was the considerably lower refinement time incurred between the development and static-dynamic test cycle in Figure 3.1. In the initial development phase, coding and design errors (like the exception handling, divide by zero along with checks for integer overflow and conditional dead logics) were trouble-shot.

The transformation and interpolation methods deployed in the registration model were available as MATLAB functions in its Image Processing Toolbox (Mathworks, nd). The Powell Brent optimisation method was implemented as in (Press et al., 2007) and then validated using the inverted version of standardised *first function of De Jong's* benchmarking test (Molga and Smutnicki, 2005). This function is convex so has a global maximum which represents the ideal image regis-

tration scenario (Modersitzki, 2004; Zitová and Flusser, 2003). Furthermore, it has the ability to extend and simulate three and four variable maximisation representing the *2D rigid* and *similarity* transformations respectively. This benchmarking test validated the functionality of Powell Brent optimisation method implementation which was then integrated into the registration model.

The software implementation of the EMPCA-MI similarity measure framework was verified as well as validated using two approaches:

1. By independently testing the functionality of each constituent component of the framework. For example, EMPCA iteratively computes the various PCA components, so the EMPCA (Roweis, 1998) implementation was tested with the conventional PCA function in the MATLAB Statistics Toolbox (Mathworks, nd) using a multivariate Iris dataset (Fisher, 1936). Similarly the MI code was based on (Cover and Thomas, 1991) and tested using the MI Least-dependent Component Analysis Toolbox (Stögbauer et al., 2004) for fixed test data. *Kaiser Rule* (Jackson, 1993; Jolliffe, 2002) and *Wichard* (Wichard et al., 2008) approach implementations were also validated using MATLAB Statistics Toolbox. These tests provide a higher degree of confidence to the software implementation as the functionality of each individual stage is evaluated independently.
2. To verify the software code of the registration model, dynamic testing was applied to the *Shepp-Logan* head phantom test image pair (see Figure 3.8) (Haidekker, 2011) in different misregistration configurations. This is employed in (Guo and Huang, 2008; Pilutti et al., 2014) as a model of the human



Figure 3.8: *Shepp-Logan* head phantom image (Guo and Huang, 2008; Haidekker, 2011)

head for the development and testing of image registration algorithms since it has a known ground truth. These experiments confirmed the convergent nature of the registration model as alignment of this test image was always achieved. Furthermore, the existing similarity measures used as comparators were publicly available. Details of the specific individual comparators used for validation will be given in the respective contribution chapters.

3.9 Summary

This chapter has described the methodology adopted for all experimental work in this thesis. A software simulation-based test-bed is used to implement the MIR model, which uses different test scenarios for robustness validation. A set of performance metrics have been selected to evaluate the similarity measures on clinical and general datasets. The choice of MATLAB as the main simulation platform for model implementation has been justified and details of the validation procedures for the code developed have been presented. The next chapter will present the first contribution, namely the EMPCA-MI similarity measure framework.

Chapter 4

EMPCA-MI for Medical Image Registration

4.1 Introduction

The performance of the registration for images of some anatomies deteriorates considerably, such as MRI images having intensity variations and noise due to radio frequency-based inhomogeneity and similarly retinal images which comprise inherently large homogeneous regions (Chanwimaluang et al., 2006; Simmons et al., 1994; Zhuang et al., 2010). It was evident from the literature in *Chapter 2* that the similarity measure plays a pivotal role in the registration process. While MI has been a popular similarity measure for image registration, two of its recent variants were identified in *Chapter 2*, namely GMI and RMI as promising similarity measures. GMI and RMI combine intensity gradient information and local pixel regions respectively with MI to improve the image registration performance in

comparison to traditional MI. However, GMI performance degrades in the presence of artefacts and noise, while RMI uses a covariance matrix instead of a high-dimensional histogram, which leads to reduced data complexity but generates a coarser approximation in certain cases.

In this chapter, a new similarity measure framework called EMPCA-MI is proposed for MIR. EMPCA-MI utilises the concept of neighbourhood region from the RMI algorithm to extract the spatial features with the help of principal component analysis. Unlike the approximation in RMI, EMPCA-MI achieves effective dimensionality reduction by using an iterative process to determine the dominant principal component. It uses only first principal component to extract the key features from a given neighbourhood radius of the image since it always has the highest variance. This evidently leads to a significant reduction in the computation cost.

This chapter also includes a thorough empirical EMPCA-MI analysis for the choice of interpolation and neighbourhood radius on mono and multimodal images. The rest of the chapter is organised as follows: The new EMPCA-MI framework is presented in *Section 4.2*. In *Section 4.3*, experimental results are conducted to analyse and choose the interpolation and radius of neighbourhood region from three perspectives i.e. smoothness of the similarity measure traces, computational cost involved and finally the quantitative performance in terms of RE. These choices will be used in the next chapter. Finally a summary of the chapter is provided in *Section 4.4*.

4.2 EMPCA-MI

In *Chapter 2*, various power iteration and competitive learning-based dimensionality reduction methods were discussed. From them, EMPCA was identified as an attractive solution since it requires fewer number of iterations to find the number of principal components required and can be deployed with lower computational overheads (Roweis, 1998). In the past, MI has been utilised to evaluate and select features for a diverse range of applications (Battiti, 1994; Hossain et al., 2011; Peng et al., 2005; Yao et al., 2010). Hence its statistical background and ability to perform on multimodal images makes it suitable for quantifying the level of alignment between the EMPCA-extracted features (Paragios et al., 2015). The EMPCA-MI framework combines the spatial features of neighbourhood region with MI using EMPCA in three sequential steps (Reel et al., 2012a,b). *Step I* comprises of rearranging the image data such that the neighbourhood region features can be effectively extracted. *Step II* employs EMPCA to iteratively compute the first dominant principal component. Finally *Step III* computes the mutual information between the features of reference and sensed images.

4.2.1 *Step I: Image Neighbourhood Rearrangement*

Considering an interpolated sensed image $I_S^* \in \mathbb{N}^{n \times m}$ with n rows and m columns, a neighbourhood region-based sliding window of size $(2r + 1) \times (2r + 1)$ pixels, using a given neighbourhood radius r can be rearranged as a row vector $s \in \mathbb{N}^{1 \times d}$, where $d = (2r + 1)^2$. This can be further generalised as:

$$S_k \triangleq \{h \in I_S^* \mid D_\infty(h, g) \leq r\} \quad (4.1)$$

$$D_\infty(h, g) := \max(|g_i - h_i|, |g_j - h_j|) \quad (4.2)$$

Here, $D_\infty(h, g)$ denotes the *Chebyshev* distance (Fernandez-Maloigne, 2012) of a given pixel location h from the centre pixel g of the neighbourhood region sliding window at i^{th} row and j^{th} column location. Also, $r \leq i \leq (n-r)$, $r \leq j \leq (m-r)$ and $1 < k < q$ with $q = (n-2r) \times (m-2r)$. Hence, all such q neighbourhood region windows for the complete I_S^* , can be concatenated and defined as $Q_s \in \mathbb{N}^{q \times d}$, such that:

$$Q_s \triangleq \begin{bmatrix} S_1 \\ S_2 \\ \vdots \\ S_k \\ \vdots \\ S_q \end{bmatrix} \quad (4.3)$$

Here, S_k denotes the k^{th} neighbourhood region window. Here, Q_s can be considered as a matrix consisting of q observed data vectors in d dimensional subspace. Forming this neighbourhood region reduces the artefact effects because the intensity variations across a localised region will be significantly lower compared to across the whole image. Since neighbourhood region pixels are more likely to be locally correlated compared to pixels located further apart, each neighbourhood region is rearranged as a d -dimensional vector, enabling the features to be extracted along with dimensionality reduction.

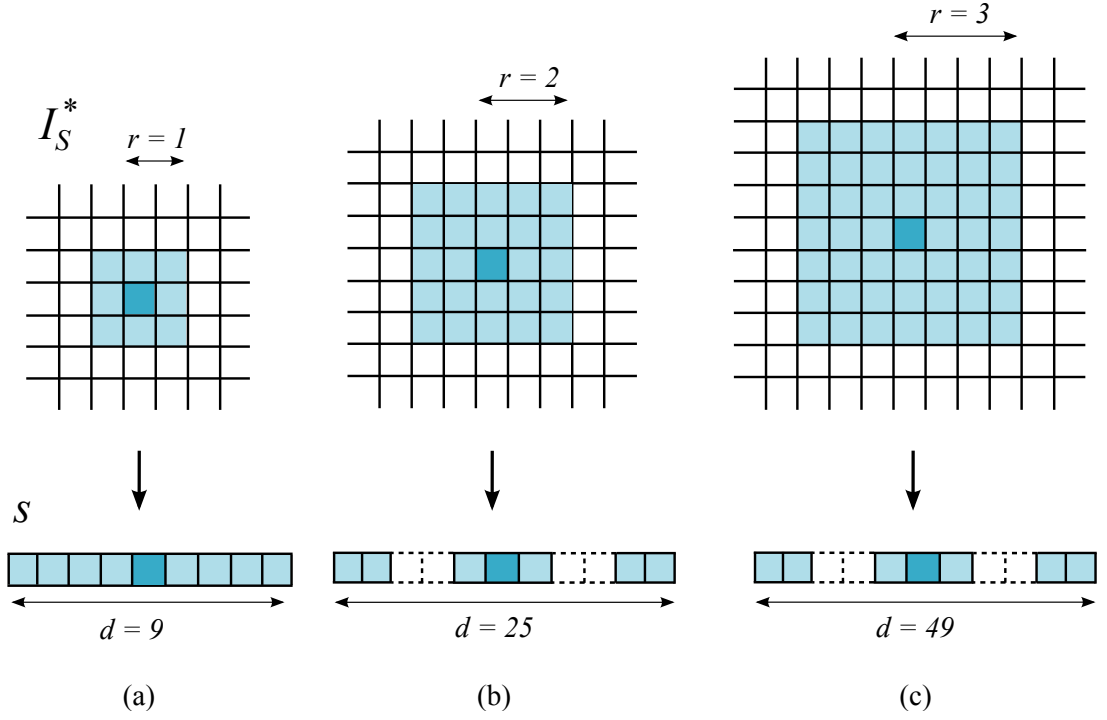


Figure 4.1: The neighbourhood region selection for feature extraction in EMPCA-MI, showing the dimensionality d with radius (a) $r=1$, (b) $r=2$ and (c) $r=3$ pixels.

Figure 4.1 illustrates the neighbourhood region sliding window for I_S^* with radius r increasing from 1 to 3. Figure 4.1(a) shows using the central pixel of the neighbourhood (shown in dark *blue* colour) for which the neighbourhood region (shown in light *blue* colour) for radius $r=1$ is rearranged as s , having $d=9$. It is apparent d increases with r^2 , emphasising that a larger region is considered as a higher dimensionality for the feature extraction process. For example, in Figures 4.1(a) – (c), the value of d increases from 9 to 49, as r is increased from 1 to 3.

The overall impact of choosing a particular value of r for EMPCA-MI computation will be rigorously analysed in *Section 4.3.2*.

4.2.2 Step II: EMPCA-based feature extraction

This step of EMPCA-MI comprises of dimensionality reduction of the neighbourhood region features. Although in *Chapter 2*, various dimensionality reduction methods were discussed but EMPCA was identified as an appropriate method due to its iterative nature and lower computational overheads instead of conventional PCA which computes all the components simultaneously. As mentioned in the literature, the sum of the variances of the principal components is equal to the variance of the original variables. While the first principal component accounts for most of the variability in the data (Rencher, 1998), various stopping rules such as Scree Graph and *Kaiser Rule* (Jackson, 1993; Jolliffe, 2002) are also used for determining the best P principal components to be retained, which represent the high percentage of the variation in the data.

Hence, considering that Q_s is a linear transformation of a latent variable $z \in \mathbb{N}^{P \times d}$, transformed by $\Phi \in \mathbb{N}^{d \times P}$ and additive Gaussian noise $v \in \mathbb{N}^{q \times d}$ (having a covariance matrix V) such that:

$$Q_s = \Phi z + v \quad z \sim N(0, 1) \quad v \sim N(0, V) \quad (4.4)$$

Here, z is assumed to be independent and have unity variance. Also v is independent of z and is normal distributed. Therefore, EMPCA algorithm (Roweis, 1998) can be used for dimensionality reduction to extract the most prominent P principal components (such that $P < d$). The expectation step estimates the unknown states $\Omega_s \in \mathbb{N}^{P \times d}$ and then choose Φ and the restricted V in the maximisation step so as to maximise the expected joint likelihood of the estimated Ω_s and the observed Q_s . This can be written as:

$$e\text{-step} : \quad \Omega_s = (\Phi^T \Phi)^{-1} \Phi^T Q_s \quad (4.5)$$

$$m\text{-step} : \quad \Phi^{new} = Q_s \Omega_s^T (\Omega_s \Omega_s^T)^{-1} \quad (4.6)$$

Here, Q_s is a matrix with dimensions $q \times d$ for all neighbourhood regions as in (4.3). In (4.5), an orientation for the principal subspace is randomly initialised. Then considering this subspace as fixed, Q_s is projected onto it to get the values of the hidden states Ω_s . Then in (4.6), keeping the values of the hidden states fixed, choose the subspace orientation which minimises the squared reconstruction errors of the given data-points.

Rowies et al (Roweis, 1998) explains the above-mentioned two steps using a simple two-dimensional physical analogy. Assuming a rod pinned at the origin which is free to rotate, consider picking an orientation for the rod. Now, holding the rod still, project every data-point onto the rod, and attach each projected point to its original point with a spring. Next release the rod and repeat. The direction of the rod represents the guess of the principal component of the dataset. The energy stored in the springs is the reconstruction error which needs to be minimised.

Hence, from the final iteration, the first P principal components can be stored in $X_s \in \mathbb{N}^{P \times q}$ from Φ . In a similar way, X_R can be computed from I_R . EMPCA offers a significant saving in the computation cost in comparison to using conventional PCA for this step of EMPCA-MI, with latter computing all the principal components at once using the covariance matrix (Jolliffe, 2002). A discussion comparing the computational complexity between conventional PCA and EMPCA will follow later in *Section 4.3.2*.

4.2.3 *Step III: Finding MI for Registration*

This final step of EMPCA-MI aims to find the similarity between the extracted features of reference and interpolated sensed images. As discussed in *Section 2.4*, MI represents the amount of information one variable contains within another and hence is computed between X_S and X_R . It assumes that a statistical relationship exists between X_S and X_R , which is reflected by their marginal probabilities and joint probability. Hence, employing (2.7 - 2.15), the marginal entropies $H(X_R)$ and $H(X_S)$, as well as joint entropy $H(X_R, X_S)$ are:

$$H(X_R) = - \sum_{X_R} p_{X_R}(X_R) \log_2 p_{X_R}(X_R) \quad (4.7)$$

$$H(X_S) = - \sum_{X_S} p_{X_S}(X_S) \log_2 p_{X_S}(X_S) \quad (4.8)$$

$$H(X_R, X_S) = - \sum_{X_R, X_S} p_{X_R X_S}(X_R, X_S) \log_2 p_{X_R X_S}(X_R, X_S) \quad (4.9)$$

and

$$p_{X_R}(X_R) = \frac{U_{X_R}}{U} \quad (4.10)$$

$$p_{X_S}(X_S) = \frac{U_{X_S}}{U} \quad (4.11)$$

$$p_{X_R X_S}(X_R, X_S) = \frac{U_{X_R X_S}}{U} \quad (4.12)$$

Hence, the MI between X_R and X_S can be expressed as:

$$\text{MI}(X_R, X_S) = \sum_{X_R, X_S} p_{X_R X_S}(X_R, X_S) \log_2 \left\{ \frac{p_{X_R X_S}(X_R, X_S)}{p_{X_R}(X_R) p_{X_S}(X_S)} \right\} \quad (4.13)$$

Here, $p_{X_S}(X_S)$ and $p_{X_R}(X_R)$ are the marginal probabilities for X_S and X_R respectively, and $p_{X_RX_S}(X_R, X_S)$ represents their joint probability as defined in *Section 2.4*. These probability distributions are computed using b number of bins. The value of MI computed between the extracted features X_R and X_S will reflect the measure of alignment between I_R and I_S^* , for a given set of transformation parameters. Hence an increasing value of MI for different sets of transformation parameters will signify the better spatial alignment. This will be more evident when the EMPCA-MI similarity measure framework is incorporated into the registration test-bed described in *Chapter 3*, which will use the optimisation process to maximise the EMPCA-MI to achieve the best alignment between given I_R and I_S^* .

The corresponding pseudo-code of EMPCA-MI framework is given in Algorithm 4.1.

Algorithm 4.1 Pseudo Code for EMPCA-MI similarity measure framework

Inputs: I_R and I_S^* each with spatial resolution $m \times n$ pixels; r – neighbourhood radius; P – number of principal components.

Variables: d – dimensional space; q – total no. of pixels; Q_R, Q_S –output from rearranging I_R and I_S^* ; X_R, X_S – first principal component using EMPCA for Q_R and Q_S .

Output: EMPCA-MI value

- 1: **Initialise** $d = (2r + 1)^2$ and $q = (m - 2r) \times (n - 2r)$.
 - 2: **Calculate** Q_R using (4.1) and (4.3) from I_R .
 - 3: **Calculate** X_R using (4.4 – 4.6) from Q_R for a given P .
 - 4: **REPEAT** Steps 2 to 3 for I_S^* to give X_S .
 - 5: **Calculate** $MI(X_R, X_S)$ using (4.7– 4.13).
 - 6: **STOP**
-

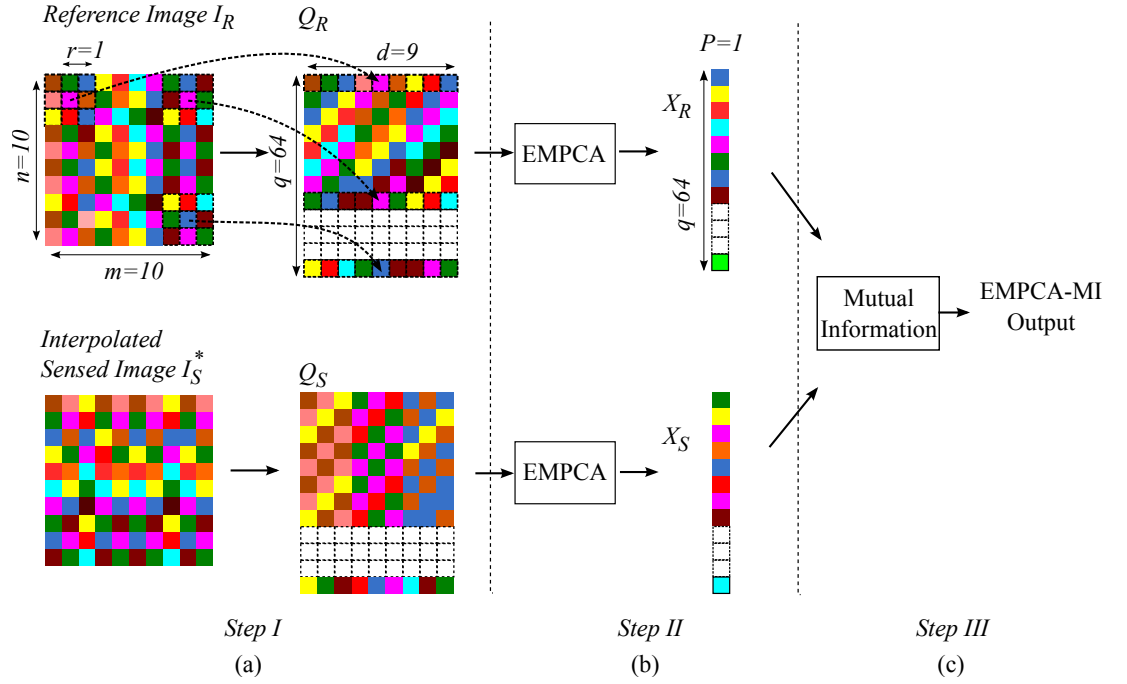


Figure 4.2: Illustration showing EMPCA-MI computation steps on reference I_R and interpolated sensed I_S^* images.

Figure 4.2 illustrates the various steps of EMPCA-MI with the help of example images having spatial dimensions 10×10 pixels. In Figure 4.2(a), the *Step I* uses neighbourhood radius $r=1$ and rearrange I_R and I_S^* as Q_R and Q_S respectively. Note the colour used for pixels represents the pre-processing step and does not represent actual image data. Figure 4.2(b) shows the *Step II* computation of extracting the most prominent, first principal component X_R and X_S using EMPCA. Finally, Figure 4.2(c) shows the *Step III* where the MI between them is computed according to (4.13).

A numerical example illustrating the calculation of EMPCA-MI between two matrices (I_R and I_S^*) which represent image data having spatial dimensions 6×6 pixels, is as follows:

Let,

$$I_R = \begin{bmatrix} 132 & 140 & 133 & 129 & 124 & 127 \\ 140 & 121 & 120 & 112 & 111 & 102 \\ 122 & 118 & 98 & 96 & 81 & 80 \\ 108 & 92 & 78 & 58 & 59 & 51 \\ 84 & 64 & 45 & 42 & 35 & 51 \\ 57 & 46 & 42 & 41 & 40 & 48 \end{bmatrix} \quad \text{and} \quad I_S^* = \begin{bmatrix} 120 & 116 & 112 & 106 & 99 & 98 \\ 107 & 97 & 88 & 80 & 77 & 75 \\ 85 & 66 & 58 & 54 & 52 & 59 \\ 53 & 43 & 37 & 43 & 54 & 49 \\ 43 & 41 & 40 & 45 & 45 & 44 \\ 46 & 42 & 38 & 41 & 48 & 49 \end{bmatrix}.$$

Where $n = m = 6$. Therefore, considering $r = 1$, $d = 9$ and $q = 16$.

Thus, in *Step I* using (4.1) and (4.3):

$$Q_R = \begin{bmatrix} 132 & 140 & 133 & 140 & 121 & 120 & 122 & 118 & 98 \\ 140 & 133 & 129 & 121 & 120 & 112 & 118 & 98 & 96 \\ 133 & 129 & 124 & 120 & 112 & 111 & 98 & 96 & 81 \\ 129 & 124 & 127 & 112 & 111 & 102 & 96 & 81 & 80 \\ 140 & 121 & 120 & 122 & 118 & 98 & 108 & 92 & 78 \\ 121 & 120 & 112 & 118 & 98 & 96 & 92 & 78 & 58 \\ 120 & 112 & 111 & 98 & 96 & 81 & 78 & 58 & 59 \\ 112 & 111 & 102 & 96 & 81 & 80 & 58 & 59 & 51 \\ 122 & 118 & 98 & 108 & 92 & 78 & 84 & 64 & 45 \\ 118 & 98 & 96 & 92 & 78 & 58 & 64 & 45 & 42 \\ 98 & 96 & 81 & 78 & 58 & 59 & 45 & 42 & 35 \\ 96 & 81 & 80 & 58 & 59 & 51 & 42 & 35 & 51 \\ 108 & 92 & 78 & 84 & 64 & 45 & 57 & 46 & 42 \\ 92 & 78 & 58 & 64 & 45 & 42 & 46 & 42 & 41 \\ 78 & 58 & 59 & 45 & 42 & 35 & 42 & 41 & 40 \\ 58 & 59 & 51 & 42 & 35 & 51 & 41 & 40 & 48 \end{bmatrix}$$

$$\text{and } Q_S = \begin{bmatrix} 120 & 116 & 112 & 107 & 97 & 88 & 85 & 66 & 58 \\ 116 & 112 & 106 & 97 & 88 & 80 & 66 & 58 & 54 \\ 112 & 106 & 99 & 88 & 80 & 77 & 58 & 54 & 52 \\ 106 & 99 & 98 & 80 & 77 & 75 & 54 & 52 & 59 \\ 107 & 97 & 88 & 85 & 66 & 58 & 53 & 43 & 37 \\ 97 & 88 & 80 & 66 & 58 & 54 & 43 & 37 & 43 \\ 88 & 80 & 77 & 58 & 54 & 52 & 37 & 43 & 54 \\ 80 & 77 & 75 & 54 & 52 & 59 & 43 & 54 & 49 \\ 85 & 66 & 58 & 53 & 43 & 37 & 43 & 41 & 40 \\ 66 & 58 & 54 & 43 & 37 & 43 & 41 & 40 & 45 \\ 58 & 54 & 52 & 37 & 43 & 54 & 40 & 45 & 45 \\ 54 & 52 & 59 & 43 & 54 & 49 & 45 & 45 & 44 \\ 53 & 43 & 37 & 43 & 41 & 40 & 46 & 42 & 38 \\ 43 & 37 & 43 & 41 & 40 & 45 & 42 & 38 & 41 \\ 37 & 43 & 54 & 40 & 45 & 45 & 38 & 41 & 48 \\ 43 & 54 & 49 & 45 & 45 & 44 & 41 & 48 & 49 \end{bmatrix}.$$

And, in *Step II*, the corresponding values of X_R and X_S assuming $P = 1$ in (4.4 – 4.6) are:

$$X_R = \begin{bmatrix} -0.1500 \\ -0.1895 \\ \vdots \\ -0.1498 \\ -0.0623 \end{bmatrix}_{16 \times 1} \quad \text{and} \quad X_S = \begin{bmatrix} -0.3462 \\ -0.3820 \\ \vdots \\ 0.0011 \\ -0.0132 \end{bmatrix}_{16 \times 1}$$

Finally, in *Step III*, choosing $b = 256$ for (4.7– 4.13), is $\text{MI}(X_R, X_S) \approx 2.6875$.

From the literature review in *Chapter 2*, the interpolation used for the transformation of the image during the registration impacts upon the performance of a similarity measure (Aljabar et al., 2005; Pluim et al., 2000b; Soleimani and

Khosravifard, 2011; Tsao, 2003). Similarly, as observed in (4.1), the underlying pre-processing stage of EMPCA-MI is dependent on the neighbourhood radius. Hence in order to critically assess the performance of the new EMPCA-MI framework, it is important that key parameter choices related to the interpolation and neighbourhood radius r are appropriately made.

4.3 Choosing interpolation and neighbourhood radius for EMPCA-MI

This section investigates the various choices available for interpolation and neighbourhood radius parameter settings and then evaluates the EMPCA-MI performance with the help of registration experiments. These experiments are conducted on the registration test-bed using the mono and multimodal pairs of MRI T1, T2 and PD human brain images from the *BrainWeb* dataset (with α_{20} and β) which was described in research methodology *Chapter 3*.

During this analysis, to compute *Step II* of EMPCA-MI a fixed value of $P=1$ is used in (4.5) and (4.6). This value of P is chosen because as mentioned before, it represents the first principal component which has the highest variance and contains most of the prominent information (Jolliffe, 2002). The value of P will be relaxed later in *Chapter 7*, where it will be shown that EMPCA-MI can iteratively determine the best P from a dataset, instead of calculating all components using a covariance matrix. Similarly, in *Step III* of EMPCA-MI, a fixed value of $b=256$ has been empirically chosen for the number of bins in (4.13), as in (Argyriou et al.,

2015; Hahn et al., 2010; Legg et al., 2007; Maintz et al., 1998). These fixed number of bins will be relaxed from *Chapter 6* onwards, where its impact on registration performance is investigated in detail. Next, to evaluate the most appropriate interpolation strategy as well as the neighbourhood radius, three issues need to be considered:

1. The smoothness of EMPCA-MI as a cost function.
2. The computational cost.
3. The preliminary registration performance.

The next two sections describe the experiments and results for the choice of interpolation and then neighbourhood radius.

4.3.1 Choice of Interpolation Technique

The first series of experiments involved the process of determining the most appropriate interpolation method to be used to compute the EMPCA-MI similarity measure value for an image registration pair. As discussed in *Chapter 2*, the choice of interpolation for estimating intensity values of the transformed image has a significant impact on the registration algorithm in determining the final transformation value. Nearest neighbour, bilinear and bicubic methods have emerged as the most commonly used interpolation methods (Acharya and Tsai, 2007). Hence, these three interpolation schemes were examined as possible choices for the EMPCA-MI framework for image registration purposes using the above three criteria for assessment.

Smoothness of EMPCA-MI plots

Each EMPCA-MI trace is obtained by shifting the sensed image along x and y axis translation and θ rotation and keeping the reference image fixed. The EMPCA-MI values between the two images are then plotted. These traces emphasise that a global maximum is attained when the reference and sensed images are fully aligned and the EMPCA-MI values gradually decrease as higher values of shift are introduced.

For example, Figures 4.3 and 4.4 show the x and y axis translation EMPCA-MI traces using different interpolation methods for monomodal T2/T2 and multimodal PD/T1 image pairs respectively. The x axis translation plots in Figures 4.3(a) and (c) show both bilinear and bicubic interpolation methods give a similar and smooth EMPCA-MI output. On the other hand, a closer inspection in the zoomed-in view in Figure 4.3(a), shows the nearest neighbour method provides a non-smooth, stepwise output. A similar trend is also evident in the corresponding θ rotation plot included in Figure B.2 of *Appendix B*. Furthermore, for y axis translation plots in Figure 4.3(b) zoomed-in view it is seen that bilinear method also has unsmooth behaviour which further aggravates in Figure 4.3(d). Furthermore, in Figure 4.4(b) a similar trend for the nearest neighbour and bilinear methods is seen for multimodal PD/T1 image pair. The bilinear method performance worsens further with the presence of many local maxima on both sides of global maximum, as seen in Figure 4.4(d) for translation along y axis. For completeness, *Appendix B* includes the EMPCA-MI traces for other mono and multimodal T1, T2 and PD image pairs. On closely examining the behaviour of these plots, bicubic inter-

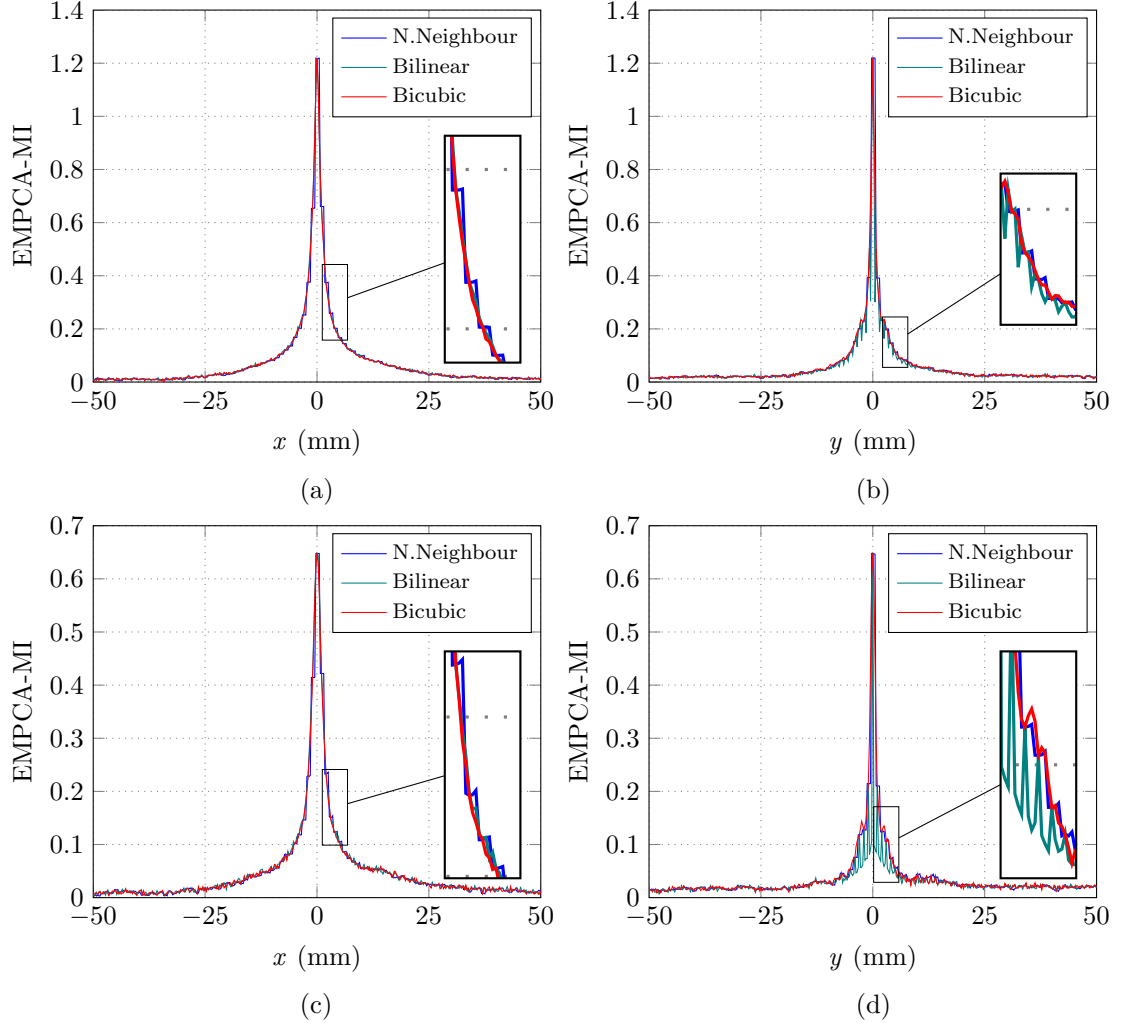


Figure 4.3: EMPCA-MI Traces with nearest neighbour, bilinear and bicubic interpolation for x and y axis translation for monomodal T2/T2 image pairs (a & b) T2+ α_{20} /T2, (c & d) T2+ β /T2 with inset showing zoomed-in view.

pulation is found to be the most effective interpolation method in terms of cost function smoothness. The better performance of bicubic method is due to the fact that it utilises a wider weighted average of 4×4 pixels window, leading to more accurate pixel representation in the transformed sensed image. In contrast the nearest neighbour method gives a non-smooth, step-like trace resulting from the output pixels assuming the value of nearest neighbouring pixels in the input image. As neighbouring pixels will generally have similar values, it results in identical EMPCA-MI values for a range of small shifts. Similarly, the bilinear method intro-

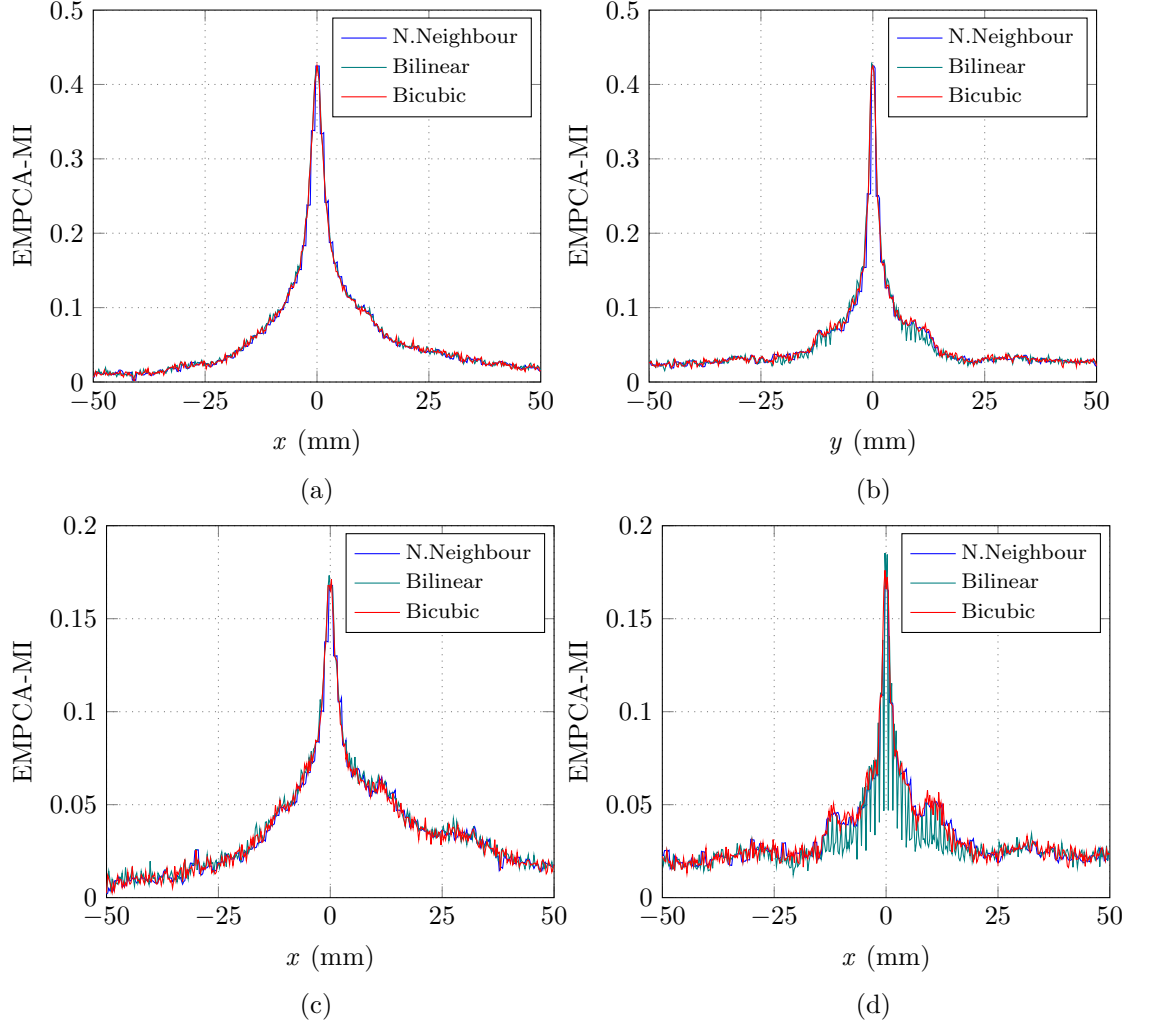


Figure 4.4: EMPCA-MI Traces with nearest neighbour, bilinear and bicubic interpolation for x and y axis translation for multimodal PD/T1 image pairs (a & b) PD+ α_{20} /T1, (c & d) PD+ β /T1.

duces artefacts that result in many local minima. Hence, bicubic method provides overall smoother plot for EMPCA-MI compared to both nearest neighbour and bilinear methods.

Computational Cost

Figure 4.5 shows the ART performance for computing the EMPCA-MI value using nearest neighbour, bilinear and bicubic interpolation methods. It is apparent that

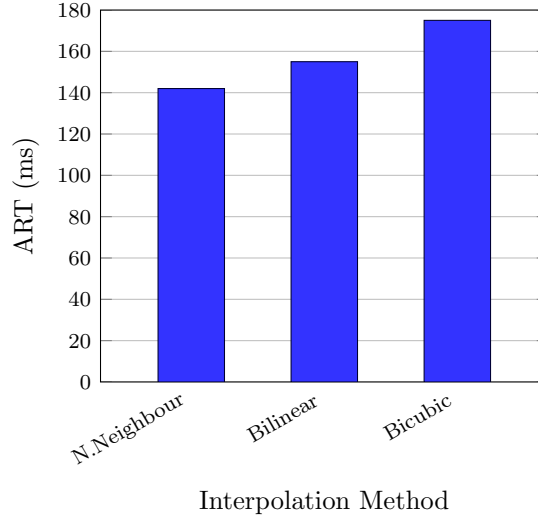


Figure 4.5: ART performance of EMPCA-MI using nearest neighbour, bilinear and bicubic interpolation methods for monomodal T2/T2 and multimodal PD/T1 image pairs.

bicubic method is approximately *15%* and *25%* slower than bilinear and nearest neighbour methods respectively. Although, bicubic interpolation incurs higher computation time in order to determine the gradients and cross derivative at each re-sampled pixel location (Acharya and Tsai, 2007), but offers more accurate interpolated values and especially smoother EMPCA-MI traces.

The nearest neighbour method despite of being fastest, due to its step-like behaviour requires more overall registration time since the optimisation process does not converge effectively to the best transformation value. Similarly deploying bilinear for EMPCA-MI computation for registration will not be effective, since it will have a higher likelihood of obtaining a sub-optimal solution due to the optimisation process falling into false maxima instead of the true global maximum (Wang et al., 2008).

Preliminary Registration Performance

The preliminary registration performance is evaluated in terms of the RE for nearest neighbour, bilinear and bicubic interpolation methods in the EMPCA-MI framework. For this set of experiments, monomodal T2/T2 and multimodal PD/T1 image pairs having α_{20} and β artefacts are used. As explained in the research methodology *Chapter 3*, 20 levels of initial misregistration will be used so there are in total 240 separate registration experiments performed for 2 modality pairs, 2 INU and Gaussian noise settings, 20 initial misregistrations and 3 interpolation methods. Figure 4.6(a) shows the RE vs. iteration plot for the registration of six monomodal T2/T2 pairs, starting with 1st initial misregistration scenario $(-5.55, 17.74, 0.35^\circ)$. This initial misregistration scenario was chosen as in (Kotsas and Dodd, 2011), as already discussed in *Section 3.5.1*. Instead of only evaluating the *final* RE for each registration, RE vs. iteration plots is used. They give an insight into the registration process by highlighting the converging capability of a similarity measure.

In Figure 4.6(a), all six registrations start from a common *initial* RE and thereon RE is computed at the end of each Powell multidimensional direction set method iteration. As discussed in *Sections 2.3.4* and *3.3*, each iteration comprise of Brent-based line minimisation, with the process stopping either when the maximum number of iterations is completed or else when the tolerance for the line minimisation is achieved. The RE at the end of this process is denoted as *final* RE. For example, in Figure 4.6(a), T2+ α_{20} /T2 registrations using nearest neighbour, bilinear and bicubic interpolation start with an *initial* RE=18.6 pixels and finish with a *final* RE=1.03, 4.05 and 0.03 pixels respectively.

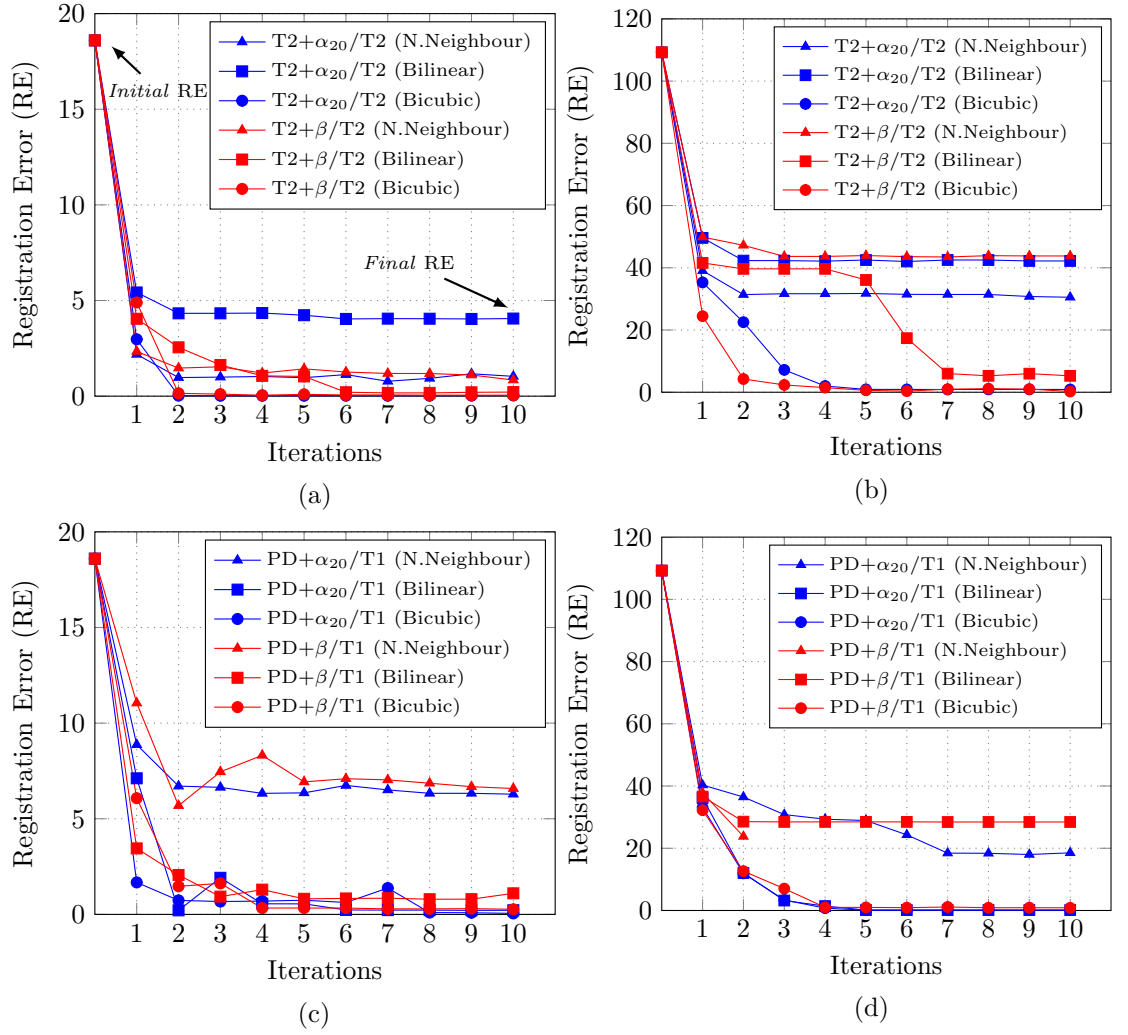


Figure 4.6: RE versus iterations plots for nearest neighbour, bilinear and bicubic interpolation with EMPCA-MI-based monomodal T2/T2 registration using (a) 1st initial misregistration scenario and (b) 20th initial misregistration scenario, multimodal PD/T1 registration using (c) 1st initial misregistration scenario and (d) 20th initial misregistration scenario.

Similarly, Figure 4.6(b) shows another set of registrations using 20th initial misregistration scenario $(0.55, 29.63, -44.71^\circ)$ having *initial* RE=109.20 pixels. Both plots show that bicubic interpolation-based registration outperforms the bilinear and nearest neighbour interpolations. It is clear that bicubic interpolation consistently leads to a lower *final* RE for both the initial misregistration scenarios. Especially striking is the monotonic rate of convergence in Figure 4.6(b) for bicubic interpolation, in contrast to bilinear which converges after only the 7th iteration

but to a higher RE value. These results are congruent with the EMPCA-MI results discussed above. Since bicubic interpolation has smoother EMPCA-MI trace, it will allow the registration process to converge towards actual global maxima compared with the other interpolators. Figures 4.6(c) and (d) show the multimodal PD/T1 registrations with 1st and 20th initial misregistration scenario respectively. The nearest neighbour interpolation exhibits the poorest rate of convergence with interestingly in Figure 4.6(d) for PD+ α_{20} /T1 registration, the process terminates after only the 2nd iteration because the tolerance defined for the Powell-Brent optimisation is reached. While computationally being the fastest in terms of ART, this example highlights the inconsistent RE performance of the nearest neighbour interpolator.

Figures 4.7(a) and (b) show the detailed RE summary boxplots for monomodal T2/T2 and multimodal PD/T1 registration using the three interpolators with EMPCA-MI for all 20 initial misregistration scenarios. Each boxplot shows a bounding box defining the interquartile range with the bar across representing the median and whiskers denoting the RE range. The boxplots on top also include the number of *out-of-range* RE values corresponding to each interpolation method. The boxplots in Figure 4.7 reveal the overall better registration performance of bicubic interpolation which consistently achieves lower *mean* RE for all cases. Bicubic interpolation also exhibits the lowest number of *out-of-range* outliers, due to the fact that it has a steady converge as seen in Figures 4.6(a) – (d). On the other hand, nearest neighbour-based registrations lead to higher *mean* RE as well as more number of *out-of-range* outliers because of the inaccurate pixel values computed during the image transformation process during registration.

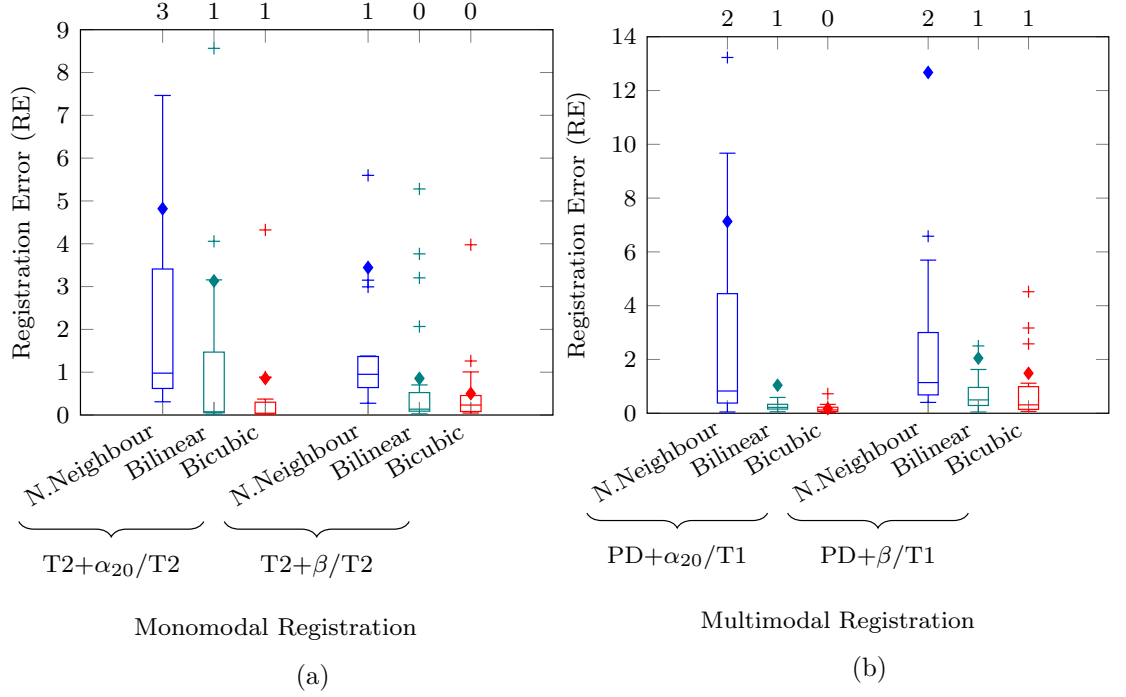


Figure 4.7: RE summary boxplot of (a) monomodal T2/T2 registration and (b) multimodal PD/T1 registration using nearest neighbour, bilinear and bicubic interpolation with EMPCA-MI for all 20 initial misregistration scenarios. The *mean* and *outliers* are denoted by \blacklozenge and $+$ shapes. The numbers on top of the plots refer to the number of *out-of-range* outliers with RE higher than 9 and 14 pixels respectively.

In summarising, on the basis of above critical evaluation of EMPCA-MI traces, ART and image RE performance, bicubic interpolation was selected for the rest of the experimental work presented in this thesis.

4.3.2 Choice of neighbourhood radius

The impact of varying the neighbourhood radius for EMPCA-MI was studied next. These experiments were applied to determine the most appropriate neighbourhood radius to be used in EMPCA-MI for registration. As discussed in *Section 4.2.1*, the neighbourhood region selection uses *Chebyshev* distance radius r to determine Q_S having $q \times d$ dimensions.

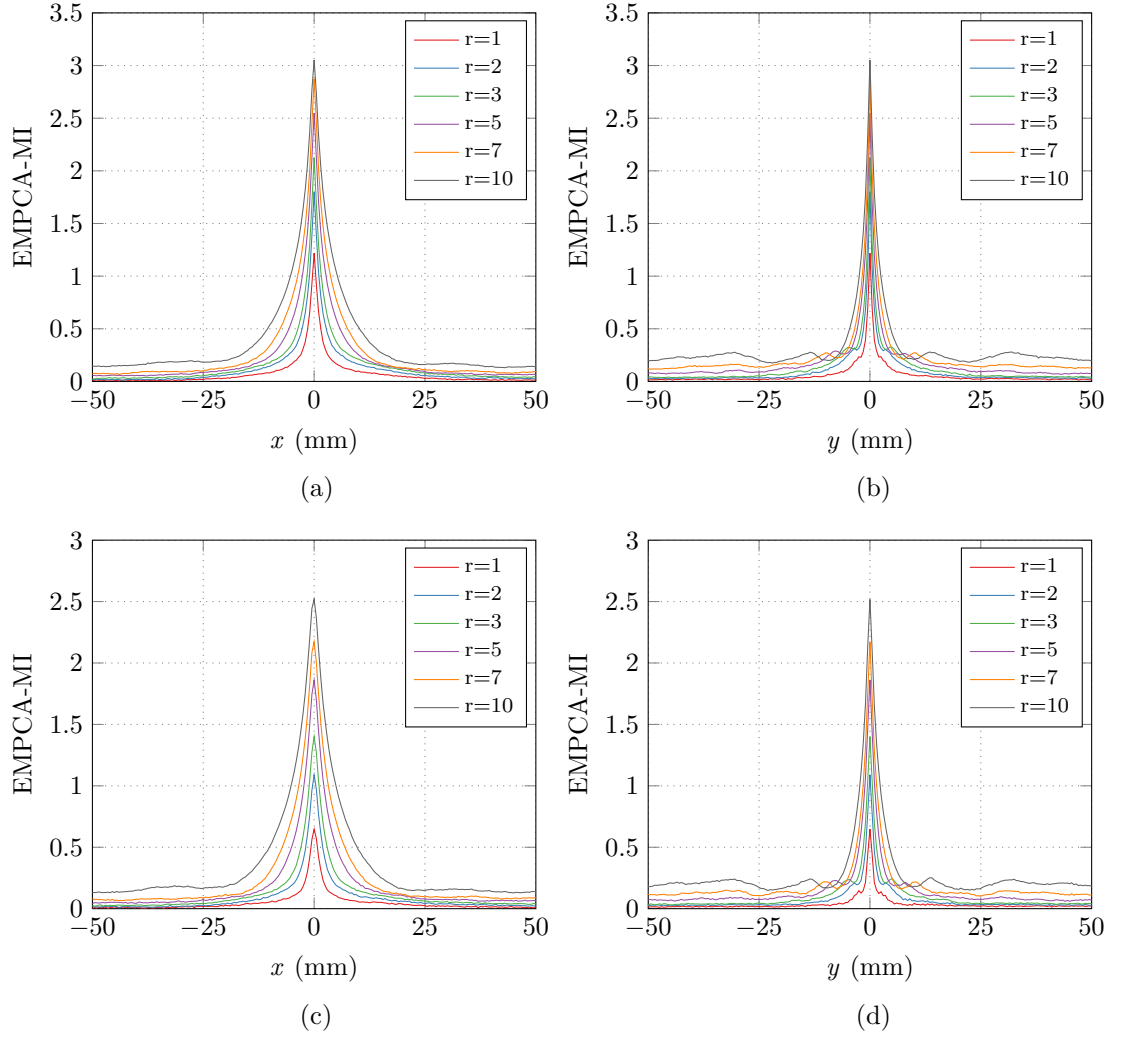


Figure 4.8: EMPCA-MI Traces with different radius values for x and y axis translation for monomodal T2/T2 image pairs (a & b) $T2+\alpha_{20}/T2$, (c & d) $T2+\beta/T2$.

Smoothness of EMPCA-MI plots

In order to evaluate the neighbourhood radius, EMPCA-MI traces are generated as elaborated in the previous section. In this experimentation, the value of r is varied between 1, 2, 3, 5, 7 and 10, keeping the interpolation scheme as bicubic. Figures 4.8 and 4.9 show the corresponding EMPCA-MI traces for different r values for monomodal T2/T2 and multimodal PD/T1 image pairs respectively. As before, α_{20} and β was introduced in these image pairs. The x axis translation plots in Figures 4.8(a) and (c) have a vertical symmetry in-comparison to the asymmetric y

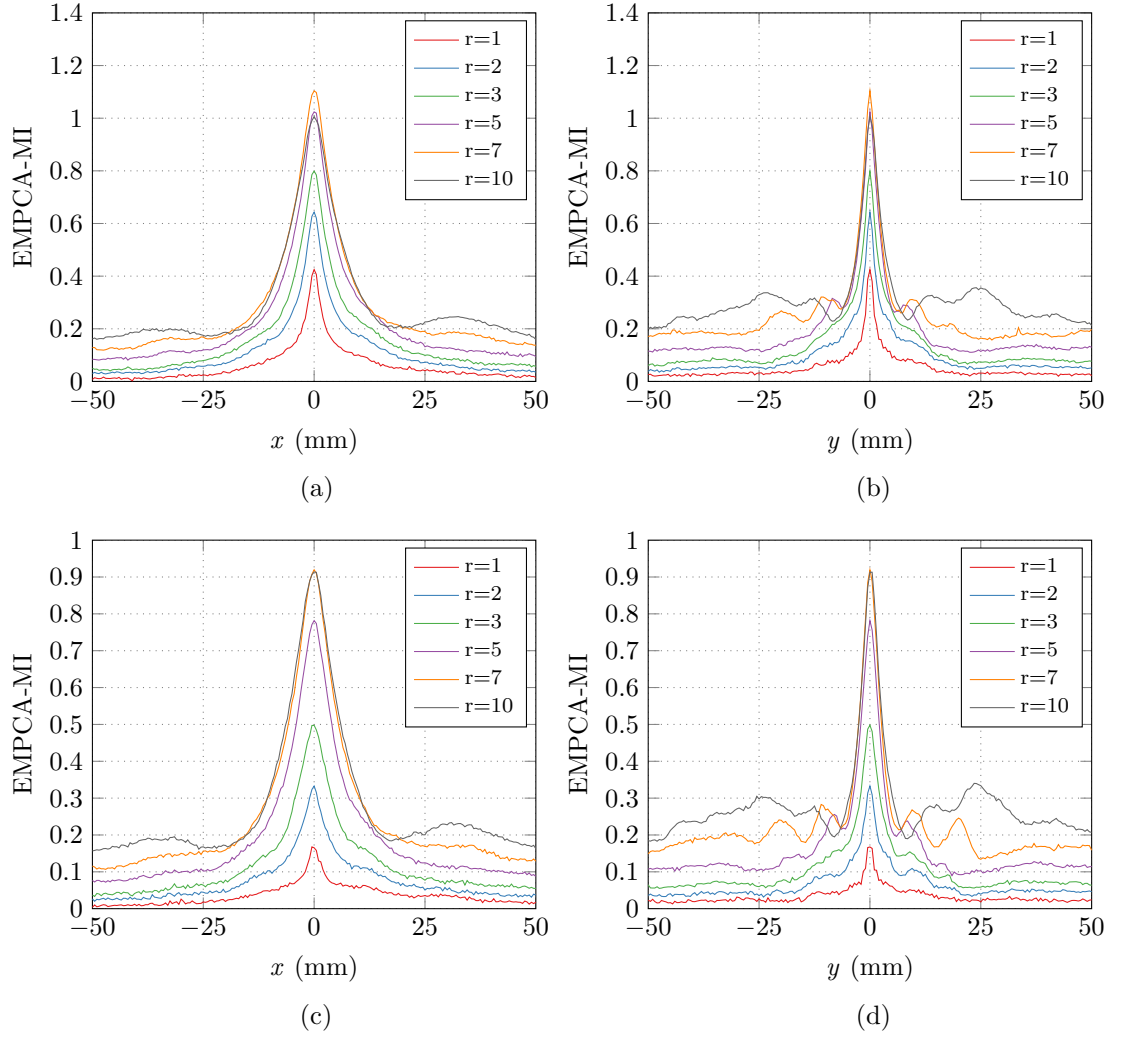


Figure 4.9: EMPCA-MI Traces with different radius values for x and y axis translation for multimodal PD/T1 image pairs (a & b) PD+ α_{20} /T1, (c & d) PD+ β /T1.

axis translation plots in Figures 4.8(b) and (d), highlighting the vertical symmetry in the anatomic structure of human brain shown earlier, in Figures 2.4(a) and (b).

Furthermore, the x axis translation plots in Figures 4.8(a) and (c) show smoother EMPCA-MI output at higher radius values. A similar trend is observed for the y axis translation in Figures 4.8(b) and (d), and θ rotation plots included in Figure C.2 in *Appendix C* respectively. But on close inspection, the y axis translation plot in Figures 4.8(b) and (d) highlight that while EMPCA-MI output value increases on choosing higher radius also some local maxima are generated around the global

maximum. These are due to the fact that as the α_{20} and β is introduced, their impact on the EMPCA-MI value is higher as the neighbourhood region is larger. The occurrence of local maxima is more adverse in the y axis translation plots of multimodal PD/T1 image pair as shown in Figures 4.9(b) and (d). These local maxima become more pronounced as r increases, with an analogous trend being seen in the other EMPCA-MI traces for various mono and multimodal T1, T2 and PD image pairs presented in *Appendix C* for completeness. The presence of local maxima around the global maximum is a well-documented problem in image registration (Hajnal and Hill, 2001), which can undermine the registration performance during optimisation. As a consequence, in the experiments using a lower radius value for EMPCA-MI will give a greater likelihood of convergence to the lowest RE value in comparison to using higher r values.

Computational Cost

To evaluate the impact upon computation complexity of varying the neighbourhood radius, it is vital to understand the relationship between the radius and dimensionality d . As mentioned in *Section 4.2.1*, d is dependent only on the choice of r . Consequently, d will be the same for all images irrespective of their resolution, for a given fixed neighbourhood radius. Therefore, increasing r from 1 to 10, will lead to quadratic increase of d , from 9 to 441, which will clearly have a commensurate effect on the ART performance. Furthermore, Figure 4.10 shows a semi-log plot for number of samples q as the function of r for all the datasets used in the experimental analysis. It is apparent from (4.2) that q is also dependent on the image resolution in addition to r . For example, as r increases from 1 to 10, the

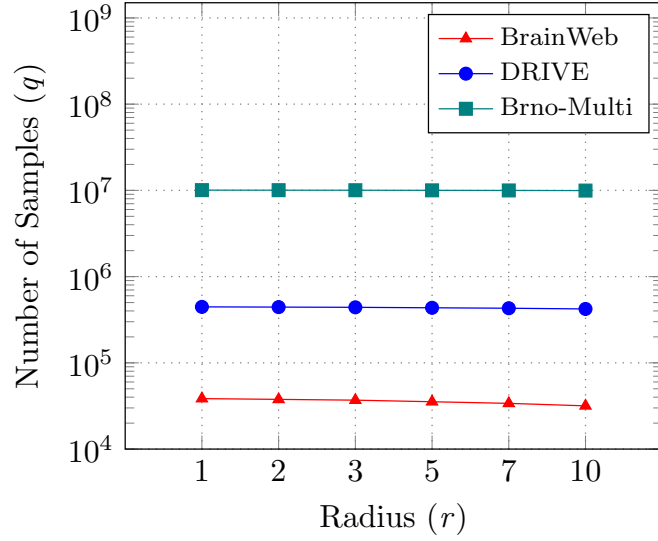


Figure 4.10: Number of samples (q) with respect to different neighbourhood radii for the variety of datasets.

corresponding number of samples in the *BrainWeb* dataset (consisting of images with resolution 181×217 pixels) decrease by approximately 20% (from 3.8×10^4 to 3.1×10^4), while for *Brno-Multi* dataset (consisting of images with resolution 3888×2592 pixels) they reduce by 11% (from 1.0×10^7 to 0.9×10^7). Hence for a fixed dataset, q decreases as r increases.

Figure 4.11 shows the ART performance for EMPCA-MI computation along with the conventional PCA with MI calculation (PCA-MI), for different radii values of r , using a log-log plot. It highlights the faster performance of the EMPCA-MI in comparison to the conventional PCA-MI. For example when $r=2$, EMPCA-MI is approximately five times faster than conventional PCA-MI, while in terms of order of complexity, the Q_S matrix in *Step II* of the EMPCA-MI (discussed in *Section 4.2.2*) has dimensions $q \times d$ so for the conventional PCA-MI, $\mathcal{O}(qd^2)$ operations are required to compute the covariance matrix and determine the first PCA component.

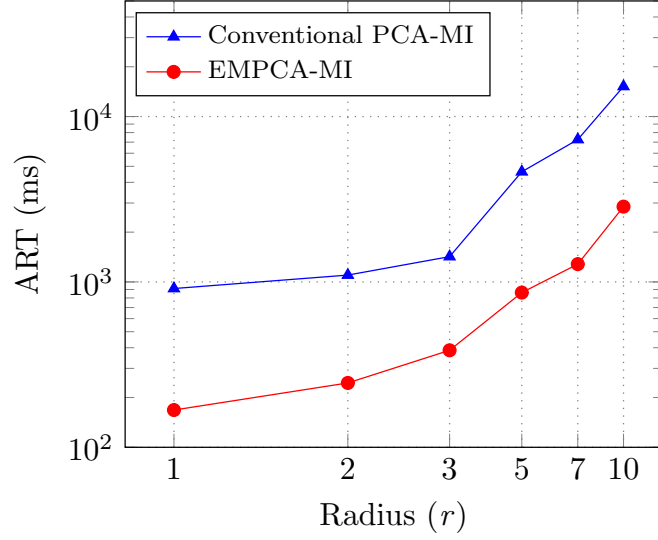


Figure 4.11: ART performances for EMPCA-MI and conventional PCA-MI with respect to different neighbourhood radii.

In contrast, EMPCA-MI which does not need to compute the covariance matrix, so only requires $\mathcal{O}(qd)$ operations. Hence, for different r values and corresponding d and q values, EMPCA-MI requires lower computation time than conventional PCA-MI.

Preliminary Registration Performance

Now, the quantitative registration performance in terms of RE is analysed for various r values with EMPCA-MI for monomodal T2/T2 and multimodal PD/T1 *BrainWeb* image pairs having α_{20} and β artefacts. As in *Section 4.3.1* where the registration experimentation for the choice of interpolation were conducted, the same 20 levels of initial misregistration are used now for these experiments. Hence, in all 480 separate registration experiments are performed, consisting of 2 modalities pairs, 2 INU and Gaussian noise settings, 20 initial misregistration and 6 neighbourhood radii settings.

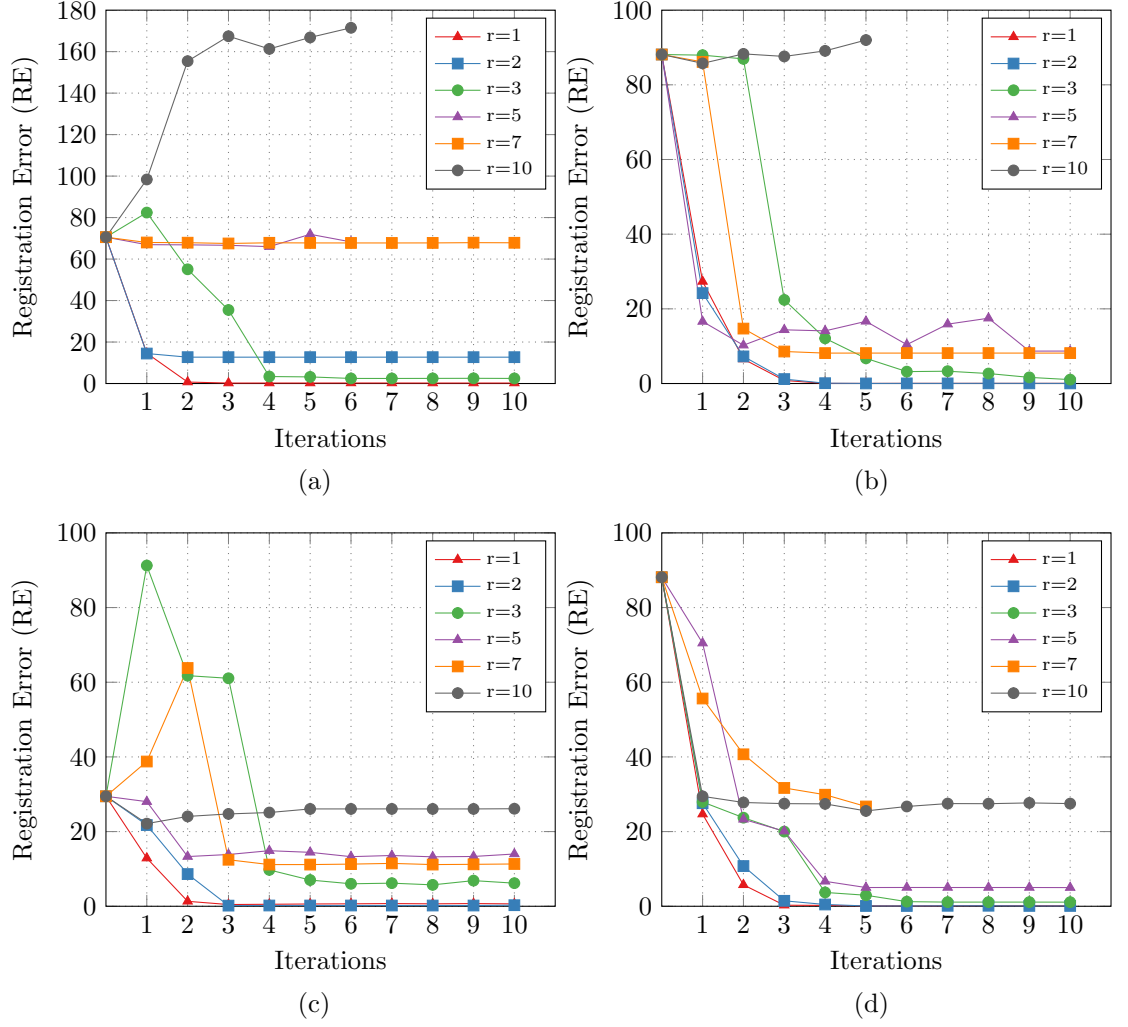


Figure 4.12: RE versus iterations plots for EMPCA-MI with varying neighbourhood radius for monomodal (a) $T2+\alpha_{20}/T2$ pair (using 12^{th} initial misregistration scenario) and (b) $T2+\beta/T2$ pair (using 16^{th} initial misregistration scenario). Multimodal (c) $PD+\alpha_{20}/T1$ pair (using 3^{rd} initial misregistration scenario) and (d) $PD+\beta/T1$ pair (using 17^{th} initial misregistration scenario).

Figure 4.12 consists of four RE vs. iteration plots with each one having six registration experiments using EMPCA-MI with increasing neighbourhood radius $r=1, 2, 3, 5, 7$ and 10 . Figures 4.12(a) and (b) shows monomodal results for $T2+\alpha_{20}/T2$ pair, starting with the 12^{th} initial misregistration scenario $(-19.11, 9.08, -28.42^\circ)$ and $T2+\beta/T2$ pair, starting with 16^{th} initial misregistration scenario $(-5.65, 16.94, -36.06^\circ)$ respectively.

Similarly, Figures 4.12(c) and (d) show multimodal results for PD+ α_{20} /T1 pairs, starting with 3rd initial misregistration scenario (10.11, 27.22, -2.67°) and PD+ β /T1 pair, starting with 17th initial misregistration scenario (0.21, -16.41, -36.15°) respectively. All the above initial misregistration scenarios were chosen as in (Kotsas and Dodd, 2011) as already described in the research methodology *Chapter 3*.

The results confirm that $r=1$ has the best rate of convergence as well as a lower RE in comparison to all other neighbourhood radii for both mono and multimodal pairs. Choosing $r=2$ also provide good convergence and lower RE, except in case of the monomodal T2+ α_{20} /T2 registration in Figure 4.12(a) where the optimisation converges at a local maxima leading to high final RE. However, as the neighbourhood radius increases, the corresponding registrations all provide higher RE allied with poorer rates of convergence, incurring more iterations to achieve their final RE value. This is evident in the cases of T2+ β /T2 and PD+ α_{20} /T1 registrations for $r=3, 5$, and 7 shown in Figures 4.12(b) and (c) respectively.

Interestingly at $r=10$, only multimodal pairs in Figures 4.12(c) and (d) converged but at a considerably higher RE. On the other hand, in the case of monomodal registrations in Figures 4.12(a) and (b), the iterations end prematurely before the maximum number of iterations are completed with final RE even higher than the initial RE. This happens due to the convergence of the registration process to the false local maxima present near the initial misregistration. Hence, increasing r decreases the level of granularity needed for best feature extraction, which generates local maxima as seen previously on examining the smoothness of the EMPCA-MI plots.

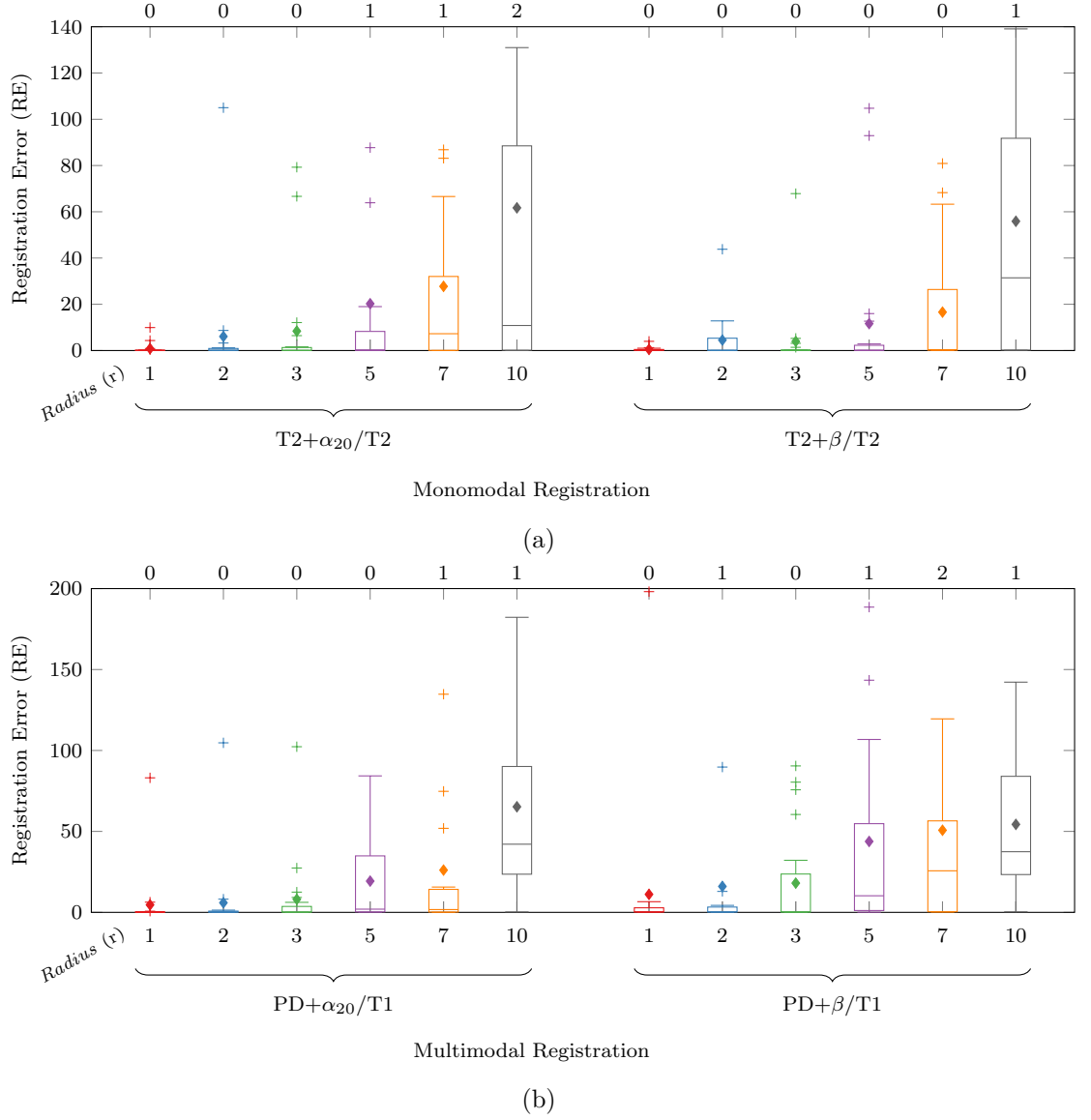


Figure 4.13: RE summary boxplot of (a) monomodal T2/T2 registration and (b) multimodal PD/T1 registration using varying neighbourhood radius with EMPCA-MI for all 20 initial mis-registration scenarios. The *mean* and *outliers* are denoted by \blacklozenge and $+$ shapes. The numbers on top of the plots refer to the number of *out-of-range* outliers with RE higher than 140 and 200 pixels respectively.

Figures 4.13(a) and (b) show the detailed RE summary boxplot results for registration using the varying r values with EMPCA-MI for all 20 initial mis-registration scenarios for monomodal T2/T2 and multimodal PD/T1 respectively. These boxplots confirm the improved registration performance at $r=1$ of EMPCA-MI with the lowest mean RE and no *out-of-range* outliers. But as r increases, the

registration performance deteriorates as mean RE increasing progressively. From $r=5$ and beyond, the interquartile range is also prominent along with the presence of *out-of-range* outliers.

These results strongly support the earlier qualitative analysis of the EMPCA-MI traces for varying neighbourhood radius, which means that choosing the lowest r in the *Step I* of EMPCA-MI helps to attain the granularity needed for optimal feature extraction. As and when the higher radii are chosen, local maxima were generated due to the INU and noise artefacts as in Figures 4.9(c) and (d), which consequently lead to poor registration performance. As $r=1$ has smoother EMPCA-MI traces, clearly it led to better convergence to the real maxima, in comparison to others.

Thus, considering the above qualitative analysis of EMPCA-MI traces, computation complexity/cost and finally registration performance, $r=1$ is chosen to be used for the rest of the experimentation work in this thesis.

4.4 Summary

In this chapter, a new hybrid similarity measure framework called EMPCA-MI has been introduced for MIR, with the aim of providing superior performance in the presence of artefacts and noise in both mono and multimodal images. EMPCA-MI utilises the concept of neighbourhood region from the RMI to extract the spatial features via principal component analysis, but unlike RMI, EMPCA-MI provides dimensionality reduction by iteratively determining the dominant principal com-

ponents. The computation of EMPCA-MI in this chapter was based on choosing one dominant principal component for EMPCA and fixed number of bins for MI computation, though these assumptions will be relaxed in subsequent chapters.

A critical analysis and evaluation of various system choices and parameters relating to interpolation and neighbourhood radius for the EMPCA-MI framework has been presented based on their impact on three factors, namely smoothness of the EMPCA-MI traces, computational complexity/cost involved and RE performance. This analysis showed how the choices of these parameters influence the overall registration performance, with bicubic interpolation and unity radius for neighbourhood regions emerging as the best choices for EMPCA-MI framework. While bicubic interpolation is computationally expensive, it still provided a smoother EMPCA-MI trace and lowest RE during preliminary registration. Similarly, $r=1$ for neighbourhood regions for EMPCA-MI gives consistently smoother traces, lower RE and minimal computational cost.

The next chapter will further investigate the quantitative as well as qualitative registration performance of EMPCA-MI framework on different mono and multimodal medical images. Furthermore, it will include a comparative analysis of EMPCA-MI framework with other existing similarity measures from the literature.

Chapter 5

EMPCA-MI-based Registration

Results

5.1 Introduction

This chapter investigates the performance of the proposed EMPCA-MI similarity measure framework for the registration of medical image datasets. As evident from the rigorous analysis in the previous chapter, the bicubic interpolation and neighbourhood region with $r=1$ were chosen as the most appropriate parameter choices for EMPCA-MI, so they are deployed through all the experiments of this chapter. Other than testing the EMPCA-MI framework, the experiments will also draw a comparison with MI, GMI, RMI, GFM and RIR-BS which were identified as comparators in *Chapter 3*. This comparative study will examine them from the perspective of both quantitative and qualitative registration performance as well as the computational cost involved.

EMPCA-MI Framework	
<i>Parameter Setting</i>	<i>Value</i>
Neighbourhood radius (r)	1
Principal components (P)	1
Number of bins (b)	256

Table 5.1: Parameter settings for EMPCA-MI framework.

Different initial misregistration scenarios along with various INU and noise levels were used during the experiments to test the robustness of EMPCA-MI framework as well as other comparators.

5.2 Experimental Setup

To critically assess the performance of the new EMPCA-MI framework, various experimental steps are employed. Firstly, EMPCA-MI framework is integrated within the MIR test bed. Then, the test trials using *Shepp-Logan* head phantom test image pair are used to validate and verify the implementation, as already elaborated in the research methodology *Chapter 3*. The generic MIR model discussed in *Section 3.3* is employed for experiments along with the parameter settings of the EMPCA-MI framework shown in Table 5.1.

For the EMPCA-MI framework fixed values of P and b are chosen. This assumption for P and b values will be relaxed and investigated in the next chapters. Registration experiments were conducted in two sets namely *Set 1* and *Set 2* as detailed in Table 5.2.

Experiment Set	Set 1		Set 2	
Dataset Name	BrainWeb		DRIVE	Brno-Multi
Dataset Modality	Monomodal	Multimodal	Monomodal	Multimodal
Dataset Images	T1/T1, T2/T2, PD/PD	T1/T2, T2/PD, PD/T1	Fundus/Fundus	Fundus/SLO
Added INU & Noise	5 levels (No INU & noise, α_{20} , α_{40} , β and $\alpha_{40} + \beta$)		N.A (inherently low contrast and homogeneous regions present)	
Initial Misregistration Scenarios	20 (See Section 3.5.1)		4	3
Transformation	Rigid		Similarity	
Comparators	MI, GMI, RMI		GFM	RIR-BS
Total Registrations	2400		160	60

Table 5.2: Experiments and their relevant parameter details.

The *Set 1* of registration experiments uses the mono and multimodal pairs of MRI T1, T2 and PD human brain images of the *BrainWeb* dataset. It comprises of all 2400 separate registration experiments, which include 3 monomodal image pairs, 3 multimodal image pairs, 5 levels of INU and Gaussian noise settings, 20 initial misregistration scenarios and 4 similarity measures (including the EMPCA-MI framework). Also, MI, GMI and RMI have emerged as prominent intensity-based similarity measures and were used as the comparators. The *Set 2* of registration experiments is performed on the mono and multimodal pairs of retinal images from the *DRIVE* and *Brno-Multi* datasets respectively. The monomodal retinal Fundus registration uses GFM (Gharabaghi et al., 2013) for comparison. This subset consists of 160 registrations, which include 20 monomodal image pairs, 4 initial misregistration scenarios and 2 methods (GFM and EMPCA-MI framework) (Reel et al., 2013c). Similarly, the multimodal registration of Fundus and SLO images

uses the recent RIR-BS (Chen et al., 2015, 2011) as a comparator. This subset consists of 60 registrations, which include 10 multimodal pairs, 3 initial misregistration scenarios and 2 methods (RIR-BS and EMPCA-MI framework) (Reel et al., 2013b). The quantitative *final* RE and the qualitative *checkerboard* overlay are used to compare all the registration results.

5.3 Experimental Results Discussion

5.3.1 *Set 1: BrainWeb* Dataset-based Experiments

The first set of experimental results is for the *Set 1* of registration experiments which included both mono and multimodal *BrainWeb* dataset.

Monomodal Results

Figure 5.1 consists of five RE vs. iteration plots for the monomodal subset for five levels of INU and noise levels in Table 5.2. It shows the 18th initial misregistration scenario $(-23.6, -7.72, -37.6^\circ)$ with *initial* RE=92.12 pixels. Each of these five plots of Figures 5.1(a) – (e) shows four registration experiments using EMPCA-MI alongside the comparators MI, GMI and RMI. They are plotted with a broken *y* axis, in order to highlight and zoom on the lower RE value as the registration process progresses to higher iteration values. It is clear from Figures 5.1(a) and (b) that all four similarity measures converge to a lower RE for monomodal T1/T1 registration both when no INU and noise are present and when α_{20} INU is introduced.

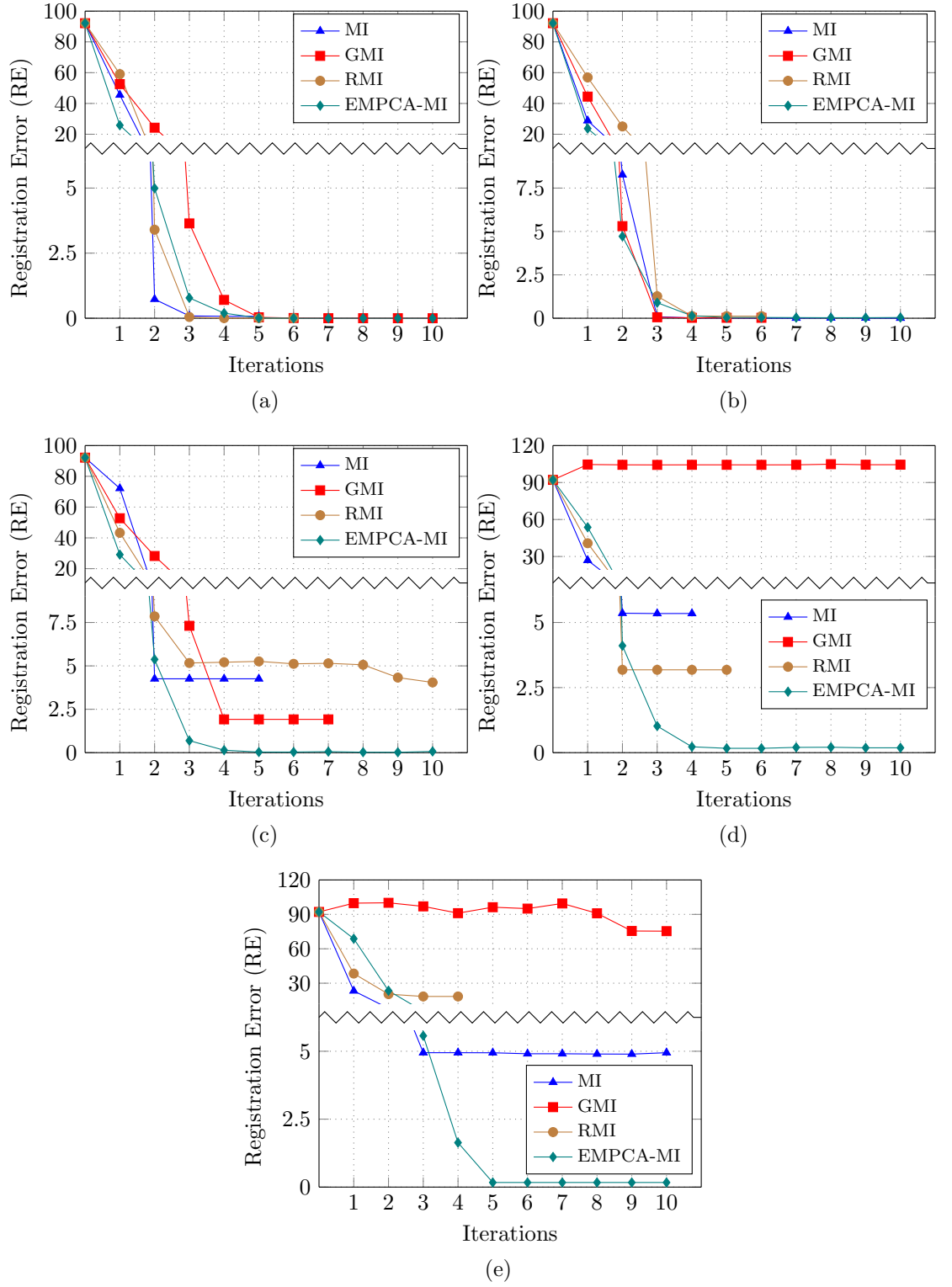


Figure 5.1: RE versus iteration plots for MI, GMI, RMI and EMPCA-MI using 18th initial mis-registration scenario for monomodal registration of (a) T1/T1, (b) T1+ α_{20} /T1, (c) T1+ α_{40} /T1, (d) T1+ β /T1 and (e) T1+ α_{40} + β /T1 pairs.

But as INU is increased to α_{40} as observed in Figure 5.1(c) only EMPCA-MI provides a lower RE and better rate of convergence with less number of iterations in comparison to others.

Furthermore, as β (Figure 5.1(d)) and then finally $\alpha_{40} + \beta$ (Figure 5.1(e)) are used, EMPCA-MI consistently provides lower RE throughout. This is due to the fact that the neighbourhood region (with $r=1$) pre-processing used for extraction of first principal component with EMPCA provides accurate information for the computation of MI, even when high levels of INU and Gaussian noise are introduced. In addition, using bicubic interpolation during the registration helped EMPCA-MI to achieve smoother EMPCA-MI traces, which leads to its better convergence. On the other hand, GMI used gradient information for its computation. Hence, in cases with higher INU and Gaussian noise levels, more noise is introduced into the gradient information, which leads to its inferior convergence (Figures 5.1(d) and (e)). For example, in Figure 5.1(d) GMI failed to register the monomodal pair and gave *final* RE even higher than the initial misregistration value. While EMPCA-MI is able to accurately quantify the spatial alignment between the image pairs with lower RE, RMI using a rough approximation of MI shows a degrading performance with increasing levels of INU and noise conditions (Figures 5.1(c) – (e)).

To have a qualitative assessment of the registration process outcome, Figures 5.2(a) – (f) show the *Canny edge detection* overlay results corresponding to the monomodal $T1+\alpha_{40}+\beta/T1$ pair registration shown in Figure 5.1(e). Figure 5.2(a) shows the initial misregistration for 18th initial misregistration scenario and the ground truth in Figure 5.2(b).

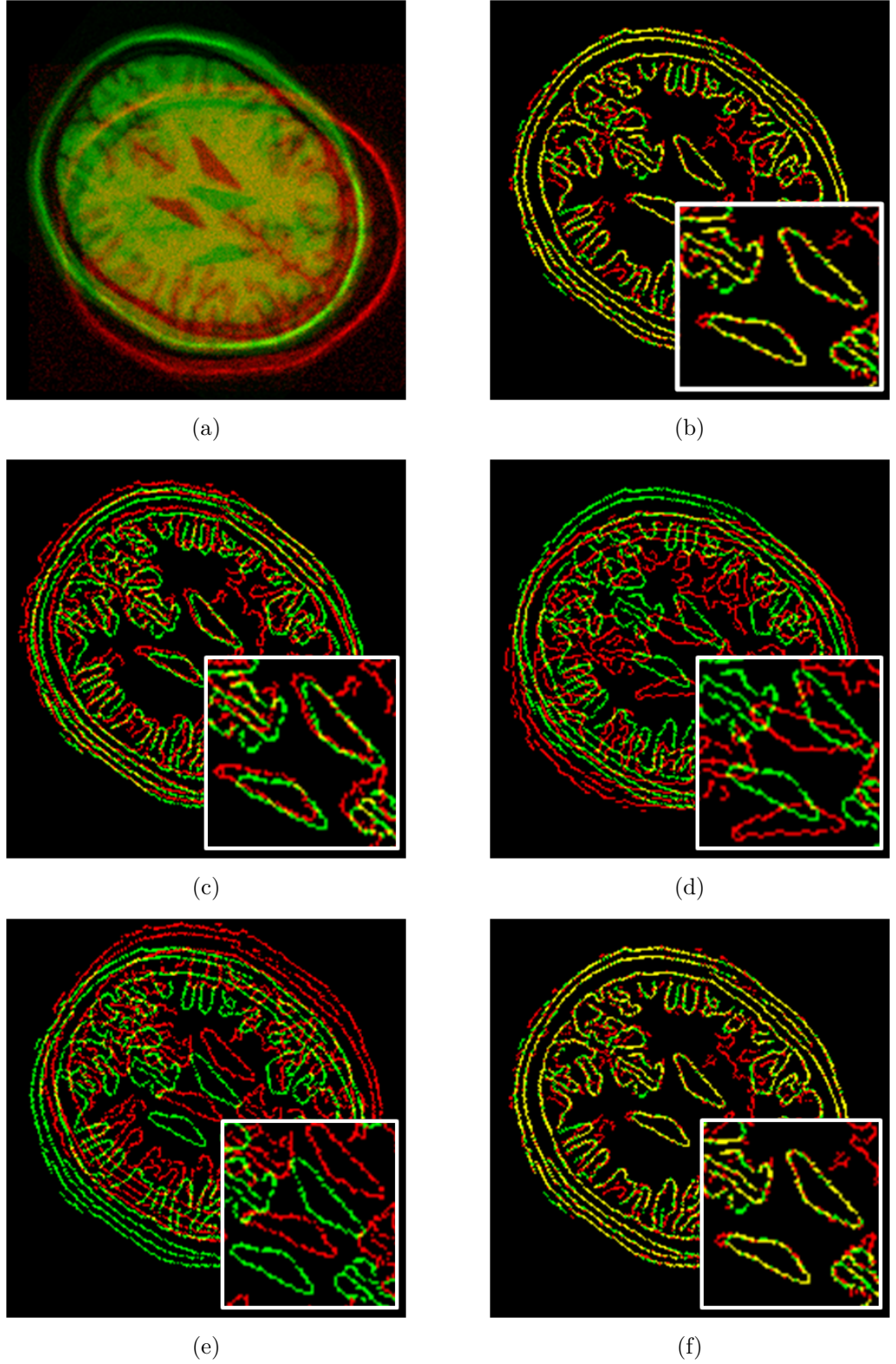


Figure 5.2: Qualitative results of monomodal $T1+\alpha_{40}+\beta/T1$ pair using 18th initial misregistration scenario showing (a) initial misregistration, (b) ground truth and (c) MI, (d) GMI, (e) RMI, (f) EMPCA-MI output with inset showing zoomed-in central lobes.

Figures 5.2(c) – (f) show the registration output for MI, GMI, RMI and EMPCA-MI respectively. The *yellow* colour in these images represents the correct alignment of the region, while *red* and *green* colour shows the misalignment. The quality of registration is apparent, particularly from the alignment of the two central lobes in the insets of Figures 5.2(c) – (f) of the registration output. Figure 5.2(f) clearly shows that EMPCA-MI provides best alignment in comparison to MI, GMI and RMI output and is nearest to the ground truth shown in Figure 5.2(b). These results are consistent with the earlier qualitative results and highlight the superior registration performance of EMPCA-MI in comparison to others.

Similar results were also observed for monomodal T2/T2 and PD/PD pair registrations for the same initial misregistration scenario. For completeness, Figures D.1(a) and (b) in *Appendix D*, shows the RE versus iterations plots for MI, GMI, RMI and EMPCA-MI for $T2+\alpha_{40}+\beta/T2$ and $PD+\alpha_{40}+\beta/PD$ pairs respectively. They were predominantly chosen for display since they show the results for the images with highest level of INU and noise present. Similarly, Figures D.2 and D.3 show the qualitative results of the above two mentioned pairs with their corresponding ground truths.

Multimodal Results

Figure 5.3 shows the RE vs. iteration plots for the multimodal $T1+\alpha_{40}+\beta/T2$ pair using 15^{th} initial misregistration scenario $(-5.23, 2.31, 34.8^\circ)$ with *initial* RE=84.16 pixels. It is again evident that EMPCA-MI provides a better rate of convergence and leading to the lowest RE, followed by GMI and MI.

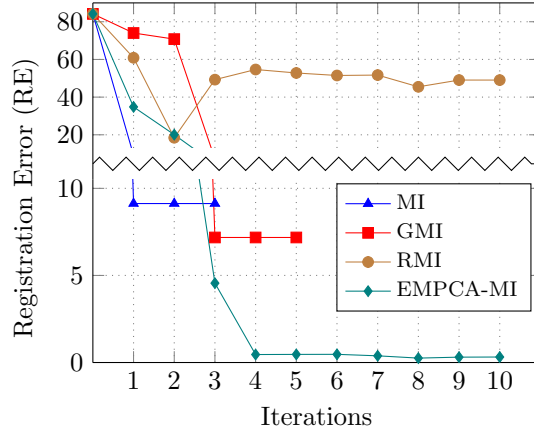


Figure 5.3: RE versus iterations plots for MI, GMI, RMI and EMPCA-MI using 15th initial misregistration scenario for multimodal registration of (a) T1+ $\alpha_{40}+\beta$ /T2 pair.

Even at higher level of INU and Gaussian noise, EMPCA-MI converges to a lower RE from 4th iteration onwards due to its ability to accurately represent the neighbourhood region features and quantify the spatial alignment between them. On the contrary, MI and GMI provide much higher RE, while RMI exhibits poor rate of convergence which locks into a local maximum too far from the global maximum.

To have a qualitative assessment of this particular multimodal T1+ $\alpha_{40}+\beta$ /T2 pair, Figures 5.4(a) – (f) shows the *Canny edge detection* overlaid corresponding results. Figure 5.4(a) shows the initial misregistration for 15th initial misregistration scenario and the corresponding ground truth in Figure 5.4(b). While Figure 5.4(c) – (f) show the registration output for MI, GMI, RMI and EMPCA-MI respectively. It is apparent, particularly from the alignment of the two central lobes in the insets of Figures 5.4(c) – (f) showing the registration output. Figure 5.4(f) clearly shows that EMPCA-MI provides best alignment followed by GMI output and is the closest to the ground truth in Figure 5.4(b).

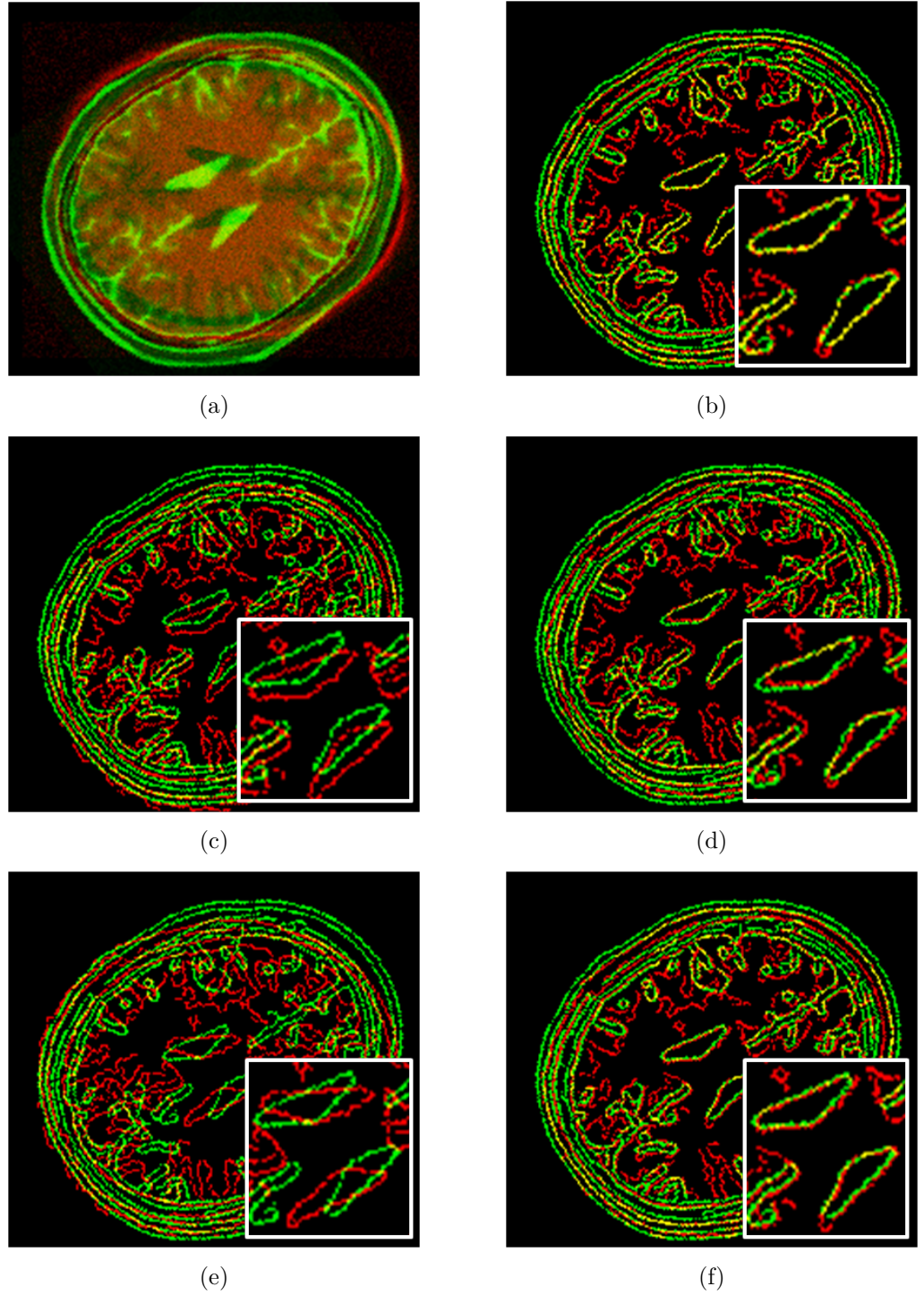


Figure 5.4: Qualitative results of multimodal $T1+\alpha_{40}+\beta/T2$ pair using 15th initial misregistration scenario showing (a) initial misregistration, (b) ground truth and (c) MI, (d) GMI, (e) RMI, (f) EMPCA-MI output with inset showing zoomed-in central lobes.

In addition, similar trends are seen in the results for the registration of the other four INU and Gaussian noise levels of this multimodal pair, included in Figures D.4(a) – (d) of *Appendix D* for completeness. These plots show the subsequent RE vs. iteration plots for the $T1/T2$, $T1+\alpha_{20}/T2$, $T1+\alpha_{40}/T2$ and $T1+\beta/T2$ pairs. It is clear from them that MI, GMI and RMI perform well when no or low INU is present, but as high INU and Gaussian noise are introduced, their performance worsens significantly with a lower rate of convergence. This can be further verified from the multimodal $T2/PD$ and $PD/T1$ pair registrations for the same initial misregistration scenario. Figures D.4(e) and (f) in *Appendix D*, show the RE versus iterations plots for $T2+\alpha_{40}+\beta/PD$ and $PD+\alpha_{40}+\beta/T1$ pairs. They were chosen because they represent the results for the most challenging pairs with highest level of INU and Gaussian noise. Similarly, Figures D.5 and D.6 of *Appendix D* show the qualitative results of both these pairs with their corresponding ground truths.

Results Summary

Finally, the overall RE performance for the *Set 1* experiments are summarised. Figures 5.5(a) and (b) show the detailed summary boxplot for all INU and noise levels, over the 20 initial misregistration scenarios for monomodal $T1/T1$ and multimodal $T1/T2$ registration experiments respectively. Each boxplot shows a bounding box defining the interquartile range with the bar across representing the median and whiskers denoting the RE range. The boxplots on top also include the number of *out-of-range* RE values corresponding to each similarity measure used.

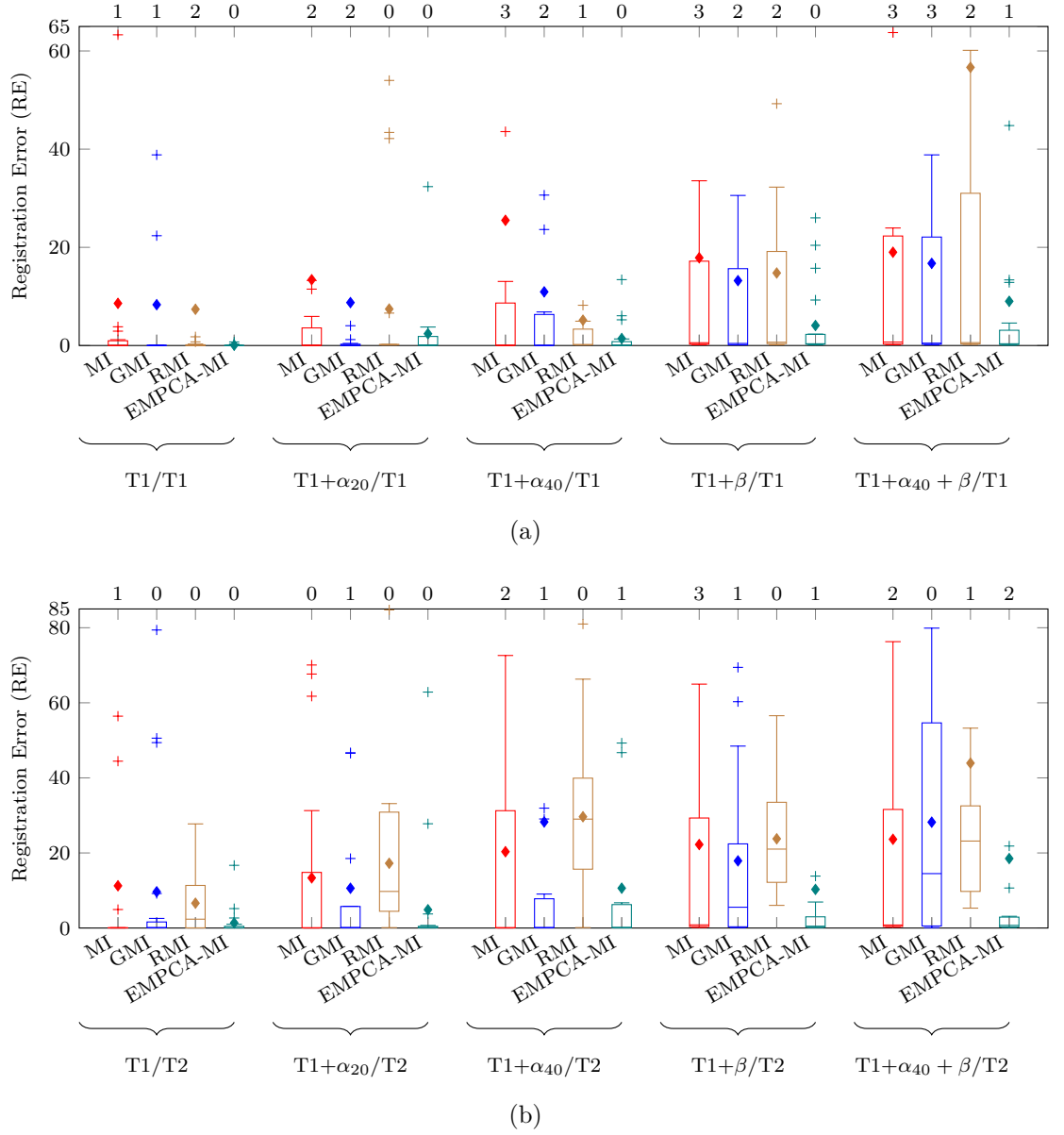


Figure 5.5: RE summary boxplot of (a) monomodal T1/T1 pair and (b) multimodal T1/T2 pair using MI, GMI, RMI and EMPCA-MI for all 20 initial misregistration scenarios. The *mean* and *outliers* are denoted by \blacklozenge and $+$ shapes. The numbers on top of the plots refer to the number of *out-of-range* outliers with RE higher than 65 and 85 pixels respectively.

Both boxplots in Figure 5.5 confirm the improved registration performance of EMPCA-MI with the lowest *mean* RE and few number of *out-of-range* outliers in comparison to the other three comparative similarity measures. For monomodal T1/T1 pair in Figure 5.5(a), EMPCA-MI consistently achieve better RE than all other similarity measure, especially in the latter two cases (β and $\alpha_{40} + \beta$).

For example in case of the monomodal $T1+\alpha_{40}+\beta/T1$ pair, EMPCA-MI maintains a lower RE and interquartile range with single *out-of-range* outlier, on the contrary the *mean* RE for RMI overshoots due to the large RE values for two *out-of-range* outliers. Similarly for multimodal $T1/T2$ pair in Figure 5.5(b), EMPCA-MI has lowest *mean* RE for all five INU and noise settings, while GMI performance degrades in the last two challenging cases (α_{40} and $\alpha_{40}+\beta$). Furthermore, the *mean* RE and *interquartile* range for RMI is also significantly large as higher INU and noise levels are introduced.

These results strongly support the individual RE vs. iteration plots for mono and multimodal registration experiments. Similar observations can be deduced from the boxplots for the mono ($T2/T2$ and PD/PD) and multimodal ($T2/PD$ and $PD/T1$) registration experiments, which are included as Figures D.7 and D.8 of *Appendix D* for completeness. In summary, considering all these boxplots for all the set of registrations for *BrainWeb* dataset, EMPCA-MI is able to reduce the RE on an average by 45%, 42% and 61% for MI, GMI and RMI respectively. These results clearly help to draw the conclusion that EMPCA-MI using $r=1$ for neighbourhood region pre-processing with $P=1$, to select the most prominent feature to calculate the MI, while other comparators perform well when no or low INU is present, at higher levels of INU and Gaussian noise their performance degrades.

On closer examination however, it is also evident from these results that there are few cases of EMPCA-MI-based registrations, which gave higher RE. For example, the outlier (with *final* RE value of 44.80 pixels) shown in the EMPCA-MI boxplot for monomodal $T1+\alpha_{40}+\beta/T1$ in Figure 5.5(a). A few other results with

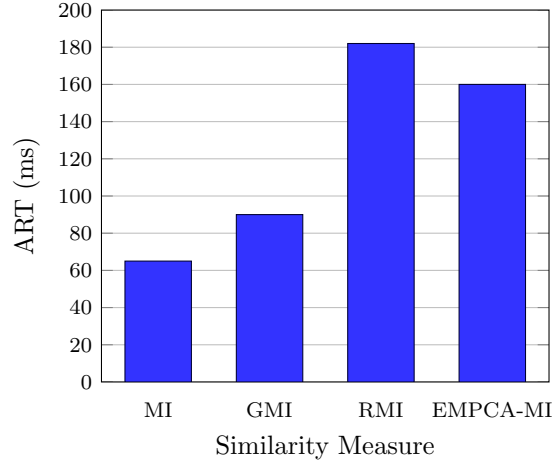


Figure 5.6: ART performance of various similarity measures for *Set 1: BrainWeb* Dataset-based mono and multimodal registration experiments.

higher RE for EMPCA-MI can also be seen in Figure D.7 and D.8 of *Appendix D*. Interestingly, all these cases are mostly observed where high INU and noise levels are present. The reason of EMPCA-MI underperformance particularly in these cases will be discussed later in *Section 5.3.3* of this chapter.

To evaluate the computational cost involved in the iterative registration process, an ART analysis was undertaken of all the similarity measures. Figure 5.6 shows the corresponding ART performance of all the four similarity measures considered for the mono and multimodal *BrainWeb* dataset registration experiments of *Set 1*. Here, EMPCA-MI requires around 15% less computation time in comparison to RMI and despite of being slower than other two comparators (MI and GMI) it is able to afford more robust and accurate registration performance both quantitatively and qualitatively. This is due to the fact that it utilises the iterative EMPCA mechanism to compute the first principal component from the neighbour region features, which helps in overcoming the artefacts due to the high INU and noise levels. While, MI takes the minimum computation time among all the sim-

ilarity measures since it bins the intensity values of the image into histograms to compute the individual and joint probability distribution, it was observed to have degraded registration performance. Also in case of GMI, the computation time increases by 25% with respect to MI, which reflects the added overhead of gradient information computation needed in addition to the MI calculation. Although RMI deploys a covariance matrix-based approximation to compute the individual and joint entropies, it consequently leads to doubling of the computation time with respect to GMI.

Overall, it is comprehensible that while EMPCA-MI has higher ART in contrast with other two similarity measure (MI and GMI), it is still able to provide better registration performance in terms of quantitative RE and qualitative assessment.

5.3.2 *Set 2: DRIVE and Brno-Multi Dataset Experiments*

This section discusses the experimental results for EMPCA-MI on *Set 2* of monomodal *DRIVE* dataset followed by those of the multimodal *Brno-Multi* dataset.

Monomodal Results

For the monomodal registrations, GFM was chosen as a comparator since it has emerged as one of the recent methods developed specifically for monomodal Fundus registration and has been used upon the same *DRIVE* dataset. In these experiments four initial misregistration scenarios were used. The first three initial misregistration scenarios were chosen as in (Gharabaghi et al., 2013) in order to enable a direct comparison.

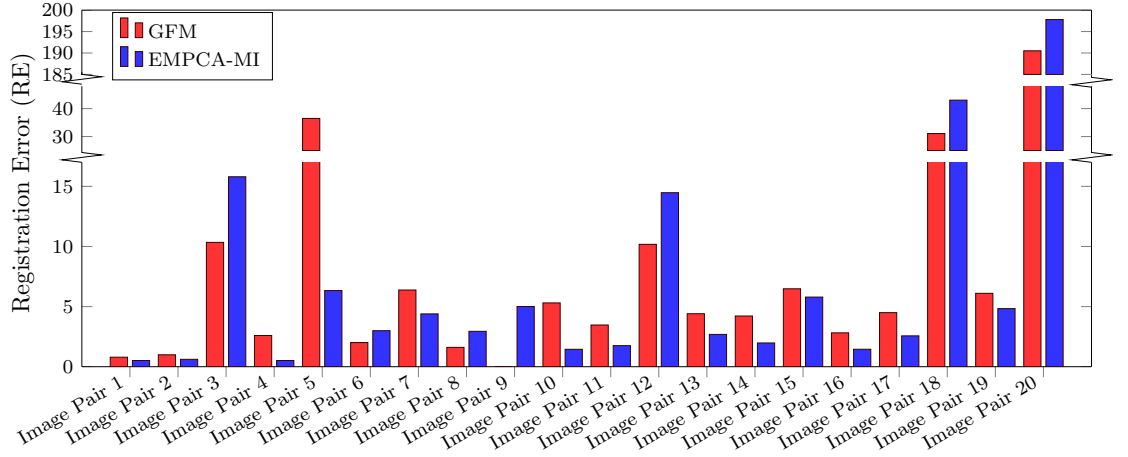


Figure 5.7: RE summary bar graph of 20 monomodal Fundus retinal image pairs using GFM and EMPCA-MI for 3rd initial misregistration scenario. *N.B.* Bar graph does not show GFM result for Image Pair 9 since the registration fails for the particular image pair.

Moreover, in order to further investigate the performance of EMPCA-MI, an additional 4th initial misregistration scenario was introduced. In the 1st and 2nd initial misregistration scenarios, only one registration parameter varies i.e. rotation $\theta=5^\circ$ and $\theta=60^\circ$ with the other parameters being fixed. While in 3rd and 4th initial misregistration scenario all four registration parameters are varied. This includes S , which simulates that Fundus image have been acquired using different equipment magnifications.

Figure 5.7 consists of RE summary bar graph of 20 monomodal Fundus image pairs using EMPCA-MI and GFM for the 3rd initial misregistration scenario (5, 5, 20°, 2.8). This bar graph are plotted with twice broken y axis in order to accommodate all the RE values on the same plot as well as to able to show the lower RE values. For example, the RE for *Image Pair 5* using EMPCA –MI is almost 5 times lower than GFM. *Image Pair 5* highlights the inherent characteristics present in all retinal images which lead to challenges in their registration. The EMPCA-MI framework is able to register with lower RE since by using a neighbourhood region-

based extraction of the first principal component helps in accurately compute MI despite of homogeneous regions and low contrast present, whereas GFM being a point-based method provided a false match for the registration and had significant RE for this *Image Pair*.

To have a qualitative assessment of the registration outcome in this subset, Figures 5.8(a) – (e) show the *checkerboard* overlay results of *Image Pair 5* using 3rd initial misregistration scenario. Figure 5.8(a) shows the initial misregistration for 3rd initial misregistration scenario and the ground truth with three marked regions in Figure 5.8(b). Also, Figures 5.8(c) and (d) show the registration output for GFM and EMPCA-MI with corresponding marked regions respectively. In Figure 5.8(e) the zoomed three marked regions of the ground truth and two registration outputs are shown. It is clear from Figure 5.8(e) that EMPCA-MI provides best vascular structure continuity in comparison to GFM and is also nearer to the ground truth in terms of alignment. Overall, these results confirm that EMPCA-MI afforded better registration performance compared to GFM in variable contrast and illumination conditions.

It is especially notable to highlight that EMPCA-MI successfully registered *Image Pair 9* as shown in Figures 5.9(a) – (e), whereas GFM failed to converge (Gharabaghi et al., 2013). This is due to the fact that EMPCA-MI does not rely on point-based feature extraction, but uses intensity-based feature extraction and hence it was more robust in being able to successfully registering *Image Pair 9*. In contrast, GFM extracts the closed boundary regions from *Image Pair 9* but since they have similar shapes and their corresponding affine moment invariant descriptors were very close to each other, it led to its failure in registering them.

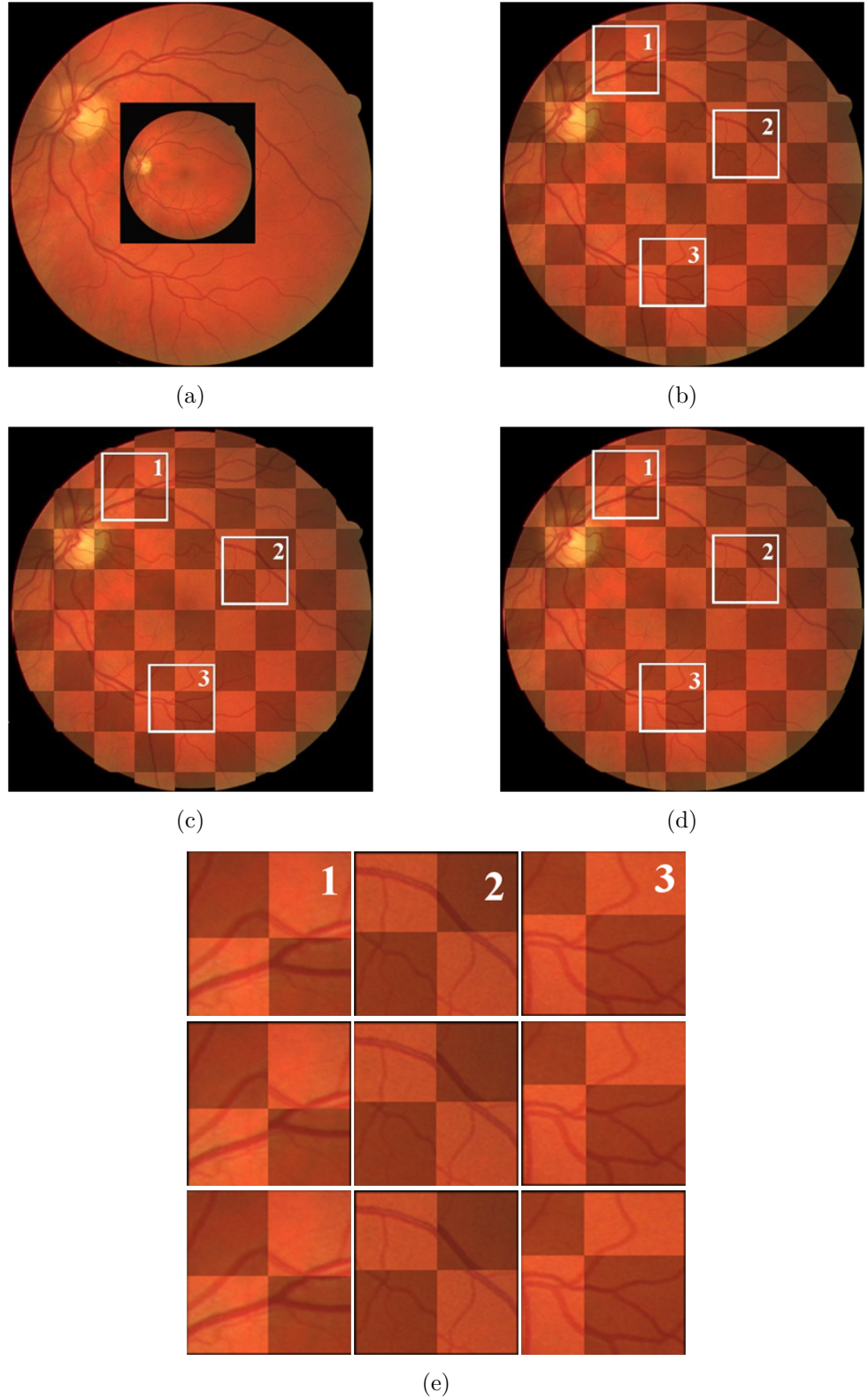


Figure 5.8: Qualitative results of monomodal Fundus retinal *Image Pair 5* using 3^{rd} initial misregistration scenario, showing (a) initial misregistration, (b) ground truth, (c) GFM and (d) EMPCA-MI output. Also (e) shows the zoomed-in regions of ground truth (1^{st} row), GFM (2^{nd} row) and EMPCA-MI output (3^{rd} row) respectively.

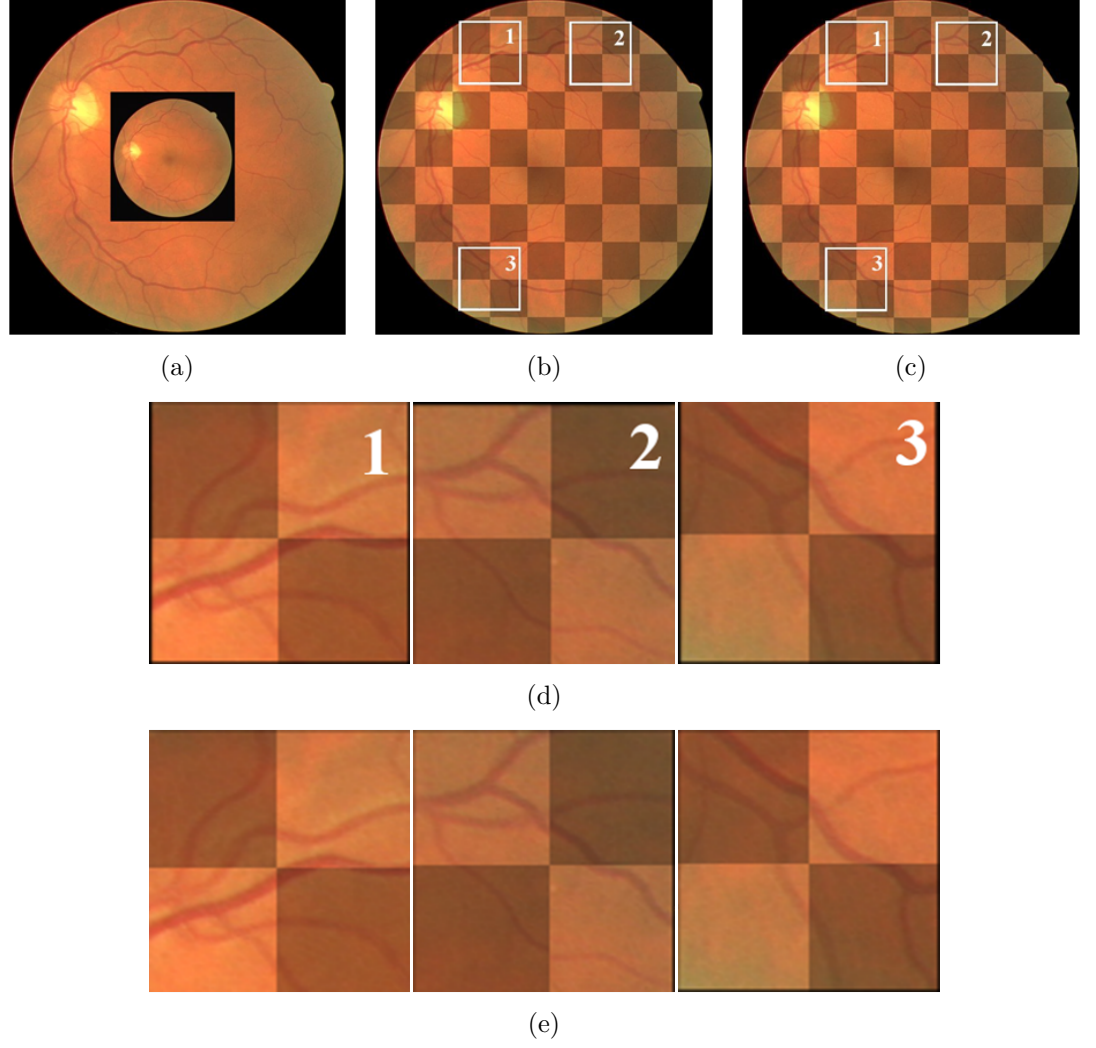


Figure 5.9: Qualitative results of monomodal Fundus retinal *Image Pair 9* using 3^{rd} initial misregistration scenario, showing (a) initial misregistration, (b) ground truth, (c) EMPCA-MI output, with (d) zoomed-in ground truth and (e) EMPCA-MI regions. *N.B. GFM failed to register this image pair.*

The zoomed in qualitative results for *Image Pair 9* using EMPCA-MI along with the corresponding ground truth are shown in Figures 5.9(e) and (d) respectively.

Finally, Figure 5.10 summarises the first subset of *Set 2* registration experiments. It shows the RE summary boxplot of all monomodal Fundus retinal image pairs using GFM and EMPCA-MI for the 4 test initial misregistration scenarios. The boxplots reveal the overall better registration performance of EMPCA-MI

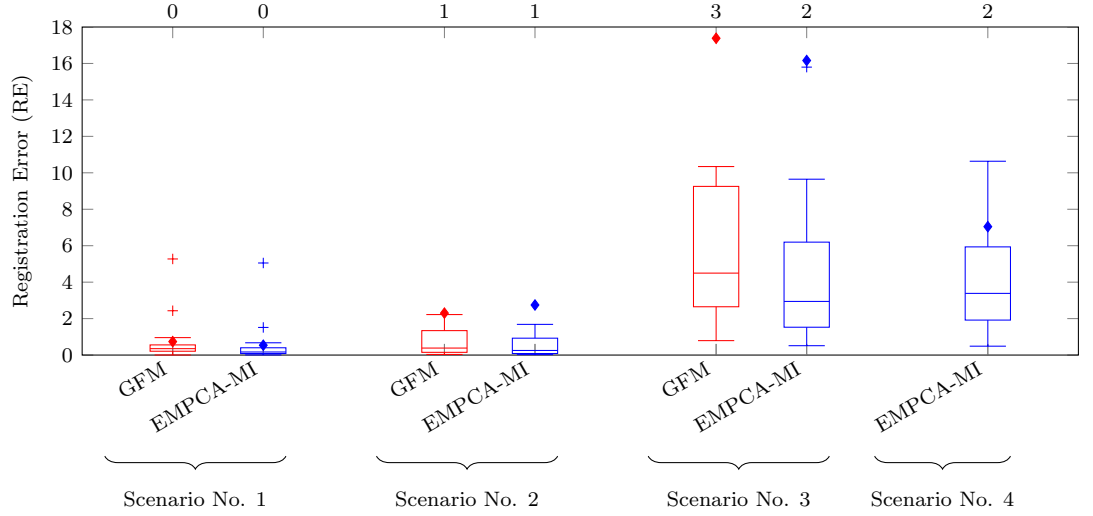


Figure 5.10: RE summary boxplot of 20 monomodal Fundus retinal image pairs using GFM and EMPCA-MI for all 4 initial misregistration scenarios. The *mean* and *outliers* are denoted by \blacklozenge and $+$ shapes. The numbers on top of the plot refer to the number of *out-of-range* outliers with RE higher than 18 pixels. *N.B.* GFM results for scenario no. 4 were unavailable.

over GFM. In all the initial misregistration scenarios EMPCA-MI achieves a lower *mean* RE as well the *interquartile* range, except for 2nd initial misregistration scenario where its *mean* RE is marginally higher than GFM, despite of having a lower *interquartile* range. This was due to the one *out-of-range* outlier for which the *final* RE was much higher and was challenging for both EMPCA-MI and GFM to register. Such particular cases will be discussed in detail in *Section 5.3.3*.

Multimodal Results

Now the registration experiment results for the second subset of *Set 2* using multimodal Fundus/SLO *Brno-Multi* dataset are discussed. To draw a comparison, RIR-BS was chosen as a comparator for these multimodal registrations, as it was recently developed specifically for multimodal retinal registration. As discussed earlier in *Section 2.3.3*, it employs a bifurcation structure matching which comprises of a master bifurcation point and three connected neighbours (Chen et al., 2015, 2011).

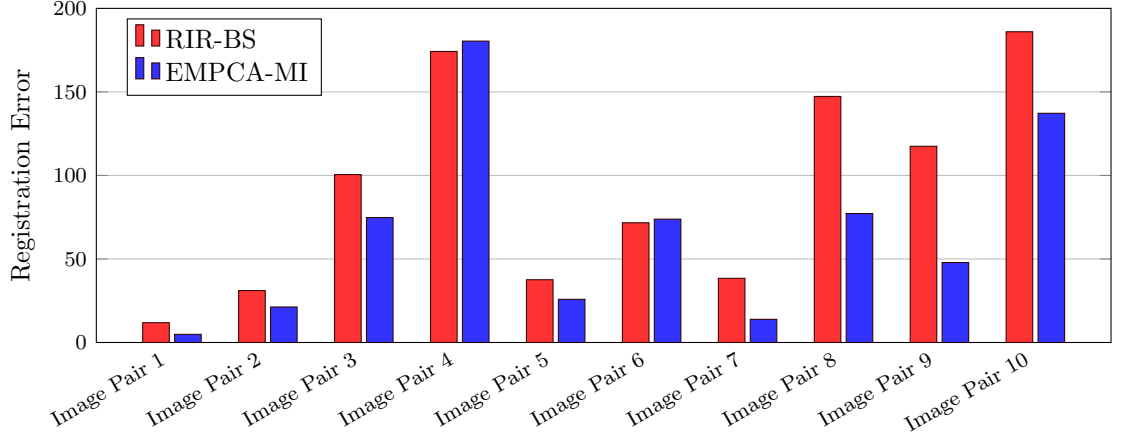


Figure 5.11: RE summary bar graph of 10 multimodal Fundus/SLO retinal image pairs using RIR-BS and EMPCA-MI for 2^{nd} initial misregistration scenario.

In these registration experiments, three initial misregistration scenarios were used. In the 1^{st} initial misregistration scenario, only the rotation parameter was varied to $\theta=60^\circ$ with the other parameters being fixed. The 2^{nd} and 3^{rd} misregistration represents more challenging scenarios with all the four registration parameters being varied. The value of S as in previous subset reflects the multimodal pair has been acquired with different equipment magnifications while the translations are pragmatically kept low as these motions are generally minimal during the image acquisition process.

In Figure 5.11, the RE summary bar graph of 10 multimodal Fundus/SLO image pairs using EMPCA-MI and RIR-BS for the 2^{nd} initial misregistration scenario $(10, 10, 30^\circ, 2)$ are shown. For example, for *Image Pair 3* and *8*, EMPCA-MI provides 25% and 50% less RE respectively, in comparison to RIR-BS. EMPCA-MI is in fact able to attain a lower RE since it utilises the local neighbourhood region using $r=1$ to extract the most prominent feature from the largely homogeneous and variable contrasted multimodal image pairs. Other than evaluating the quantitative RE performance, in order to appreciate the superiority of the

EMPCA-MI results, a qualitative assessment of the registration outcome in also conducted.

Figures 5.12(a) – (e) show the *checkerboard* overlay result of *Image Pair 3* using 2^{nd} initial misregistration scenario. Figures 5.12(a) and (b) show the initial misregistration for 2^{nd} initial misregistration scenario and the ground truth with three marked regions respectively. Whereas, Figures 5.12(c) and (d) show the registration output for RIR-BS and EMPCA-MI with corresponding marked regions respectively. In Figure 5.12(e) the zoomed three marked regions of the ground truth and two registration outputs are shown. It is evidently clear that EMPCA-MI provides much better structural continuity in comparison to RIR-BS output. Overall, it is apparent that EMPCA-MI provided lower RE for almost all image pairs, except *Image Pair 4* and *6*.

Interestingly, notable exceptions for EMPCA-MI are *Image Pair 4* and *6* where RIR-BS has a marginally lower RE. Similar higher RE for EMPCA-MI was again observed for the 3^{rd} initial misregistration scenario for *Image Pair 4*. This is due to the fact that two image pairs, especially *Image Pair 4* is one of the most challenging pairs in the *Brno-Multi* dataset as it exhibits pathology alongside low contrast and large homogeneous regions, which compromises EMPCA-MI performance when only one principal component is used. In contrast, since RIR-BS method uses segmentation, its registration quality is influenced much more by low contrast in the images rather than the presence of large homogeneous regions in this pair. The higher RE of EMPCA-MI highlights a limitation of the EMPCA-MI in the case of such challenging *Image Pair*, which will be analysed in the next section.

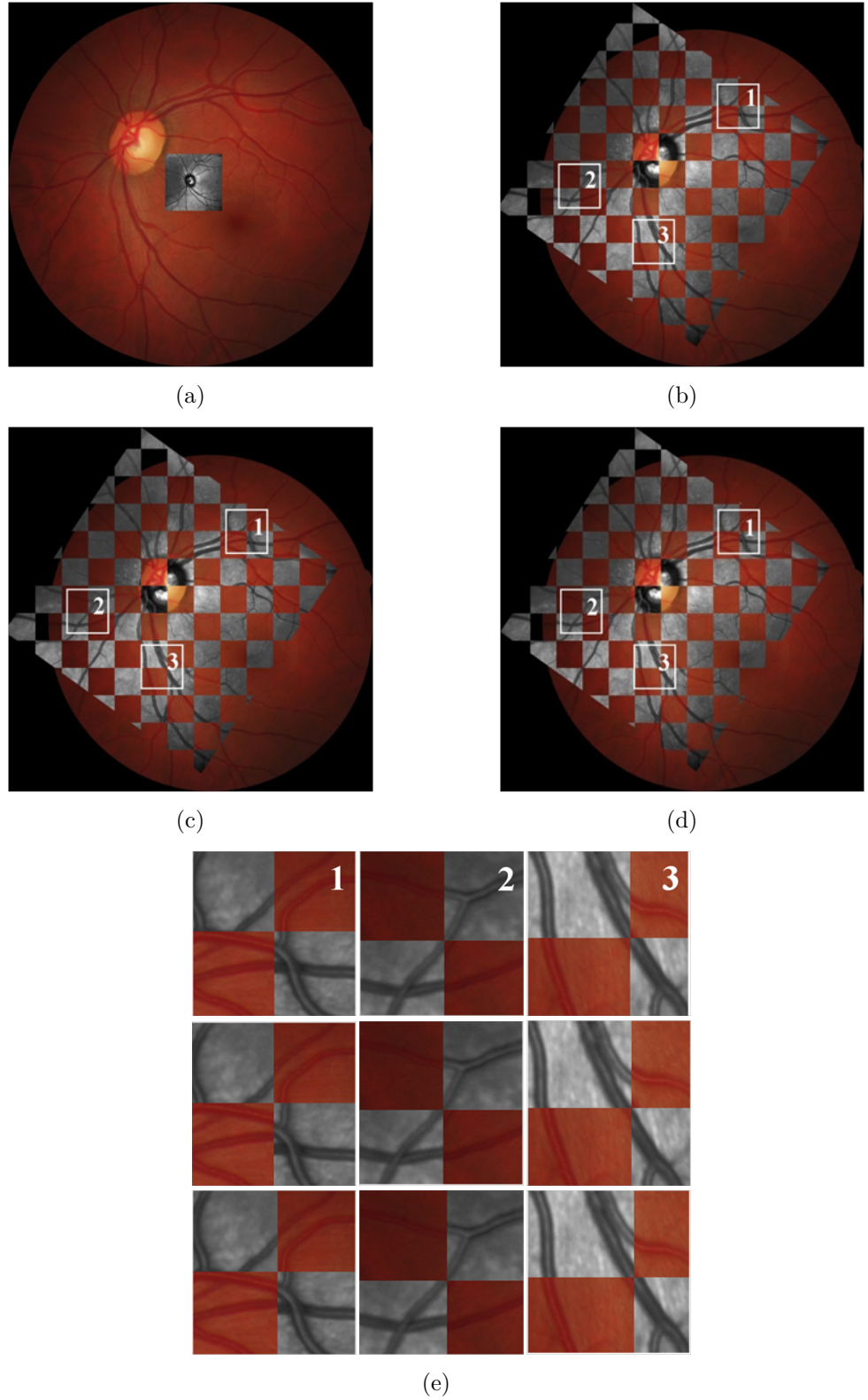


Figure 5.12: Qualitative results of multimodal Fundus/SLO retinal *Image Pair 3* using 2nd initial misregistration scenario, showing (a) initial misregistration, (b) ground truth, (c) RIR-BS and (d) EMPCA-MI output. Also (e) shows the zoomed-in regions of ground truth (1st row), RIR-BS (2nd row) and EMPCA-MI output (3rd row) respectively.

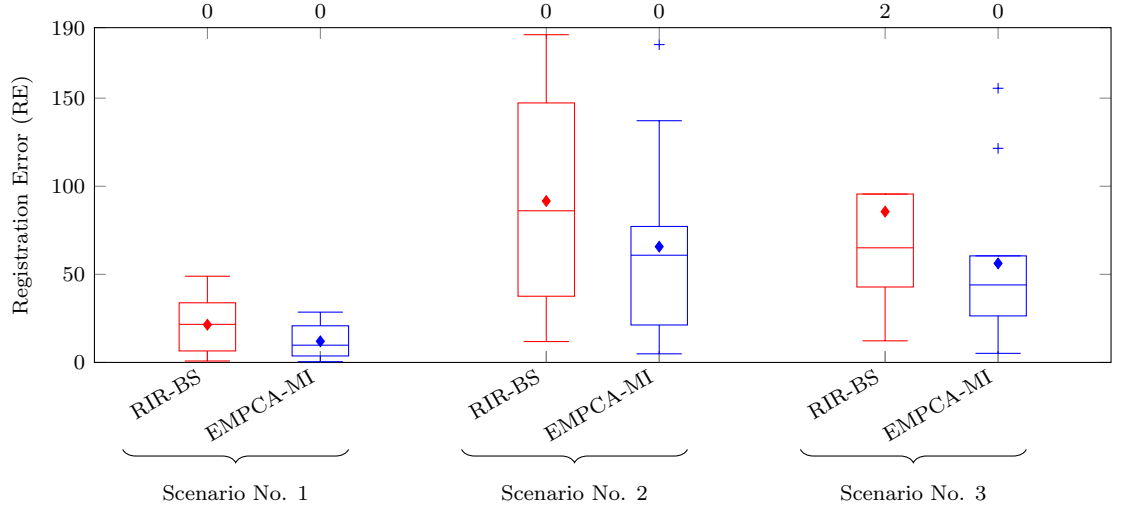


Figure 5.13: RE summary boxplot of 10 multimodal Fundus/SLO retinal image pairs using RIR-BS and EMPCA-MI for all 3 initial misregistration scenarios. The *mean* and *outliers* are denoted by ◆ and + shapes. The numbers on top of the plot refer to the number of *out-of-range* outliers with RE higher than 190 pixels.

Finally, Figure 5.13 summarises the second subset of *Set 2* registration experiments. It shows the RE summary boxplot of all multimodal Fundus/SLO retinal image pairs using RIR-BS and EMPCA-MI for the three initial misregistration scenarios. The boxplots reveal the overall superior registration performance of EMPCA-MI in terms of both *mean* RE and *interquartile* range over RIR-BS in all scenarios.

The boxplot for the 3rd initial misregistration scenario highlights the better RE performance achieved by EMPCA-MI with lower *mean* RE, smaller *interquartile* range and no *out-of-range* outlier RE value. Here, the neighbourhood region-based pre-processing followed by the feature extraction for MI computation enables the EMPCA-MI to perform better multimodal registration. On the contrary, despite of using a point-based approach, RIR-BS does not avail from any vessel width-based refinement (Chen et al., 2011) for its matching, which leads to an overall higher *mean* RE in these multimodal experiments. Hence, these results confirm

that overall EMPCA-MI provided better registration performance compared to RIR-BS especially in the presence of low contrast and large homogeneous non-vascular regions.

Moreover, the summary boxplots in Figures 5.10 and 5.13 help to conclude that EMPCA-MI is able to overall reduce the RE on an average by 30% for mono and multimodal retinal image registrations with respect to GFM and RIR-BS.

5.3.3 EMPCA-MI Framework Robustness

The previous sections have investigated the performance of EMPCA-MI framework along with other comparators for two sets of mono and multimodal registration experiments. Although overall EMPCA-MI achieved lower RE in comparison to others, as shown in Figures 5.5, 5.10 and 5.13, there were cases when EMPCA-MI performance is not as accurate as the comparators. To critically evaluate the reasons for this, two worst case scenarios are considered.

In *Section 5.3.1*, there were few individual cases in the mono and multimodal registration of *Set 1*, having high levels of INU and noise (for example α_{40} and $\alpha_{40}+\beta$) where EMPCA-MI gave higher RE values. For example in Figure 5.5(a) the EMPCA-MI boxplot for monomodal $T1+\alpha_{40}+\beta/T1$ shows one such outlier (with RE value of 44.80 pixels) for 11th initial misregistration scenario (24.21, -25.2, -25.8°). Few similar cases can also be observed for multimodal registrations of *Set 1*. The EMPCA-MI boxplot for multimodal $T2+\alpha_{40}+\beta/PD$ in Figure D.8(a) of *Appendix D* shows two such outliers (with RE values of 29.48 and 49.35 pixels) representing result of 7th and 20th initial misregistration scenarios.

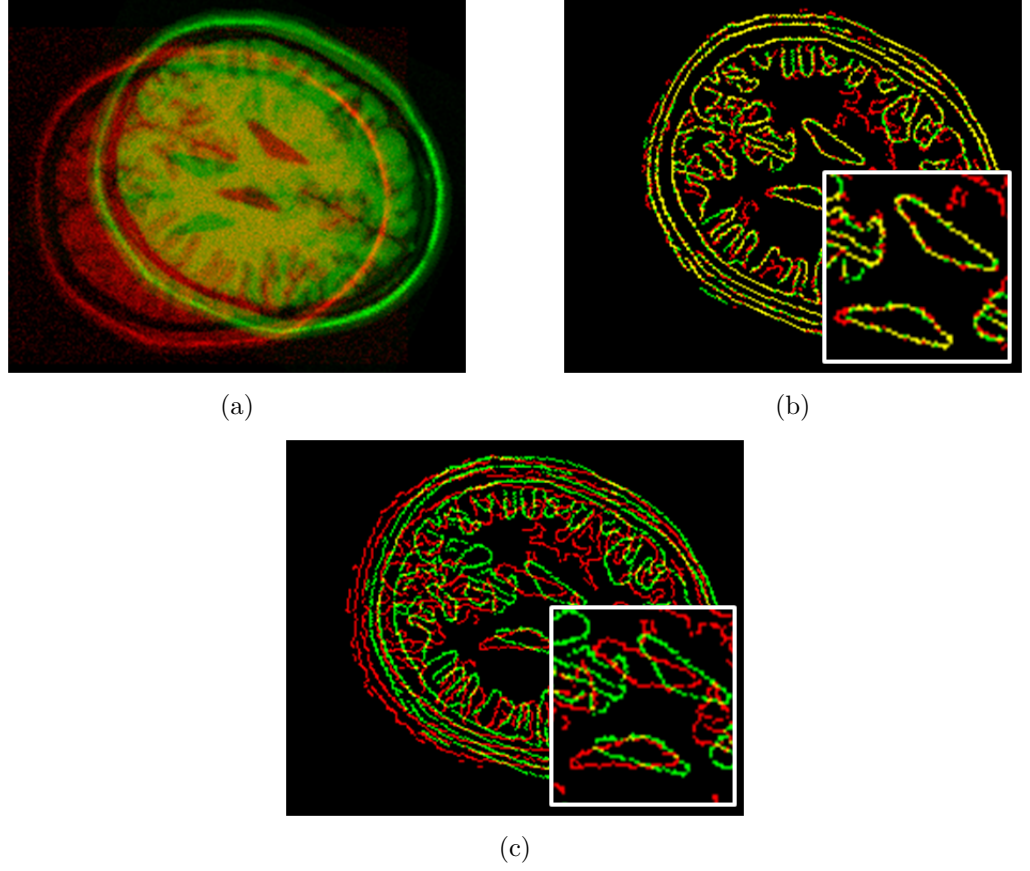


Figure 5.14: Qualitative results of multimodal $T1+\alpha_{40}+\beta/T1$ pair using 11^{th} initial misregistration scenario showing (a) initial misregistration with (b) ground truth and (c) EMPCA-MI output with inset showing zoomed-in central lobes.

To analyse the impact on the quality of registration, Figures 5.14(a) – (c) show the qualitative result for EMPCA-MI of monomodal $T1+\alpha_{40}+\beta/T1$ registration with 11^{th} initial misregistration scenario. The initial misregistration for this monomodal pair is shown in Figure 5.14(a). It is clear from the misaligned central lobes shown in the zoomed-in inset in Figure 5.14(c) that the EMPCA-MI registration performance is inferior in comparison to the ground truth in Figure 5.14(b). It can be argued that the deterioration in the EMPCA-MI performance specifically in the presence of high levels of INU and noise is due to the design of *Step I* of the EMPCA-MI framework in Figure 4.2 (which shows an example of the EMPCA-MI framework).

However, in closely observing Figure 4.2, there is a noticeable repetitive pattern in Q_R and Q_S which correspond to the rearranged neighbourhood region information for the reference and sensed image respectively. This 1st order representation of the neighbourhood region does not include any relative information about neighbourhood pixels, so at higher levels of INU and noise, the *Step I* of the EMPCA-MI framework may not always be able to represent the neighbourhood information accurately. This could indeed lead to inaccurate EMPCA-based extraction of features, which are used for the MI computation.

Moreover, as mentioned in Legg et al. (2013), the number of bins for MI computation has been shown to be a critical parameter for accurate MI computation. Therefore, the empirically fixed number of bins in the *Step III* of the EMPCA-MI framework may lead to inaccurate MI calculation especially when the image intensity values are corrupted by noise due to high levels of INU. Hence, the role of the neighbourhood region rearrangement (in *Step I*) and number of bins for MI (in *Step III*) in EMPCA-MI framework will be separately investigated in the next chapter, with an aim to enhance the EMPCA-MI framework as described in Figure 1.1.

Furthermore in *Section 5.3.2*, which discussed the *Set 2* of registration experiments, EMPCA-MI provided high RE for the *Image Pair 4*, which is one of the most challenging pairs in the multimodal *Brno-Multi* dataset. To understand the reasons behind this degraded performance for this particular case, further experimentation was conducted by choosing two principal components i.e. $P=2$ manually in the *Step II* of EMPCA-MI framework, while keeping all other parameters fixed for both the 2nd and 3rd initial misregistration scenarios.

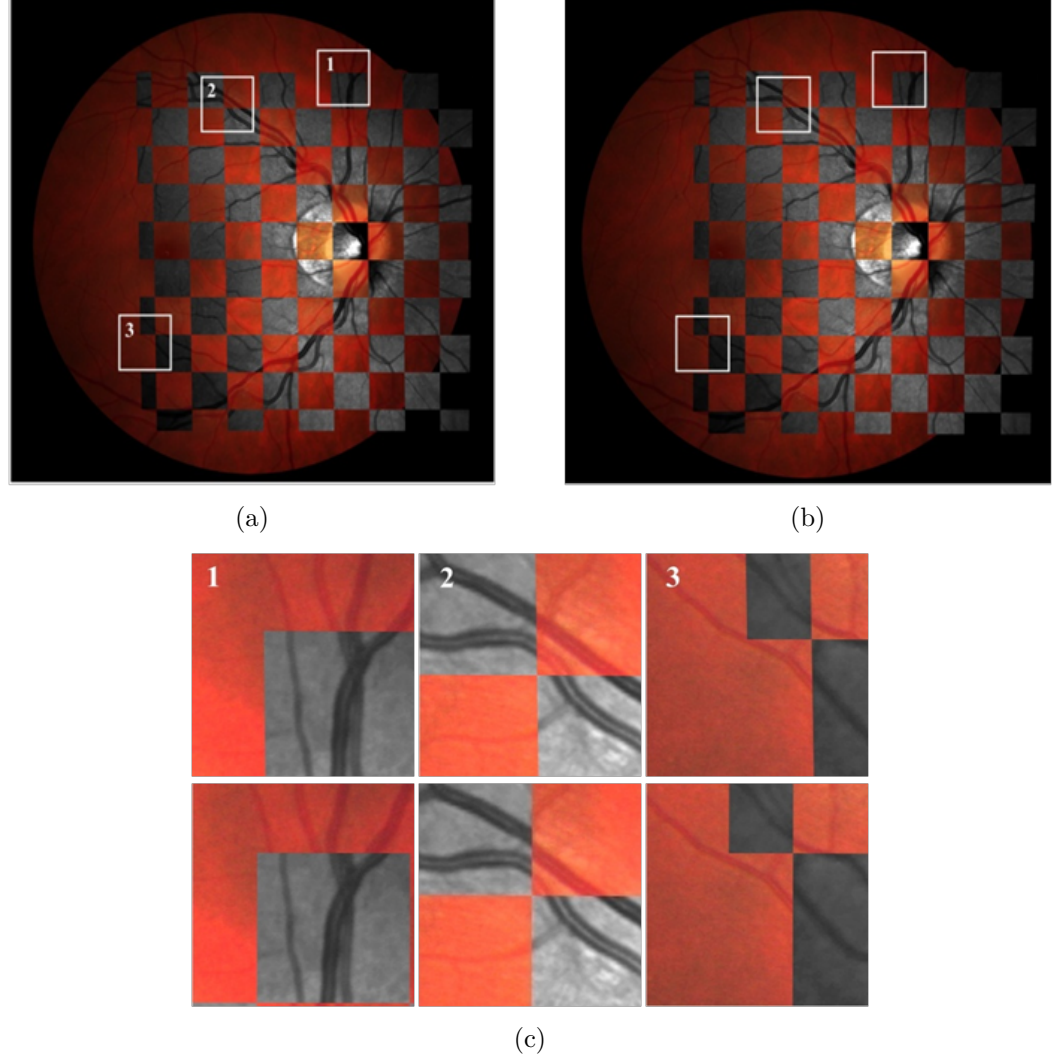


Figure 5.15: Qualitative results of multimodal Fundus/SLO retinal *Image Pair 4* using 3^{rd} initial misregistration scenario, showing (a) EMPCA-MI output (with $P=2$) and (b) RIR-BS output. Also (c) shows the three zoomed-in regions of EMPCA-MI output (with $P=2$) (1^{st} row) and RIR-BS (2^{nd} row) respectively.

Figures 5.15(a) – (c) show the qualitative results for this particular multimodal experiment for the 3^{rd} initial misregistration scenario. It is clear, that using EMPCA-MI with $P=2$ provided improved registration results in comparison to RIR-BS, which is attributed to the empirically chosen $P=2$, which represents the overall variance of the image pair, but now with two orthogonal principal components. This also highlights the versatility of the EMPCA-MI framework to iteratively determine more principal components and this feature can be exploited

in such cases. This provided the motivation to investigate this feature of EMPCA-MI framework in more detail. Hence, *Chapter 7* of this thesis will investigate a mechanism, which has the ability, in *Step II* of EMPCA-MI framework to automatically select the number of principal components adaptively instead of manually as shown in Figure 1.1.

5.4 Summary

This chapter investigated the registration performance of EMPCA-MI framework using human brain *BrainWeb* dataset followed by monomodal retinal *DRIVE* dataset and multimodal *Brno-Multi* dataset. It also conducted a comparative performance study using recent suitable comparators from the literature to enable a critical and thorough analysis of registration experiments using RE vs. iteration plot, quantitative and qualitative RE and ART as the performance metrics. This chapter showed how the EMPCA-MI framework is able to outperform its comparators by reducing the RE and providing a robust registration performance for the various mono and multimodal datasets, even when high levels of INU, low contrast and large homogeneous regions, which are known to make the registration process challenging. Finally, this chapter also gave an insight into the shortfalls of EMPCA-MI framework, while discussing two such cases in detail, where the registration performance degraded. The next chapter will propose and investigate enhancements based on the rearrangement of neighbourhood region and number of bins for MI computation in the EMPCA-MI framework, with an aim to further increase the robustness and achieve lower RE.

Chapter 6

EMPCA-MI Framework

Enhancements

6.1 Introduction

In the previous chapter, the experimental results of proposed EMPCA-MI framework provided consistent and robust registration performance for both mono and multimodal medical datasets. However, in a few registration experiments, the performance of EMPCA-MI framework was observed to be compromised, especially where high INU noise and large homogeneous regions were present. This was associated to the 1st order-based rearrangement of the neighbourhood region and choosing fixed number of bins for the MI computation for the EMPCA-MI framework. Hence, this chapter proposes two novel modifications to the EMPCA-MI framework, primarily in its pre-processing and MI computation steps. Firstly, it utilises the 2nd order representation of the image intensity values for direct

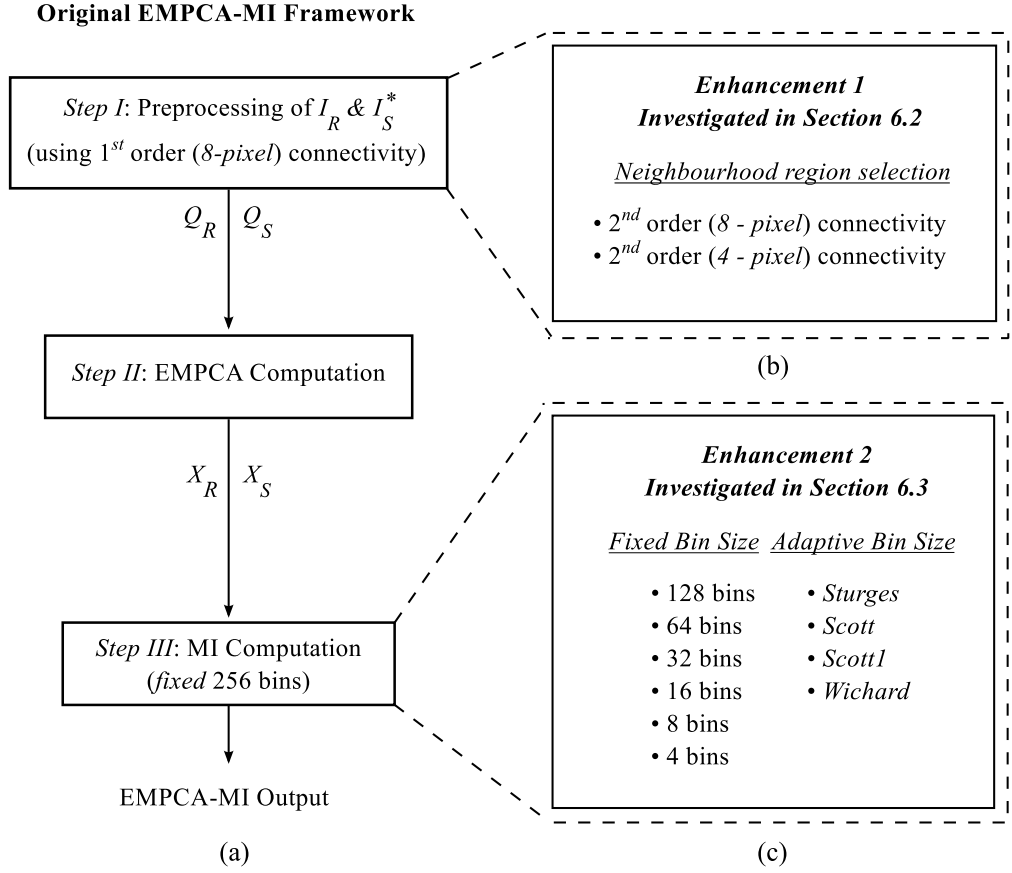


Figure 6.1: Schematic showing (a) the original EMPCA-MI framework and the various approaches investigated as enhancements in (b) *Step I* and (c) *Step III* respectively.

(4-pixel) and indirect (8-pixel) neighbourhood connectivity, instead of just rearranging the pixels in the pre-processing stage. Secondly, it explores the effect of introducing either fixed or adaptive number of bins selection strategy for the MI computation stage. Both these enhancements have been rigorously investigated using separate experiments to provide the numerical and qualitative registration results which confirm the improved robustness and show their corresponding computational cost. Figure 6.1(a) shows the original EMPCA-MI framework, which utilised the 1st order indirect (8-pixel) neighbourhood region connectivity for the pre-processing stage and fixed number of bins for MI computation. *Section 6.2* describes the introduction of 2nd order direct (4-pixel) and indirect (8-pixel) neighbourhood connectivity for the pre-processing of the reference and sensed images.

Section 6.3 explores the use of different fixed and adaptive number of bins selection approaches for the MI computation step. Figures 6.1(b) and (c) show the various approaches explored as *Enhancement 1* and *2*, which will be discussed in *Sections 6.2* and *6.3* respectively.

6.2 EMPCA-MI Framework *Enhancement 1*

As detailed in *Chapter 4*, the pre-processing step of EMPCA-MI framework rearranges the neighbourhood region *grayscale* data values into a vector form to preserve both the spatial and intensity information of the images. Figure 6.2(a) shows the illustration of EMPCA-MI framework with *Step I* in detail, which reorganises the image *grayscale* values using 1st order-based (*8-pixel*) neighbourhood region to incorporate the spatial information. This provided noteworthy performance in the registration experiments in *Chapter 5*, particularly when there is neither INU nor noise present. However, when there was high levels of INU and noise, the corresponding registration performance dropped.

This limitation of EMPCA-MI framework was due to the 1st order-based neighbourhood region representation, which considers each pixel independently and without cognisance of any neighbourhood relations. This was reflected in the repetitive patterns in the columns of Q_R and Q_S matrix for the neighbouring position of the sliding window, which can be seen in Figure 6.2(b). This provides the motivation for modifying this step of EMPCA-MI framework such that the neighbouring relations within a given neighbourhood region are preserved for other steps in the EMPCA-MI framework.

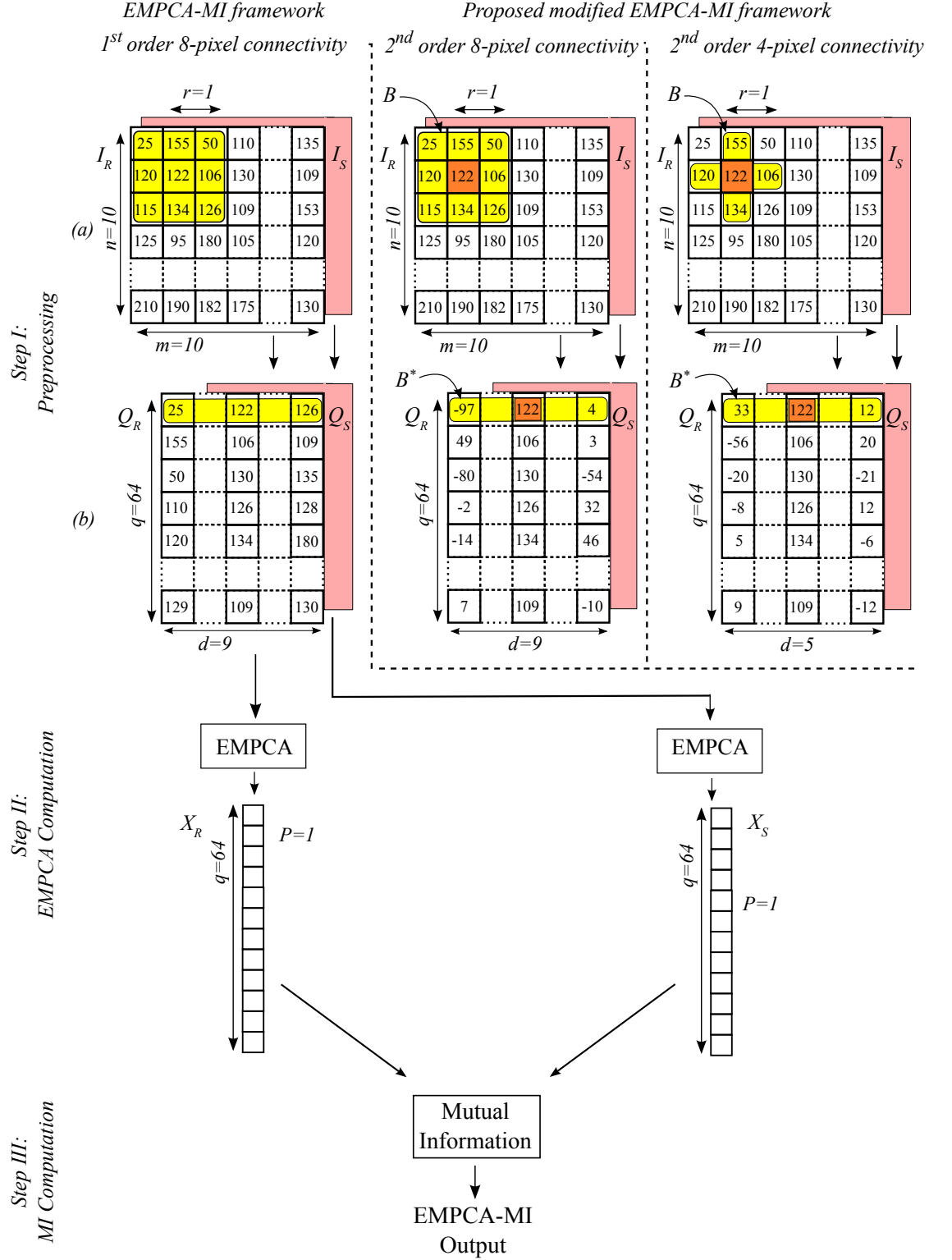


Figure 6.2: Illustration of the original EMPCA-MI framework with 1^{st} order (8-pixel) and the proposed 2^{nd} order (8-pixel and 4-pixel) region connectivity-based pre-processing in *Step I*, for an image pair with size of 10×10 pixels.

Hence, in order to achieve more robust registration between the reference and sensed images, this rationale during the pre-processing step a neighbourhood region can be more precisely characterised by a 2^{nd} order representation, where the relationship between pixels can be exploited instead of just pixel values.

6.2.1 Neighbourhood Region Selection

This section illustrates the modified pre-processing step for EMPCA-MI similarity measure framework (Reel et al., 2013a). Considering a sliding window B with radius r having a $(2r + 1) \times (2r + 1)$ pixels neighbourhood region. Then the resulting single row vector B^* will have length $c+1$, and can be represented as:

$$B_i^* = \begin{cases} B_i - B_{\frac{c}{2}+1} & i \in [1, c + 1]; i \neq \frac{c}{2} + 1 \\ B_{\frac{c}{2}+1} & i = \frac{c}{2} + 1 \end{cases} \quad (6.1)$$

Each row vector B^* now represents the differential value of c connected pixels with respect to the centre pixel $B_{\frac{c}{2}+1}$. Figure 6.2(a) gives an example using an image pair with size of 10×10 pixels showing the proposed 2^{nd} order *4-pixel* (direct neighbours) and *8-pixel* (indirect neighbours) connectivity alongside the original EMPCA-MI framework. Here, B is having a 3×3 pixel neighbourhood region when $r=1$ for both $c=4$ and 8 (shown with *yellow* colour in Figure 6.2(a)) and the corresponding row vector B^* with centre pixel B_3 and B_5 (shown with *orange* colour in Figure 6.2(b)) respectively. Here, the modified EMPCA-MI pre-processing no longer generates repetitive pattern as in original EMPCA-MI, but instead provides unique relative intensity values (See B^* in Figure 6.2) for its next

computational steps. Hence this enhancement helps in representing the spatial information for effectively and thus now leading to more accurate EMPCA-MI value in comparison to the original EMPCA-MI.

Although both 2^{nd} order (8-pixel and 4-pixel) neighbourhood connectivity will provide better spatial information in comparison to the 1^{st} order (8-pixel) neighbourhood, amongst the latter both, the 2^{nd} order (8-pixel) neighbourhood is known to have degraded performance (Demirkaya et al., 2008). Since, 8-pixel connectivity assumes all the 8 pixels to be connected to the centre pixel, it gives an equal weighting to them but in fact the diagonal pixels have a weaker linkage to the centre pixel in comparison to the horizontal and vertical neighbouring pixels. Also as observed from Figure 6.2(b), the dimensionality d for 2^{nd} order (8-pixel and 4-pixel) neighbourhood connectivity will be 9 and 5, respectively.

6.2.2 Experiment Setup

To assess the performance of the EMPCA-MI framework *Enhancement 1*, registration experiments on mono and multimodal *BrainWeb* dataset are performed while keeping the remaining two processing steps (*Step II* and *Step III*) of EMPCA-MI framework the same in *Chapter 4*. All the parameter settings of the generic registration model and the EMPCA-MI framework for the experiments are same as mentioned in Tables 3.1 and 5.1, respectively, except the neighbourhood region enhancement in the EMPCA-MI framework.

Furthermore, the mono and multimodal *BrainWeb* dataset was chosen with all experimental settings same as in the previous chapter, as shown in Table 5.2.

In all 1800 separate registration experiments are performed in this set, which include, 3 monomodal image pairs, 3 multimodal image pairs, 5 levels of INU and Gaussian noise settings, 20 initial misregistration scenarios and 3 similarity measures (including the 2^{nd} order (8-pixel and 4-pixel) modifications along with the original EMPCA-MI framework).

6.2.3 Experimental Results Discussion

The first set of experiments included both mono and multimodal *BrainWeb* dataset in order to evaluate the impact of modifying the *Step I* of EMPCA-MI framework on the registration performance, especially in the presence of high INU and noise levels. The three neighbourhood region connectivity considered for these experiments were the 2^{nd} order (8-pixel and 4-pixel) based enhancements as well as the original EMPCA-MI similarity measure with 1^{st} order (8-pixel) connectivity.

Figures 6.3(a) and (b) show the detailed summary boxplot for all INU and noise levels, over the 20 initial misregistration scenarios for monomodal T1/T1 and multimodal T1/T2 registration experiments respectively. Both boxplots in Figure 6.3 confirm the improved registration performance of EMPCA-MI framework using 2^{nd} order (4-pixel) neighbourhood region connectivity with the lowest *mean* RE and fewer *out-of-range* outliers in comparison to the other two neighbourhood region connectivity schemes.

For example, in Figure 6.3(a) which shows the monomodal T1/T1 pair registrations, 2^{nd} order (4-pixel) neighbourhood region connectivity consistently have lower *mean* RE than the original EMPCA-MI (1^{st} order (8-pixel)) as well as 2^{nd}

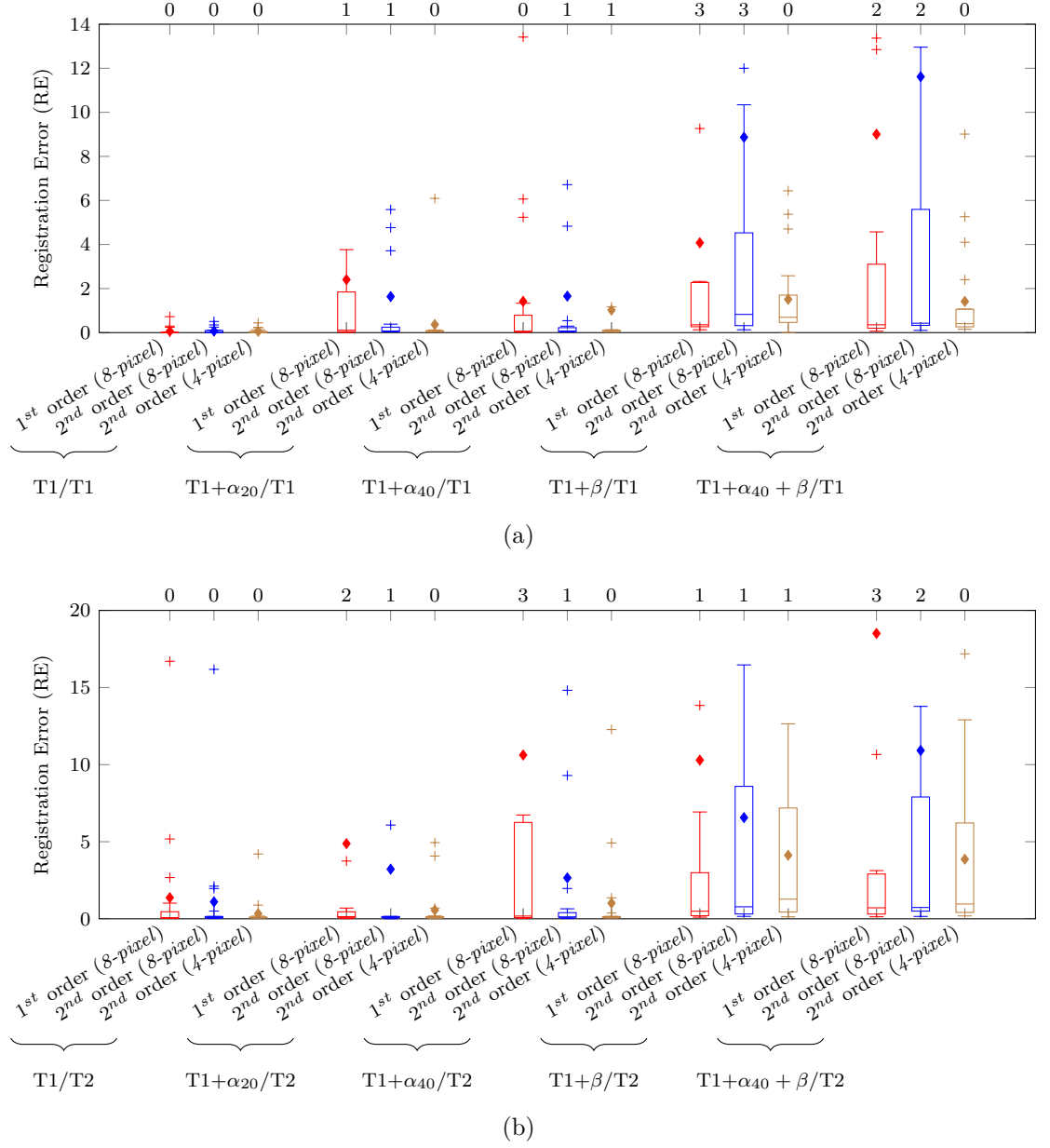


Figure 6.3: RE summary boxplot of (a) monomodal T1/T1 pair and (b) multimodal T1/T2 pair using 1st order (8-pixel), 2nd order (8-pixel) and 2nd order (4-pixel) neighbourhood region connectivity in EMPCA-MI framework for all 20 initial misregistration scenarios. The *mean* and *outliers* are denoted by \blacklozenge and $+$ shapes. The numbers on top of the plots refer to the number of *out-of-range* outliers with RE higher than 14 and 20 pixels respectively.

order (8-pixel) due to the more accurate representation of relative spatial information.

On the other hand, the performance of 1st order (8-pixel) and 2nd order (8-pixel) neighbourhood connectivity worsens in the later three cases (α_{40} , β and

$\alpha_{40} + \beta$) due to the presence of high INU and noise. The 2^{nd} order (4-pixel) neighbourhood region connectivity still provides consistent lower *mean* RE performance, with an exception of one *out-of-range* outlier in case of monomodal T1+ α_{40} /T1 pair. Both 2^{nd} order (8-pixel) and original EMPCA-MI (1^{st} order (8-pixel)) have more *out-of-range* outliers as well as larger *interquartile* range as the level of INU and noise increases.

These results show that using 2^{nd} order (4-pixel) neighbourhood region connectivity in the *Step I* of EMPCA-MI framework reflects neighbourhood spatial information more accurately by considering a 2^{nd} order representation of the directly related pixel values with respect to the centre pixel of the neighbourhood region.

In the case of multimodal T1/T2 pair, Figure 6.3(b) shows that both 2^{nd} order (8-pixel and 4-pixel) neighbourhood region connectivity perform better than original EMPCA-MI (1^{st} order (8-pixel)) for all INU and noise levels. Since, the 2^{nd} order (4-pixel) neighbourhood region connectivity exploits the strong pixel relations providing more relevant spatial information about a region's local neighbourhood for subsequent EMPCA and MI computation. Whereas, the 2^{nd} order (8-pixel) neighbourhood region connectivity has higher number of *out-of-range* outliers, which emphasises its poor rate of convergence due to the weaker indirect pixel neighbours, especially when higher INU and noise levels are present. Similar trends can also be observed from the summary boxplots of the remaining mono (T2/T2 and PD/PD) and multimodal (T2/PD and PD/T1) registration experiments, which are included as Figures E.1 and E.2 of *Appendix E* for completeness.

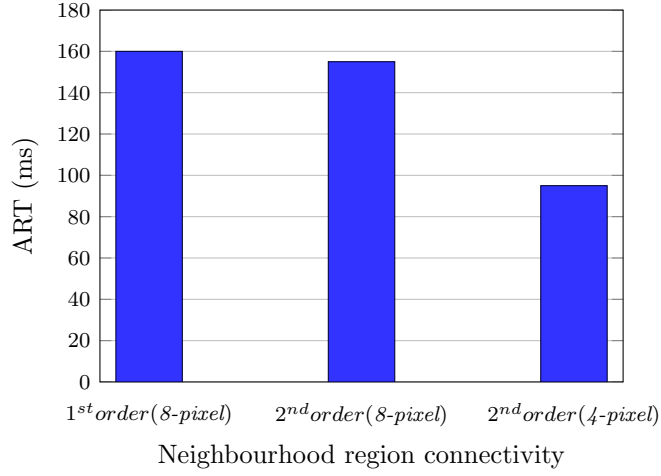


Figure 6.4: ART performance for using original EMPCA-MI (1st order (8-pixel)) followed by 2nd order (8-pixel) and 2nd order (4-pixel) neighbourhood region connectivity in the EMPCA-MI framework for *BrainWeb* dataset-based mono and multimodal registration experiments.

In summary, considering all these boxplots for all the set of registrations for *BrainWeb* dataset, EMPCA-MI framework using 2nd order (4-pixel) is able to reduce the average RE by 79% and 71% with respect to original EMPCA-MI (1st order (8-pixel)) and 2nd order (8-pixel), respectively. Hence, it helps to draw the conclusion that 2nd order (4-pixel) provides more accurate features of the reference and the sensed images in comparison to both the original EMPCA-MI (1st order (8-pixel)) and 2nd order (8-pixel), especially when higher INU and noise levels were present.

In order to evaluate the computational cost of *Enhancement 1*, an ART analysis for the registration experiments is considered. Figure 6.4 shows the ART performance of all the neighbourhood region connectivity considered for the mono and multimodal *BrainWeb* dataset registration experiments. As illustrated in Figure 6.2, since the data dimensionality of EMPCA-MI framework using 2nd order (4-pixel) neighbourhood region connectivity is reduced to 5 from the fixed value of 9 for both original EMPCA-MI framework using 1st order (8-pixel) and 2nd

order (*8-pixel*), the corresponding ART value is considerably lower, i.e., 95 ms compared to 155 ms for 2^{nd} order (*8-pixel*) and 160 ms for 1^{st} order (*8-pixel*) to determine only the first principal component. Hence, evidently EMPCA-MI framework using 2^{nd} order (*4-pixel*) neighbourhood connectivity is able to provide 40% improvement in computational efficiency along with the better registration performance in comparison to others.

In *Section 5.3.1*, there were few individual cases in both mono and multimodal registration of *BrainWeb* dataset, having high levels of INU and noise (for example α_{40} and $\alpha_{40}+\beta$) where the standard EMPCA-MI framework (using 1^{st} order (*8-pixel*) neighbourhood region connectivity) provided higher RE. One particular example of deteriorated registration performance was monomodal $T1+\alpha_{40}+\beta/T1$ registration (with RE value of 44.80 pixels) with 11^{th} initial misregistration scenario ($24.21, -25.2, -25.8^\circ$), shown in Figure 5.14.

The EMPCA-MI framework using 2^{nd} order (*4-pixel*) gave lowest RE (RE value of 0.39 pixels) in comparison to both the 2^{nd} order (*8-pixel*) (RE value of 10.30 pixels) and original EMPCA-MI framework (1^{st} order (*8-pixel*)) (RE value of 44.80 pixels) respectively. In order to observe the corresponding quality of registrations, Figure 6.5 shows the qualitative results.

Figures 6.5(a) and (b) display the initial misregistration of 11^{th} initial misregistration scenario and the ground truth respectively. Also Figures 6.5(c) – (e) consist of *Canny edge detection* overlay results for EMPCA-MI framework using original EMPCA-MI framework (1^{st} order (*8-pixel*)) and 2^{nd} order (*8-pixel* and *4-pixel*) neighbourhood region connectivity respectively.

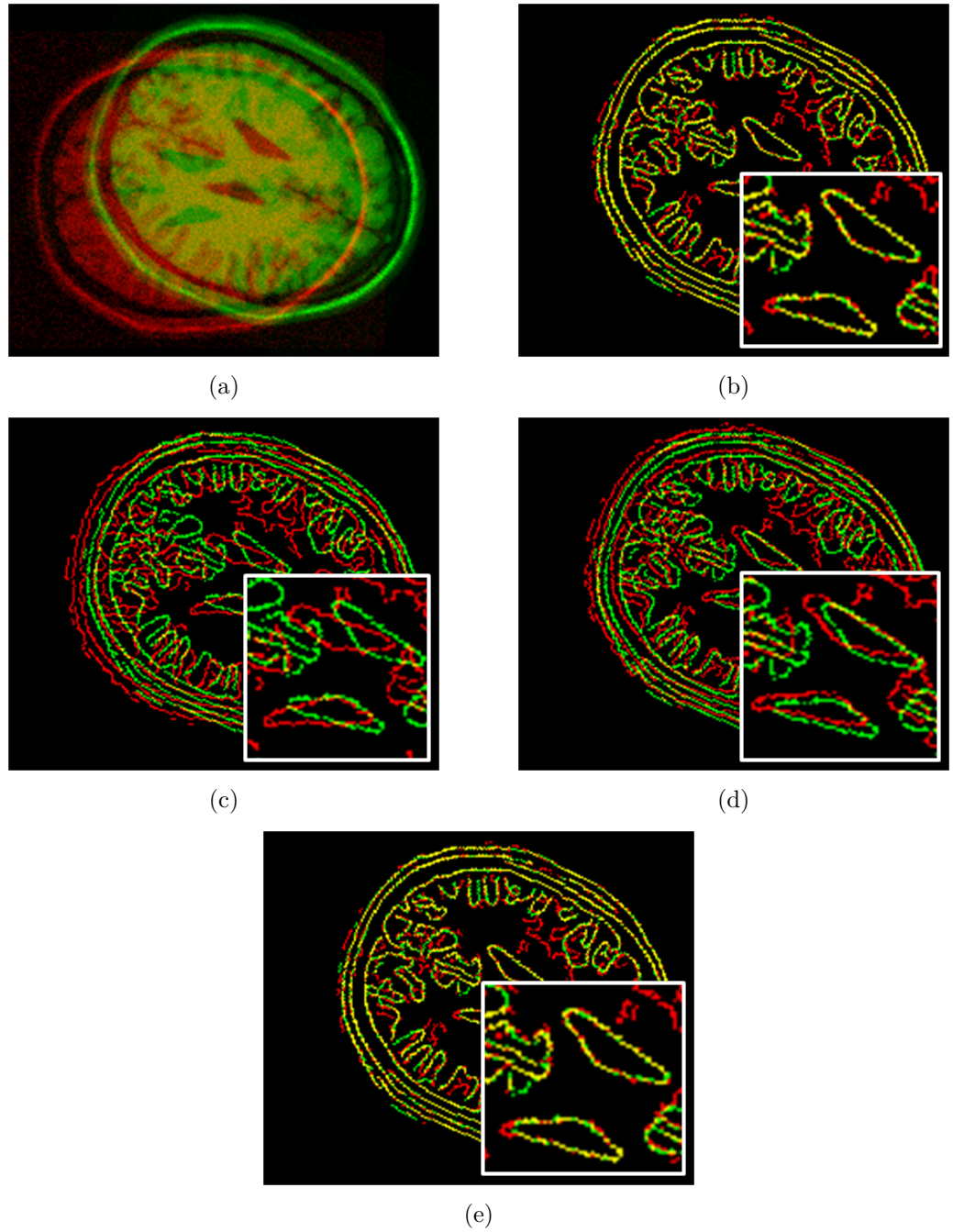


Figure 6.5: Qualitative results of monomodal $T1+\alpha_{40}+\beta/T1$ pair using 11th initial misregistration scenario showing (a) initial misregistration and (b) ground truth followed results for (c) original EMPCA-MI framework (1st order (8-pixel)), then EMPCA-MI framework with (d) 2nd order (8-pixel) and (e) 2nd order (4-pixel) neighbourhood region connectivity enhancements (with inset showing the zoomed-in central lobes).

Clearly, the EMPCA-MI framework using 2nd order (4-pixel) neighbourhood region connectivity outperformed the other two connectivity schemes. This is evid-

ent from the aligned central lobes in Figure 6.5(e), which is in correspondence to the ground truth illustrated in Figure 6.5(b). The other two connectivity schemes have significant misalignments, as seen in Figures 6.5(c) and (d).

Hence, the EMPCA-MI framework using 2^{nd} order (4-pixel) is consistently able to provide better registration performance in terms of RE and qualitative assessment with also the lowest computational cost in comparison to both the 2^{nd} order (8-pixel) and original 1^{st} order (8-pixel) connectivity schemes.

The aforementioned connectivity schemes explored as enhancement for EMPCA-MI framework are not exhaustive and can be deployed in many more shapes as well as sizes. In order to explore these possibilities and investigating them, they are considered as one of the major future works which are discussed later in *Chapter 8*.

6.3 EMPCA-MI Framework *Enhancement 2*

The standard EMPCA-MI framework computes MI between the principal components X_R and X_S to determine the final EMPCA-MI value using fixed number of bins value $b=256$. While, the registration results in *Chapter 5* showed the framework was robust and efficient in its performance with lower computational overheads, due to the challenging characteristics of some medical modalities, such as retinal images, the EMPCA-MI framework performance can deteriorate. For example the inherently large homogeneous regions in retinal images mean that choosing a high number of bins for probability distribution estimation can produce

many empty bins and more inaccurate MI value. This provided the motivation to develop a formal mechanism for the best number of bins selection in the *Step III* of EMPCA-MI framework, which is based on image statistics.

6.3.1 Number of bins for MI computation

In the MI literature, as noted in (Legg et al., 2013), the role of number of bins selection has often been overlooked with initial works (Collignon et al., 1995; Pluim et al., 2003) not specifically stating the chosen choices for number of bins. Though later on (Maes et al., 1997) have primarily relied on experimental selection rather than any statistical basis, they still highlight that an appropriate choice of number of bins for MI computation can significantly improve the overall registration performance (Breitner et al., 2008; Nam et al., 2009; Ritter et al., 1999). These optimal number of bins selection methods, used for probability distribution estimation to compute MI, were also successfully employed for registration applications in remote sensing domain (Moigne et al., 2011). While, some methods employ empirically testing of fixed number of bins in the range from 256 to 4 bins, in a binary-reducing approach (Kang et al., 2011; Tsao, 2003; Zhu and Cochoff, 2002), others use different statistical analysis (Birgé and Rozenholc, 2006; Davies et al., 2009, 2007; Parmehr et al., 2013) such as *skewness* and *kurtosis* factors to choose the most appropriate number of bins for MI computation.

Hence, different fixed and adaptive number of bins selection approaches were considered to be incorporated for individual and joint probability estimation for more accurate MI computation between X_R and X_S in *Step III* of EMPCA-MI

framework (Reel et al., 2014a). The first set of approaches investigated empirically reducing the fixed number of bins from 256 in the original EMPCA-MI framework to 128, 64, 32, 16, 8 and 4 bins respectively and analysing the corresponding impact on registration performance. Intuitively, reducing the number of bins will improve the probability distribution estimation, since the data is now distributed across fewer sparse bins. Conversely, radically reducing the number of bins will lead to a loss of the unique features, which could lead to inaccurate MI between them. Furthermore, in terms of computation cost, the approach of fixed number of bins is faster since the number of bins are predefined and not iteratively computed, though more bins require more computation time for calculating the individual and joint probabilities.

An alternative number of bins selection strategy was to investigate the various statistical methods which are adaptive in nature, as they are dependent on the statistical characteristics of the given data Z . Sturges (1926) proposed a rule which utilised the properties of Z assuming it to be normal, then its histogram can be approximated with a binomial distribution. Hence the *Sturges Rule* defined the number of bins as:

$$\frac{R}{(1 + \log_2(w))} \quad (6.2)$$

Here, R and w represent the range and number of elements in Z respectively.

Since *Sturges Rule* assumes Z to be normally distributed, it will give inaccurate results when this condition is not met. Meanwhile, Scott (Scott, 1979) proposed a rule similar to *Sturges Rule*-based on the standard deviation of Z . It defined the

number of bins as:

$$\frac{R}{3.49\sigma w^{-\frac{1}{3}}} \quad (6.3)$$

Here, σ represents the standard deviation of Z .

While *Scott* Rule also assumed Z to be normal, it would provide number of bins based on the actual values of Z . Various closely related variants of *Scott* and *Sturges* Rules also exist which have change the number of bins based on similar properties (Devroye and Györfi, 1985; Izenman, 1991; Kanazawa, 1993; Taylor, 1987). Later, Scott proposed a new extension to its own previous work by multiplying by a *skewness* factor (Scott, 1992), defined as:

$$\text{skewness factor} = \frac{2^{\frac{1}{3}}\sigma}{e^{\frac{5\sigma^2}{4}}(\sigma^2 + 2)^{\frac{1}{3}}(e^{\sigma^2} - 1)^{\frac{1}{2}}} \quad (6.4)$$

The amount of skewness allowed the Scott's New Rule (denoted as *Scott1*) to recommend slightly higher number of bins, which improved the registration performance. Similarly, the peak or flat nature of the distribution in comparison to normal distribution can also be estimated using *kurtosis*. While, higher *kurtosis* signifies the steep peak close to the mean of Z , a lower *kurtosis* denotes that Z has a much flatter distribution. This was deployed by (Wichard et al., 2008), which adapted the *Sturges* Rule to incorporate *kurtosis* such that the number of bins is:

$$\frac{R}{\log_2(n) + 1 + \log_2(1 + K(\frac{n}{6})^{\frac{1}{2}}))} \quad (6.5)$$

$$K = \frac{\sum_{i=1}^n (Z_i - \bar{Z})^4}{(n-1)\sigma^4} \quad (6.6)$$

Here, \bar{Z} and K represent the mean and *kurtosis* of Z respectively.

Here, including the higher-order moments (*skewness* and *kurtosis*) of Z will accurately model their flat or peak distribution nature, which will be better represented in the number of bins selection strategy. Though, inclusion of higher-order moments will impact on the computational times for *Scott1* and *Wichard*, it will be marginally lower for *Sturges* and *Scott*. Overall, adaptive number of bins selection approaches will incur higher computational costs because of their iterative nature, as the number of bins will be computed for every iteration.

These different approaches for *Step III* of EMPCA-MI framework will provide a mechanism for determining the best number of bins for accurate MI calculation between X_R and X_S . In comparison to the fixed 256 bins used for original EMPCA-MI framework, these approaches will introduce a new degree-of-freedom based on the statistical characteristics of the reference and sensed images. Hence, a fixed number of bins approach (along with the 256 bins) and four adaptive selection methods (Scott, 1979, 1992; Sturges, 1926; Wichard et al., 2008) will be incorporated into the MI computation (*Step III*) of EMPCA-MI framework as shown in Figures 6.1(a) and (c), and a comparative analysis will be undertaken to evaluate their impact on the overall registration performance.

6.3.2 Experimental Setup

In order to evaluate the performance of the EMPCA-MI framework with the adaptive number of bins enhancement, various registrations experiments were conducted using the generic registration model and EMPCA-MI with parameter settings same as mentioned in Tables 3.1 and 5.1, respectively, except the various fixed and adaptive number of bins for MI computation in the EMPCA-MI framework. These registration experiments were especially performed on the monomodal pairs of retinal images from the *Brno-Mono* dataset (details in *Section 3.4.2*) for the analysis since they are considered challenging for registration due to the presence of different pathologies including haemorrhages, retinal scars and clumping of the dark pigment which all accentuated the registration. Unlike in the previous chapter where four initial misregistration scenarios were used, this set of experiment only uses one initial misregistration scenario $(100, 100, 45^\circ, 0.8)$, which had emerged as the most challenging. Therefore, this experiment consisted of 484 registrations which included 44 monomodal image pairs, 1 initial misregistration scenario and 11 methods (including the 7 fixed number of bins settings along with 256 for original EMPCA-MI framework and the 4 adaptive number of bins strategies).

6.3.3 Experimental Results and Discussion

Now the results for registration experiments corresponding to the adaptive number of bins enhancement of *Step III* of EMPCA-MI framework are presented. The detailed boxplot in Figure 6.6 summarises the RE results of the retinal registration experiments using different fixed and adaptive techniques integrated with the original EMPCA-MI framework.

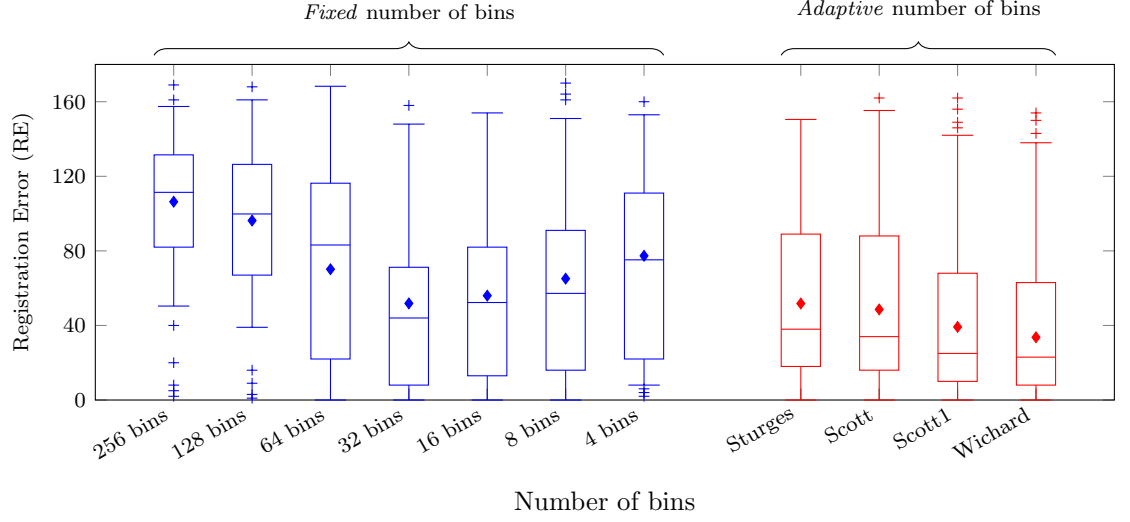


Figure 6.6: RE summary boxplot for EMPCA-MI framework using different number of bins selection strategies for monomodal *Brno-Mono* retinal dataset registration. *Blue* and *red* colour represent the fixed and adaptive number of bins selection approaches, while *mean* and *outliers* are denoted by \blacklozenge and $+$ shapes.

It is evident from Figure 6.6 that in terms of registration performance, that the *Wichard* adaptive approach (Wichard et al., 2008) has the lowest *mean* RE of 33.65 pixels since it iteratively computes the best number of bins based upon the characteristics of X_R and X_S for each monomodal retinal pair. In terms of the empirically fixed number of bins approaches, 32 bins performed best with a *mean* RE of 51.82 pixels. The boxplot reveals a clear trend the *mean* RE decreases as the fixed number of bins is reduced from the standard 256 bins of the original EMPCA-MI framework to 32, before it then starts increasing again when the number of bins are further reduced. The reason for this is that when large numbers of bins are used in the MI computation in *Step III*, there is a tendency to have more sparsely-populated bins within the joint histogram which leads to poorly estimated entropy. Conversely, for fewer number of bins (16, 8 and 4), unique features will tend to be assigned to the same bin, leading to a corresponding degradation in retinal registration performance.

Hence for this particular clinical dataset, 32 number of bins is most appropriate within the fixed bin approaches. This may vary for different retinal datasets depending upon the precise characteristics of the retinal dataset, which highlights one of the limitations of adopting a fixed number of bins approach. For adaptive number of bins selection, the results show that *Wichard* approach (Wichard et al., 2008) achieved the lowest *mean* RE followed by *Scott1* adaptive strategy (Scott, 1992). These techniques include higher-order moments of *kurtosis* and *skewness* of the data distribution which assists to better model the retinal characteristics. In contrast, the performance of both *Sturges* (Sturges, 1926) and *Scott* (Scott, 1979) is much lower which is due to the fact that their underlying assumption is that the retinal data is normally distributed which leads to inaccurate MI computation and higher *mean* RE. In summary, considering the *mean* RE values, it is clear from Figure 6.6 that the EMPCA-MI framework using *Wichard* adaptive approach is able to reduce the RE by upto 68% in comparison to the original EMPCA-MI using 256 fixed bins.

Moreover, Figure 6.7 shows the computational overheads in terms of ART for EMPCA-MI framework-based retinal registration, when integrated with different fixed and adaptive number of bins selection strategies. It is clear from Figure 6.7 that the ART decreases for fewer fixed number of bins e.g., 1.32 s to 0.86 s for 256 to 4 bins respectively, due to the lower individual and joint probability computational times incurred for fewer number of bins. While, higher ART of 3.98 s and 3.14 s are respectively observed for the two adaptive approaches of *Wichard* and *Scott1* since they required the calculation of higher-order moments in their number of bins selections for determining the respective individual and joint probabilities to

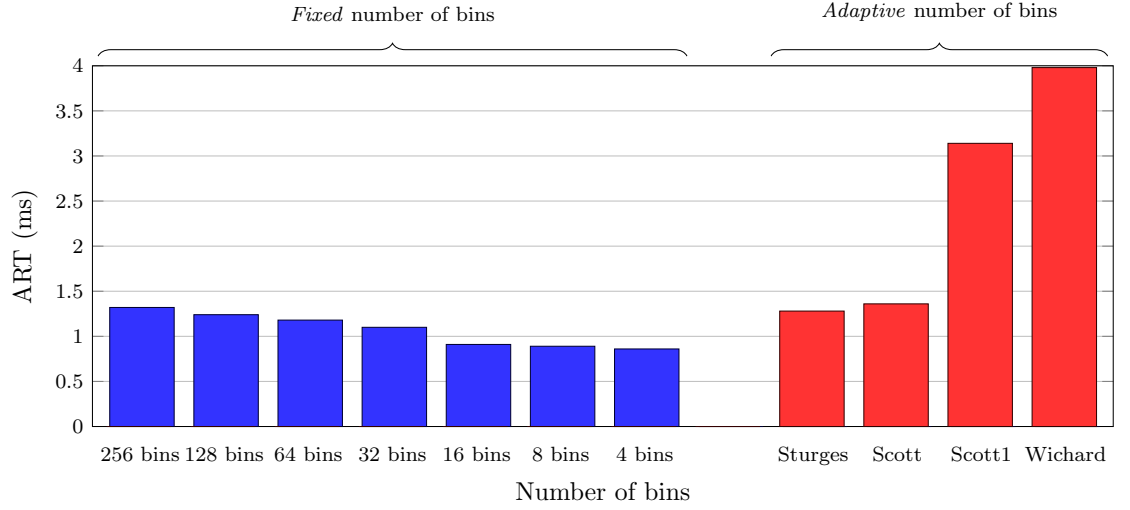


Figure 6.7: ART summary bar graph for EMPCA-MI framework for monomodal *Brno-Mono* retinal dataset registration using different number of bins selection strategies. *Blue* and *red* colour represent the *fixed* and *adaptive* number of bins approaches.

compute MI and provide much lower *mean* RE in comparison to other strategies.

Finally, Figure 6.8 shows the qualitative results for *Image Pair 22*, using the *checkerboard* overlay, with reference and sensed retinal images in light and dark respectively. This particular retinal pair was especially challenging as it includes pathologies along with low contrast and large homogeneous regions. Hence it was chosen for qualitative comparison. Figure 6.8(a) and (b) shows the initial misregistration and ground truth respectively. Furthermore, Figure 6.8(c) consists of the zoomed in ground truth for a given region and the corresponding results for different fixed and adaptive number of bins selection strategies. The superior continuity of the vessel structures is evident for the *Wichard* adaptive approach and fixed 32 bins. It also validates their effective qualitative performance in contrast to employing either 256 bins-based standard EMPCA-MI framework or minimum number of bins (4 bins) in EMPCA-MI. Clearly, using 32 bins gives both the best numerical and qualitative results amongst fixed number of bins considered

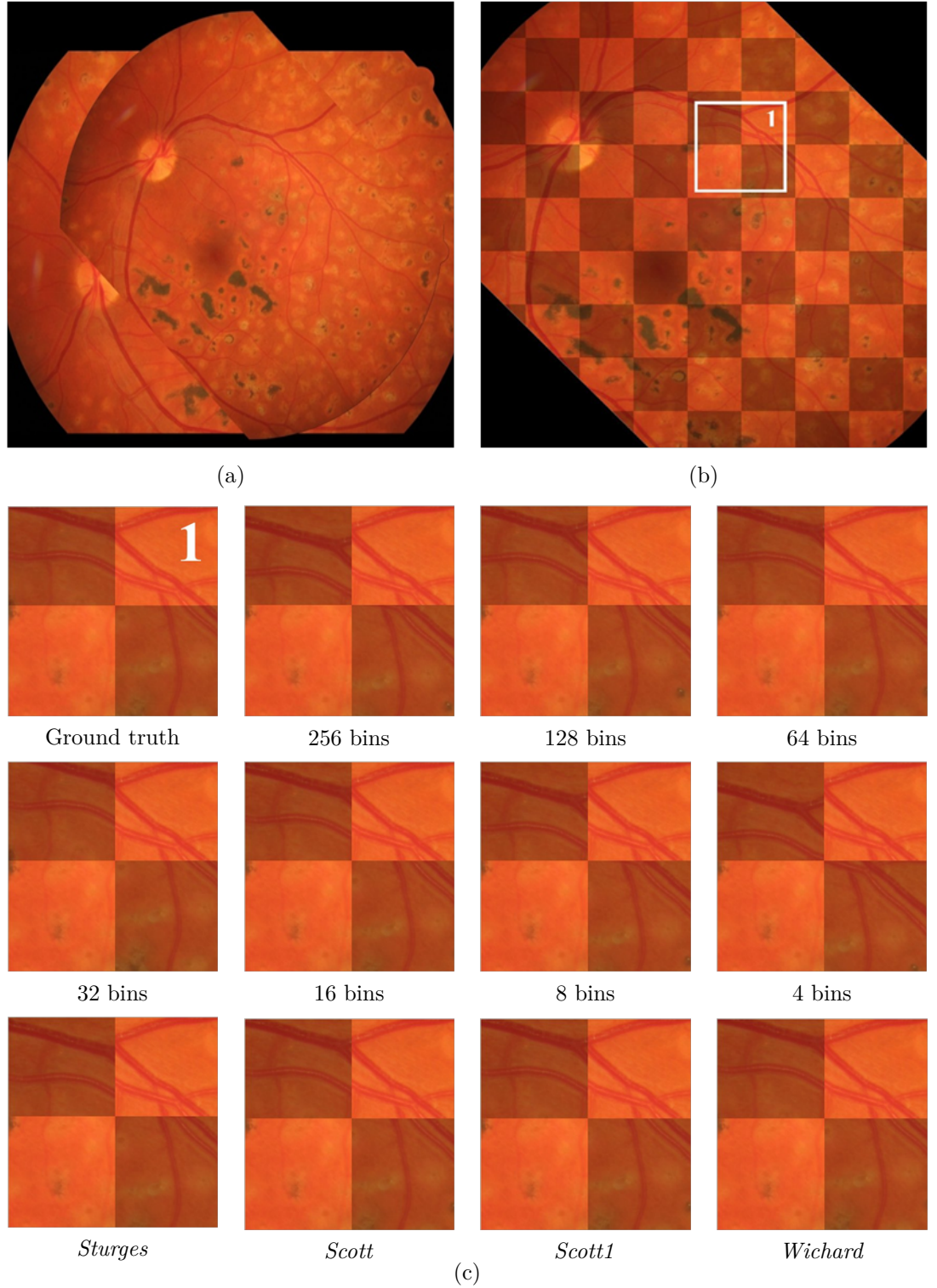


Figure 6.8: Qualitative results of monomodal Fundus retinal *Image Pair 22*, showing (a) initial misregistration, (b) ground truth and (c) the zoomed-in regions of ground truth and different *fixed* and *adaptive* number of bins selection strategies with EMPCA-MI framework.

because it represents the probability distribution most accurately, leading to an overall retinal performance improvement. But as mentioned earlier, this choice of fixed number of bins was empirical in nature and hence provided better registration performance on this particular retinal dataset.

Hence, overall, it is confirmed that using *Wichard* adaptive approach in *Step III* of the EMPCA-MI framework gave better registration performance in terms of quantitative RE and qualitative assessment in comparison to other with a trade-off in terms of computational cost.

6.4 Summary

This chapter proposed and investigated *Enhancement 1* and *2* in the *Step I* and *III* of EMPCA-MI framework respectively. *Enhancement 1* uses the 2^{nd} order neighbourhood region connectivity for the pre-processing, while *Enhancement 2* proposes to use different fixed and adaptive number of bins selection strategies for the MI computation in EMPCA-MI framework. The experimental results for *Enhancement 1* of EMPCA-MI framework showed that 2^{nd} order (4-pixel) neighbourhood region connectivity provided robust registration performance for *BrainWeb* dataset and was also computationally more efficient in comparison to the 2^{nd} order (8-pixel) as well as the original EMPCA-MI using 1^{st} order (8-pixel) scheme. Similarly, the experimentation for *Enhancement 2* of EMPCA-MI framework showed that fixed 32 bins and *Wichard* adaptive number of bins selection strategy provided lower RE performances for the retinal *Brno-Mono* dataset amongst all the fixed and adaptive approaches analysed. Although *Wichard* approach provided lowest

overall RE, it still had a trade-off in terms of higher computational cost in comparison to others. Furthermore, all the experiments for these enhancements used the underlying assumption of choosing only one principal component ($P=1$) in the *Step II* of the EMPCA-MI framework. Therefore, the next chapter will propose a mechanism for relaxing this assumption and allow adaptively choosing the number of principal components within the EMPCA-MI framework. In addition, it will also integrate the enhancements presented in this chapter to make all the steps of EMPCA-MI framework more effective.

Chapter 7

Adaptive EMPCA-MI Framework

7.1 Introduction

In the previous chapter, *Steps I* and *III* of EMPCA-MI framework in Figure 6.1, were modified by respectively utilising *Enhancement 1* and *2*, both of which incurred corresponding computational costs. The experimental results for these two enhancements were independently evaluated and both provided improved and robust registration performance for different medical datasets. These datasets are difficult to register due to their inherent characteristics. However, the EMPCA-MI framework still makes the same assumption as in *Chapter 4*, of calculating only the first principal component using EMPCA in *Step II*.

Interestingly, in *Section 5.3.3* it was shown that by empirically increasing the number of principal components (from $P=1$ to $P=2$), the framework provided considerably improved performance for multimodal retinal registration of Fundus/SLO

image pair from the *Brno-Multi* dataset. This was due to the fact that two orthogonal principal components provided more variance than a single component for this retinal image pair. This provided the impetus to formalise the new EMPCA-MI framework so that it is able to adaptively determine the most appropriate number of principal components to represent prominent neighbourhood region features for a particular dataset.

This chapter proposes an *adaptive* EMPCA-MI framework for MIR. It exploits the *Kaiser Rule* (Jackson, 1993; Jolliffe, 2002) to iteratively find the best number of principal components to be computed by the EMPCA framework in *Step II* of the registration process. In addition, it also employs both the *Enhancement 1* and *2* proposed in *Chapter 6* for *Steps I* and *III*.

Two sets of experiments using human brain *BrainWeb* and retinal *DRIVE* and *Brno-Multi* datasets confirm that the *adaptive* EMPCA-MI framework provides consistently lower RE and improved robustness with a corresponding trade-off in computational overheads.

7.2 *Adaptive* EMPCA-MI framework

This section describes the *adaptive* EMPCA-MI framework (Reel et al., 2014b). *Section 7.2.1* briefly discusses the concept of stopping rules for PCA, before *Section 7.2.2* explores the use of applying the *Kaiser Rule* (Jackson, 1993; Jolliffe, 2002) to find the most appropriate number of principal components for EMPCA.

7.2.1 Stopping Rules for PCA

In PCA, selecting the best number P of principal components is a major challenge, because while retaining too many components can potentially lead to overfitting by including noise in the data, choosing too few components can equally mean discarding valuable information (Jackson, 1993). Commonly the first principal component is empirically chosen since it accounts for the majority of variability in the data (Rencher, 1998), and so was used for the EMPCA-MI framework. But as mentioned in *Chapter 2*, various approaches for selecting the best subset of significant principal components have been proposed including Scree Graph, Broken-stick and their variants (Cangelosi and Goriely, 2007; Jolliffe, 2002), which select a subset by computing the cumulative variance for all components. In contrast, the *Kaiser Rule* (Jackson, 1993; Jolliffe, 2002) retains all principal components whose eigenvalues are greater than one. It assumes that image data variables are independent. Hence their principal components are same as variable, having unity variance in case of correlation matrix. Hence, any component with an eigenvalue less than one is assumed to not contain valuable information (Ravi and Palaniappan, 2005). This important attribute of the *Kaiser Rule* is image dependent, so it can automatically choose the number of significant principal components required to represent image features for a given accuracy. Furthermore, it is suited to the EMPCA-MI framework since it iteratively determines the P principal components in descending order of eigenvalues. These two distinct and relevant characteristics provided the motivation to investigate incorporating the *Kaiser Rule* into the *Step II* of the EMPCA-MI framework to determine the best P value choice for a particular dataset.

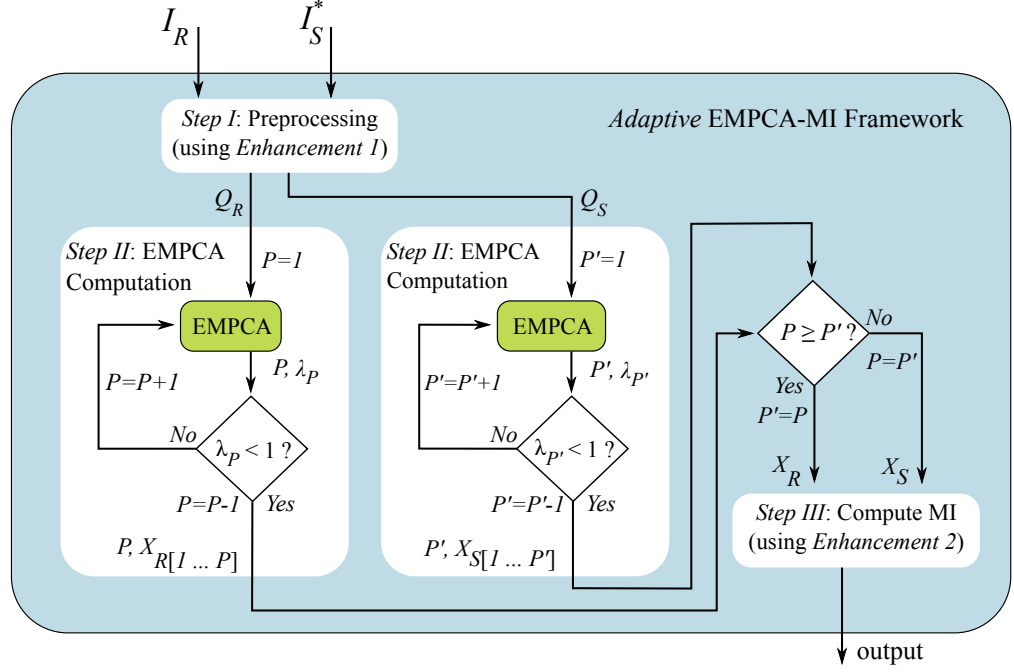


Figure 7.1: Flowchart for the *adaptive* EMPCA-MI framework.

7.2.2 Adaptively choosing P in the EMPCA-MI framework

This section describes the adaptive mechanism for choosing P for the EMPCA-MI framework. The three primary computation steps include the pre-processing of neighbourhood region information for both I_R and I_S^* followed by adaptively determining the P principal components using EMPCA. Finally, the MI output is computed. Figure 7.1 shows the flowchart diagram of the *adaptive* EMPCA-MI framework with these three steps indicated.

Step I of *adaptive* EMPCA-MI pre-processes the various image *grayscale* values by using the *Enhancement 1*-based 2nd order (*4-pixel*) neighbourhood region connectivity between them as described in *Section 6.2*. This retains the local spatial neighbourhood relationship rather than using pixel values as in 1st order (*8-pixel*)

neighbourhood relations. Hence, by using (6.1), Q_R and Q_S are computed using I_R and I_S^* respectively.

Step II of the *adaptive* EMPCA-MI proposes the dimensionality reduction for Q_R and Q_S using *Kaiser Rule* (Jackson, 1993; Jolliffe, 2002) to adaptively find the most significant P principal components using EMPCA. The flowchart in Figure 7.1 shows how the *adaptive* EMPCA computes the first P principal components from Q_R having eigenvalue $\lambda_P > 1$. Similarly the first P' principal components from Q_S are computed with these then concatenated as X_R and X_S respectively. Crucially, unlike $P=1$ assumption considered in earlier chapters, this adaptive approach retains accurate image features which will be reflected in the corresponding registration performance.

Finally, *Step III* of *adaptive* EMPCA-MI determines the MI between the highest number of common principal components in both X_R and X_S of the reference and sensed images. This step adopts the *Enhancement 2* proposed in *Section 6.3*, with the *Wichard* (Wichard et al., 2008) approach chosen to select the best number of bins to calculate the individual and joint probabilities, since it exploits the *kurtosis* measure of the data distribution to facilitate a more accurate MI value. Next section discusses the experimental setup used for the registration experiments.

7.3 Experimental Setup

In order to assess the performance of the *adaptive* EMPCA-MI framework, various registration experiments were conducted. The nomenclature used in this chapter

<i>Adaptive</i> EMPCA-MI framework	
<i>Parameters</i>	<i>Selection</i>
Neighbourhood radius (r)	1 (using <i>Enhancement 1</i>)
Number of Principal Components (P)	Adaptively (using <i>Kaiser Rule</i>)
Number of bins (b)	Variable (using <i>Enhancement 2</i>)

Table 7.1: The different parameter selections for the *adaptive* EMPCA-MI framework.

is *adaptive* EMPCA-MI $\{P\}$, where P denotes the number of principal components determined by the *Kaiser Rule* in *Section 7.2.2*. Similarly, the EMPCA-MI framework with $P=1$ in *Chapter 4, 5* and *6* will be denoted as EMPCA-MI $\{1\}$. These notations allow a clear distinction to be made between both the original and *adaptive* EMPCA-MI frameworks in the subsequent result analysis. To evaluate *adaptive* EMPCA-MI $\{P\}$, the registration experiments were categorised into two sets (*Set 1* and *Set 2*) as in Table 5.2, with the parameter selections for the *adaptive* EMPCA-MI $\{P\}$ and EMPCA-MI $\{1\}$ models being given in Tables 7.1 and 5.1, respectively. The MIR model used for experiments employ the same parameter settings as in Table 3.1.

The *Set 1* of registration experiments used the mono and multimodal pairs of MRI T1, T2 and PD human brain images of the *BrainWeb* dataset, with all experimental settings as in the previous chapters. In all 1200 individual registration experiments were performed in this set, which included: 3 monomodal pairs, 3 multimodal pairs, 5 levels of INU and Gaussian noise settings, 20 initial misregistration scenarios and 2 similarity measures, including both the *adaptive* EMPCA-MI $\{P\}$ and EMPCA-MI $\{1\}$ frameworks.

The *Set 2* of registration experiments were performed on the mono and multimodal pairs of retinal images from the *DRIVE* and *Brno-Multi* datasets respectively. A detailed description of these datasets was discussed earlier in *Section 3.4.2*. The monomodal subset using Fundus retinal images of *DRIVE* dataset consists of 160 registrations which include 20 monomodal pairs, 4 initial misregistration scenarios and 2 similarity measures including the *adaptive* EMPCA-MI $\{P\}$ and EMPCA-MI $\{1\}$ frameworks. Similarly for the multimodal subset using Fundus and SLO retinal images from the *Brno-Multi* dataset consists of 60 registrations which include 10 multimodal pairs, 3 initial misregistration scenarios and 2 similarity measures including the *adaptive* EMPCA-MI $\{P\}$ and EMPCA-MI $\{1\}$ frameworks.

7.4 Experimental Results Discussion

7.4.1 *Set 1: BrainWeb Dataset Registration Experiments*

This section discusses the registration experiments results for *adaptive* EMPCA-MI $\{P\}$ on *Set 1* of the *BrainWeb* dataset, with EMPCA-MI $\{1\}$ used as the comparator. Figure 7.2(a) and (b) show the detailed summary boxplot for all INU and noise levels of 20 initial misregistration scenarios for the monomodal T1/T1 and multimodal T1/T2 registration experiments respectively. Each boxplot shows a bounding box defining the *interquartile* range with the bar across representing the median and whiskers denoting the RE range. The boxplots also include the number of *out-of-range* RE values corresponding to either the EMPCA-MI $\{1\}$ or

adaptive EMPCA-MI $\{P\}$ frameworks.

The two boxplots in Figure 7.2 confirm the superior registration quality of *adaptive* EMPCA-MI $\{P\}$ with both lower *mean* RE and smaller *interquartile* ranges compared with EMPCA-MI $\{1\}$. For the T1/T1 pairs in Figure 7.2(a), no *out-of-range* outliers with high RE are observed for *adaptive* EMPCA-MI $\{P\}$ with the exception of the monomodal T1+ $\alpha_{40}+\beta$ /T1 pair. In contrast the RE monotonically increases in the case of EMPCA-MI $\{1\}$ reflecting its poor convergence in achieving the best alignment between the reference and sensed images. This trend is also manifest in Figure 7.2(b) for the multimodal T1/T2 pairs, with again the improved registration performance of *adaptive* EMPCA-MI $\{P\}$ clearly evident. Similar conclusions can be deduced from the boxplots for the remaining mono (T2/T2 and PD/PD) and multimodal (T2/PD and PD/T1) registration experiments which for completeness, are included in Figures F.1 and F.2 respectively in *Appendix F*.

In analysing all the *BrainWeb* dataset results for different registrations, *adaptive* EMPCA-MI $\{P\}$ has been able to reduce RE by an average of 84% in comparison to the EMPCA-MI $\{1\}$. Similarly, comparing the *adaptive* EMPCA-MI $\{P\}$ with MI, GMI and RMI (See *Section 5.3.1*) reveals an overall RE reduction of by an average of 93%. These results confirm that *adaptive* EMPCA-MI $\{P\}$ is able to more accurately extract features from the reference and sensed images enabling a consistently superior quality of registration, even in the presence of significant INU and noise levels. In contrast, EMPCA-MI $\{1\}$ performs satisfactorily only when little or no INU is present in the images and as the levels of INU and Gaussian noise increase, its performance deteriorates.

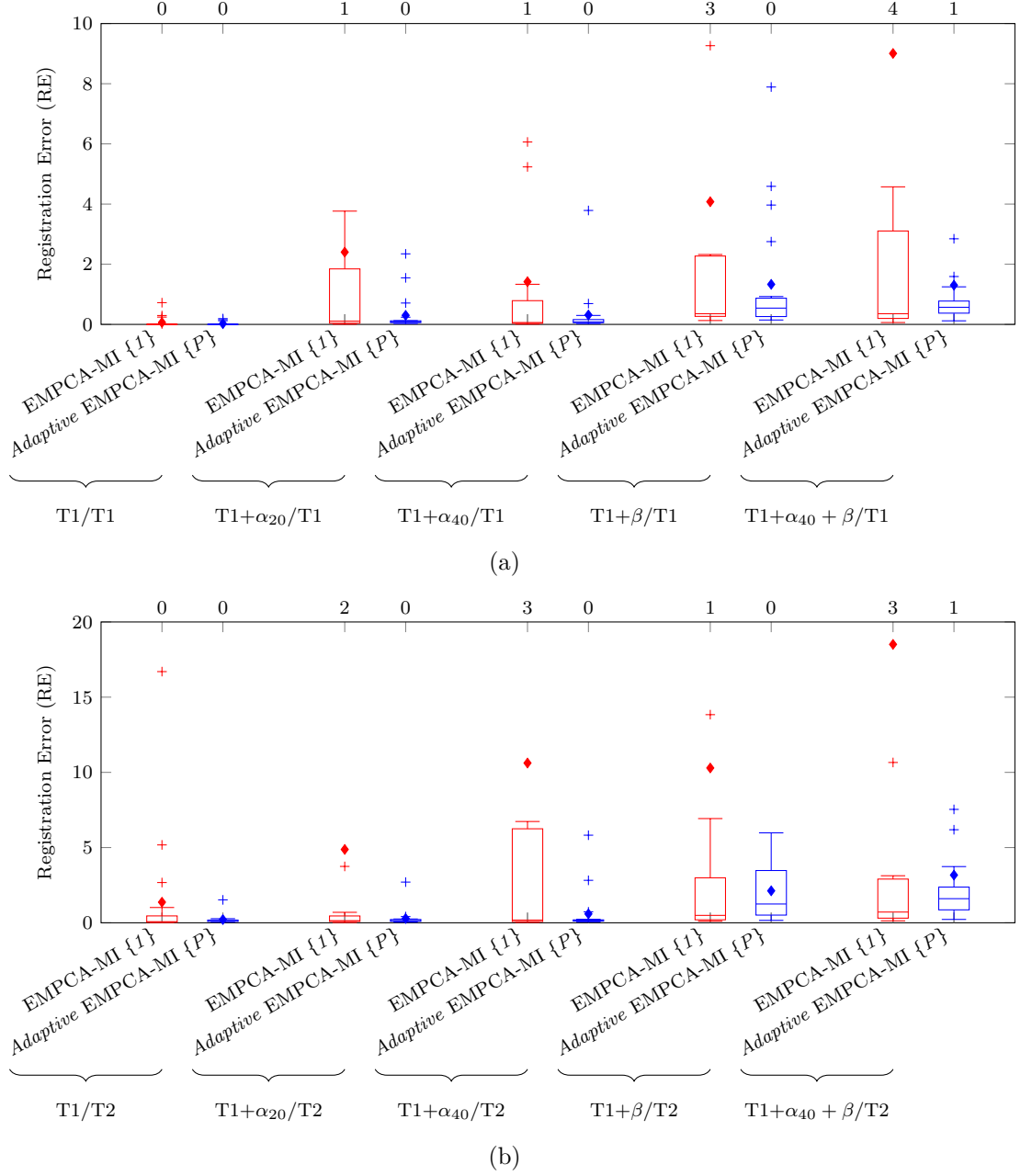


Figure 7.2: RE summary boxplot of (a) monomodal T1/T1 pair and (b) multimodal T1/T2 pair using EMPCA-MI $\{1\}$ and *adaptive* EMPCA-MI $\{P\}$ for all 20 initial misregistration scenarios. The *mean* and *outliers* are denoted by \blacklozenge and $+$ shapes. The numbers on top of the plots refer to the number of *out-of-range* outliers with RE higher than 10 and 20 pixels respectively.

In order to demonstrate the performance of *adaptive* EMPCA-MI $\{P\}$ especially in presence of higher INU and noise, one of the individual registrations of monomodal $T1+\alpha_{40}+\beta/T1$ pair shown in Figure 7.2(a) is analysed. Registration of the $T1+\alpha_{40}+\beta/T1$ pair with the 14th initial misregistration scenario (-26.32 ,

$0.55, 33.23^\circ$) has an *initial* RE of 82.27 pixels. The *adaptive* EMPCA-MI $\{3\}$ for this registration computed with *Kaiser Rule* in combination with *Enhancement 1* and *2*, provides a significantly lower *final* RE value of just 1.59 pixels. Conversely, the EMPCA-MI $\{1\}$ provides a *final* RE value of 98.91 pixels and therefore it is demarcated as an *out-of-range* outlier in Figure 7.2(a). Interestingly, reflecting on the registration performance of the $T1+\alpha_{40}+\beta/T1$ pair with same initial misregistration scenario analysed in *Chapter 6*, EMPCA-MI $\{1\}$ using *Enhancement 1* provided *final* RE of 9.01 pixels, which is seen as an outlier in Figure 6.3(a). This highlights the improved performance attained by the *adaptive* EMPCA-MI $\{3\}$ by choosing higher numbers of principal components and more accurate MI computation, to facilitate lower RE and better convergence, even for registration cases which have higher INU and noise levels.

Figure 7.3 shows the qualitative performance for the above mentioned monomodal $T1+\alpha_{40}+\beta/T1$ pair registration. The initial misregistration and the corresponding *Canny edge detection* ground truth are displayed in Figures 7.3(a) and (b) respectively, with Figures 7.3(c) and (d) showing the corresponding registered images using the EMPCA-MI $\{1\}$ and *adaptive* EMPCA-MI $\{3\}$ frameworks. The latter clearly outperforms the EMPCA-MI $\{1\}$ in terms of its alignment with the ground truth, as the three zoomed-in areas confirm.

Analogous findings are observed for the multimodal registrations. For example, the multimodal $T1+\alpha_{40}+\beta/T2$ pair shown in Figure 7.2(b) for the 13th initial misregistration scenario $(-6.45, -20.83, -32.64^\circ)$ has an *initial* RE of 80.60 pixels. The *adaptive* EMPCA-MI $\{2\}$ for this registration computed with *Kaiser Rule* and using *Enhancement 1* and *2*, affords a *final* RE value of only 0.67 pixels. In con-

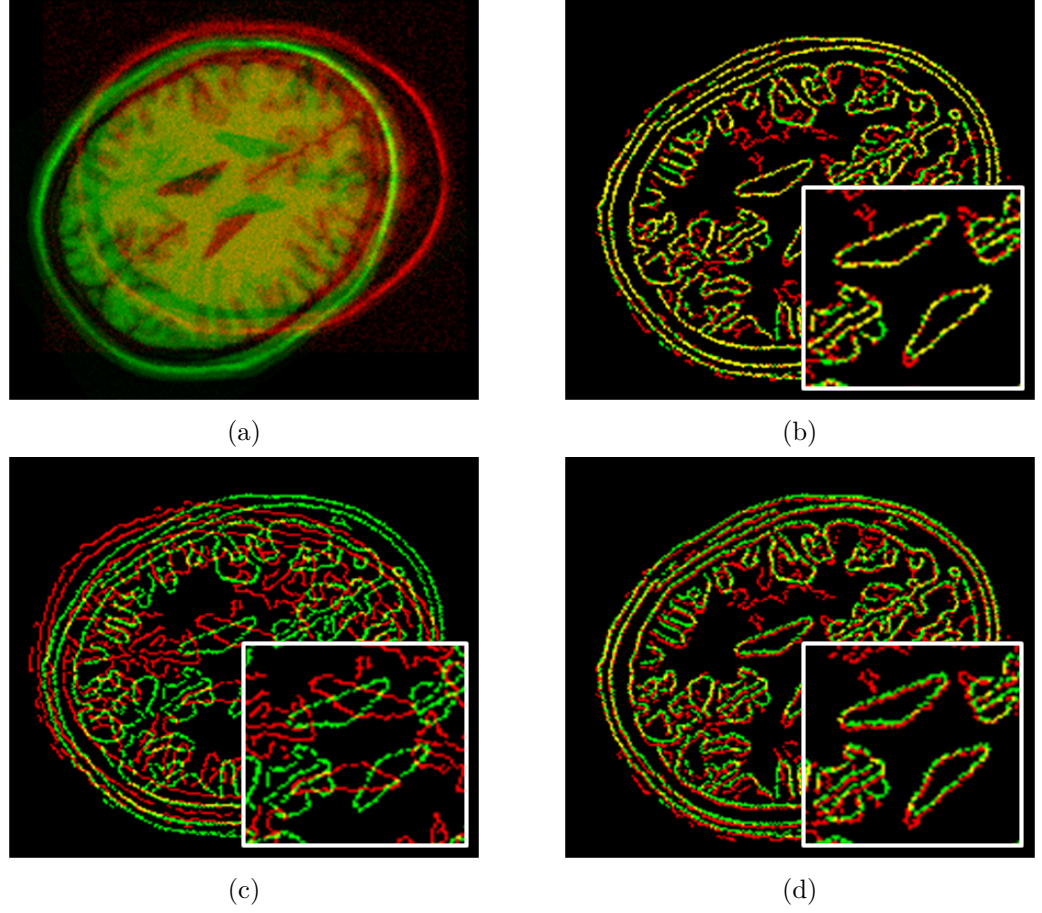


Figure 7.3: Qualitative results of monomodal $T1+\alpha_{40}+\beta/T1$ pair using 14^{th} initial misregistration scenario showing (a) initial misregistration, (b) ground truth and (c) EMPCA-MI $\{1\}$ and (d) *adaptive* EMPCA-MI $\{3\}$ output (with inset showing the zoomed-in central lobes).

trast, EMPCA-MI $\{1\}$ provided a *final* RE value of 21.85 pixels and so has been demarcated as an *out-of-range* outlier in Figure 7.2(b). Similarly, EMPCA-MI $\{1\}$ using *Enhancement 1* gave a *final* RE of 17.18 pixels, and was also designated as an outlier in Figure 6.3(b).

Figure 7.4 shows the corresponding qualitative performance for this particular multimodal $T1+\alpha_{40}+\beta/T2$ pair registration, which has high INU and Gaussian noise. Figures 7.4(a) and (b) display the initial misregistration and the corresponding *Canny edge detection* ground truth. While the registered images using the EMPCA-MI $\{1\}$ and *adaptive* EMPCA-MI $\{2\}$ framework are shown in Figures

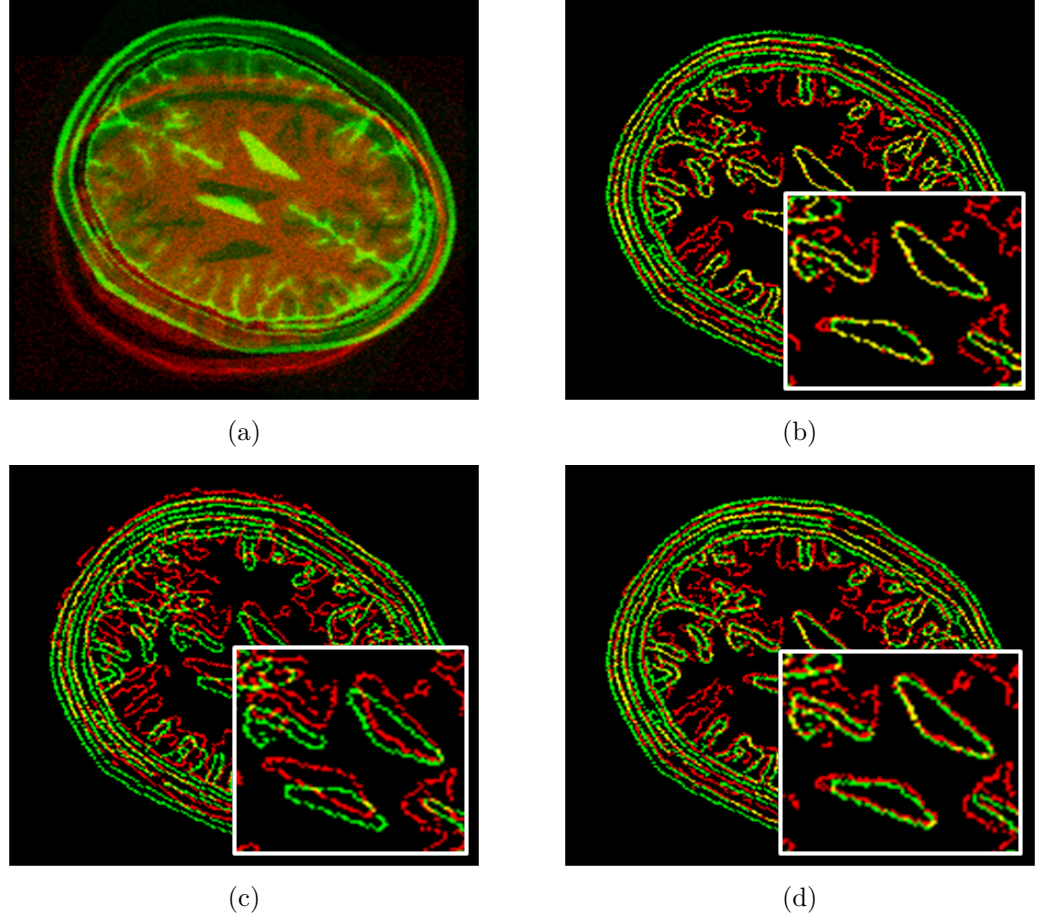


Figure 7.4: Qualitative results of multimodal $T1+\alpha_{40}+\beta/T2$ pair using 13th initial misregistration scenario showing (a) initial misregistration, (b) ground truth and (c) EMPCA-MI $\{1\}$ and (d) *adaptive* EMPCA-MI $\{2\}$ output (with inset showing the zoomed-in central lobes).

7.4(c) and (d) respectively, with strikingly *adaptive* EMPCA-MI $\{2\}$ providing a better perceptual outcome than EMPCA-MI $\{1\}$ when compared with the ground truth shown in Figure 7.4(b).

These mono and multimodal results confirm that the *adaptive* EMPCA-MI $\{P\}$ framework is able to achieve more consistent improved registration performance for the *BrainWeb* dataset, even in the presence of high INU and noise levels.

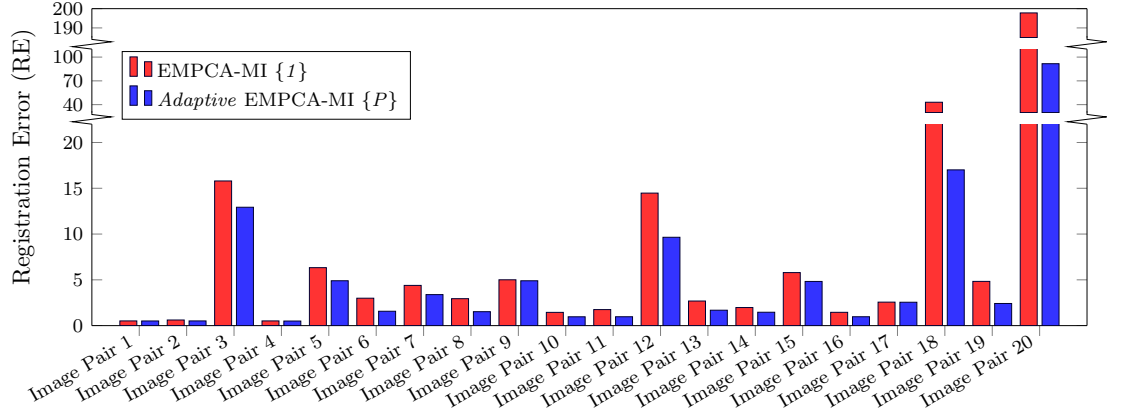


Figure 7.5: RE summary bar graph of 20 monomodal Fundus retinal image pairs using EMPCA-MI $\{1\}$ and *adaptive* EMPCA-MI $\{P\}$ for 3^{rd} initial misregistration scenario.

7.4.2 Set 2: *DRIVE* and *Brno-Multi* Dataset Experiments

This section analyses the registration results for *adaptive* EMPCA-MI $\{P\}$ on Set 2 of monomodal retinal *DRIVE* dataset and multimodal retinal *Brno-Multi* dataset. To draw a comparison as in earlier section, EMPCA-MI $\{1\}$ was used as a comparator.

The first subset of registration experiments of *DRIVE* dataset used four initial misregistration scenarios, the same as in Chapter 5. In the first two initial misregistration scenarios, only one registration parameter (namely rotation θ) was varied, while in the last two scenarios all the four registration parameters are varied. Figure 7.5 shows the RE summary bar graph of 20 monomodal Fundus image pairs using EMPCA-MI $\{1\}$ and *adaptive* EMPCA-MI $\{P\}$ for the 3^{rd} initial misregistration scenario $(5, 5, 20^\circ, 2.8)$. This bar graph is plotted with twice broken y axis in order to accommodate all the RE values on the same plot as well as to equitably show the lower RE values. The RE results confirm *adaptive* EMPCA-MI $\{P\}$ provided superior registration performance with consistently lower RE compared

with the EMPCA-MI $\{1\}$ in challenging contrast and illumination conditions.

For example, the RE for *Image Pair 20* using *adaptive* EMPCA-MI $\{P\}$ is nearly half that of EMPCA-MI $\{1\}$. It was stressed in *Chapter 5*, that for this particular *Image Pair*, EMPCA-MI $\{1\}$ provided poorer registration performance than GFM as shown earlier in Figure 5.7, because EMPCA-MI $\{1\}$ uses only one principal component, which is insufficient for the inherent challenging homogeneous regions and leads to its underperformance. On the other hand, *adaptive* EMPCA-MI $\{3\}$ with *Kaiser Rule* computation and using *Enhancement 1* and *2* for this particular *Image Pair* gives a better registration performance with RE reduction of 54% and 52% respectively compared with EMPCA-MI $\{1\}$ and GFM.

The qualitative assessment of the registration for *Image Pair 20* can be observed in Figure 7.6. It shows the *checkerboard* overlay results with the initial misregistration in Figure 7.6(a) and the ground truth with three marked regions for visual inspection in Figure 7.6(b). Figures 7.6(c) and (d) show the registration output for EMPCA-MI $\{1\}$ and *adaptive* EMPCA-MI $\{3\}$ frameworks, with the correspondingly marked regions. Moreover, Figure 7.6(e) shows the zoomed three marked regions of the ground truth and two registration outputs. It is clear from the Figure 7.6(e) results that *adaptive* EMPCA-MI $\{3\}$ gives better vascular structure continuity in comparison to EMPCA-MI $\{1\}$, and in terms of alignment, is also much closer to the ground truth by virtue of adaptively choosing more principal components to better represent the localised features in *Image Pair 20*.

Finally, Figure 7.7 summarises the first subset of *Set 2* registration experiments. It shows the RE summary boxplot of all monomodal Fundus retinal image pairs

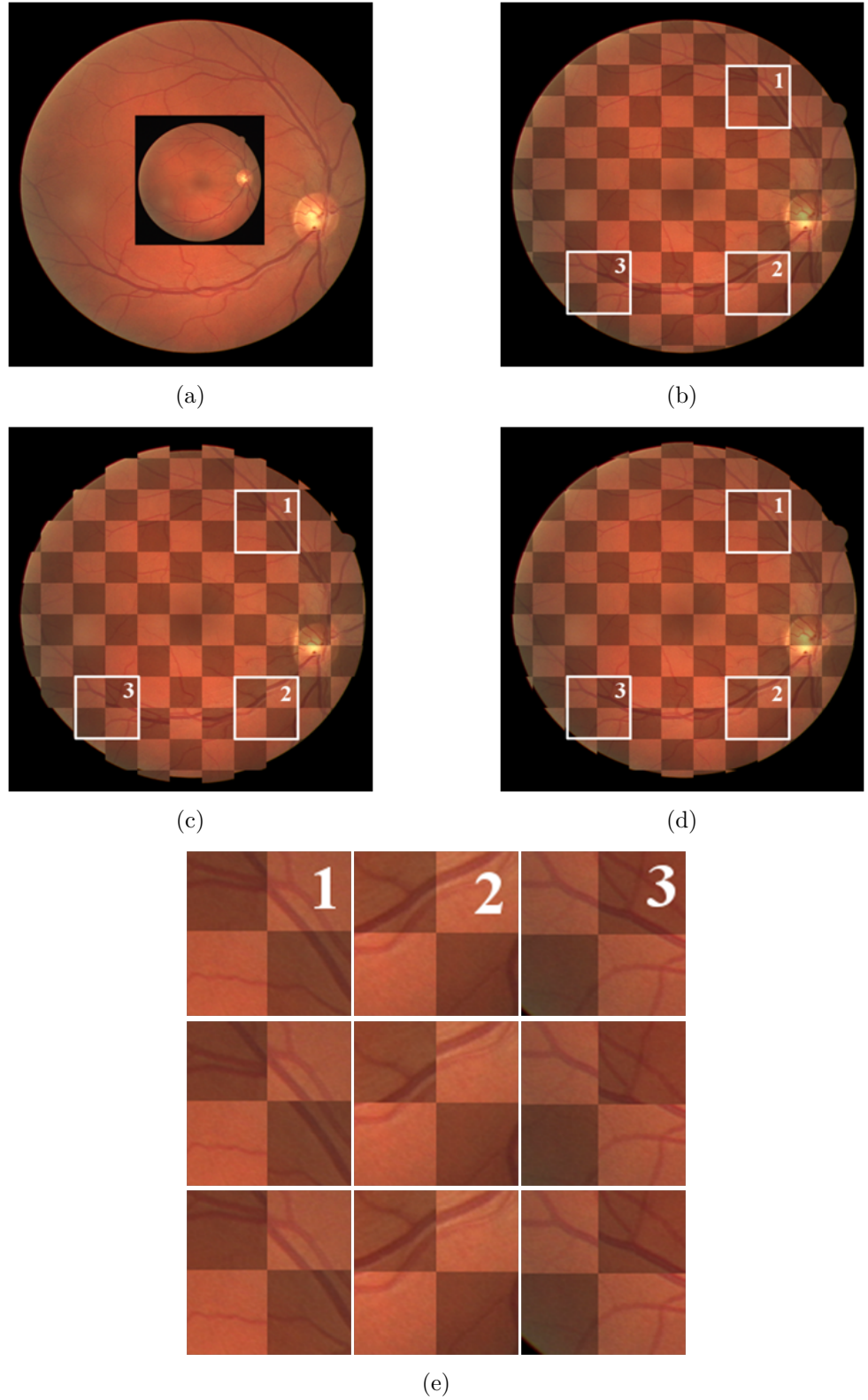


Figure 7.6: Qualitative results of monomodal Fundus retinal *Image Pair 20* using the 3^{rd} initial misregistration scenario, showing (a) initial misregistration, (b) ground truth, (c) EMPCA-MI $\{1\}$ and (d) *adaptive* EMPCA-MI $\{3\}$ output. Also (e) shows the zoomed-in regions of ground truth (1^{st} row), EMPCA-MI $\{1\}$ (2^{nd} row) and *adaptive* EMPCA-MI $\{3\}$ (3^{rd} row).

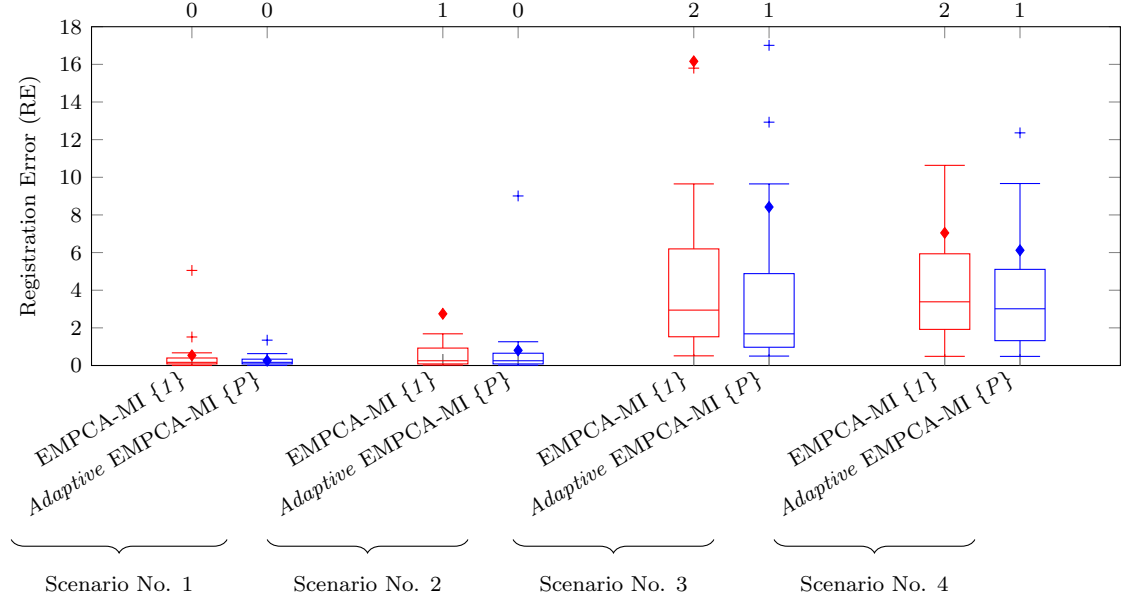


Figure 7.7: RE summary boxplot of 20 monomodal Fundus retinal image pairs using EMPCA-MI $\{1\}$ and *adaptive* EMPCA-MI $\{P\}$ for all 4 initial misregistration scenarios. The *mean* and *outliers* are denoted by \blacklozenge and $+$ shapes. The numbers on top of the plot refer to the number of *out-of-range* outliers with RE higher than 18 pixels.

using EMPCA-MI $\{1\}$ and *adaptive* EMPCA-MI $\{P\}$ for all 4 initial misregistration scenarios. The boxplot highlights the overall superior registration performance of *adaptive* EMPCA-MI $\{P\}$ over EMPCA-MI $\{1\}$, consistently providing lower *mean* RE in all scenarios, as well as fewer *out-of-range* outliers. The monomodal results of *adaptive* EMPCA-MI $\{P\}$ provide an overall RE reduction of 54% and 51% respectively compared with GFM and EMPCA-MI $\{1\}$.

Now considering the results for second subset of *Set 2* using multimodal Fundus/SLO *Brno-Multi* dataset, as in *Chapter 5*, this subset utilises three separate initial misregistration scenarios. In the first, just one registration parameter (θ) is varied, while in the other two scenarios all the four registration parameters are varied. Figure 7.8 shows the corresponding RE summary bar graph of 10 multimodal Fundus/SLO image pairs using *adaptive* EMPCA-MI $\{P\}$ and EMPCA-MI $\{1\}$ for the 2nd initial misregistration scenario (10, 10, 30°, 2). It is apparent *adaptive*

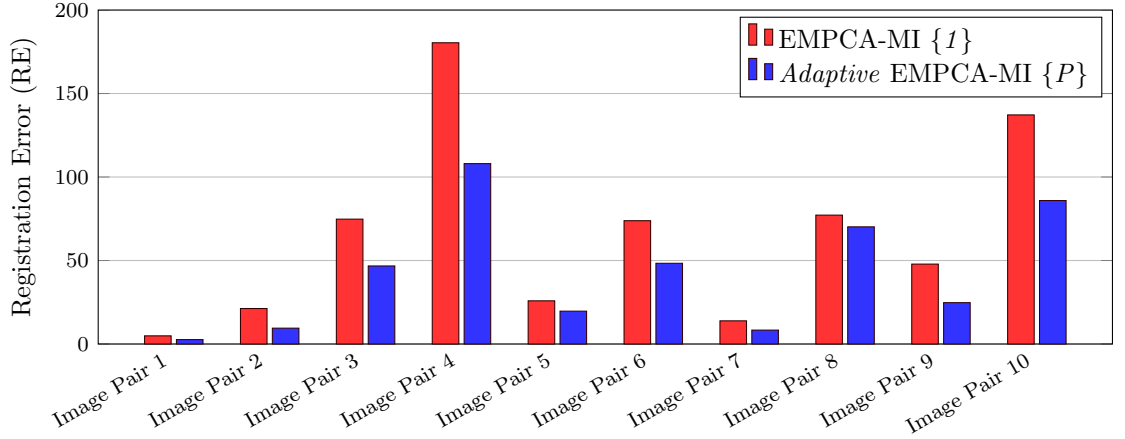


Figure 7.8: RE summary bar graph of 10 multimodal Fundus/SLO retinal image pairs using EMPCA-MI $\{1\}$ and *adaptive* EMPCA-MI $\{P\}$ for the 2nd initial misregistration scenario.

EMPCA-MI $\{P\}$ again consistently provides lower RE than EMPCA-MI $\{1\}$ for all *Image Pairs*. It is especially notable to scrutinise the results for the challenging *Image Pair 6*, which previously in Figure 5.11, produced a higher RE for EMPCA-MI $\{1\}$ in comparison to RIR-BS. Using *adaptive* EMPCA-MI $\{2\}$ with *Kaiser Rule*, together with *Enhancement 1* and *2* now gives better registration with an average RE reduction of 35% and 33% respectively compared to EMPCA-MI $\{1\}$ and RIR-BS.

To affirm this superior performance, Figure 7.9 shows the matching qualitative results for *Image Pair 6* for the 2nd initial misregistration scenario, with three zoomed-in regions shown in Figure 7.9(e). Figures 7.9(a) and (b) show the initial misregistration for the 2nd scenario and the ground truth respectively with three marked regions. Also, Figures 7.9(c) and (d) show the registration output for EMPCA-MI $\{1\}$ and *adaptive* EMPCA-MI $\{P\}$ with corresponding marked regions respectively. Figure 7.9(e) shows the zoomed three marked regions of the ground truth and two registration outputs. Note, in all three marked regions, *adaptive* EMPCA-MI $\{2\}$ provides enhanced structural continuity com-

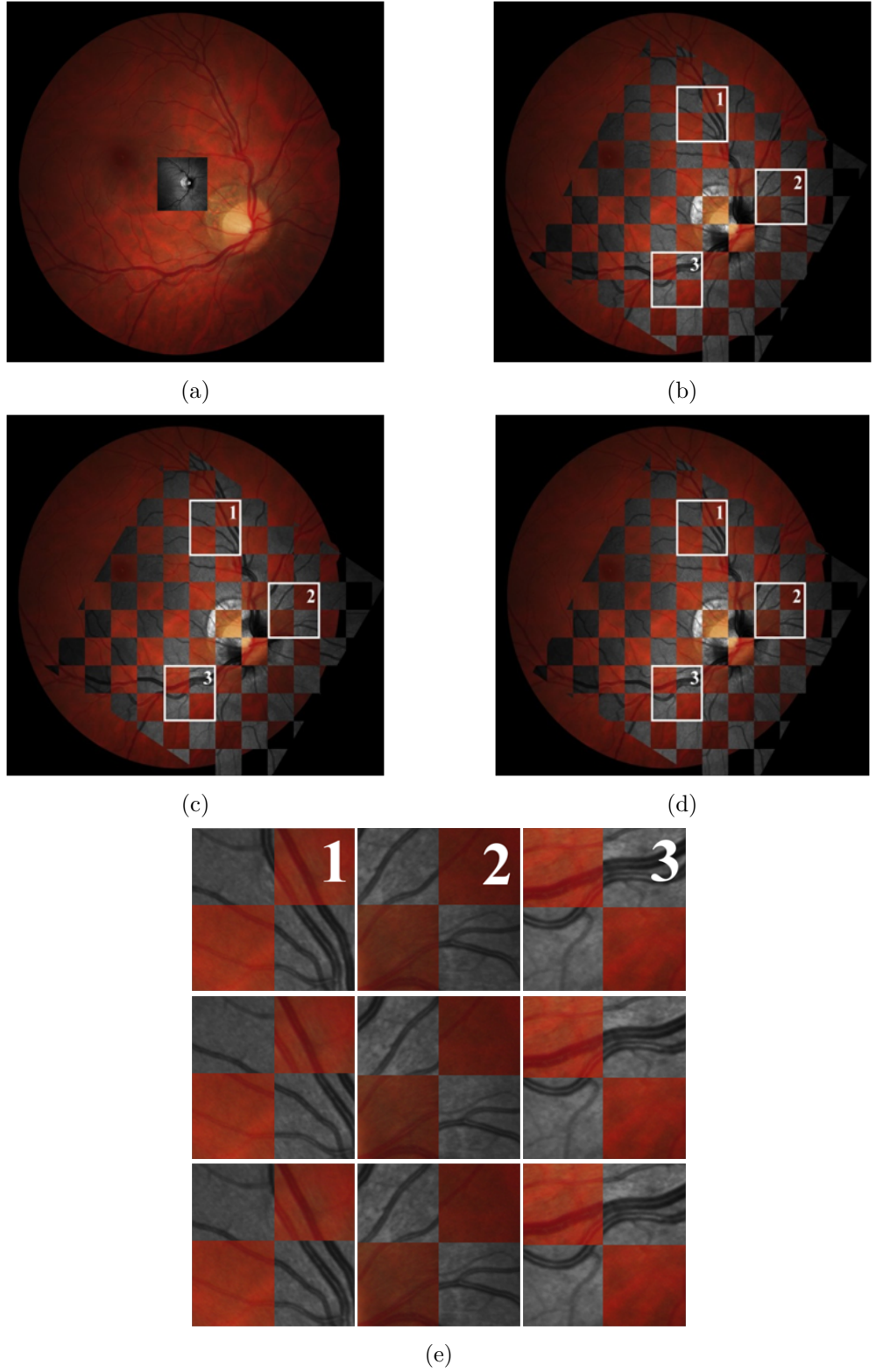


Figure 7.9: Qualitative results of multimodal Fundus/SLO retinal *Image Pair 6* using the 2^{nd} initial misregistration scenario, showing (a) initial misregistration, (b) ground truth, (c) EMPCA-MI $\{1\}$ and (d) *adaptive* EMPCA-MI $\{2\}$ output. Also (e) shows the zoomed-in regions of ground truth (1^{st} row), EMPCA-MI $\{1\}$ (2^{nd} row) and *adaptive* EMPCA-MI $\{2\}$ (3^{rd} row).

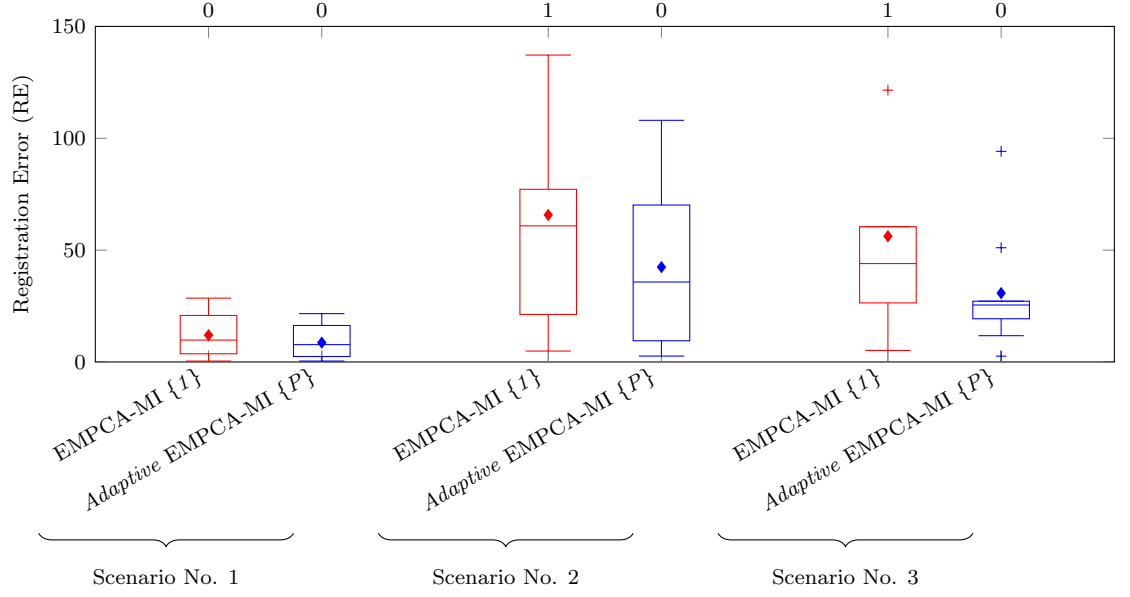


Figure 7.10: RE summary boxplot of 10 multimodal Fundus/SLO retinal image pairs using EMPCA-MI $\{1\}$ and *adaptive* EMPCA-MI $\{P\}$ for all 3 initial misregistration scenarios. The *mean* and *outliers* are denoted by \blacklozenge and $+$ shapes. The numbers on top of the plot refer to the number of *out-of-range* outliers with RE higher than 150 pixels.

pared with EMPCA-MI $\{1\}$ by adaptively determining P directly from the images and thereby leading to consistently superior and more robust registration, even for challenging *Image Pairs*.

Figure 7.10 summarises the second subset of *Set 2* registration experiments for the multimodal Fundus/SLO retinal image pairs using EMPCA-MI $\{1\}$ and *adaptive* EMPCA-MI $\{P\}$ for the three initial misregistration scenarios. The results reveal the superior registration performance of *adaptive* EMPCA-MI $\{P\}$ in terms of both lower *mean* RE and *interquartile* range over EMPCA-MI $\{1\}$ in all the scenarios. Moreover, the underperformance of EMPCA-MI $\{1\}$ is evident from the presence of one *out-of-range* outlier in last two scenarios, while in contrast *adaptive* EMPCA-MI $\{P\}$ is able to consistently afford lower RE with no *out-of-range* outliers. Overall these multimodal results of *adaptive* EMPCA-MI $\{P\}$ provide a respective average reduction in RE by 59% and 39% in comparison to those of

RIR-BS and EMPCA-MI $\{1\}$ in *Section 5.3.2*.

In summary, these findings confirm that *adaptive* EMPCA-MI $\{P\}$ provides better image registration performance compared to EMPCA-MI $\{1\}$ with an overall 45% reduction for the *DRIVE* and *Brno-Multi* datasets, which are especially characterised by the presence of low contrast and large homogeneous non-vascular regions.

7.4.3 Computational Cost of *Adaptive* EMPCA-MI

Framework

As shown earlier in *Section 4.3.2*, the order of computational complexity for the EMPCA $\{1\}$ was $\mathcal{O}(qd)$. Similarly for the adaptive EMPCA $\{P\}$, the order of complexity is $\mathcal{O}(Pqd)$, but as $q \gg P$, d the order will be same as EMPCA $\{1\}$, though the iterative nature of the *Kaiser Rule* to determine the best P means the overall time cost will tend to be slightly higher. Adaptive EMPCA-MI $\{P\}$ can thus be viewed as a generalisation of the EMPCA-MI framework, with EMPCA-MI $\{1\}$ being a special case.

While the *adaptive* EMPCA-MI $\{P\}$ framework more effectively registers the mono and multimodal *BrainWeb*, *DRIVE* and *Brno-Multi* medical datasets, it does incur a commensurate increase in computational time due to its inherently iterative nature. While the order of computational complexity remains the same as EMPCA-MI $\{1\}$, it is insightful to undertake an ART analysis to evaluate the extra cost of using the *Kaiser Rule* to determine the best P value.

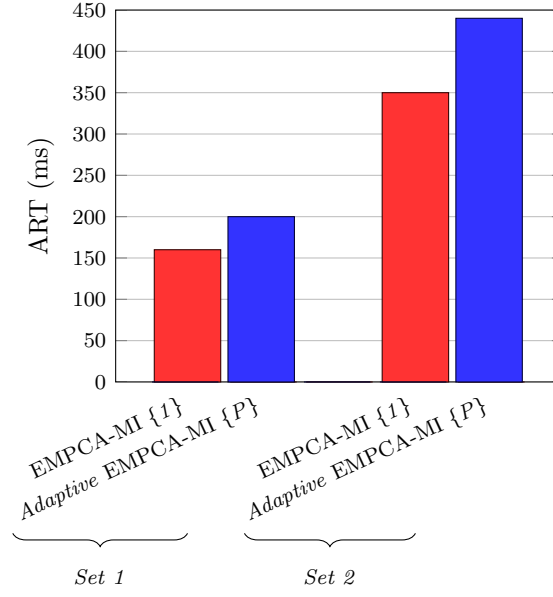


Figure 7.11: ART performance for EMPCA-MI $\{1\}$ and *adaptive* EMPCA-MI $\{P\}$ frameworks for *Set 1* and *Set 2* registration experiments.

Figure 7.11 shows the ART performance of *adaptive* EMPCA-MI $\{P\}$ for registration of the *Sets 1* and *2* clinical datasets in comparison with EMPCA-MI $\{1\}$. Clearly the *adaptive* EMPCA-MI $\{P\}$ computation time for both *Set 1* and *2* registration results is higher, with in case of *Set 1*, the increase being 25% with respect to EMPCA-MI $\{1\}$ and 35% for *Set 2*. Note, the reason for the overall higher *Set 2* registration ART values is they reflect the greater resolution of the Fundus/SLO retinal images.

While the *Enhancement 1* introduced in *Chapter 6* reduces data dimensionality by using 2^{nd} order region connectivity, overall the *adaptive* EMPCA-MI $\{P\}$ framework does incur a higher computational cost because of the inclusion of the adaptive *Kaiser Rule* to find P and then use *Enhancement 2* to determine the best number of bins for MI computation. This pragmatically, however, is more than offset by the significant improvements achieved by the framework in superior and more robust registration performance, particularly in the processing of multimodal

image datasets characterised by high INU and noise, and large homogeneous non-vascular regions.

7.5 Summary

This chapter has presented an *adaptive* EMPCA-MI framework for MIR. It exploits one of the popular stopping rules for principal components namely the *Kaiser Rule* to adaptively find the number of principal components to be computed by the iterative EMPCA. In addition, it also employs *Enhancement 1* and *2* proposed in *Chapter 6*. Two sets (*Set 1* and *2*) of rigorous experiments using mono and multimodal human brain *BrainWeb* and retinal *DRIVE* and *Brno-Multi* datasets proved that *adaptive* EMPCA-MI provides consistently better registration performance with a corresponding trade-off in computational cost. Overall, the numerical and qualitative results for *adaptive* EMPCA-MI show improved robustness and consistently lower RE in comparison to EMPCA-MI using only one principal component. The next chapter presents some ideas for the future to extend the findings from this thesis.

Chapter 8

Future Work

There are a number of potential opportunities to extend the EMPCA-MI similarity measure framework presented in this thesis, as well as exploring other domains for its applicability. Some of these prospective research avenues will now be reviewed.

1. The presented work had the overarching objective of achieving effective robust registration of 2D medical images without incurring high computational cost. As most advanced medical imaging modalities nowadays generate 3D images, one promising area of investigation would be to extend the framework to 3D image registration. A new 3D region connectivity (using the 6, 18 or 26 neighbourhood) based sliding window could be considered as the pre-processing stage for the framework (J. Toriwaki and H. Yoshida, 2009; J. Toriwaki and T. Yonekura, 2002; Noël and Biri, 2015), exploiting the proven enhanced neighbourhood region relations shown in *Section 6.2*, while leaving the other two processing blocks of the EMPCA-MI similarity measure framework as is. In addition, it would be interesting to assess the impact

of using different interpolations and higher neighbourhood radius for the EMPCA-MI similarity measure in the above mentioned extension, with an overall objective to reduce the computational costs.

2. The EMPCA-MI similarity measure framework processes local neighbourhood regions in order to extract spatial features. The thesis has focused upon the direct (*4-pixel*) and indirect (*8-pixel*) connectivity-based $1^{st}/2^{nd}$ order neighbourhood relationships, so the underlying idea could be extended to higher-order patterns and object shapes. More neighbourhood patterns could be inspired from the Local Binary Pattern (LBP) scheme and its recent variants (Liu et al., 2012; Pietikäinen et al., 2011), which have gained popularity in the texture classification domain due to its ability to deal with illumination variations and computational simplicity. It would be insightful to study the impact of integrating a LBP-based approach into the pre-processing stage of the EMPCA-MI similarity measure framework which can help to robustly extract the spatial information from the neighbourhood region leading to more effective registration.
3. The EMPCA-MI similarity measure framework could be applied to other domains in addition to medical imaging. While the framework determines the statistical relationship between different medical modalities, it is feasible to use it in other domains such as remote sensing image registration (Chen et al., 2003) and high dimensional hyper-spectral imagery (Yao et al., 2010). Furthermore, since it integrates local spatial information along with mutual information, it can be used for quantitative assessment of the visual quality of generic images (Li et al., 2012).

4. Although 3D registration is used in both medical and non-medical applications, the long run times involved in the convergence of these registrations is an obstacle to their deployment in time-critical applications (Argyriou et al., 2015). Hence in order to develop time sensitive registration process for such applications, it is desirable to utilise graphic processing unit-based computing. This requires granularity level visualisation of the various blocks of registration process in terms of memory and mathematical operations (Shi et al., 2012). Another extension to the EMPCA-MI similarity measure framework would be to examine graphic processing unit-based implementations for accelerated registration. The iterative and parallel process flows of EMPCA-MI could be leveraged from multi-core processor architectures, especially when deployed together with multi-resolution approaches for significant speed-ups.
5. While the EMPCA-MI similarity measure framework has been developed for rigid transform-based registration of medical images, it can be generalised to non-rigid registration scenarios for different imaging modalities as well as being utilised for sequential rigid followed by non-rigid registration in advanced biomedical applications. For example, EMPCA-MI similarity measure framework could be used for non-rigid B-Spline registration experiments on 2D mouse embryonic micro-CT data using a multi-resolution approach. This could facilitate the high-throughput mouse embryonic micro-CT data phenotyping which aims to map each mouse gene to its corresponding physiological functionality in line with International Mouse Phenotyping Consortium (Roy et al., 2013).

Chapter 9

Conclusion

Medical imaging is increasingly used for diagnosis and treatment planning applications in healthcare as well as an innovative tool for medical research. The ability to establish correspondences between locations in medical images is ubiquitous in most applications. Even though research into MIR has progressed rapidly in the last three decades, there are still many challenges. Previously, various *feature* and *intensity*-based similarity measures have been proposed for registration purposes, with MI establishing itself as a popular similarity measure due to its information-theoretic properties and ability to register multimodal medical images. Some modalities include inherent characteristics like high INU, noise and large non-vascular homogeneous regions, which makes the registration process especially challenging. Recent efforts at the robust registration of multimodal images have used *hybrid* similarity measures utilising spatial information from local regions along with MI, though they either incur a significant computational cost or use covariance-based approximation leading to poorer registration quality.

A new flexible, robust hybrid EMPCA-MI similarity measure framework has been presented which comprises a suite of innovative algorithms to improve the registration performance by extracting the local features from the neighbourhood region using iterative EMPCA in combination with MI to lower the computational time complexity. The new EMPCA-MI framework has been critically evaluated using different mono and multimodal clinical datasets, and makes three original contributions to the rigid image registration domain, which are summarised as follows:

1. The most significant contribution is the *adaptive* EMPCA-MI similarity measure framework which has the capability to flexibly choose the number of principal components from the neighbourhood region, based on the image characteristics and then to compute the MI thereby affording a key computational trade-off mechanism. The framework uses a stopping rule for guiding the iterative EMPCA to ascertain the most appropriate number of features, so EMPCA-MI becomes image dependent with the features reflecting the image information. Rigorous mono and multimodal registration experiments confirm the improved quantitative performance for the challenging brain MRI and retinal images, with the average registration error being reduced by up to *93%* and *60%* respectively, compared to existing similarity measures.
2. The underlying EMPCA-MI similarity measure framework also utilises local neighbourhood region information of the image, though it only employs the first iteratively computed principal component in EMPCA when computing the MI. This means it is computationally more efficient than the *adaptive*

EMPCA-MI similarity measure framework and crucially provides the user with the flexibility to trade between speed and registration quality. Nonetheless it has been conclusively shown to afford superior mono and multimodal registration performance compared with current techniques, with registration errors reduced by on average, *61%* and *30%* for the brain MRI and retinal datasets respectively.

3. Finally, a series of novel enhancements has been embedded into the EMPCA-MI similarity measure framework to further improve its performance. *Enhancement 1* exploits the neighbourhood region relationships to remove information redundancy, while *Enhancement 2* employs variable number of bins selection strategies to enable more accurate MI computation. Experimental results confirm both enhancements collectively provide reductions in the average registration error of up to *79%* and *68%* respectively, compared with the original EMPCA-MI similarity measure model.

In summarising, this new hybrid EMPCA-MI similarity measure framework makes a notable contribution to the registration performance of multimodal clinical images characterised by high INU, noise and non-vascular homogeneous regions. Most importantly, it offers a flexible and robust solution for 2D rigid registration which is able to, not only be extended to non-rigid registration, but also the 3D registration domain in the future.

References

- Acharya, T. and Tsai, P.-S. (2007). Computational Foundations of Image Interpolation Algorithms. *Ubiquity*, 2007(October):4:1–4:17.
- Ackerman, M. J. (1998). The Visible Human Project. *Proceedings of the IEEE*, 86(3):504–511.
- Alberto, R.-R. (2011). Multimodal Imaging. In *Minimally Invasive Medical Technology*, Series in Medical Physics and Biomedical Engineering, pages 107–121. Taylor & Francis.
- Aljabar, P., Hajnal, J. V., Boyes, R. G., and Rueckert, D. (2005). Interpolation Artefacts in Non-rigid Registration. In Duncan, J. S. and Gerig, G., editors, *Medical Image Computing and Computer-Assisted Intervention – MICCAI 2005*, volume 3750 of *Lecture Notes in Computer Science*, pages 247–254. Springer Berlin Heidelberg.
- Allen, R. L., Kamangar, F. A., and Stokely, E. M. (1993). Laplacian and orthogonal wavelet pyramid decompositions in coarse-to-fine registration. *IEEE Transactions on Signal Processing*, 41(12):3536–3541.
- Alpert, N. M., Bradshaw, J. F., Kennedy, D., and Correia, J. A. (1990). The principal axes transformation—a method for image registration. *Journal of Nuclear Medicine: Official Publication, Society of Nuclear Medicine*, 31(10):1717–1722.

- Amanatiadis, A., Kaburlasos, V. G., Gasteratos, A., and Papadakis, S. E. (2009). A comparative study of invariant descriptors for shape retrieval. In *2009 IEEE International Workshop on Imaging Systems and Techniques*, pages 391–394.
- Amit, Y. (1994). A Nonlinear Variational Problem for Image Matching. *SIAM Journal on Scientific Computing*, 15(1):207–224.
- Analoui, M., Bronzino, J. D., and Peterson, D. R. (2012). *Medical Imaging: Principles and Practices*. CRC Press.
- Andronache, A., Cattin, P., and Székely, G. (2006). Local Intensity Mapping for Hierarchical Non-rigid Registration of Multi-modal Images Using the Cross-Correlation Coefficient. In Hutchison, D., Kanade, T., Kittler, J., Kleinberg, J. M., Mattern, F., Mitchell, J. C., Naor, M., Nierstrasz, O., Pandu Rangan, C., Steffen, B., Sudan, M., Terzopoulos, D., Tygar, D., Vardi, M. Y., Weikum, G., Pluim, J. P. W., Likar, B., and Gerritsen, F. A., editors, *Biomedical Image Registration*, volume 4057 of *Lecture Notes in Computer Science*, pages 26–33. Springer Berlin Heidelberg.
- Andronache, A., von Siebenthal, M., Székely, G., and Cattin, P. (2008). Non-rigid registration of multi-modal images using both mutual information and cross-correlation. *Medical Image Analysis*, 12(1):3–15.
- Argyriou, V., Rincon, J. M. D., Villarini, B., and Roche, A. (2015). *Image, Video and 3D Data Registration: Medical, Satellite and Video Processing Applications with Quality Metrics*. John Wiley & Sons.
- Bajcsy, R. and Kovačič, S. (1989). Multiresolution elastic matching. *Computer Vision, Graphics, and Image Processing*, 46(1):1–21.

- Battiti, R. (1994). Using mutual information for selecting features in supervised neural net learning. *IEEE Transactions on Neural Networks*, 5(4):537–550.
- Beckmann, E. C. (2006). CT scanning the early days. *The British Journal of Radiology*, 79(937):5–8.
- Belaroussi, B., Milles, J., Carme, S., Zhu, Y. M., and Benoit-Cattin, H. (2006). Intensity non-uniformity correction in mri: Existing methods and their validation. *Medical Image Analysis*, 10(2):234 – 246.
- Bernardes, R., Guimarães, P., Rodrigues, P., and Serranho, P. (2014). Fully-Automatic Multimodal Co-Registration of Retinal Fundus Images. In Zhang, Y.-T., editor, *The International Conference on Health Informatics*, volume 42 of *IFMBE Proceedings*, pages 248–251. Springer International Publishing.
- Beutel, J. (2000). *Handbook of Medical Imaging: Medical image processing and analysis*. SPIE Press.
- Birgé, L. and Rozenholc, Y. (2006). How many bins should be put in a regular histogram. *ESAIM: Probability and Statistics*, 10:24–45.
- Bookstein, F. L. (1989). Principal warps: thin-plate splines and the decomposition of deformations. *IEEE Transactions on Pattern Analysis and Machine Intelligence*, 11(6):567–585.
- Bourland, J. D. (2012). *Image-Guided Radiation Therapy*. CRC Press.
- Brase, C. H. and Brase, C. P. (1999). *Understanding Statistics*. Houghton Mifflin Company.

- Breitner, M. H., Denk, G., and Rentrop, P., editors (2008). *From Nano to Space*. Springer Berlin Heidelberg.
- Brock, K. K. (2013). *Image Processing in Radiation Therapy*. CRC Press.
- Brooks, D. (2001). Emerging medical imaging modalities. *IEEE Signal Processing Magazine*, 18(6):12–13.
- Brown, L. G. (1992). A survey of image registration techniques. *ACM Computing Surveys*, 24(4):325–376.
- Burt, P. and Adelson, E. (1983). The Laplacian Pyramid as a Compact Image Code. *IEEE Transactions on Communications*, 31(4):532–540.
- Bushong, S. C. and Clarke, G. (2013). *Magnetic Resonance Imaging: Physical and Biological Principles*. Elsevier Health Sciences.
- Butz, T. and Thiran, J.-P. (2001). Affine Registration with Feature Space Mutual Information. In Niessen, W. J. and Viergever, M. A., editors, *Medical Image Computing and Computer-Assisted Intervention – MICCAI 2001*, volume 2208 of *Lecture Notes in Computer Science*, pages 549–556. Springer Berlin Heidelberg.
- Cangelosi, R. and Goriely, A. (2007). Component retention in principal component analysis with application to cDNA microarray data. *Biology Direct*, 2:2.
- Chanwimaluang, T., Fan, G., and Fransen, S. (2006). Hybrid retinal image registration. *IEEE Transactions on Information Technology in Biomedicine*, 10(1):129–142.

- Chappelow, J. and Madabhushi, A. (2010). Multi-attribute combined mutual information (MACMI): An image registration framework for leveraging multiple data channels. In *2010 IEEE International Symposium on Biomedical Imaging: From Nano to Macro*, pages 376–379.
- Chen, H.-M., Varshney, P. K., and Arora, M. K. (2003). Performance of mutual information similarity measure for registration of multitemporal remote sensing images. *IEEE Transactions on Geoscience and Remote Sensing*, 41(11):2445–2454.
- Chen, L., Huang, X., and Tian, J. (2015). Retinal image registration using topological vascular tree segmentation and bifurcation structures. *Biomedical Signal Processing and Control*, 16:22–31.
- Chen, L., Xiang, Y., Chen, Y., and Zhang, X. (2011). Retinal image registration using bifurcation structures. In *2011 18th IEEE International Conference on Image Processing (ICIP)*, pages 2169 –2172.
- Chen, Y.-W. and Lin, C.-L. (2011). PCA Based Regional Mutual Information for Robust Medical Image Registration. In Liu, D., Zhang, H., Polycarpou, M., Alippi, C., and He, H., editors, *Advances in Neural Networks – ISNN 2011*, volume 6677 of *Lecture Notes in Computer Science*, pages 355–362. Springer Berlin Heidelberg.
- Cherry, S. R. (2009). MULTIMODALITY IMAGING: BEYOND PET/CT AND SPECT/CT. *Seminars in nuclear medicine*, 39(5):348–353.
- Chityala, R. and Pudipeddi, S. (2014). *Image Processing and Acquisition using Python*. Chapman and Hall/CRC.

- Christensen, G. E., Joshi, S. C., and Miller, M. I. (1997). Volumetric transformation of brain anatomy. *IEEE Transactions on Medical Imaging*, 16(6):864–877.
- Cideciyan, A. (1995). Registration of ocular fundus images: an algorithm using cross-correlation of triple invariant image descriptors. *IEEE Engineering in Medicine and Biology Magazine*, 14(1):52–58.
- Collignon, Maes, F., Delaere, D., Vandermeulen, D., Suetens, P., and Marchal, G. (1995). Automated multi-modality image registration based on information theory. *Imaging*, 3(1):263–274.
- Collins, D. L., Zijdenbos, A. P., Kollokian, V., Sled, J. G., Kabani, N. J., Holmes, C. J., and Evans, A. C. (1998). Design and construction of a realistic digital brain phantom. *IEEE Transactions on Medical Imaging*, 17(3):463–468.
- Cooper, L., Huang, K., and Ujaldon, M. (2011). Parallel Automatic Registration of Large Scale Microscopic Images on Multiprocessor CPUs and GPUs. In *2011 IEEE International Symposium on Parallel and Distributed Processing Workshops and Phd Forum (IPDPSW)*, pages 1367–1376.
- Cover, T. M. and Thomas, J. A. (1991). *Elements of Information Theory*. Wiley-Blackwell, New York.
- Crum, W. R. (2004). Non-rigid image registration: theory and practice. *British Journal of Radiology*, 77(suppl 2):S140–S153.
- D. Forsberg (2013). *Robust Image Registration for Improved Clinical Efficiency: Using Local Structure Analysis and Model-Based Processing*. Linköping Studies in Science and Technology. Dissertations No. 1514, Linköping University, Sweden.

- Damas, S., Cordon, O., and Santamaria, J. (2011a). Evaluation of various evolutionary methods for medical image registration. In *Computational Intelligence In Medical Imaging (CIMI), 2011 IEEE Third International Workshop On*, pages 1–7.
- Damas, S., Cordon, O., and Santamariia, J. (2011b). Medical Image Registration Using Evolutionary Computation: An Experimental Survey. *IEEE Computational Intelligence Magazine*, 6(4):26–42.
- Dame, A. and Marchand, E. (2010). Accurate real-time tracking using mutual information. In *2010 9th IEEE International Symposium on Mixed and Augmented Reality (ISMAR)*, pages 47–56.
- Davies, L., Gather, U., Nordman, D., and Weinert, H. (2009). A comparison of automatic histogram constructions. *ESAIM: Probability and Statistics*, 13:181–196.
- Davies, P. L., Gather, U., Nordman, D., and Weinert, H. (2007). Constructing a regular histogram: a comparison of methods. Technical Reports 2007,14, Technische Universität Dortmund, Sonderforschungsbereich 475: Komplexitätsreduktion in multivariaten Datenstrukturen.
- Dawant, B. M., Zijdenbos, A. P., and Margolin, R. A. (1993). Correction of intensity variations in mr images for computer-aided tissue classification. *IEEE Transactions on Medical Imaging*, 12(4):770–781.

- De Craene, M., du Bois d'Aische, A., Macq, B., Kipfmüller, F., Weisenfeld, N., Haker, S., and Warfield, S. K. (2004). Multimodal nonrigid registration using a stochastic gradient approximation. In *IEEE International Symposium on Biomedical Imaging: Nano to Macro, 2004*, pages 1459–1462 Vol. 2.
- Demirkaya, O., Asyali, M. H., and Sahoo, P. K. (2008). *Image Processing with MATLAB: Applications in Medicine and Biology*. CRC Press.
- Denton, E. R., Sonoda, L. I., Rueckert, D., Rankin, S. C., Hayes, C., Leach, M. O., Hill, D. L., and Hawkes, D. J. (1999). Comparison and evaluation of rigid, affine, and nonrigid registration of breast MR images. *Journal of Computer Assisted Tomography*, 23(5):800–805.
- Deubler, J. and Olivo, J.-C. (1997). A Wavelet-Based Multiresolution Method to Automatically Register Images. *J. Math. Imaging Vis.*, 7(3):199–209.
- Devroye, L. and Györfi, L. (1985). *Nonparametric Density Estimation: The L1 View*. Wiley.
- Eklund, A., Dufort, P., Forsberg, D., and LaConte, S. M. (2013). Medical image processing on the GPU – Past, present and future. *Medical Image Analysis*, 17(8):1073–1094.
- Fang, B., You, X., and Tang, Y. Y. (2005). A Novel Fusing Algorithm for Retinal Fundus Images. In Hao, Y., Liu, J., Wang, Y., Cheung, Y.-m., Yin, H., Jiao, L., Ma, J., and Jiao, Y.-C., editors, *Computational Intelligence and Security*, volume 3801 of *Lecture Notes in Computer Science*, pages 833–838. Springer Berlin Heidelberg.

- Fedorov, A., Beichel, R., Kalpathy-Cramer, J., Finet, J., Fillion-Robin, J.-C., Pujol, S., Bauer, C., Jennings, D., Fennessy, F., Sonka, M., Buatti, J., Aylward, S., Miller, J. V., Pieper, S., and Kikinis, R. (2012). 3d Slicer as an image computing platform for the Quantitative Imaging Network. *Magnetic Resonance Imaging*, 30(9):1323–1341.
- Fernandez-de Manuel, L., Wollny, G., Kybic, J., Jimenez-Carretero, D., Tellado, J. M., Ramon, E., Desco, M., Santos, A., Pascau, J., and Ledesma-Carbayo, M. J. (2014). Organ-focused mutual information for nonrigid multimodal registration of liver CT and Gd-EOB-DTPA-enhanced MRI. *Medical Image Analysis*, 18(1):22–35.
- Fernandez-Maloigne, C. (2012). *Advanced Color Image Processing and Analysis*. Springer Science & Business Media.
- Fisher, R. A. (1936). The Use of Multiple Measurements in Taxonomic Problems. *Annals of Eugenics*, 7(2):179–188.
- Fluck, O., Vetter, C., Wein, W., Kamen, A., Preim, B., and Westermann, R. (2011). A survey of medical image registration on graphics hardware. *Computer Methods and Programs in Biomedicine*, 104(3):e45–e57.
- Flusser, J. and Suk, T. (1993). Pattern recognition by affine moment invariants. *Pattern Recognition*, 26(1):167 – 174.
- Flusser, J. and Suk, T. (1994). A moment-based approach to registration of images with affine geometric distortion. *IEEE Transactions on Geoscience and Remote Sensing*, 32(2):382–387.

- Fornefett, M., Rohr, K., and Stiehl, H. (2001). Radial basis functions with compact support for elastic registration of medical images. *Image and Vision Computing*, 19(1–2):87–96.
- Fraz, M. M., Remagnino, P., Hoppe, A., Uyyanonvara, B., Rudnicka, A. R., Owen, C. G., and Barman, S. A. (2012). Blood vessel segmentation methodologies in retinal images – A survey. *Computer Methods and Programs in Biomedicine*, 108(1):407–433.
- Friston, K. J., Ashburner, J., Frith, C. D., Poline, J.-B., Heather, J. D., and Frackowiak, R. S. J. (1995). Spatial registration and normalization of images. *Human Brain Mapping*, 3(3):165–189.
- Gan, R. and Chung, A. C. S. (2005). Multi-dimensional Mutual Information Based Robust Image Registration Using Maximum Distance-Gradient-Magnitude. In Christensen, G. E. and Sonka, M., editors, *Information Processing in Medical Imaging*, volume 3565 of *Lecture Notes in Computer Science*, pages 210–221. Springer Berlin Heidelberg.
- Ganzetti, M., Wenderoth, N., and Mantini, D. (2016). Quantitative evaluation of intensity inhomogeneity correction methods for structural mr brain images. *Neuroinformatics*, 14(1):5–21.
- Gao, Z., Gu, B., and Lin, J. (2008). Monomodal image registration using mutual information based methods. *Image and Vision Computing*, 26(2):164–173.

- Garcia-Arteaga, J. D. and Kybic, J. (2008). Regional image similarity criteria based on the Kozachenko-Leonenko entropy estimator. In *IEEE Computer Society Conference on Computer Vision and Pattern Recognition Workshops, 2008. CVPRW '08*, pages 1–8.
- Gefen, S., Tretiak, O., and Nissanov, J. (2003). Elastic 3-D alignment of rat brain histological images. *IEEE Transactions on Medical Imaging*, 22(11):1480–1489.
- George, M. (2011). Medical Image Registration and Fusion Techniques. In *Advanced Signal Processing, Electrical Engineering & Applied Signal Processing Series*, pages 221–249. CRC Press.
- Gharabaghi, S., Daneshvar, S., and Sedaaghi, M. H. (2013). Retinal Image Registration Using Geometrical Features. *Journal of Digital Imaging*, 26(2):248–258.
- Gholipour, A., Kehtarnavaz, N., Briggs, R., Devous, M., and Gopinath, K. (2007). Brain Functional Localization: A Survey of Image Registration Techniques. *IEEE Transactions on Medical Imaging*, 26(4):427–451.
- Goshtasby, A. A. (2012). *Image Registration: Principles, Tools and Methods*. Springer, London.
- Grevera, G. J., Udupa, J. K., and Miki, Y. (1999). A task-specific evaluation of three-dimensional image interpolation techniques. *IEEE Transactions on Medical Imaging*, 18(2):137–143.
- Gudbjartsson, H. and Patz, S. (1995). The rician distribution of noisy mri data. *Magnetic Resonance in Medicine*, 34(6):910–914.

- Gunderman, R. B. (2013). *X-Ray Vision: The Evolution of Medical Imaging and Its Human Significance*. Oxford University Press.
- Guo, W. and Huang, F. (2008). A local mutual information guided denoising technique and its application to self-calibrated partially parallel imaging. In Metaxas, Dimitris, Axel, Leon, Fichtinger, Gabor, and Székely, Gábor, editors, *Medical Image Computing and Computer-Assisted Intervention – MICCAI 2008*, volume 5242 of *Lecture Notes in Computer Science*, pages 939–947. Springer Berlin Heidelberg.
- H. R. Novotny and D. L. Alvis (1961). A method of photographing fluorescence in circulating blood in the human retina. *Circulation*, 24:82–86.
- Hahn, D., Daum, V., and Hornegger, J. (2010). Automatic Parameter Selection for Multimodal Image Registration. *IEEE Transactions on Medical Imaging*, 29(5):1140–1155.
- Haidekker, M. (2011). *Advanced Biomedical Image Analysis*. John Wiley & Sons.
- Hajnal, J. V. and Hill, D. L. G., editors (2001). *Medical Image Registration*. CRC Press.
- Hancock, P. J. B., Baddeley, R. J., and Smith, L. S. (1992). The principal components of natural images. *Network: Computation in Neural Systems*, 3(1):61–70.
- Hartley, R. V. L. (1928). Transmission of Information. *Bell System Technical Journal*, 7(3):535–563.
- HAWKES, D. J. (1998). Algorithms for radiological image registration and their clinical application. *Journal of Anatomy*, 193(Pt 3):347–361.

- Hayton, P. M., Brady, M., Smith, S. M., and Moore, N. (1999). A non-rigid registration algorithm for dynamic breast MR images. *Artificial Intelligence*, 114(1–2):125–156.
- Heinrich, M. P., Jenkinson, M., Bhushan, M., Matin, T., Gleeson, F. V., Brady, S. M., and Schnabel, J. A. (2012). MIND: Modality independent neighbourhood descriptor for multi-modal deformable registration. *Medical Image Analysis*, 16(7):1423–1435.
- Hendee, W. R. and Ritenour, E. R. (2002). *Medical Imaging Physics*. Wiley-Liss, 4 edition.
- Henkelman, R. M. (1985). Measurement of signal intensities in the presence of noise in mr images. *Medical Physics*, 12(2):232–233.
- Hero, A. O., Ma, B., Michel, O. J., and Gorman, J. (2002). Applications of entropic spanning graphs. *IEEE Signal Processing Magazine*, 19(5):85–95.
- Hill, D. L. G., Batchelor, P. G., Holden, M., and Hawkes, D. J. (2001). Medical image registration. *Physics in Medicine and Biology*, 46:R1–R45.
- Hill, D. L. G., Hawkes, D. J., Harrison, N. A., and Ruff, C. F. (1993). A strategy for automated multimodality image registration incorporating anatomical knowledge and imager characteristics. In Barrett, H. H. and Gmitro, A. F., editors, *Information Processing in Medical Imaging*, volume 687 of *Lecture Notes in Computer Science*, pages 182–196. Springer Berlin Heidelberg.
- Hobbie, R. K. (2001). *Intermediate Physics for Medicine and Biology*. American Institute of Physics, 3rd edition.

- Holden, M. (2008). A Review of Geometric Transformations for Nonrigid Body Registration. *IEEE Transactions on Medical Imaging*, 27(1):111–128.
- Holden, M., Griffin, L. D., Saeed, N., and Hill, D. L. G. (2004). Multi-channel Mutual Information Using Scale Space. In Barillot, C., Haynor, D. R., and Hellier, P., editors, *Medical Image Computing and Computer-Assisted Intervention – MICCAI 2004*, volume 3216 of *Lecture Notes in Computer Science*, pages 797–804. Springer Berlin Heidelberg.
- Holden, M., Hill, D. L., Denton, E. R., Jarosz, J. M., Cox, T. C., Rohlfing, T., Goodey, J., and Hawkes, D. J. (2000). Voxel similarity measures for 3-D serial MR brain image registration. *IEEE Transactions on Medical Imaging*, 19(2):94–102.
- Holz, F. G. and Spaide, R. F. (2010). *Medical Retina: Focus on Retinal Imaging*. Springer Science & Business Media.
- Horn, B. K. and Schunck, B. G. (1981). Determining optical flow. *Artificial Intelligence*, 17(1–3):185–203.
- Hossain, M. A., Pickering, M., and Jia, X. (2011). Unsupervised feature extraction based on a mutual information measure for hyperspectral image classification. In *Geoscience and Remote Sensing Symposium (IGARSS), 2011 IEEE International*, pages 1720–1723.
- Hsu, L.-Y. and Loew, M. (2001). Fully automatic 3d feature-based registration of multi-modality medical images. *Image and Vision Computing*, 19(1–2):75–85.
- Ibanez, L., Schroeder, W., Ng, L., and Cates, J. (2003). *The ITK Software Guide: The Insight Segmentation and Registration Toolkit*. Kitware Inc.

- Image Sciences Institute (n.d.). Drive: Digital retinal images for vessel extraction. [Online]. Available at <http://www.isi.uu.nl/Research/Databases/DRIVE/> (Accessed 11th December 2014).
- Insko, E. and Bolinger, L. (1993). Mapping of the radiofrequency field. *Journal of Magnetic Resonance, Series A*, 103(1):82 – 85.
- Izenman, A. J. (1991). Review Papers: Recent Developments in Nonparametric Density Estimation. *Journal of the American Statistical Association*, 86(413):205–224.
- J. Toriwaki and H. Yoshida (2009). *Fundamentals of Three-dimensional Digital Image Processing*. Springer Science & Business Media.
- J. Toriwaki and T. Yonekura (2002). Local Patterns and Connectivity Indexes in a Three Dimensional Digital Picture. *Forma*, 17(4):275–291.
- Jackson, D. A. (1993). Stopping rules in principal components analysis: a comparison of heuristical and statistical approaches. *Ecology*, pages 2204–2214.
- Jacquet, W., Nyssen, E., de Groen, P., and Sijbers, J. (2010). Benefits and shortcomings of partial volume interpolation for MI based image registration. In *2010 10th IEEE International Conference on Information Technology and Applications in Biomedicine (ITAB)*, pages 1–6.
- Jenkinson, M. and Smith, S. (2001). A global optimisation method for robust affine registration of brain images. *Medical Image Analysis*, 5(2):143–156.

- Jin, S., Li, D., Wang, H., and Yin, Y. (2013). Registration of PET and CT images based on multiresolution gradient of mutual information demons algorithm for positioning esophageal cancer patients. *Journal of Applied Clinical Medical Physics / American College of Medical Physics*, 14(1):3931.
- Jolliffe, I. (2002). *Principal Component Analysis*. Springer, 2nd edition.
- Kabus, S., Netsch, T., Fischer, B., and Modersitzki, J. (2004). B-spline registration of 3d images with Levenberg-Marquardt optimization. *Proceedings of SPIE*, 5370(1):304–313.
- Kanazawa, Y. (1993). Hellinger distance and Akaike’s information criterion for the histogram. *Statistics & Probability Letters*, 17(4):293–298.
- Kang, J., Xiao, C., Deng, M., Yu, J., and Liu, H. (2011). Image registration based on harris corner and mutual information. In *2011 International Conference on Electronic and Mechanical Engineering and Information Technology (EMEIT)*, volume 7, pages 3434–3437.
- Karnowski, T., Giancardo, L., Li, Y., Tobin, K., and Chaum, E. (2013). Retina image analysis and ocular telehealth: The oak ridge national laboratory-hamilton eye institute case study. In *2013 35th Annual International Conference of the IEEE Engineering in Medicine and Biology Society (EMBC)*, pages 7140–7143.
- Keenan, T. D. L., Johnston, R. L., Donachie, P. H. J., Sparrow, J. M., Stratton, I. M., and Scanlon, P. (2013). United Kingdom National Ophthalmology Database Study: Diabetic Retinopathy; Report 1: prevalence of centre-involving diabetic macular oedema and other grades of maculopathy and retinopathy in hospital eye services. *Eye*, 27(12):1397–1404.

- Kevles, B. (1997). *Naked to the Bone: Medical Imaging in the Twentieth Century*. Rutgers University Press.
- Khademi, A., Venetsanopoulos, A., and Moody, A. R. (2014). Generalized method for partial volume estimation and tissue segmentation in cerebral magnetic resonance images. *Journal of Medical Imaging*, 1(1):014002.
- Khalifa, F., Beache, G. M., Gimel'farb, G., Suri, J. S., and El-Baz, A. S. (2011). State-of-the-Art Medical Image Registration Methodologies: A Survey. In El-Baz, A. S., U, R. A., Mirmehdi, M., and Suri, J. S., editors, *Multi Modality State-of-the-Art Medical Image Segmentation and Registration Methodologies*, pages 235–280. Springer US.
- Klein, A., Andersson, J., Ardekani, B. A., Ashburner, J., Avants, B., Chiang, M.-C., Christensen, G. E., Collins, D. L., Gee, J., Hellier, P., Song, J. H., Jenkinson, M., Lepage, C., Rueckert, D., Thompson, P., Vercauteren, T., Woods, R. P., Mann, J. J., and Parsey, R. V. (2009). Evaluation of 14 nonlinear deformation algorithms applied to human brain MRI registration. *NeuroImage*, 46(3):786–802.
- Klein, S., Staring, M., and Pluim, J. P. (2007). Evaluation of Optimization Methods for Nonrigid Medical Image Registration Using Mutual Information and B-Splines. *IEEE Transactions on Image Processing*, 16(12):2879–2890.
- Kolar, R., Harabis, V., and Odstrcilik, J. (2013). Hybrid retinal image registration using phase correlation. *The Imaging Science Journal*, 61(4):369–384.

- Kolar, R. and Tasevsky, P. (2010). Registration of 3d Retinal Optical Coherence Tomography Data and 2d Fundus Images. In Fischer, B., Dawant, B. M., and Lorenz, C., editors, *Biomedical Image Registration*, volume 6204 of *Lecture Notes in Computer Science*, pages 72–82. Springer Berlin Heidelberg.
- Kotsas, P. and Dodd, T. (2011). Rigid registration of medical images using 1d and 2d binary projections. *Journal of Digital Imaging*, 24(5):913–925.
- Kubecka, L. and Jan, J. (2004). Registration of bimodal retinal images - improving modifications. In *26th Annual International Conference of the IEEE Engineering in Medicine and Biology Society, 2004. IEMBS '04*, volume 1, pages 1695–1698.
- Laliberte, F., Gagnon, L., and Sheng, Y. (2003). Registration and fusion of retinal images-an evaluation study. *IEEE Transactions on Medical Imaging*, 22(5):661–673.
- Legg, P. A., Rosin, P. L., Marshall, D., and Morgan, J. E. (2007). Improving accuracy and efficiency of registration by mutual information using Sturges’ histogram rule. In *11th Annual Conference in Medical Image Understanding and Analysis*, pages 26 – 30.
- Legg, P. A., Rosin, P. L., Marshall, D., and Morgan, J. E. (2008). Incorporating neighbourhood feature derivatives with mutual information to improve accuracy of multi-modal image registration. In *Medical Image Understanding and Analysis*, pages 39–43.

- Legg, P. A., Rosin, P. L., Marshall, D., and Morgan, J. E. (2009). A Robust Solution to Multi-modal Image Registration by Combining Mutual Information with Multi-scale Derivatives. In Yang, G.-Z., Hawkes, D., Rueckert, D., Noble, A., and Taylor, C., editors, *Medical Image Computing and Computer-Assisted Intervention – MICCAI 2009*, volume 5761 of *Lecture Notes in Computer Science*, pages 616–623. Springer Berlin Heidelberg.
- Legg, P. A., Rosin, P. L., Marshall, D., and Morgan, J. E. (2013). Improving accuracy and efficiency of mutual information for multi-modal retinal image registration using adaptive probability density estimation. *Computerized Medical Imaging and Graphics*, 37(7–8):597–606.
- Legg, P. A., Rosin, P. L., Marshall, D., and Morgan, J. E. (2015). Feature Neighbourhood Mutual Information for multi-modal image registration: An application to eye fundus imaging. *Pattern Recognition*, 48(6):1937–1946.
- Lehmann, T. M., Gonner, C., and Spitzer, K. (1999). Survey: interpolation methods in medical image processing. *IEEE Transactions on Medical Imaging*, 18(11):1049–1075.
- Lemieux, L., Jagoe, R., Fish, D. R., Kitchen, N. D., and Thomas, D. G. T. (1994). A patient-to-computed-tomography image registration method based on digitally reconstructed radiographs. *Medical Physics*, 21(11):1749–1760.
- Leng, C., Xiao, J., Li, M., and Zhang, H. (2015). Robust Adaptive Principal Component Analysis Based on Intergraph Matrix for Medical Image Registration. *Computational Intelligence and Neuroscience*, 2015:1–7.

- Leondes, C. T. (2005). *Medical Imaging Systems Technology: Methods in cardiovascular and brain systems*. World Scientific.
- Lester, H. and Arridge, S. R. (1999). A survey of hierarchical non-linear medical image registration. *Pattern Recognition*, 32(1):129–149.
- Li, H. and Chutatape, O. (2004). Automated feature extraction in color retinal images by a model based approach. *IEEE Transactions on Biomedical Engineering*, 51(2):246–254.
- Li, J., Wu, K., Zhang, X., and Ding, M. (2012). Image quality assessment based on multi-channel regional mutual information. *AEU - International Journal of Electronics and Communications*, 66(9):784–787.
- Likar, B. and Pernuš, F. (2001). A hierarchical approach to elastic registration based on mutual information. *Image and Vision Computing*, 19(1–2):33–44.
- Linton, O. W. (1995). Medical applications of x-rays. *SLAC Beam Line*, 25(2):25–34.
- Liu, D., Hua, K., and Sugaya, K. (2008). A Generic Framework for Internet-Based Interactive Applications of High-Resolution 3-D Medical Image Data. *IEEE Transactions on Information Technology in Biomedicine*, 12(5):618–626.
- Liu, L., Zhao, L., Long, Y., Kuang, G., and Fieguth, P. (2012). Extended local binary patterns for texture classification. *Image and Vision Computing*, 30(2):86–99.

- Loeckx, D., Slagmolen, P., Maes, F., Vandermeulen, D., and Suetens, P. (2007). Nonrigid Image Registration Using Conditional Mutual Information. In Karssemeijer, N. and Lelieveldt, B., editors, *Information Processing in Medical Imaging*, volume 4584 of *Lecture Notes in Computer Science*, pages 725–737. Springer Berlin Heidelberg.
- Loeckx, D., Slagmolen, P., Maes, F., Vandermeulen, D., and Suetens, P. (2010). Nonrigid Image Registration Using Conditional Mutual Information. *IEEE Transactions on Medical Imaging*, 29(1):19–29.
- Loi, G., Dominiotto, M., Manfreda, I., Mones, E., Carriero, A., Inglese, E., Krenqli, M., and Brambilla, M. (2008). Acceptance Test of a Commercially Available Software for Automatic Image Registration of Computed Tomography (CT), Magnetic Resonance Imaging (MRI) And 99mtc-methoxyisobutylisonitrile (MIBI) Single-Photon Emission Computed Tomography (SPECT) Brain Images. *Journal of Digital Imaging*, 21(3):329–337.
- Lowe, D. G. (2004). Distinctive Image Features from Scale-Invariant Keypoints. *International Journal of Computer Vision*, 60(2):91–110.
- Lu, Z. and Chen, W. (2007). Fast and Robust 3-D Image Registration Algorithm Based on Principal Component Analysis. In *The 1st International Conference on Bioinformatics and Biomedical Engineering, 2007. ICBBE 2007*, pages 872–875.

- Luan, H., Qi, F., and Shen, D. (2005). Multi-modal Image Registration by Quantitative-Qualitative Measure of Mutual Information (Q-MI). In Liu, Y., Jiang, T., and Zhang, C., editors, *Computer Vision for Biomedical Image Applications*, volume 3765 of *Lecture Notes in Computer Science*, pages 378–387. Springer Berlin Heidelberg.
- Luan, H., Qi, F., Xue, Z., Chen, L., and Shen, D. (2008). Multimodality image registration by maximization of quantitative-qualitative measure of mutual information. *Pattern Recogn.*, 41(1):285–298.
- Lyon, D. A. (1999). *Image Processing in Java*. Prentice Hall.
- Ma, B., Hero, A., Gorman, J., and Michel, O. (2000). Image registration with minimum spanning tree algorithm. In *2000 International Conference on Image Processing, 2000. Proceedings*, volume 1, pages 481–484 vol.1.
- Maeland, E. (1988). On the comparison of interpolation methods. *IEEE Transactions on Medical Imaging*, 7(3):213–217.
- Maes, F., Collignon, A., Vandermeulen, D., Marchal, G., and Suetens, P. (1997). Multimodality image registration by maximization of mutual information. *IEEE Transactions on Medical Imaging*, 16(2):187–198.
- Maes, F., Vandermeulen, D., and Suetens, P. (1999). Comparative evaluation of multiresolution optimization strategies for multimodality image registration by maximization of mutual information. *Medical Image Analysis*, 3(4):373–386.
- Maintz, J. and Viergever, M. A. (1998). A survey of medical image registration. *Medical Image Analysis*, 2(1):1–36.

- Maintz, J. A., Meijering, E. H., and Viergever, M. A. (1998). General multimodal elastic registration based on mutual information. In *Medical Imaging'98*, pages 144–154. International Society for Optics and Photonics.
- Maitra, S. (1979). Moment invariants. *Proceedings of the IEEE*, 67(4):697–699.
- Manduchi, R. and Mian, G. A. (1993). Accuracy analysis for correlation-based image registration algorithms. In , *ISCAS '93, 1993 IEEE International Symposium on Circuits and Systems, 1993*, pages 834–837 vol.1.
- Marrugo, A. G. and Millán, M. S. (2011). Retinal image analysis: preprocessing and feature extraction. *Journal of Physics: Conference Series*, 274(1):012039.
- Martín-Merino, E., Fortuny, J., Rivero-Ferrer, E., and García-Rodríguez, L. A. (2014). Incidence of Retinal Complications in a Cohort of Newly Diagnosed Diabetic Patients. *PLoS ONE*, 9(6):e100283.
- Mathworks (n.d.). Matlab - mathworks united kingdom. [Online]. Available at <http://uk.mathworks.com/> (Accessed 1st August 2014).
- Mazur, A. K., Mazur, E. J., and Gordon, R. (1993). Digital differential radiography (DDR): a new diagnostic procedure for locating neoplasms, such as breast cancers, in soft, deformable tissues. *Proceedings of SPIE*, 1905(1):443–455.
- mei Chen, H. and Varshney, P. K. (2003). Mutual information-based CT-MR brain image registration using generalized partial volume joint histogram estimation. *IEEE Transactions on Medical Imaging*, 22(9):1111–1119.

- Meijering, E. H. W., Niessen, W. J., Pluim, J. P. W., and Viergever, M. A. (1999). Quantitative Comparison of Sinc-Approximating Kernels for Medical Image Interpolation. In Taylor, C. and Colchester, A., editors, *Medical Image Computing and Computer-Assisted Intervention – MICCAI’99*, volume 1679 of *Lecture Notes in Computer Science*, pages 210–217. Springer Berlin Heidelberg.
- Meyer, C. R., Boes, J. L., Kim, B., and Bland, P. H. (1999). Probabilistic Brain Atlas Construction: Thin-Plate Spline Warping via Maximization of Mutual Information. In Taylor, C. and Colchester, A., editors, *Medical Image Computing and Computer-Assisted Intervention – MICCAI’99*, volume 1679 of *Lecture Notes in Computer Science*, pages 631–637. Springer Berlin Heidelberg.
- Meyer, C. R., Boes, J. L., Kim, B., Bland, P. H., Zasadny, K. R., Kison, P. V., Koral, K., Frey, K. A., and Wahl, R. L. (1997). Demonstration of accuracy and clinical versatility of mutual information for automatic multimodality image fusion using affine and thin-plate spline warped geometric deformations. *Medical Image Analysis*, 1(3):195–206.
- Meyer, J. (2007). *IMRT, IGRT, SBRT: Advances in the Treatment Planning and Delivery of Radiotherapy*. Karger Medical and Scientific Publishers.
- Miga, M. I. (2003). A new approach to elastography using mutual information and finite elements. *Physics in Medicine and Biology*, 48(4):467–480.
- Milios, E. E. (1988). Shape matching using curvature processes. In *1988 International Conference on Acoustics, Speech, and Signal Processing, ICASSP-88*, pages 960–963 vol.2.

- Modersitzki, J. (2004). *Numerical Methods for Image Registration*. Oxford University Press, Oxford ; New York.
- Moigne, J. L., Netanyahu, N. S., and Eastman, R. D. (2011). *Image Registration for Remote Sensing*. Cambridge University Press.
- Molga, M. and Smutnicki, C. (2005). Test functions for optimization needs. [Online]. Available at http://eccsia013.googlecode.com/svn/trunk/Ecc1/functions_benchmark.pdf (Accessed 10th August 2014).
- Montreal Neurological Institute and Hospital (2000). \emph{BrainWeb: Simulated Brain Database}.
- Montreal Neurological Institute and Hospital (n.d.). Brainweb: Simulated brain database. [Online]. Available at <http://brainweb.bic.mni.mcgill.ca/brainweb/> (Accessed 11th December 2014).
- Moses, C. J., Selvathi, D., Beena, J. P., and Rani, S. S. (2011). FPGA accelerated partial volume interpolation. In *2011 International Conference on Emerging Trends in Electrical and Computer Technology (ICETECT)*, pages 816–819.
- Moshfeghi, M. (1991). Elastic matching of multimodality medical images. *CVGIP: Graphical Models and Image Processing*, 53(3):271–282.

- Murphy, K., van Ginneken, B., Reinhardt, J. M., Kabus, S., Ding, K., Deng, X., Cao, K., Du, K., Christensen, G. E., Garcia, V., Vercauteren, T., Ayache, N., Commowick, O., Malandain, G., Glocker, B., Paragios, N., Navab, N., Gorbunova, V., Sporring, J., de Bruijne, M., Han, X., Heinrich, M. P., Schnabel, J. A., Jenkinson, M., Lorenz, C., Modat, M., McClelland, J. R., Ourselin, S., Muenzing, S. E. A., Viergever, M. A., De Nigris, D., Collins, D. L., Arbel, T., Peroni, M., Li, R., Sharp, G. C., Schmidt-Richberg, A., Ehrhardt, J., Werner, R., Smeets, D., Loeckx, D., Song, G., Tustison, N., Avants, B., Gee, J. C., Staring, M., Klein, S., Stoel, B. C., Urschler, M., Werlberger, M., Vandemeulebroucke, J., Rit, S., Sarrut, D., and Pluim, J. P. W. (2011). Evaluation of registration methods on thoracic CT: the EMPIRE10 challenge. *IEEE transactions on medical imaging*, 30(11):1901–1920.
- Nam, H., Renaut, R. A., Chen, K., Guo, H., and Farin, G. E. (2009). Improved inter-modality image registration using normalized mutual information with coarse-binned histograms. *Communications in Numerical Methods in Engineering*, 25(6):583–595.
- Neemuchwala, H., Hero, A., Carson, P., and Meyer, C. (2004). Local feature matching using entropic graphs. In *IEEE International Symposium on Biomedical Imaging: Nano to Macro, 2004*, pages 704–707 Vol. 1.
- Neri, E., Caramella, D., Bartolozzi, C., Baert, A. L., Knauth, M., and Sartor, K., editors (2008). *Image Processing in Radiology*. Medical Radiology. Springer Berlin Heidelberg.

- Netsch, T., Rosch, P., van Muiswinkel, A., and Weese, J. (2001). Towards real-time multi-modality 3-D medical image registration. In *Eighth IEEE International Conference on Computer Vision, 2001. ICCV 2001. Proceedings*, volume 1, pages 718–725 vol.1.
- Ng, W. S., Legg, P., Avadhanam, V., Aye, K., Evans, S. H. P., North, R. V., Marshall, A. D., Rosin, P., and Morgan, J. E. (2015). Automated Registration of Multimodal Optic Disc Images: Clinical Assessment of Alignment Accuracy. *Journal of Glaucoma*, pages 1–12.
- NHS England Analytical Services (2014). Diagnostic Imaging Dataset 2013-14 Data (Annual Statistical Release DID). Annual Statistical Release 2013/14 1, NHS, England.
- NHS England Analytical Services (2015). Diagnostic Imaging Dataset Statistical Release. Provisional monthly experimental statistics, February 2014 to February 2015 1, NHS, England.
- Noël, L. and Biri, V. (2015). Portal Extraction Based on an Opening Labeling for Ray Tracing. In Benediktsson, J. A., Chanussot, J., Najman, L., and Talbot, H., editors, *Mathematical Morphology and Its Applications to Signal and Image Processing*, volume 9082 of *Lecture Notes in Computer Science*, pages 27–38. Springer International Publishing.
- Nordenskjöld, R., Larsson, E.-M., Ahlström, H., Johansson, L., and Kullberg, J. (2014). Automated interhemispheric surface extraction in T1-weighted MRI using intensity and symmetry information. *Journal of Neuroscience Methods*, 222:97–105.

- Oberkampff, W. L. and Roy, C. J. (2010). *Verification and Validation in Scientific Computing*. Cambridge University Press, New York.
- Oliveira, F. and Tavares, J. (2014). Medical image registration: a review. *COMPUTER METHODS IN BIOMECHANICS AND BIOMEDICAL ENGINEERING*, 17(2):73–93.
- Olver, F. W., Lozier, D. W., Boisvert, R. F., and Clark, C. W. (2010). *NIST Handbook of Mathematical Functions*. Cambridge University Press, New York, NY, USA, 1st edition.
- Pan, M.-S., Yang, X.-L., and Tang, J.-T. (2012). Research on Interpolation Methods in Medical Image Processing. *Journal of Medical Systems*, 36(2):777–807.
- Paragios, N., Duncan, J., and Ayache, N., editors (2015). *Handbook of Biomedical Imaging*. Springer US, Boston, MA.
- Parmehr, E., Fraser, C., Zhang, C., and Leach, J. (2013). An effective histogram binning for mutual information based registration of optical imagery and 3d LiDAR data. In *2013 20th IEEE International Conference on Image Processing (ICIP)*, pages 1286–1290.
- Pascau, J. and Mateos, J. M. (2013). *Image Processing with Imagej*. Packt Publishing.
- Patankar, S. S. and Kulkarni, J. V. (2015). Orthogonal moments for determining correspondence between vessel bifurcations for retinal image registration. *Computer Methods and Programs in Biomedicine*, 119(3):121–141.

- Peng, H., Long, F., and Ding, C. (2005). Feature selection based on mutual information criteria of max-dependency, max-relevance, and min-redundancy. *IEEE Transactions on Pattern Analysis and Machine Intelligence*, 27(8):1226–1238.
- Penney, G. P., Weese, J., Little, J. A., Desmedt, P., Hill, D. L., and Hawkes, D. J. (1998). A comparison of similarity measures for use in 2-D-3-D medical image registration. *IEEE Transactions on Medical Imaging*, 17(4):586–595.
- Pereira, C., Martins, N., Goncalves, L., and Ferreira, M. (2012). Registration of retinal images by a MAS-ICP approach - A preliminary study. In *Bioengineering (ENBENG), 2012 IEEE 2nd Portuguese Meeting in*, pages 1–4.
- Pham, D. L. and Prince, J. L. (1999). An adaptive fuzzy c-means algorithm for image segmentation in the presence of intensity inhomogeneities. *Pattern Recognition Letters*, 20(1):57–68.
- Pietikäinen, M., Hadid, A., Zhao, G., and Ahonen, T. (2011). *Computer Vision Using Local Binary Patterns*, volume 40 of *Computational Imaging and Vision*. Springer London.
- Pilutti, D., Strumia, M., and Hadjide metriou, S. (2014). Bimodal Nonrigid Registration of Brain MRI Data With Deconvolution of Joint Statistics. *IEEE Transactions on Image Processing*, 23(9):3999–4009.
- Pluim, J., Maintz, J., and Viergever, M. (2003). Mutual-information-based registration of medical images: a survey. *IEEE Transactions on Medical Imaging*, 22(8):986–1004.

- Pluim, J. P., Maintz, J. B., and Viergever, M. A. (2000a). Image registration by maximization of combined mutual information and gradient information. *IEEE Transactions on Medical Imaging*, 19(8):809–814.
- Pluim, J. P. W., Maintz, J. B. A., and Viergever, M. A. (2000b). Interpolation artefacts in mutual information-based image registration. *Comput. Vis. Image Underst.*, 77(9):211–232.
- Pradhan, S. and Patra, D. (2013). P-spline based nonrigid brain MR image registration using regional mutual information. In *2013 Annual IEEE India Conference (INDICON)*, pages 1–5.
- Pradhan, S. and Patra, D. (2015). RMI based non-rigid image registration using BF-QPSO optimization and P-spline. *AEU - International Journal of Electronics and Communications*, 69(3):609–621.
- Press, W. H., Teukolsky, S. A., Vetterling, W. T., and Flannery, B. P. (2007). *Numerical Recipes 3rd Edition: The Art of Scientific Computing*. Cambridge University Press, 3 edition.
- Price, K. E. (1985). Relaxation Matching Techniques-A Comparison. *IEEE Transactions on Pattern Analysis and Machine Intelligence*, PAMI-7(5):617–623.
- Ravi, K. and Palaniappan, R. (2005). Leave-one-out Authentication of Persons Using 40 Hz EEG Oscillations. In *The International Conference on Computer as a Tool, EUROCON 2005*, volume 2, pages 1386–1389.
- Razlighi, Q. R., Kehtarnavaz, N., and Yousefi, S. (2013). Evaluating similarity measures for brain image registration. *Journal of Visual Communication and Image Representation*, 24(7):977–987.

- Reel, P. S., Dooley, L. S., Wong, K., and Börner, A. (2014a). Enhanced retinal image registration accuracy using expectation maximisation and variable bin-sized mutual information. In *2014 IEEE International Conference on Acoustics, Speech and Signal Processing (ICASSP)*, pages 6632–6636, Florence, Italy.
- Reel, P. S., Dooley, L. S., and Wong, K. C. P. (2012a). Efficient Image Registration using Fast Principal Component Analysis. In *19th IEEE International Conference on Image Processing (ICIP 2012)*, IEEE, 2012, pages 1661–1664, Lake Buena Vista, Orlando, Florida, USA.
- Reel, P. S., Dooley, L. S., and Wong, K. C. P. (2012b). A new mutual information based similarity measure for medical image registration. In *IET Conference on Image Processing (IPR 2012)*, pages 1–6, London, UK.
- Reel, P. S., Dooley, L. S., Wong, K. C. P., and Börner, A. (2013a). Fast EM Principal Component Analysis Image Registration Using Neighbourhood Pixel Connectivity. In Wilson, R., Hancock, E., Bors, A., and Smith, W., editors, *Computer Analysis of Images and Patterns*, volume 8047 of *Lecture Notes in Computer Science*, pages 270–277. Springer Berlin Heidelberg.
- Reel, P. S., Dooley, L. S., Wong, K. C. P., and Börner, A. (2013b). Multimodal retinal image registration using a fast principal component analysis hybrid-based similarity measure. In *20th International Conference on Image Processing (ICIP)*, pages 1428–1432.

- Reel, P. S., Dooley, L. S., Wong, K. C. P., and Börner, A. (2013c). Robust retinal image registration using expectation maximisation with mutual information. In *2013 IEEE International Conference on Acoustics, Speech and Signal Processing (ICASSP)*, pages 1118–1122, Vancouver, BC, Canada.
- Reel, P. S., Dooley, L. S., Wong, K. C. P., and Börner, A. (2014b). Robust Image Registration using Adaptive Expectation Maximisation based PCA. In *2014 IEEE Visual Communications and Image Processing Conference*, pages 105–108, Valletta, Malta.
- Rencher, A. C. (1998). *Multivariate statistical inference and applications*. Wiley.
- Rezaei, H., Azadi, S., and Ghorbani, M. (2009). A Hybrid Particle Swarm Steepest Gradient Algorithm for Elastic Brain Image Registration. In *Second International Conference on Machine Vision, 2009. ICMV '09*, pages 54–58.
- Rios, L. M. and Sahinidis, N. V. (2012). Derivative-free optimization: a review of algorithms and comparison of software implementations. *Journal of Global Optimization*, 56(3):1247–1293.
- Ritter, N., Owens, R., Cooper, J., Eikelboom, R., and Van Saarloos, P. (1999). Registration of stereo and temporal images of the retina. *IEEE Transactions on Medical Imaging*, 18(5):404–418.
- Roche, A., Malandain, G., Pennec, X., and Ayache, N. (1998). The Correlation Ratio as a New Similarity Measure for Multimodal Image Registration. In *Proceedings of the First International Conference on Medical Image Computing and Computer-Assisted Intervention, MICCAI '98*, pages 1115–1124, London, UK. Springer-Verlag.

- Rodrigues, M. A. (2000). *Invariants for pattern recognition and classification*, volume 42. World Scientific.
- Rodriguez-Carranza, C. E. and Loew, M. H. (1998). Weighted and deterministic entropy measure for image registration using mutual information. *Proceedings of SPIE*, 3338(1):155–166.
- Rogelj, P. (2001). Similarity measures for nonrigid registration. volume 4322, pages 569–578. SPIE.
- Rogelj, P. and Kovačič, S. (2003). Point Similarity Measure Based on Mutual Information. In Gee, J. C., Maintz, J. B. A., and Vannier, M. W., editors, *Bio-medical Image Registration*, volume 2717 of *Lecture Notes in Computer Science*, pages 112–121. Springer Berlin Heidelberg.
- Rohlfing, T. (2012). Image similarity and tissue overlaps as surrogates for image registration accuracy: widely used but unreliable. *IEEE Transactions on Medical Imaging*, 31(2):153–163.
- Rohlfing, T., Maurer, C. R., Bluemke, D. A., and Jacobs, M. A. (2003). Volume-preserving nonrigid registration of MR breast images using free-form deformation with an incompressibility constraint. *IEEE Transactions on Medical Imaging*, 22(6):730–741.
- Roweis, S. (1998). EM algorithms for PCA and SPCA. In *Proceedings of the 1997 conference on Advances in neural information processing systems 10*, NIPS '97, pages 626–632, Cambridge, MA, USA. MIT Press.

- Roy, S., Liang, X., Kitamoto, A., Tamura, M., Shiroishi, T., and Brown, M. S. (2013). Phenotype Detection in Morphological Mutant Mice Using Deformation Features. In Mori, K., Sakuma, I., Sato, Y., Barillot, C., and Navab, N., editors, *Medical Image Computing and Computer-Assisted Intervention – MICCAI 2013*, volume 8151 of *Lecture Notes in Computer Science*, pages 437–444. Springer Berlin Heidelberg.
- Rueckert, D., Clarkson, M. J., Hill, D. L. G., and Hawkes, D. J. (2000). Non-rigid registration using higher-order mutual information. *Proceedings of SPIE*, 3979(1):438–447.
- Rueckert, D., Sonoda, L., Hayes, C., Hill, D., Leach, M., and Hawkes, D. (1999). Nonrigid registration using free-form deformations: application to breast MR images. *IEEE Transactions on Medical Imaging*, 18(8):712 –721.
- Russakoff, D. B., Rohlfing, T., Ho, A., Kim, D. H., Shahidi, R., Jr, J. R. A., and Jr, C. R. M. (2003). Evaluation of Intensity-Based 2d-3d Spine Image Registration Using Clinical Gold-Standard Data. In Gee, J. C., Maintz, J. B. A., and Vannier, M. W., editors, *Biomedical Image Registration*, volume 2717 of *Lecture Notes in Computer Science*, pages 151–160. Springer Berlin Heidelberg.
- Russakoff, D. B., Tomasi, C., Rohlfing, T., and Calvin R. Maurer Jr (2004). Image Similarity Using Mutual Information of Regions. In Pajdla, T. and Matas, J., editors, *Computer Vision - ECCV 2004*, volume 3023 of *Lecture Notes in Computer Science*, pages 596–607. Springer Berlin Heidelberg.

- Ryan, N., Heneghan, C., and de Chazal, P. (2004). Registration of digital retinal images using landmark correspondence by expectation maximization. *Image and Vision Computing*, 22(11):883–898.
- Saad, Y. (2011). 6. Krylov Subspace Methods. In *Numerical Methods for Large Eigenvalue Problems*, Classics in Applied Mathematics, pages 125–162. Society for Industrial and Applied Mathematics.
- Saine, P. J. (1993). Landmarks in the historical development of fluorescein angiography. *The Journal of Ophthalmic Photography*, 15(1):17–23.
- Saine, P. J. and Tyler, M. E. (2002). *Ophthalmic photography : retinal photography, angiography, and electronic imaging*. Butterworth-Heinemann, Boston.
- Sanchez-Galeana, C., Bowd, C., Blumenthal, E. Z., Gokhale, P. A., Zangwill, L. M., and Weinreb, R. N. (2001). Using optical imaging summary data to detect glaucoma. *Ophthalmology*, 108(10):1812–1818.
- Schneider, G., Prince, M., Meaney, J., and Ho, V., editors (2005). *Magnetic Resonance Angiography: Techniques, Indications and Practical Applications*. Springer, 1 edition.
- Scott, D. W. (1979). On Optimal and Data-Based Histograms. *Biometrika*, 66(3):605–610.
- Scott, D. W. (1992). *Multivariate Density Estimation*. Wiley, New York.
- Shams, R., Sadeghi, P., Kennedy, R., and Hartley, R. (2010). A Survey of Medical Image Registration on Multicore and the GPU. *IEEE Signal Processing Magazine*, 27(2):50–60.

- Shannon, C. E. (1948). The mathematical theory of communication. 1963. *MD computing computers in medical practice*, 14(4):306–17.
- Shekhar, R., Zagrodsky, V., Castro-Pareja, C. R., Walimbe, V., and Jagadeesh, J. M. (2003). High-Speed Registration of Three- and Four-dimensional Medical Images by Using Voxel Similarity1. *Radiographics*, 23(6):1673–1681.
- Sherrow, V. (2006). *Medical Imaging*. Marshall Cavendish.
- Shi, J. and Reichenbach, S. E. (2006). Image interpolation by two-dimensional parametric cubic convolution. *IEEE Transactions on Image Processing*, 15(7):1857–1870.
- Shi, L., Liu, W., Zhang, H., Xie, Y., and Wang, D. (2012). A survey of GPU-based medical image computing techniques. *Quantitative Imaging in Medicine and Surgery*, 2(3):188–206.
- Sim, D. A., Keane, P. A., Tufail, A., Egan, C. A., Aiello, L. P., and Silva, P. S. (2015). Automated Retinal Image Analysis for Diabetic Retinopathy in Telemedicine. *Current Diabetes Reports*, 15(3):1–9.
- Simmons, A., Tofts, P. S., Barker, G. J., and Arridge, S. R. (1994). Sources of intensity nonuniformity in spin echo images at 1.5 T. *Magnetic resonance in medicine: official journal of the Society of Magnetic Resonance in Medicine / Society of Magnetic Resonance in Medicine*, 32(1):121–128.
- Skerl, D., Likar, B., and Pernus, F. (2006). A protocol for evaluation of similarity measures for rigid registration. *IEEE Transactions on Medical Imaging*, 25(6):779–791.

- Skerl, D., Likar, B., and Pernus, F. (2008). A protocol for evaluation of similarity measures for non-rigid registration. *Medical Image Analysis*, 12(1):42–54.
- Skokan, M., Skoupy, A., and Jan, J. (2002). Registration of multimodal images of retina. In *Engineering in Medicine and Biology, 2002. 24th Annual Conference and the Annual Fall Meeting of the Biomedical Engineering Society EMBS/BMES Conference, 2002. Proceedings of the Second Joint*, volume 2, pages 1094 – 1096 vol.2.
- Sled, J. (2015). Intensity nonuniformity correction. In Toga, A. W., editor, *Brain Mapping*, pages 295 – 299. Academic Press, Waltham.
- Sled, J. G. and Pike, G. B. (1998). Understanding intensity non-uniformity in MRI. In Wells, W. M., Colchester, A., and Delp, S., editors, *Medical Image Computing and Computer-Assisted Intervention — MICCAI’98*, volume 1496 of *Lecture Notes in Computer Science*, pages 614–622. Springer Berlin Heidelberg.
- Sofka, M. and Stewart, C. (2006). Retinal Vessel Centerline Extraction Using Multiscale Matched Filters, Confidence and Edge Measures. *IEEE Transactions on Medical Imaging*, 25(12):1531 –1546.
- Soleimani, H. and Khosravifard, M. A. (2011). Reducing interpolation artifacts for mutual information based image registration. *Journal of Medical Signals and Sensors*, 1(3):177–183.
- Spall, J. C. (1992). Multivariate stochastic approximation using a simultaneous perturbation gradient approximation. *IEEE Transactions on Automatic Control*, 37(3):332–341.

- Staal, J., Abramoff, M., Niemeijer, M., Viergever, M., and van Ginneken, B. (2004). Ridge-based vessel segmentation in color images of the retina. *IEEE Transactions on Medical Imaging*, 23(4):501–509.
- Stewart, C., Tsai, C.-L., and Roysam, B. (2003). The dual-bootstrap iterative closest point algorithm with application to retinal image registration. *IEEE Transactions on Medical Imaging*, 22(11):1379–1394.
- Stögbauer, H., Kraskov, A., Astakhov, S. A., and Grassberger, P. (2004). Least-dependent-component analysis based on mutual information. *Physical Review E*, 70(6):066123.
- Stollberger, R. and Wach, P. (1996). Imaging of the active b1 field in vivo. *Magnetic Resonance in Medicine*, 35(2):246–251.
- Studholme, C., Drapaca, C., Iordanova, B., and Cardenas, V. (2006). Deformation-based mapping of volume change from serial brain MRI in the presence of local tissue contrast change. *IEEE Transactions on Medical Imaging*, 25(5):626–639.
- Studholme, C., Hawkes, D. J., and Hill, D. L. (1998). Normalized entropy measure for multimodality image alignment. *Proceedings of SPIE*, 3338(1):132–143.
- Studholme, C., Hill, D., and Hawkes, D. (1996a). Automated 3-D registration of MR and CT images of the head. *Medical Image Analysis*, 1(2):163–175.
- Studholme, C., Hill, D. L., and Hawkes, D. J. (1996b). Incorporating connected region labelling into automated image registration using mutual information. In , *Proceedings of the Workshop on Mathematical Methods in Biomedical Image Analysis, 1996*, pages 23–31.

- Studholme, C., Hill, D. L., and Hawkes, D. J. (1997). Automated three-dimensional registration of magnetic resonance and positron emission tomography brain images by multiresolution optimization of voxel similarity measures. *Medical Physics*, 24(1):25–35.
- Studholme, C., Hill, D. L. G., and Hawkes, D. J. (1994). Using Voxel Similarity as a Measure of Medical Image Registration. In Hancock, Edwin R., editor, *Proceedings of the British Machine Vision Conference*, pages 23.1–23.10. BMVA Press.
- Sturges, H. A. (1926). The Choice of a Class Interval. *Journal of the American Statistical Association*, 21(153):65–66.
- Stytz, M. R., G. Frieder, and O. Frieder (1991). Three-dimensional medical imaging: Algorithms and computer systems. *ACM Computing Surveys*, 23(4):421–499.
- Suárez, E., Westin, C.-F., Rovaris, E., and Ruiz-Alzola, J. (2002). Nonrigid Registration Using Regularized Matching Weighted by Local Structure. In Dohi, Takeyoshi and Kikinis, Ron, editors, *Medical Image Computing and Computer-Assisted Intervention — MICCAI 2002*, volume 2489 of *Lecture Notes in Computer Science*, pages 581–589. Springer Berlin Heidelberg.
- T. Jackman and J.D. Webster (1886). On Photographing the Eye of the Living Human Retina. *Philadelphia Photographer*, 23:276–276.
- Tagare, H. and Rao, M. (2015). Why Does Mutual-Information Work for Image Registration? A Deterministic Explanation. *IEEE Transactions on Pattern Analysis and Machine Intelligence*, 37(6):1286–1296.

- Tang, L., Hamarneh, G., and Abugharbieh, R. (2010). Reliability-Driven, Spatially-Adaptive Regularization for Deformable Registration. In Fischer, B., Dawant, B. M., and Lorenz, C., editors, *Biomedical Image Registration*, volume 6204 of *Lecture Notes in Computer Science*, pages 173–185. Springer Berlin Heidelberg.
- Taylor, C. C. (1987). Akaike’s information criterion and the histogram. *Biometrika*, 74(3):636–639.
- Thevenaz, P., Blu, T., and Unser, M. (2000). Interpolation revisited [medical images application]. *IEEE Transactions on Medical Imaging*, 19(7):739–758.
- Thevenaz, P., Ruttimann, U. E., and Unser, M. (1995). Iterative multi-scale registration without landmarks. In , *International Conference on Image Processing, 1995. Proceedings*, volume 3, pages 228–231 vol.3.
- Thevenaz, P., Ruttimann, U. E., and Unser, M. (1998). A pyramid approach to subpixel registration based on intensity. *IEEE Transactions on Image Processing*, 7(1):27–41.
- Thevenaz, P. and Unser, M. (2000). Optimization of mutual information for multiresolution image registration. *IEEE Transactions on Image Processing*, 9(12):2083 – 2099.
- Thevenaz, P. and Unser, M. A. (1997). Spline pyramids for intermodal image registration using mutual information. *Proceedings of SPIE*, 3169(1):236–247.
- Thirion, J.-P. (1998). Image matching as a diffusion process: an analogy with Maxwell’s demons. *Medical Image Analysis*, 2(3):243–260.

- Tomazevic, D., Likar, B., and Pernus, F. (2004). Multifeature mutual information. In *Medical Imaging 2004: Image Processing*, volume 5370, pages 143–154. SPIE.
- Tsao, J. (2003). Interpolation artifacts in multimodality image registration based on maximization of mutual information. *Medical Imaging, IEEE Transactions on*, 22(7):854–864.
- Tsoi, K. H., Rueckert, D., Ho, C. H., and Luk, W. (2009). Reconfigurable acceleration of 3d image registration. In *5th Southern Conference on Programmable Logic, 2009. SPL*, pages 95–100.
- Unser, M., Aldroubi, A., and Eden, M. (1993). The L2-polynomial spline pyramid. *IEEE Transactions on Pattern Analysis and Machine Intelligence*, 15(4):364–379.
- van den Elsen, P. A., Pol, E. J., and Viergever, M. A. (1993). Medical image matching-a review with classification. *IEEE Engineering in Medicine and Biology Magazine*, 12(1):26–39.
- van der Bom, I. M. J., Klein, S., Staring, M., Homan, R., Bartels, L. W., and Pluim, J. P. W. (2011). Evaluation of optimization methods for intensity-based 2d-3d registration in x-ray guided interventions. In Dawant, B. M. and Haynor, D. R., editors, *Medical Imaging 2011: Image Processing*, volume 7962, page 796223.
- Villacampa, O. (2015). *Feature Selection and Classification Methods for Decision Making: A Comparative Analysis*. PhD thesis, College of Engineering and Computing, Nova Southeastern University.

- Viola, P. and Wells, W. M. (1995). Alignment by maximization of mutual information. In *Fifth International Conference on Computer Vision, 1995. Proceedings*, pages 16–23.
- Wang, B. and Shen, Y. (2006). A method on calculating high-dimensional mutual information and its application to registration of multiple ultrasound images. *Ultrasonics*, 44 Suppl 1:e79–83.
- Wang, M. and Lai, C.-H. (2008). *A Concise Introduction to Image Processing using C++*. CRC Press.
- Wang, T. L. and Jin, Y. Q. (2012). Postearthquake Building Damage Assessment Using Multi-Mutual Information From Pre-Event Optical Image and Postevent SAR Image. *IEEE Geoscience and Remote Sensing Letters*, 9(3):452–456.
- Wang, X. Y., Eberl, S., Fulham, M., Som, S., and Feng, D. D. (2008). 8 - Data Registration and Fusion. In Feng, D. D., editor, *Biomedical Information Technology*, Biomedical Engineering, pages 187–210. Academic Press, Burlington.
- Weese, J., Rösch, P., Netsch, T., Blaffert, T., and Quist, M. (1999). Gray-Value Based Registration of CT and MR Images by Maximization of Local Correlation. In Taylor, C. and Colchester, A., editors, *Medical Image Computing and Computer-Assisted Intervention – MICCAI’99*, volume 1679 of *Lecture Notes in Computer Science*, pages 656–663. Springer Berlin Heidelberg.

- Wells, W. M., Grimson, W. E. L., Kikinis, R., and Jolesz, F. A. (1995). *Computer Vision, Virtual Reality and Robotics in Medicine: First International Conference, CVRMed '95, Nice, France, April 3–6, 1995 Proceedings*, chapter Adaptive Segmentation of MRI Data, pages 59–69. Springer Berlin Heidelberg, Berlin, Heidelberg.
- Wells III, W. M., Viola, P., Atsumi, H., Nakajima, S., and Kikinis, R. (1996). Multi-modal volume registration by maximization of mutual information. *Medical Image Analysis*, 1(1):35–51.
- West, J., Fitzpatrick, J. M., Wang, M. Y., Dawant, B. M., Maurer, Jr, C. R., Kessler, R. M., Maciunas, R. J., Barillot, C., Lemoine, D., Collignon, A., Maes, F., Suetens, P., Vandermeulen, D., van den Elsen, P. A., Napel, S., Sumanaweera, T. S., Harkness, B., Hemler, P. F., Hill, D. L., Hawkes, D. J., Studholme, C., Maintz, J. B., Viergever, M. A., Malandain, G., and Woods, R. P. (1997). Comparison and evaluation of retrospective intermodality brain image registration techniques. *Journal of Computer Assisted Tomography*, 21(4):554–566.
- Wichard, J. D., Kuhne, R., and ter Laak, A. (2008). Binding site detection via mutual information. In *Fuzzy Systems, 2008. (IEEE World Congress on Computational Intelligence)*. *IEEE International Conference on*, pages 1770–1776.
- Wiest-Daesslé, N., Yger, P., Prima, S., and Barillot, C. (2007). Evaluation of a new optimisation algorithm for rigid registration of MRI data. In *Medical Imaging*, pages 651206–651206. International Society for Optics and Photonics.

- Wilson, D. and Laxminarayan, S. (2007). *Handbook of Biomedical Image Analysis: Volume 3: Registration Models*. Springer Science & Business Media.
- Wirth, M. A., Narhan, J., and Gray, D. W. S. (2002). Nonrigid mammogram registration using mutual information. *Proceedings of SPIE*, 4684(1):562–573.
- Wong, A. (2010). An Adaptive Monte Carlo Approach to Phase-Based Multimodal Image Registration. *IEEE Transactions on Information Technology in Biomedicine*, 14(1):173–179.
- Woo, J., Stone, M., and Prince, J. L. (2015). Multimodal Registration via Mutual Information Incorporating Geometric and Spatial Context. *IEEE Transactions on Image Processing*, 24(2):757–769.
- Woods, R. P. (2009). Chapter 33 - Validation of Registration Accuracy. In BANKMAN, I. N., editor, *Handbook of Medical Image Processing and Analysis*, pages 569–575. Academic Press, Burlington.
- Woods, R. P., Cherry, S. R., and Mazziotta, J. C. (1992). Rapid automated algorithm for aligning and reslicing PET images. *Journal of Computer Assisted Tomography*, 16(4):620–633.
- Woods, R. P., Mazziotta, J. C., and Cherry, S. R. (1993). MRI-PET registration with automated algorithm. *Journal of Computer Assisted Tomography*, 17(4):536–546.
- Wu, J., Kim, M., Peters, J., Chung, H., and Samant, S. S. (2009). Evaluation of similarity measures for use in the intensity-based rigid 2d-3d registration for patient positioning in radiotherapy. *Medical Physics*, 36(12):5391–5403.

- Wu, J. and Murphy, M. J. (2010). A neural network based 3d/3d image registration quality evaluator for the head-and-neck patient setup in the absence of a ground truth. *Medical Physics*, 37(11):5756–5764.
- Wu, Y.-T., Kanade, T., Li, C.-C., and Cohn, J. (2000). Image Registration Using Wavelet-Based Motion Model. *Int. J. Comput. Vision*, 38(2):129–152.
- Xu, J., Chutatape, O., Sung, E., Zheng, C., and Chew Tec Kuan, P. (2007). Optic disk feature extraction via modified deformable model technique for glaucoma analysis. *Pattern Recognition*, 40(7):2063–2076.
- Yang, C., Jiang, T., Wang, J., and Zheng, L. (2006). A Neighborhood Incorporated Method in Image Registration. *Image Rochester NY*, pages 244 – 251.
- Yang, F. and Fu, K. (2012). Medical Images Registration Based on Gradient Mutual Information and Improved Genetic Algorithm. In *2012 International Conference on Communication Systems and Network Technologies (CSNT)*, pages 250–253.
- Yang, J., Wang, H., Zhang, Y., and Yin, Y. (2015). Evaluation of GMI and PMI diffeomorphic-based demons algorithms for aligning PET and CT Images. *Journal of Applied Clinical Medical Physics*, 16(4).
- Yao, N., Lin, Z., and Zhang, J. (2010). Feature Selection Based on Mutual Information and Its Application in Hyperspectral Image Classification. In Bi, Y. and Williams, M.-A., editors, *Knowledge Science, Engineering and Management*, volume 6291 of *Lecture Notes in Computer Science*, pages 561–566. Springer Berlin Heidelberg.

- Yeung, F., Levinson, S. F., and Parker, K. J. (1998). Multilevel and Motion Model-Based Ultrasonic Speckle Tracking Algorithms. *Ultrasound in Medicine & Biology*, 24(3):427–441.
- Yi, Z. and Soatto, S. (2011). Multimodal registration via spatial-context mutual information. In Gábor, S. and Hahn, H., editors, *Information Processing in Medical Imaging*, volume 6801 of *Lecture Notes in Computer Science*, pages 424–435. Springer Berlin Heidelberg.
- Yin, L. S., Tang, L., Hamarneh, G., Gill, B., Celler, A., Shcherbinin, S., Fua, T. F., Thompson, A., Liu, M., Duzenli, C., Sheehan, F., and Moiseenko, V. (2010). Complexity and accuracy of image registration methods in SPECT-guided radiation therapy. *Physics in Medicine and Biology*, 55(1):237.
- Yu, H. (2005). *Automatic Rigid and Deformable Medical Image Registration*. PhD thesis, Worcester Polytechnic Institute.
- Zhang, J. and Rangarajan, A. (2005). Multimodality image registration using an extensible information metric and high dimensional histogramming. In GaryE., C. and Milan, S., editors, *Information Processing in Medical Imaging*, volume 3567 of *Lecture Notes in Computer Science*, pages 725–737. Springer Berlin Heidelberg.
- Zhang, S., Liu, Z., Liu, B., and Zhou, F. (2011). Medical image registration by using salient phase congruency and regional mutual information. In *2011 4th International Congress on Image and Signal Processing (CISP)*, volume 2, pages 760–764.

- Zhang, Y., Jiang, G.-P., Li, S.-X., Liu, Z.-X., Xie, X.-M., and Chen, W.-F. (2002). Elastic registration of medical images through multiquadric method. *Di 1 Jun Yi Da Xue Xue Bao = Academic Journal of the First Medical College of PLA*, 22(7):584–587.
- Zhao, L. and Jia, K. (2015). Deep Adaptive Log-Demons: Diffeomorphic Image Registration with Very Large Deformations. *Computational and Mathematical Methods in Medicine*, 2015:e836202.
- Zheng, G. (2010). Effective incorporating spatial information in a mutual information based 3d–2d registration of a CT volume to X-ray images. *Computerized Medical Imaging and Graphics*, 34(7):553–562.
- Zhu, Y.-M. and Cochoff, S. M. (2002). Influence of Implementation Parameters on Registration of MR and SPECT Brain Images by Maximization of Mutual Information. *Journal of Nuclear Medicine*, 43(2):160–166.
- Zhuang, X., Arridge, S., Hawkes, D. J., and Ourselin, S. (2011). A Nonrigid Registration Framework Using Spatially Encoded Mutual Information and Free-Form Deformations. *IEEE Transactions on Medical Imaging*, 30(10):1819–1828.
- Zhuang, X., Hawkes, D. J., and Ourselin, S. (2009). Unifying Encoding of Spatial Information in Mutual Information for Nonrigid Registration. In Prince, J. L., Pham, D. L., and Myers, K. J., editors, *Information Processing in Medical Imaging*, volume 5636 of *Lecture Notes in Computer Science*, pages 491–502. Springer Berlin Heidelberg.

- Zhuang, X., Hawkes, D. J., and Ourselin, S. (2010). Spatial Information Encoded Mutual Information for Nonrigid Registration. In Fischer, B., Dawant, B. M., and Lorenz, C., editors, *Biomedical Image Registration*, volume 6204 of *Lecture Notes in Computer Science*, pages 246–257. Springer Berlin Heidelberg.
- Zitová, B. and Flusser, J. (2003). Image registration methods: a survey. *Image and Vision Computing*, 21(11):977–1000.
- Zouqi, M., Samarabandu, J., and Zhou, Y. (2010). Multi-modal image registration using line features and mutual information. In *2010 17th IEEE International Conference on Image Processing (ICIP)*, pages 129–132.

Appendices

Appendix A

Initial Misregistration Scenarios

This Appendix includes the details of the initial misregistration scenarios ($\tau_{initial}$) mentioned in *Section 3.5.1* and used for mono and multimodal registration throughout this thesis. Table A.1 displays the details of twenty initial misregistration scenarios for *BrainWeb* dataset as adopted from (Kotsas and Dodd, 2011). Similarly, the five initial misregistration scenarios were used for *DRIVE*, *Brno-Mono* and *Brno-Multi* retinal datasets as adopted from (Gharabaghi et al., 2013).

Scenario No	Initial Misregistration ($\tau_{initial}$)			<i>Initial</i> RE (in pixels)
	$x_{initial}$	$y_{initial}$	$\theta_{initial}$	
1	-5.55	17.74	0.35	18.59
2	12.88	-8.11	7.09	20.42
3	10.11	27.22	-2.67	29.45
4	26.23	-13.42	8.17	32.58
5	-17.08	12.91	-14.40	38.24
6	-10.88	-11.62	-16.18	41.05
7	13.62	16.41	15.82	41.79
8	16.71	-23.55	20.60	54.13
9	-9.41	-19.11	21.37	54.70
10	29.72	2.83	24.54	63.11
11	24.21	-25.20	-25.82	67.98
12	-19.11	9.08	-28.42	70.55
13	-6.45	-20.83	-32.64	80.60
14	-26.32	0.55	33.23	82.27
15	-5.23	2.31	34.80	84.16
16	-5.65	16.94	-36.06	88.11
17	0.21	-16.41	-36.15	88.12
18	-23.64	-7.72	-37.63	92.12
19	7.20	0.23	-40.08	96.46
20	0.55	29.63	-44.71	109.25

Table A.1: Initial misregistration scenarios for the *BrainWeb* (Collins et al., 1998) dataset as in (Kotsas and Dodd, 2011).

Scenario	Initial Misregistration ($\tau_{initial}$)				Initial RE (in pixels)		
No	$x_{initial}$	$y_{initial}$	$\theta_{initial}$	$S_{initial}$	<i>DRIVE</i>	<i>Brno-Mono</i>	<i>Brno-Multi</i>
1	0	0	5	1	42.08	183.69	203.82
2	0	0	60	1	482.41	2105.64	2336.39
3	5	5	20	2.8	912.49	3982.79	4419.26
4	8	9	45	0.8	344.12	1501.72	1666.29
5	100	100	45	0.8	355.71	1503.80	1668.17

Table A.2: Initial misregistration scenarios for the retinal datasets as in (Gharabaghi et al., 2013).

Appendix B

EMPCA-MI Results for Interpolation

This Appendix includes the detailed x axis translation, y axis translation and θ rotation plots of EMPCA-MI traces as mentioned in *Section 4.3.1*. These plots show the results for nearest neighbour, bilinear and bicubic interpolation methods for mono and multimodal T1, T2 and PD image pairs from *BrainWeb* dataset having five INU and noise levels (No INU and noise, α_{20} , α_{40} , β and $\alpha_{40}+\beta$) as discussed in *Section 3.5.2*.

Figures B.1, B.2 and B.3 show the EMPCA-MI traces for monomodal T1/T1, T2/T2 and PD/PD image pairs respectively. Similarly, Figures B.4, B.5 and B.6 show the EMPCA-MI traces for multimodal T1/T2, T2/PD and PD/T1 image pairs respectively.

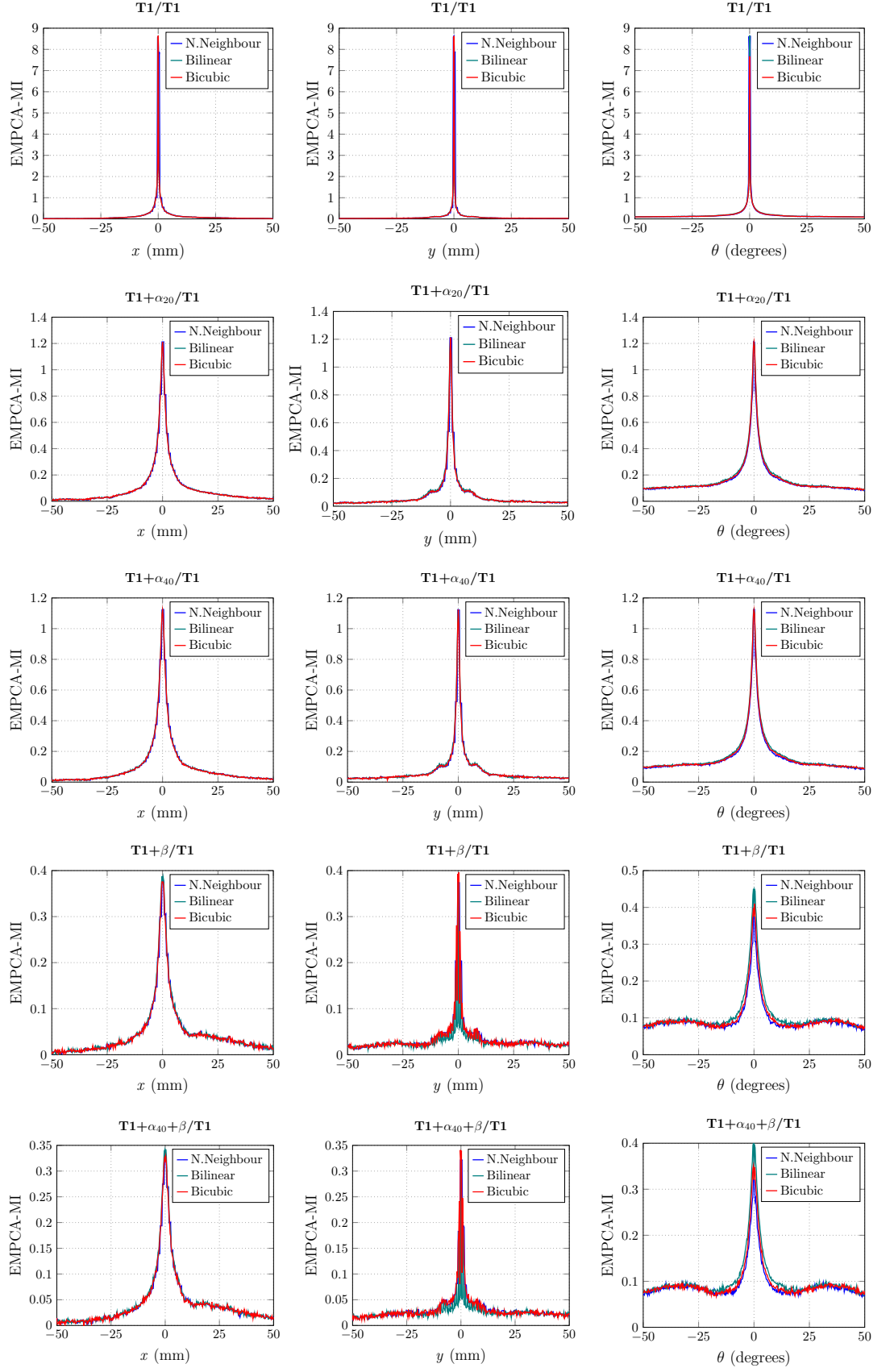


Figure B.1: EMPCA-MI Traces for monomodal $T1/T1$, $T1+\alpha_{20}/T1$, $T1+\alpha_{40}/T1$, $T1+\beta/T1$ and $T1+\alpha_{40}+\beta/T1$ image pairs for x , y translation and θ rotation.

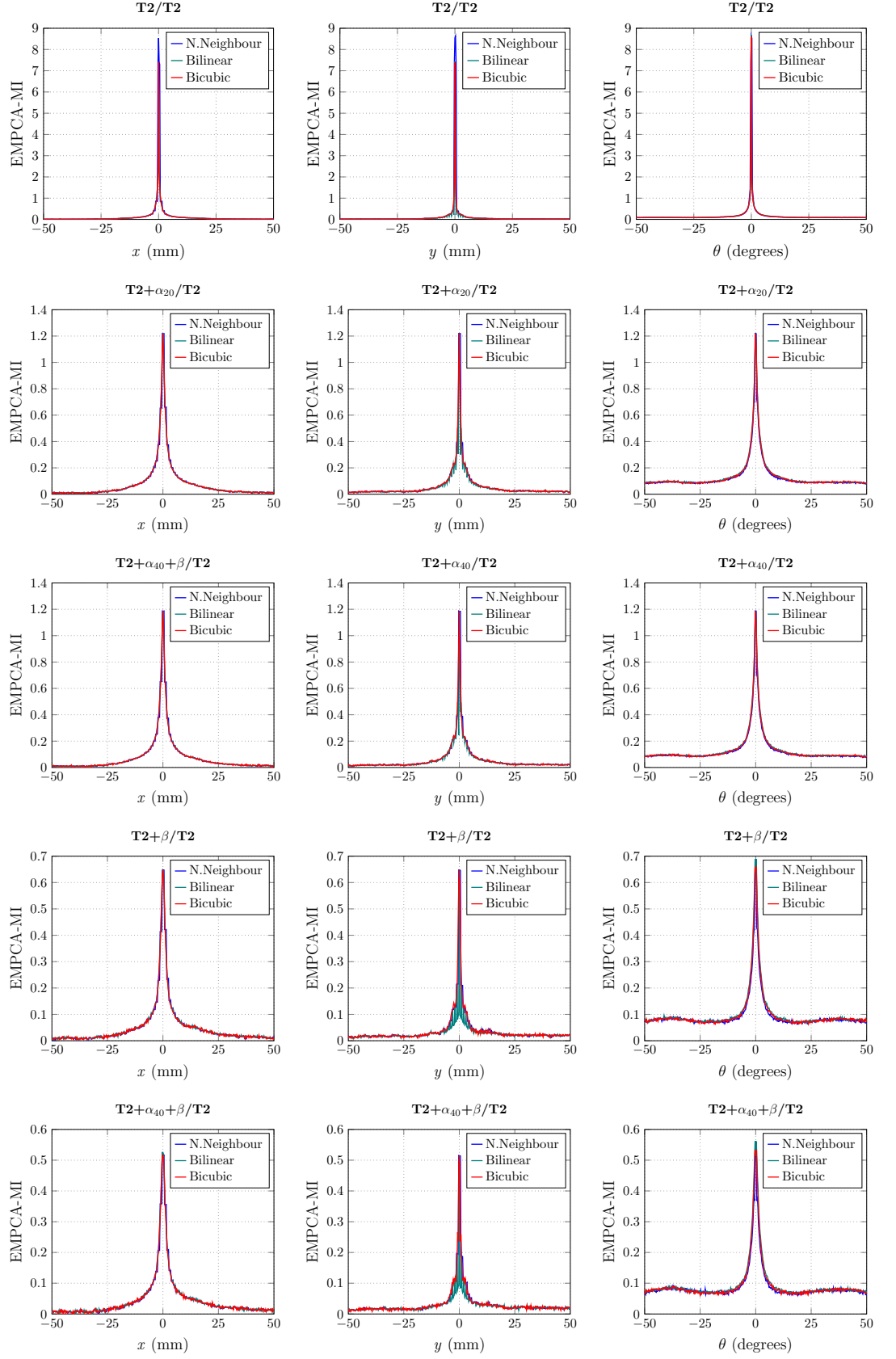


Figure B.2: EMPCA-MI Traces for monomodal $T2/T2$, $T2+\alpha_{20}/T2$, $T2+\alpha_{40}/T2$, $T2+\beta/T2$ and $T2+\alpha_{40}+\beta/T2$ image pairs for x , y translation and θ rotation.

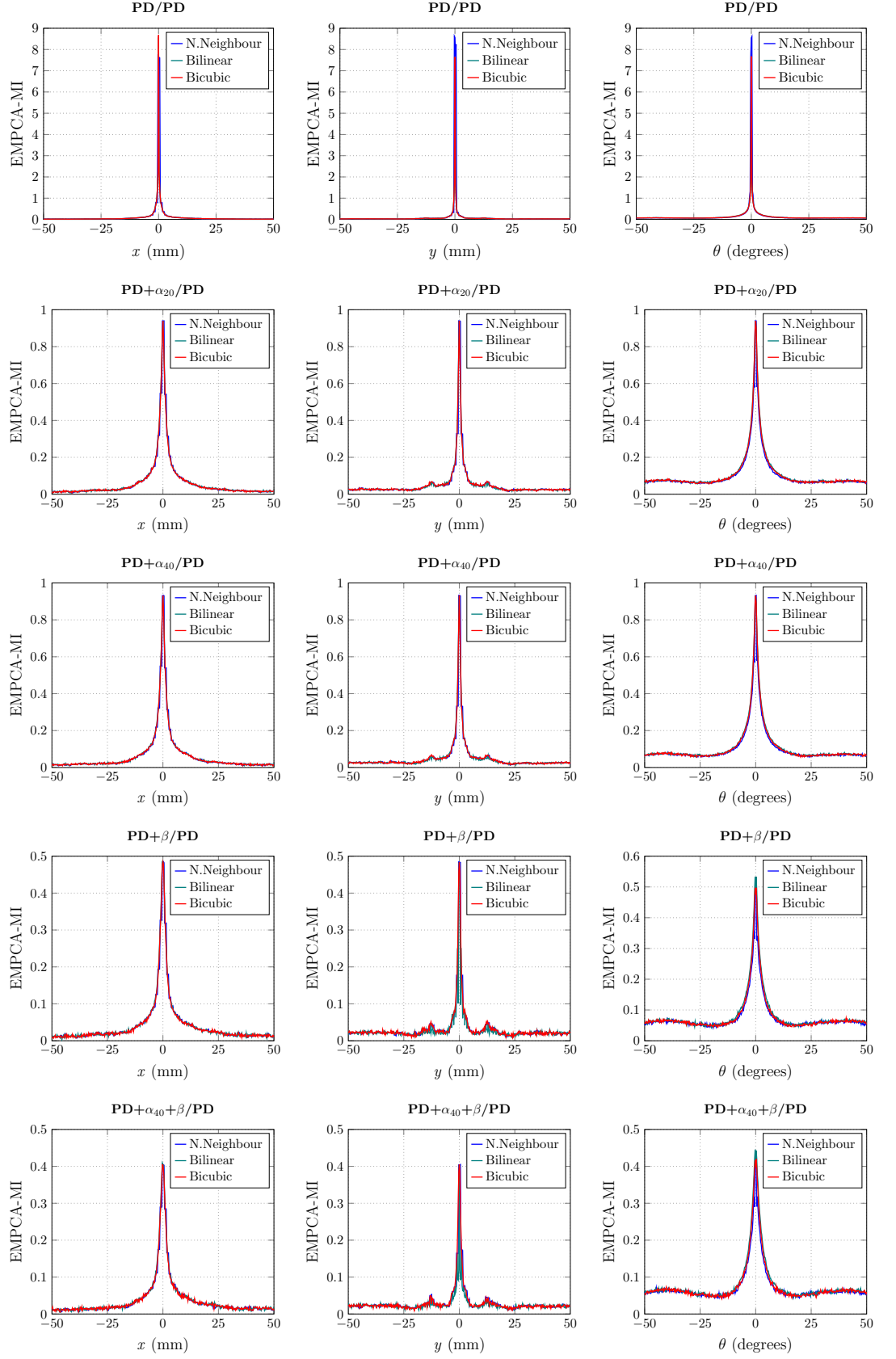


Figure B.3: EMPCA-MI Traces for monomodal PD/PD, PD+ α_{20} /PD, PD+ α_{40} /PD, PD+ β /PD and PD+ $\alpha_{40}+\beta$ /PD image pairs for x , y translation and θ rotation.

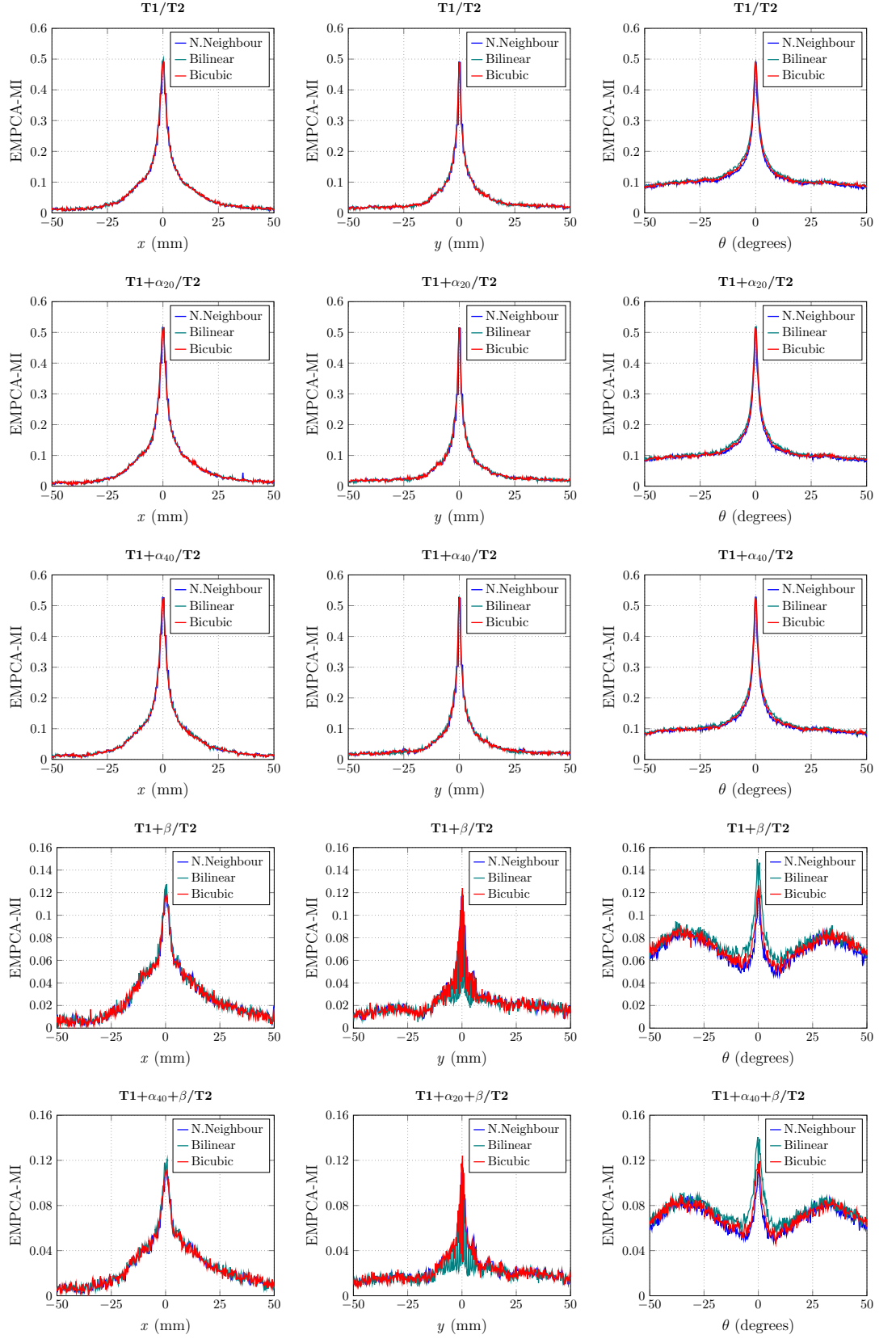


Figure B.4: EMPCA-MI Traces for multimodal $T1/T2$, $T1+\alpha_{20}/T2$, $T1+\alpha_{40}/T2$, $T1+\beta/T2$ and $T1+\alpha_{40}+\beta/T2$ image pairs for x , y translation and θ rotation.

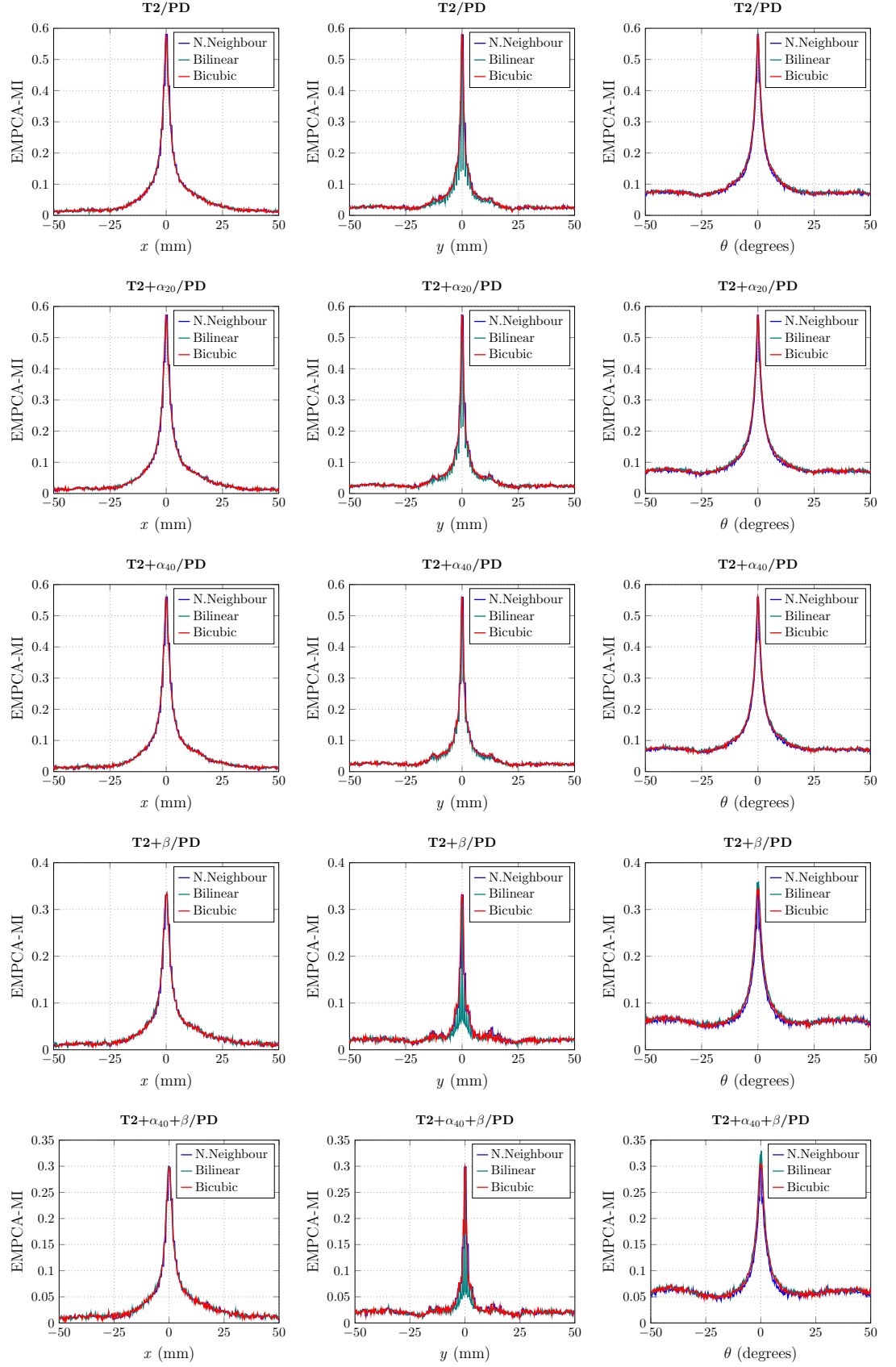


Figure B.5: EMPCA-MI Traces for multimodal T2/PD, T2+ α_{20} /PD, T2+ α_{40} /PD, T2+ β /PD and T2+ $\alpha_{40}+\beta$ /PD image pairs for x , y translation and θ rotation.

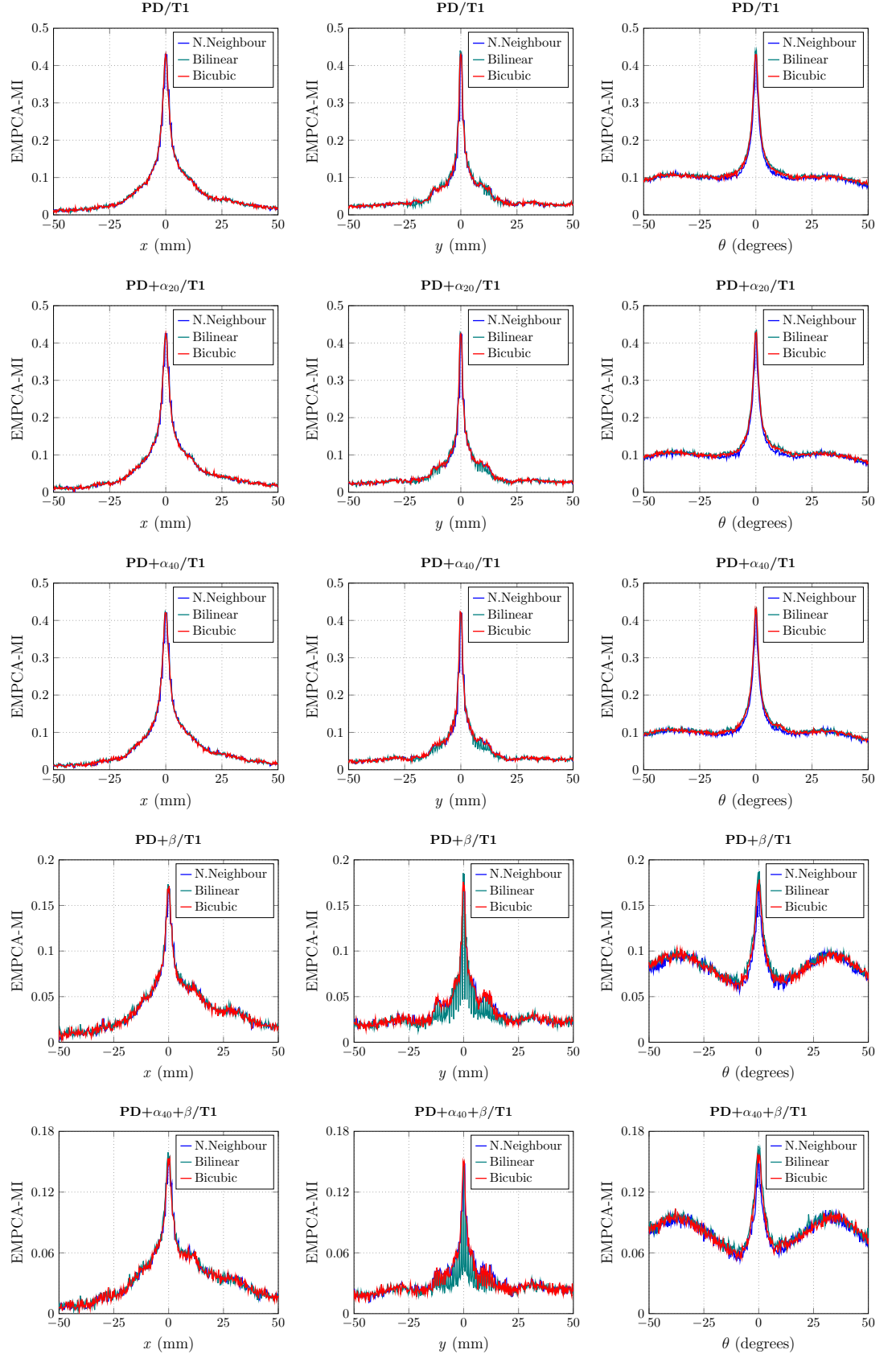


Figure B.6: EMPCA-MI Traces for multimodal PD/T1, PD+ α_{20} /T1, PD+ α_{40} /T1, PD+ β /T1 and PD+ $\alpha_{40}+\beta$ /T1 image pairs for x , y translation and θ rotation.

Appendix C

EMPCA-MI Results for Neighbourhood Radius

This Appendix includes the detailed x axis translation, y axis translation and θ rotation plots of EMPCA-MI traces as mentioned in *Section 4.3.2*. These plots show the results for value of neighbourhood radius r varied between 1, 2, 3, 5, 7 and 10, (keeping the interpolation scheme as bicubic) for mono and multimodal T1, T2 and PD image pairs from *BrainWeb* dataset having five INU and noise levels (No INU and noise, α_{20} , α_{40} , β and $\alpha_{40}+\beta$) as discussed in *Section 3.5.2*.

Figures C.1, C.2 and C.3 show the EMPCA-MI traces for monomodal T1/T1, T2/T2 and PD/PD image pairs respectively. Similarly, Figures C.4, C.5 and C.6 show the EMPCA-MI traces for multimodal T1/T2, T2/PD and PD/T1 image pairs respectively.

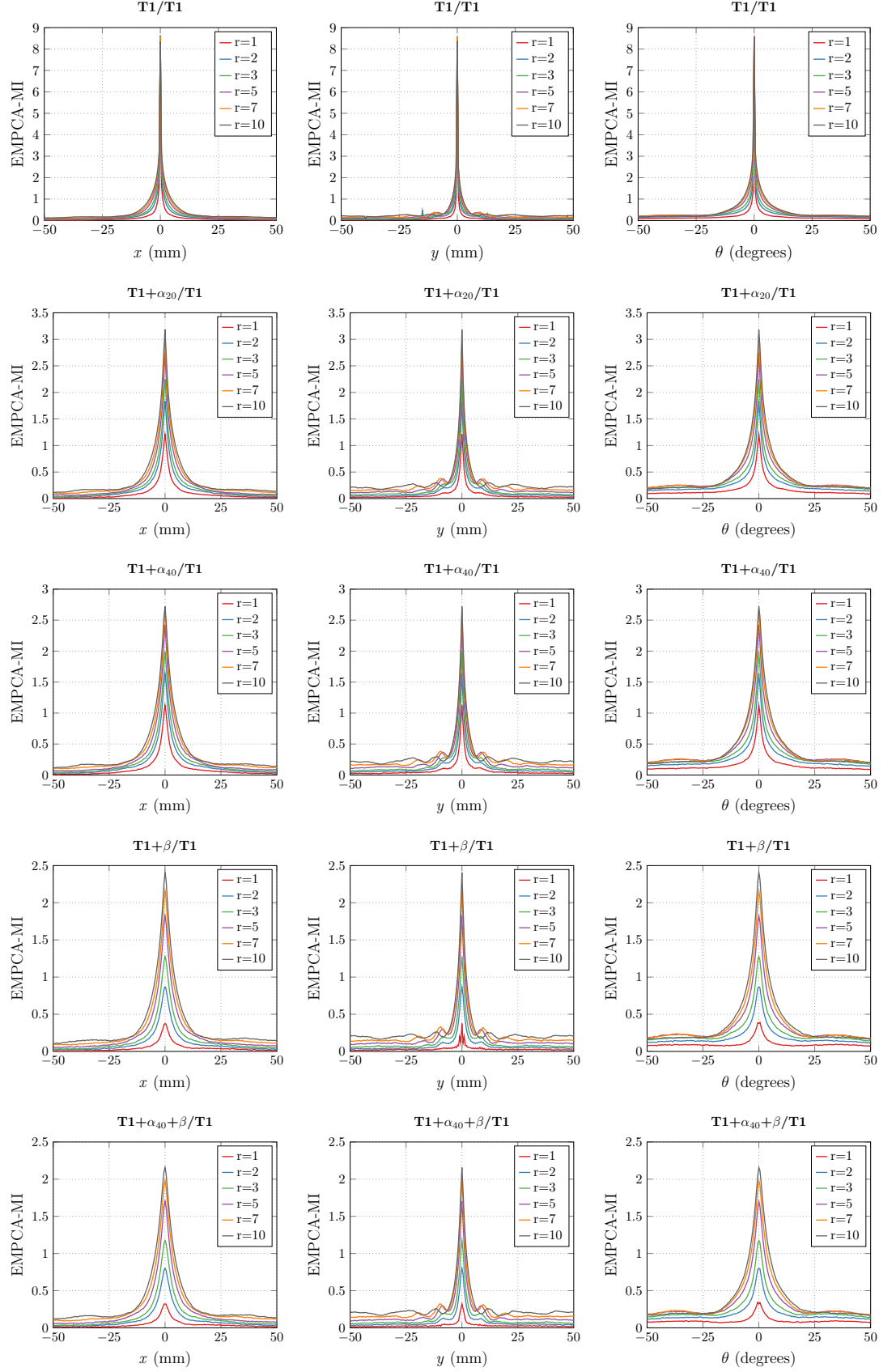


Figure C.1: EMPCA-MI Traces for monomodal $T1/T1$, $T1+\alpha_{20}/T1$, $T1+\alpha_{40}/T1$, $T1+\beta/T1$ and $T1+\alpha_{40}+\beta/T1$ image pairs for x , y translation and θ rotation.

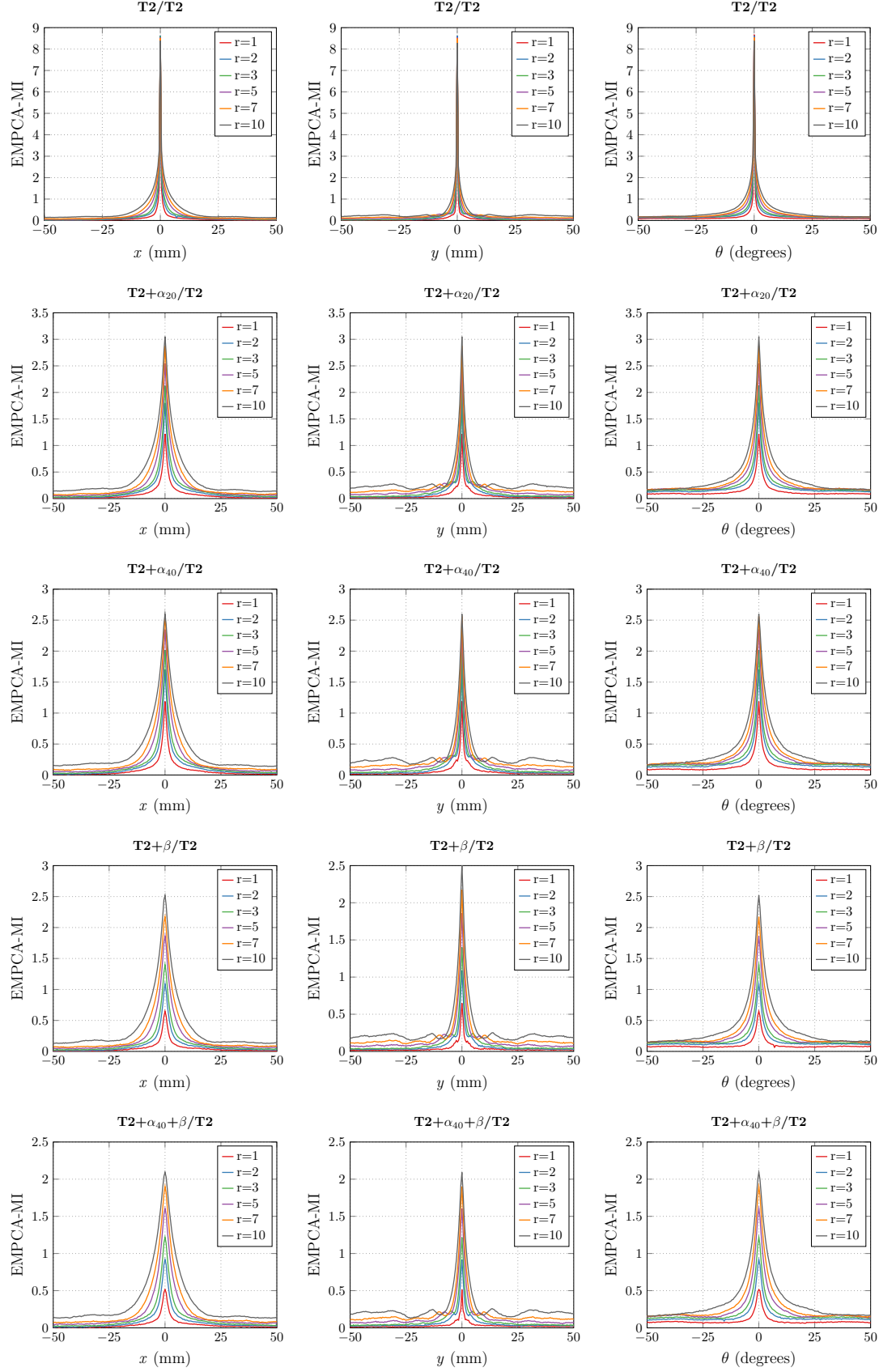


Figure C.2: EMPCA-MI Traces for monomodal $T2/T2$, $T2+\alpha_{20}/T2$, $T2+\alpha_{40}/T2$, $T2+\beta/T2$ and $T2+\alpha_{40}+\beta/T2$ image pairs for x , y translation and θ rotation.

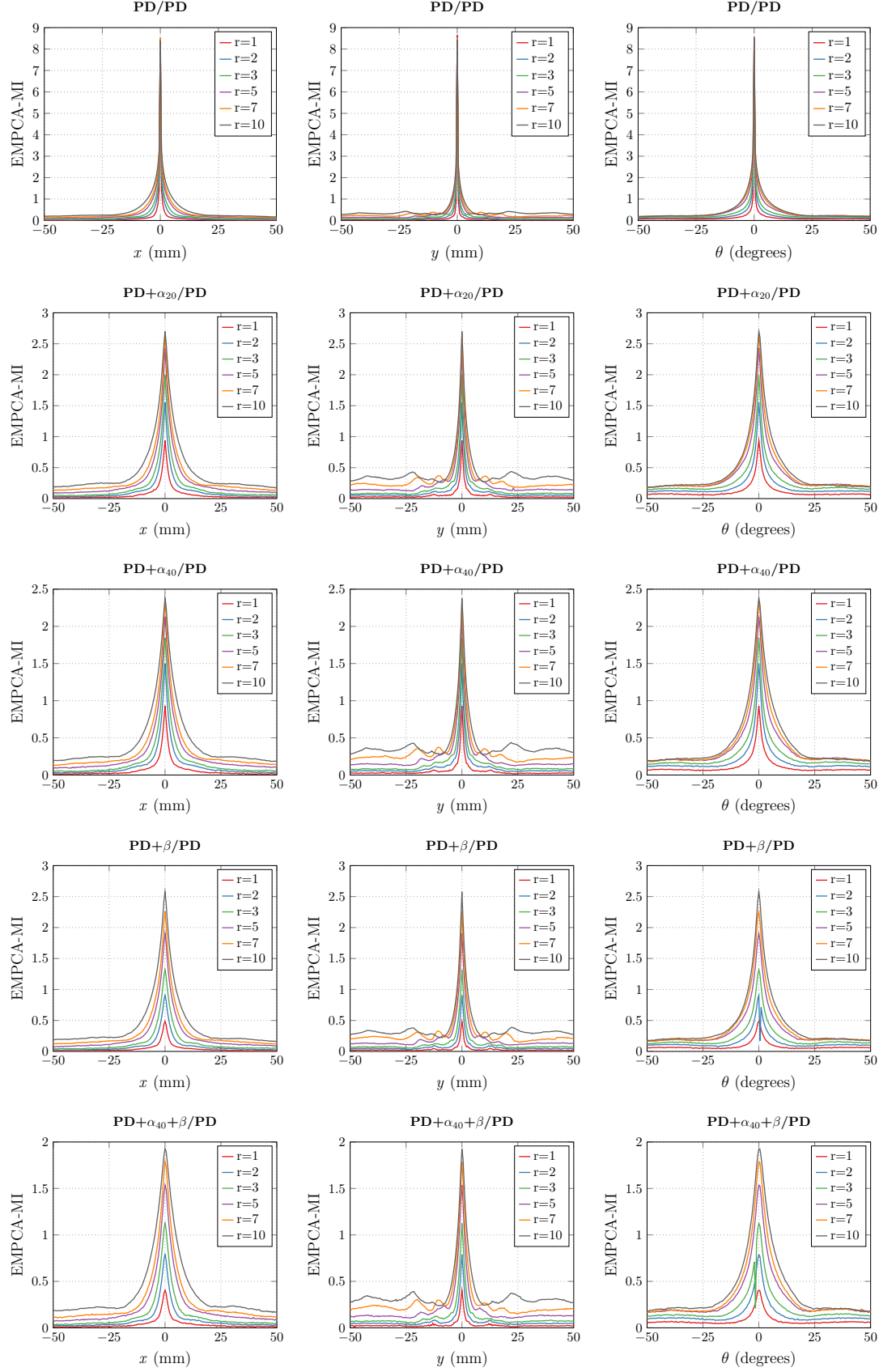


Figure C.3: EMPCA-MI Traces for monomodal PD/PD, PD+ α_{20} /PD, PD+ α_{40} /PD, PD+ β /PD and PD+ $\alpha_{40}+\beta$ /PD image pairs for x , y translation and θ rotation.

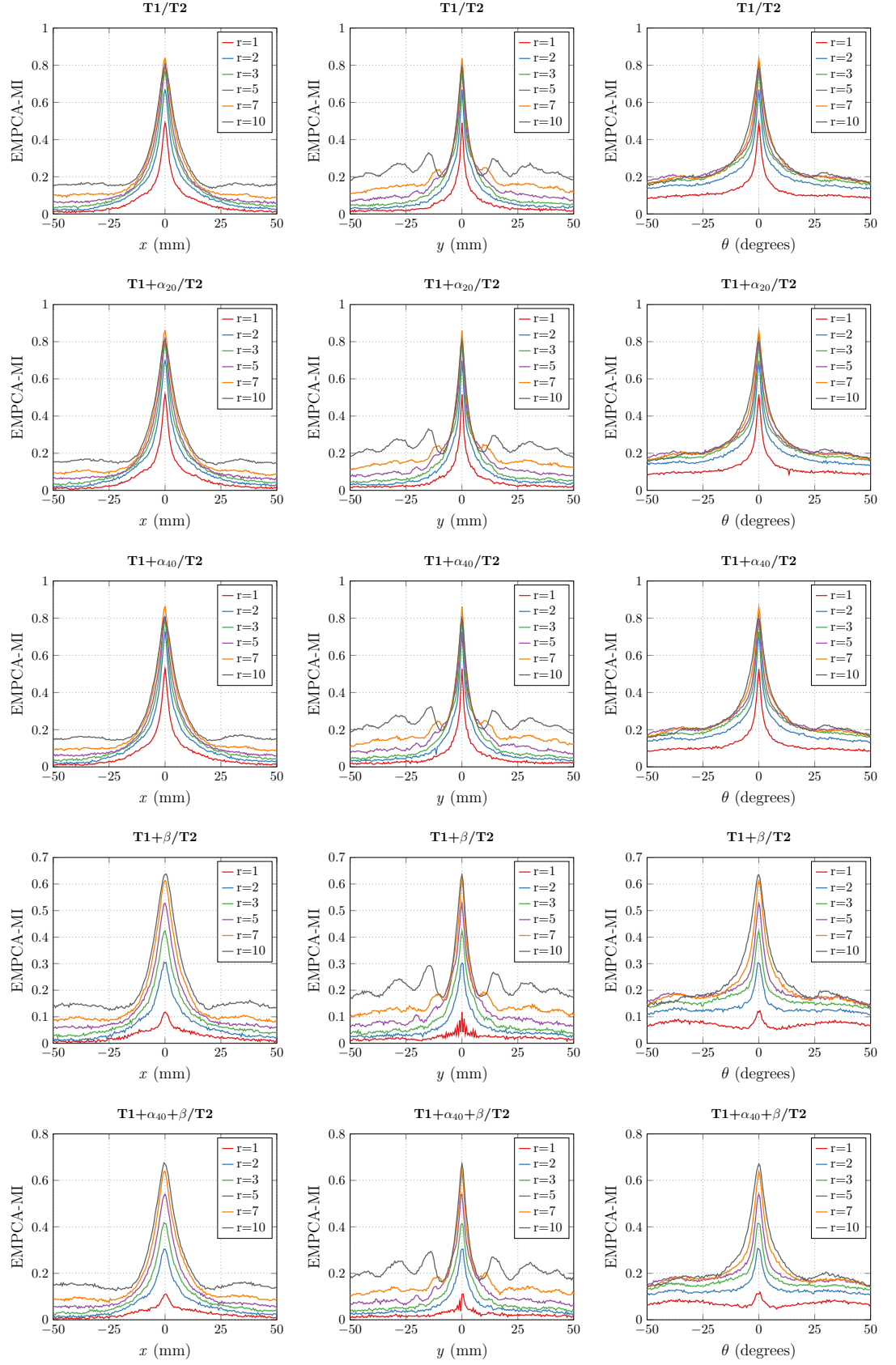


Figure C.4: EMPCA-MI Traces for multimodal $T1/T2$, $T1+\alpha_{20}/T2$, $T1+\alpha_{40}/T2$, $T1+\beta/T2$ and $T1+\alpha_{40}+\beta/T2$ image pairs for x , y translation and θ rotation.

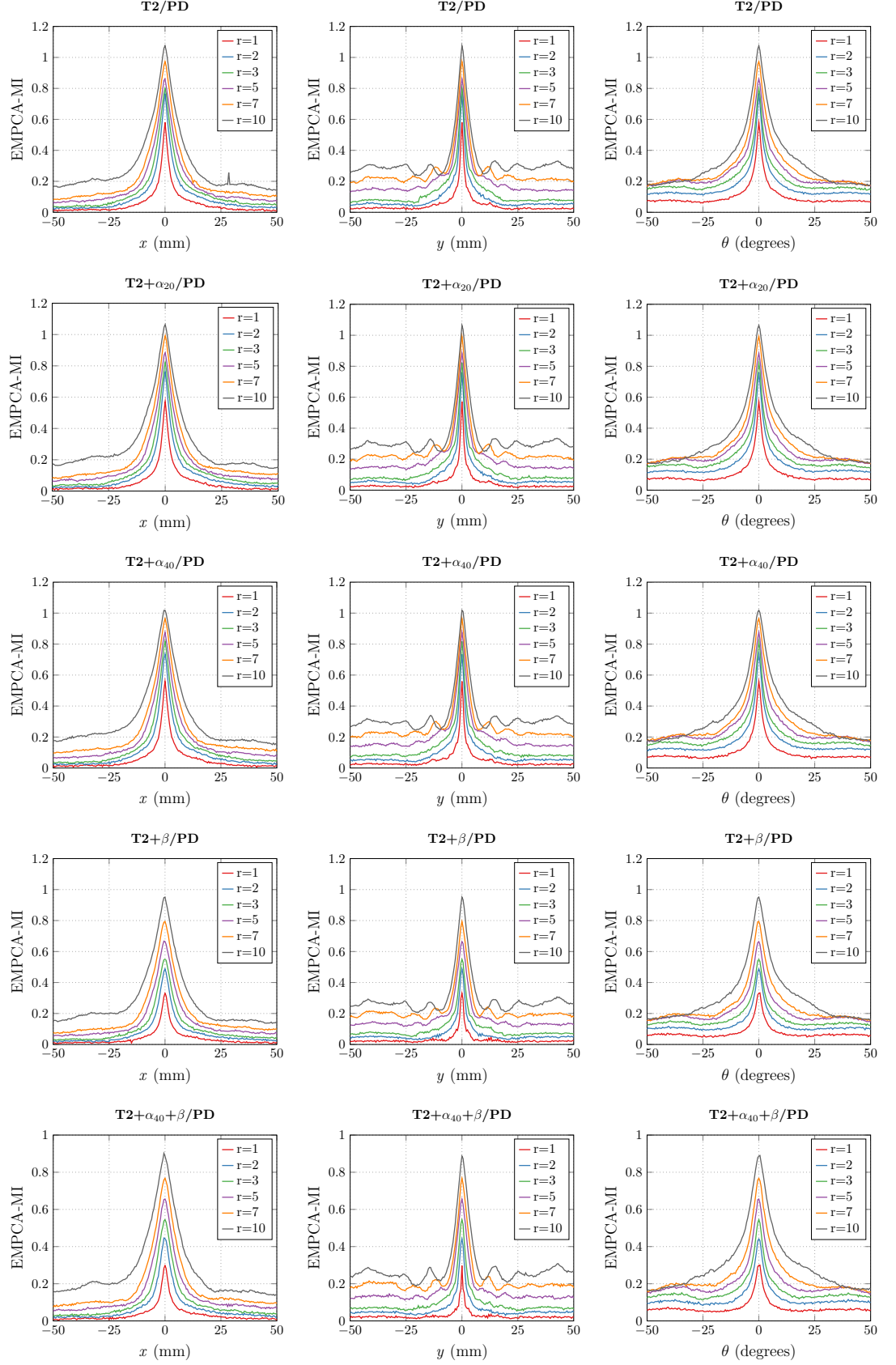


Figure C.5: EMPCA-MI Traces for multimodal $T2/PD$, $T2+\alpha_{20}/PD$, $T2+\alpha_{40}/PD$, $T2+\beta/PD$ and $T2+\alpha_{40}+\beta/PD$ image pairs for x , y translation and θ rotation.

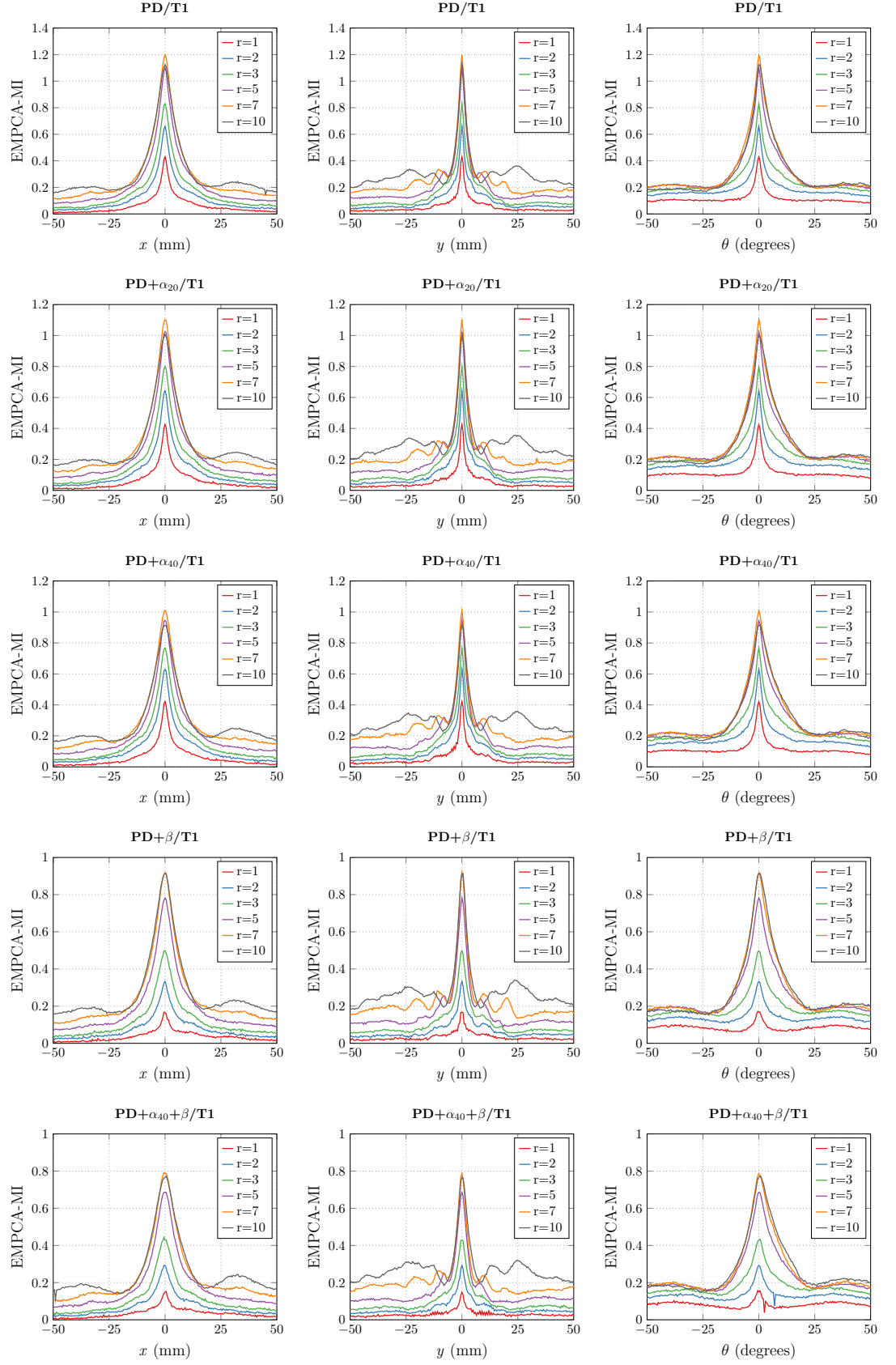


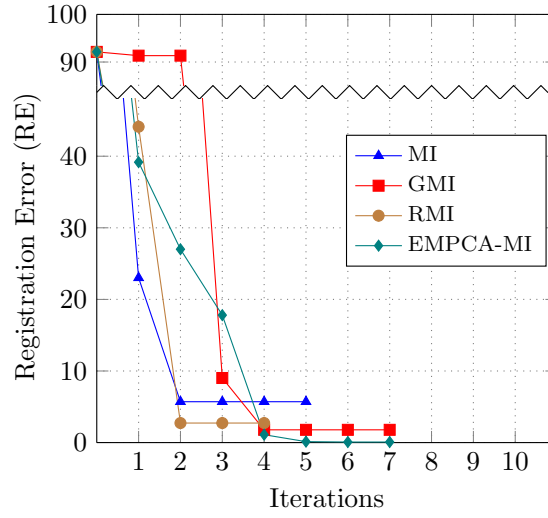
Figure C.6: EMPCA-MI Traces for multimodal PD/T1, PD+ α_{20} /T1, PD+ α_{40} /T1, PD+ β /T1 and PD+ $\alpha_{40}+\beta$ /T1 image pairs for x , y translation and θ rotation.

Appendix D

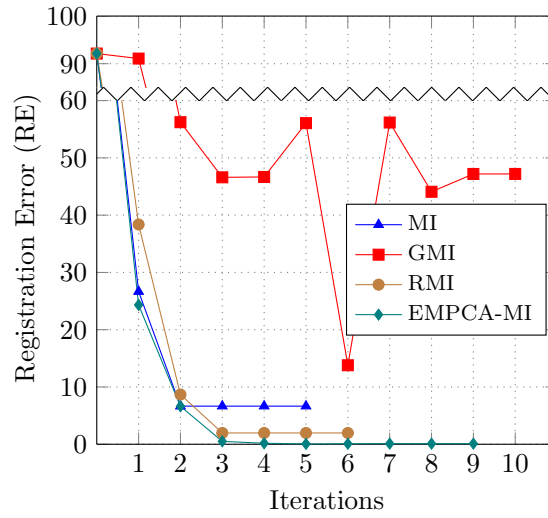
Supplementary Results for *Chapter 5*

This Appendix includes supplementary results for *Chapter 5*. Figures D.1 (a) and (b) show the RE versus iterations plots for MI, GMI, RMI and EMPCA-MI using 18^{th} initial misregistration scenario for the monomodal registration of T2/T2 and PD/PD image pairs. Figures D.2 and D.3 display the corresponding qualitative results for $T2+\alpha_{40}+\beta/T2$ and $PD+\alpha_{40}+\beta/PD$ respectively. Next, Figure D.4 shows the RE versus iterations plots for MI, GMI, RMI and EMPCA-MI using 15^{th} initial misregistration scenario for multimodal registration of T1/T2, T2/PD and PD/T1 pairs with different INU levels and noise. They are followed by Figures D.5 and D.6 which display the corresponding qualitative results for $T2+\alpha_{40}+\beta/PD$ and $PD+\alpha_{40}+\beta/T1$ respectively.

Finally, Figures D.7 and D.8 show the RE summary boxplot of mono (T2/T2 and PD/PD) and multimodal (T2/PD and PD/T1) pairs respectively using MI, GMI, RMI and EMPCA-MI for all 20 initial misregistration scenarios (having five INU and noise levels).



(a)



(b)

Figure D.1: RE versus iterations plots for MI, GMI, RMI and EMPCA-MI using 18th initial misregistration scenario for monomodal registration of (a) T2+ $\alpha_{40}+\beta$ /T2 and (b) PD+ $\alpha_{40}+\beta$ /PD pairs.

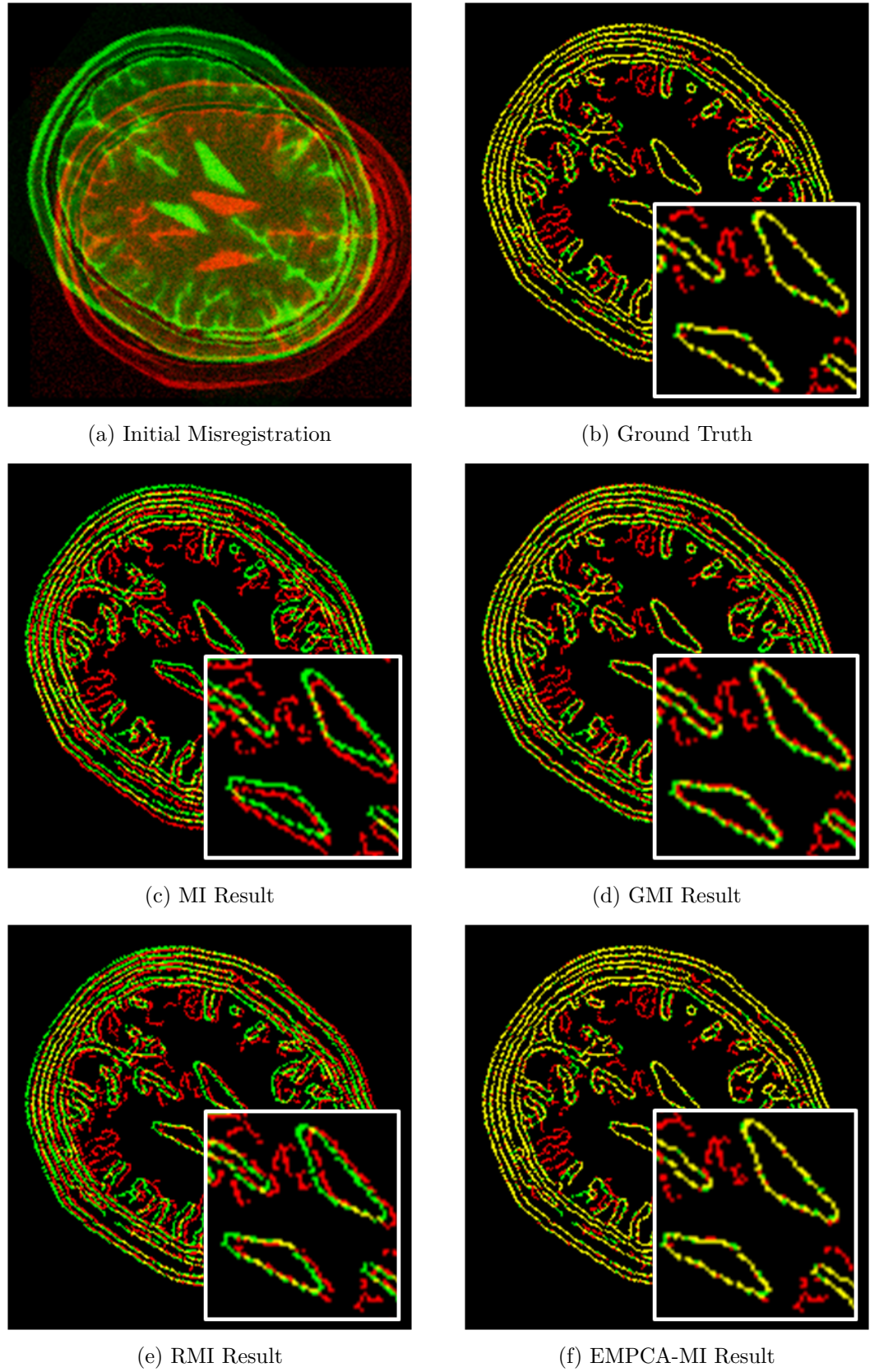


Figure D.2: Qualitative results for $T2+\alpha_{40}+\beta/T2$ with inset showing zoomed-in central lobes for 18th initial misregistration scenario.

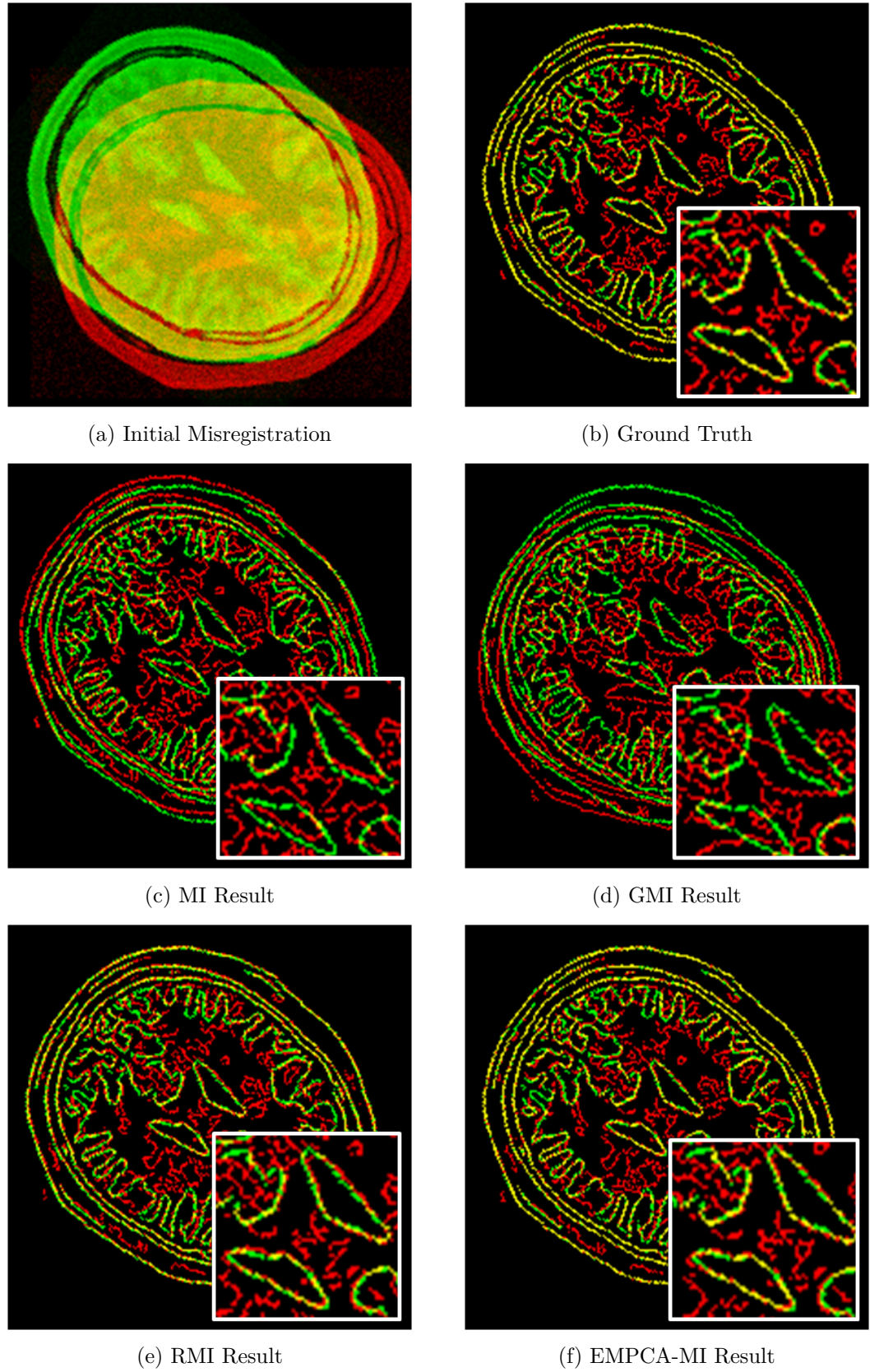


Figure D.3: Qualitative results for $PD+\alpha_{40}+\beta/PD$ with inset showing zoomed-in central lobes for 18th initial misregistration scenario.

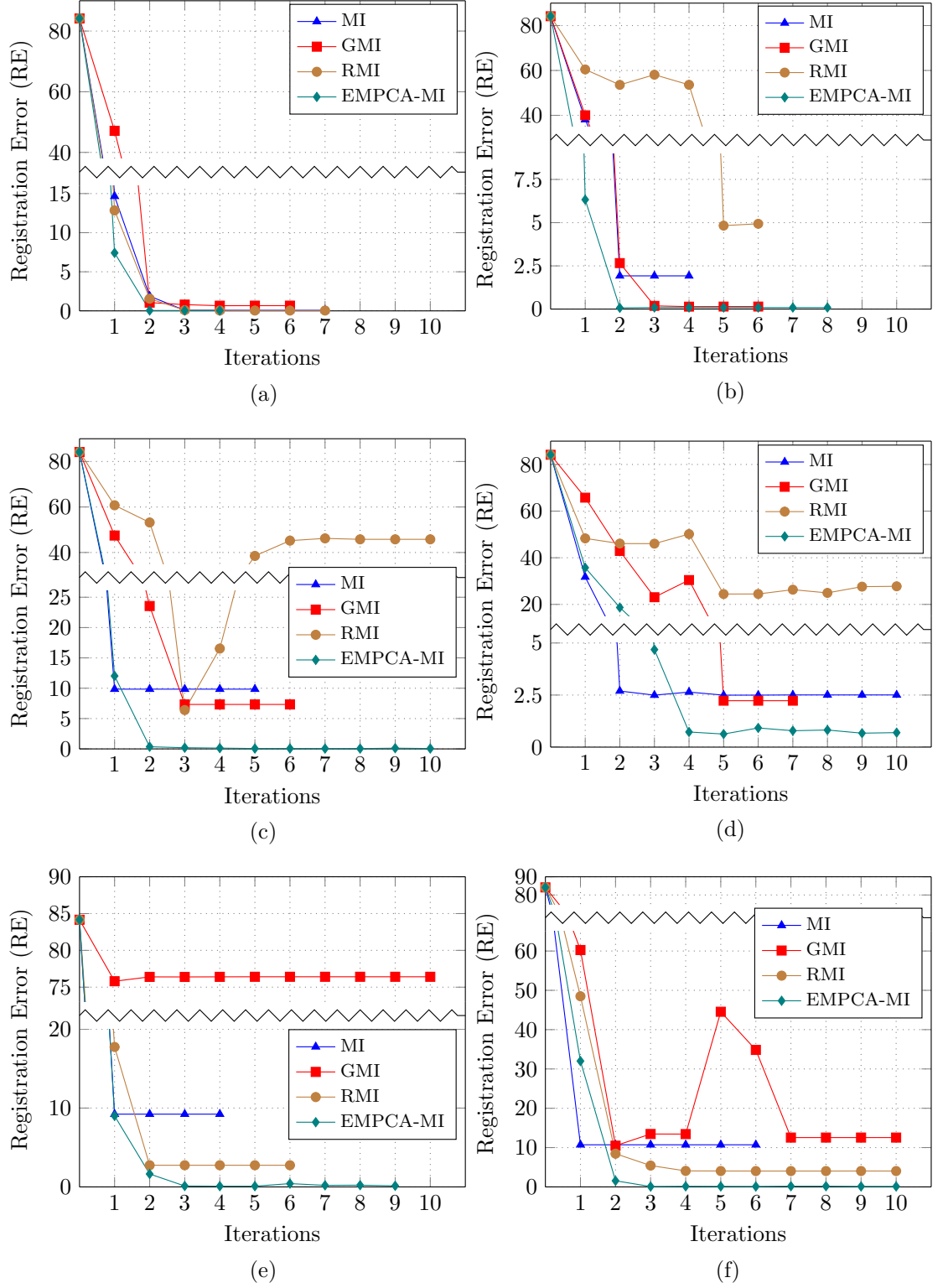
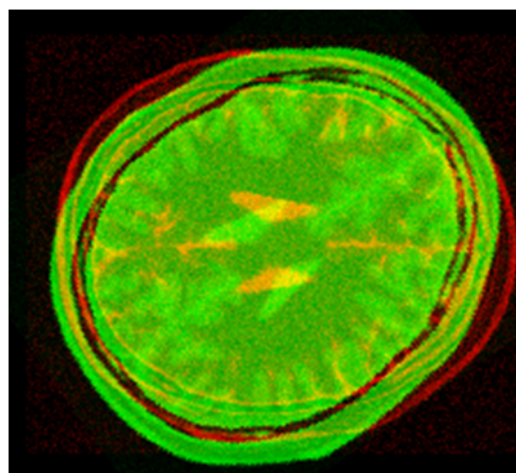
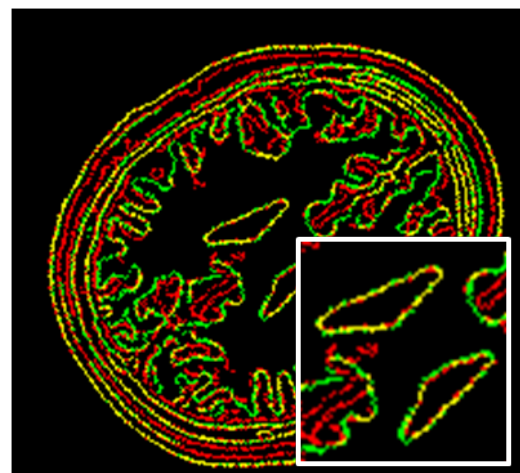


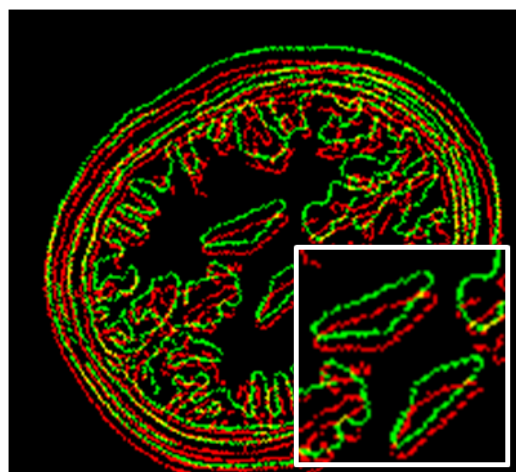
Figure D.4: RE versus iterations plots for MI, GMI, RMI and EMPCA-MI using 15th initial misregistration scenario for multimodal registration of (a) T1/T2, (b) T1+ α_{20} /T2, (c) T1+ α_{40} /T2 and (d) T1+ β /T2 (e) T2+ α_{40} + β /PD and (f) PD+ α_{40} + β /T1 pairs.



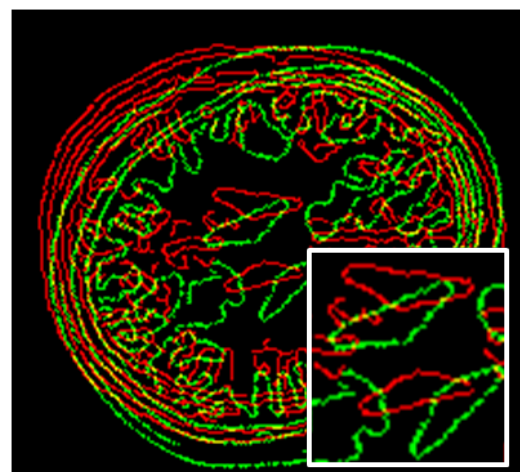
(a) Initial Misregistration



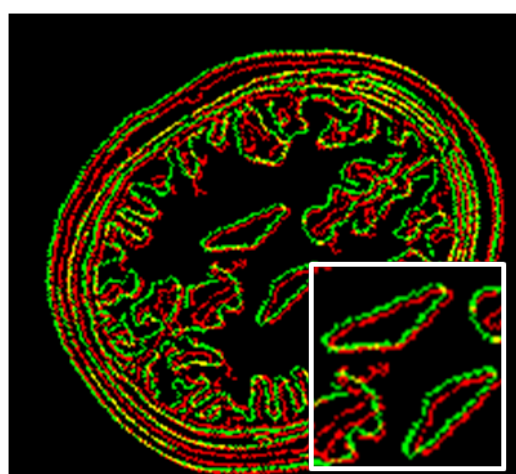
(b) Ground Truth



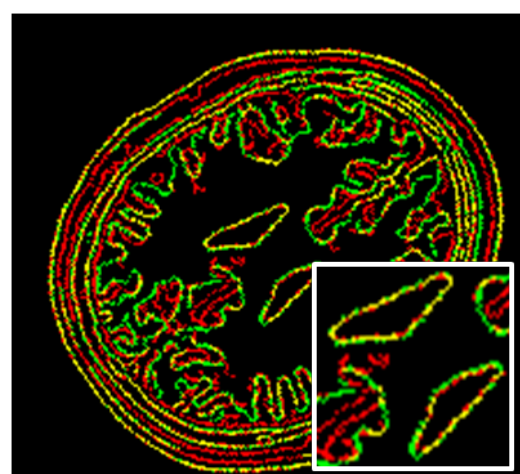
(c) MI Result



(d) GMI Result



(e) RMI Result



(f) EMPCA-MI Result

Figure D.5: Qualitative results for $T2+\alpha_{40}+\beta/PD$ with inset showing zoomed-in central lobes for 15th initial misregistration scenario.

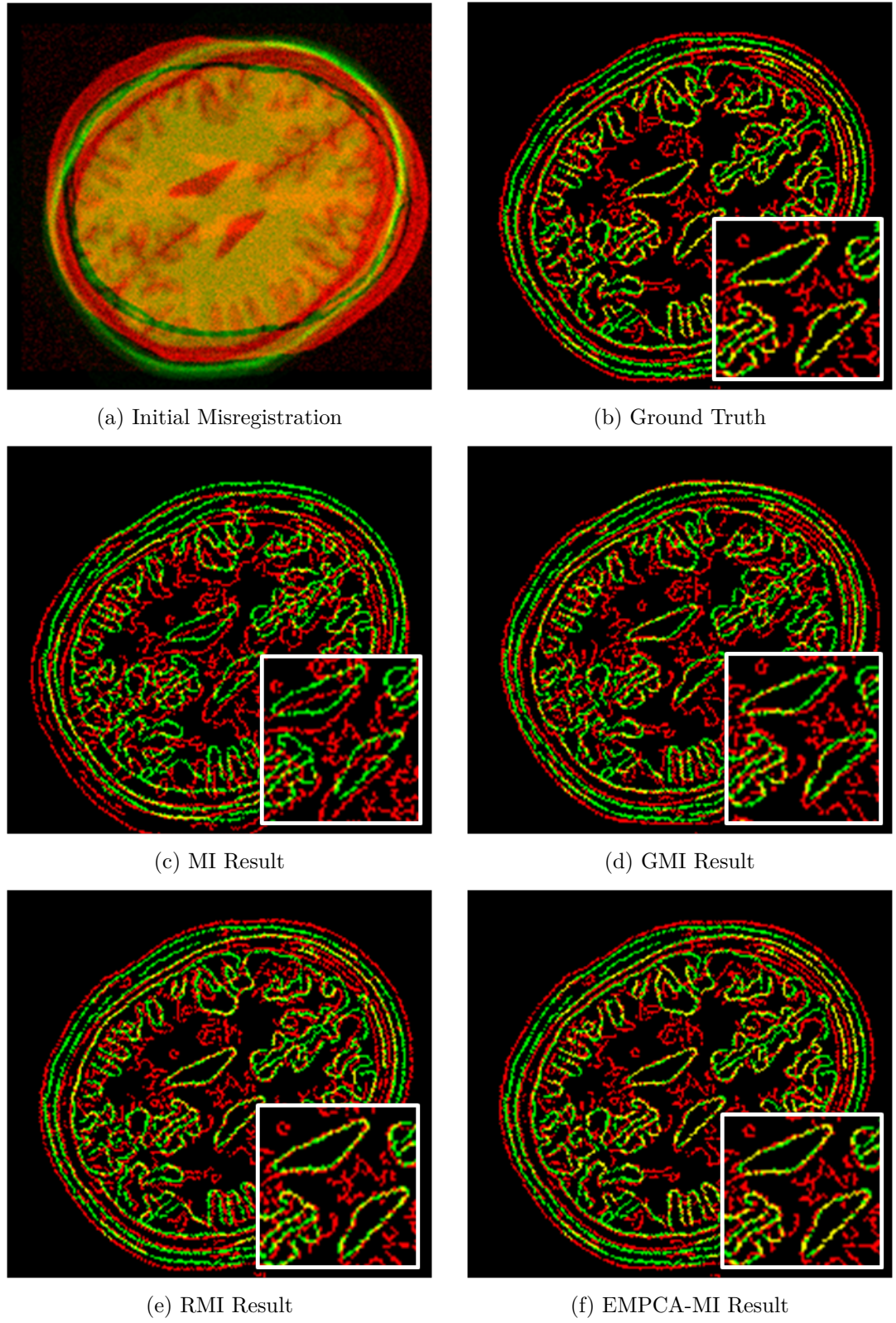


Figure D.6: Qualitative results for $PD+\alpha_{40}+\beta/T1$ with inset showing zoomed-in central lobes for 15^{th} initial misregistration scenario.

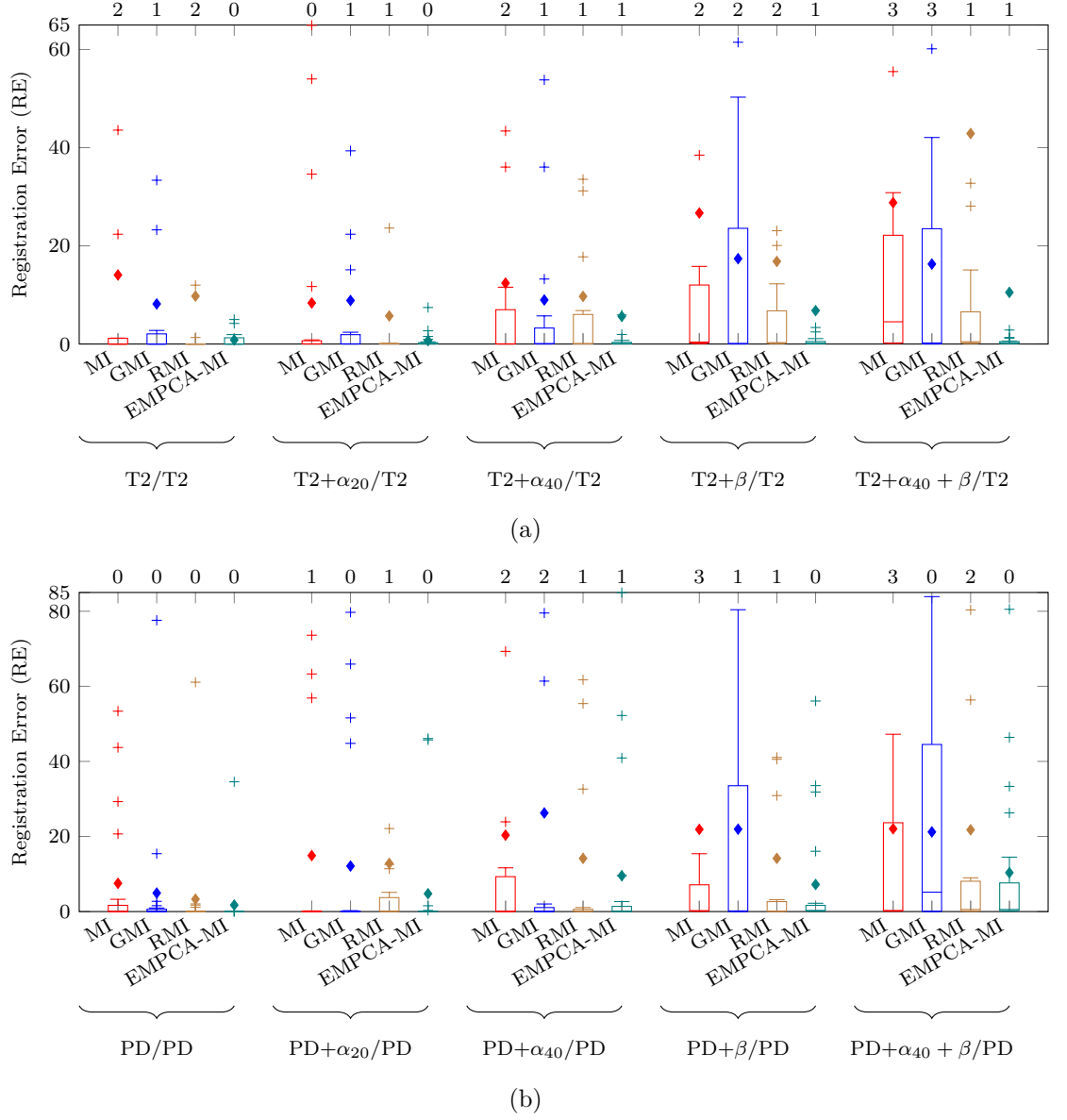


Figure D.7: RE summary boxplot of monomodal (a) T2/T2 and (b) PD/PD pairs using MI, GMI, RMI and EMPCA-MI for all 20 initial misregistration scenarios. The *mean* and *outliers* are denoted by \blacklozenge and $+$ shapes. The numbers on top of the plots refer to the number of *out-of-range* outliers with RE higher than 65 and 85 pixels respectively.

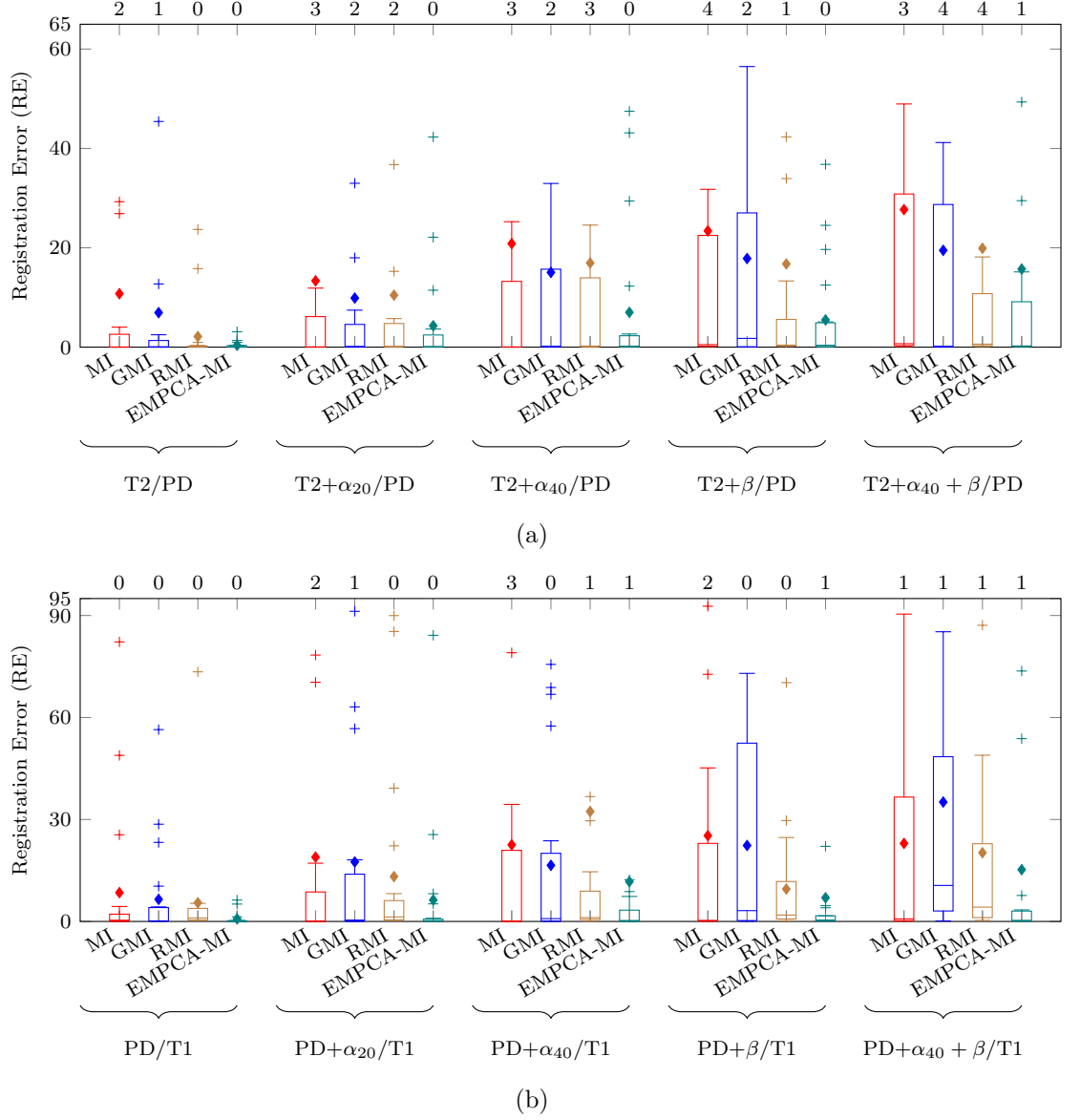


Figure D.8: RE summary boxplot of multimodal (a) T2/PD and (b) PD/T1 pairs using MI, GMI, RMI and EMPCA-MI for all 20 initial misregistration scenarios. The *mean* and *outliers* are denoted by \blacklozenge and $+$ shapes. The numbers on top of the plots refer to the number of *out-of-range* outliers with RE higher than 60 and 95 pixels respectively.

Appendix E

Supplementary Results for *Chapter 6*

This Appendix includes supplementary results for *Chapter 6*. Figures E.1 and E.2 show the RE summary boxplot of mono (T2/T2 and PD/PD) and multimodal (T2/PD and PD/T1) pairs respectively using the 1st order (*8-pixel*), 2nd order (*8-pixel*) and 2nd order (*4-pixel*) neighbourhood region connectivity in EMPCA-MI framework for all 20 initial misregistration scenarios (having five INU and noise levels).

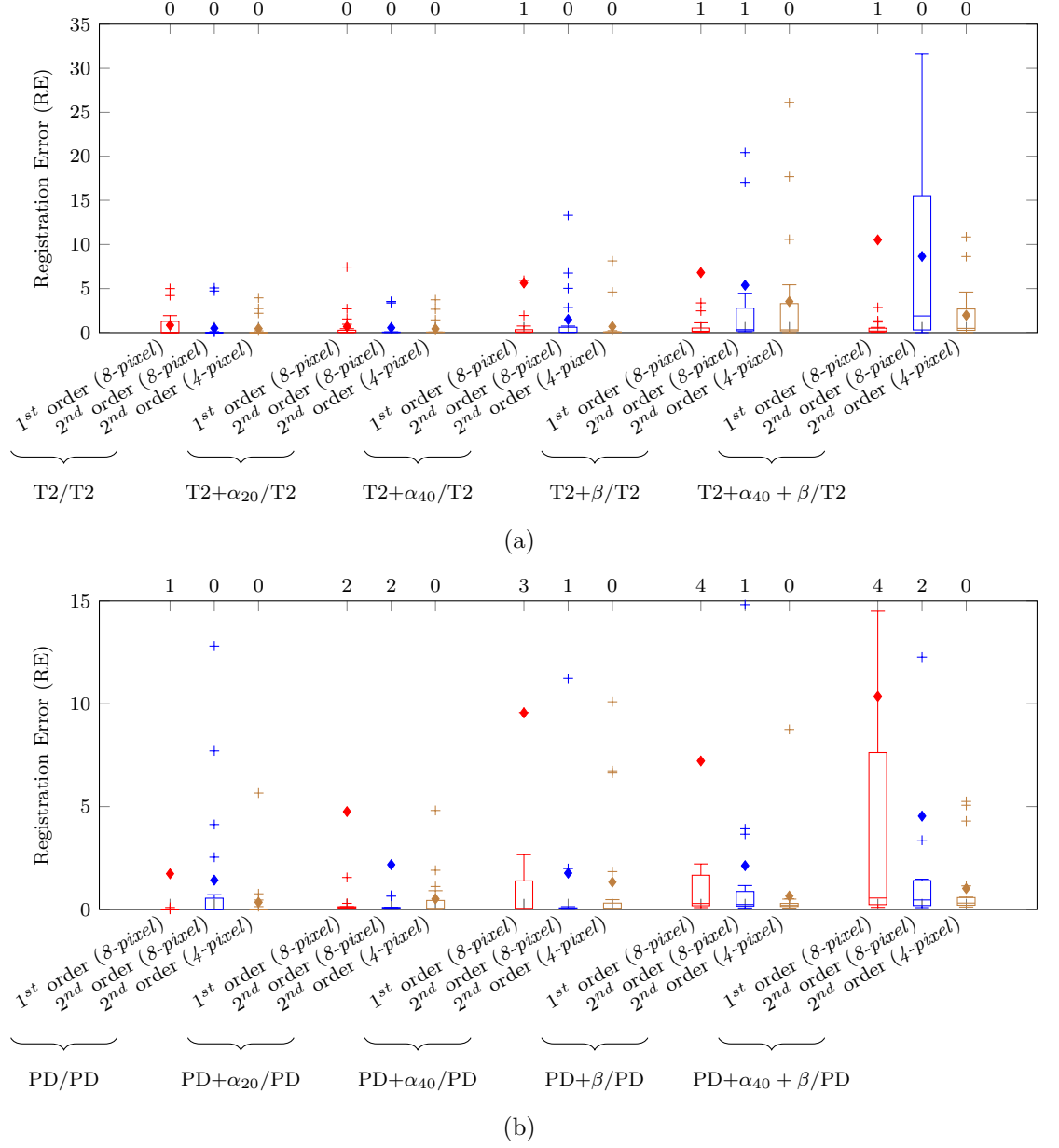


Figure E.1: RE summary boxplot of monomodal (a) T2/T2 and (b) PD/PD pairs using 1st order (8-pixel), 2nd order (8-pixel) and 2nd order (4-pixel) neighbourhood region connectivity in EMPCA-MI framework for all 20 initial misregistration scenarios. The *mean* and *outliers* are denoted by \blacklozenge and $+$ shapes. The numbers on top of the plots refer to the number of *out-of-range* outliers with RE higher than 35 and 15 pixels respectively.

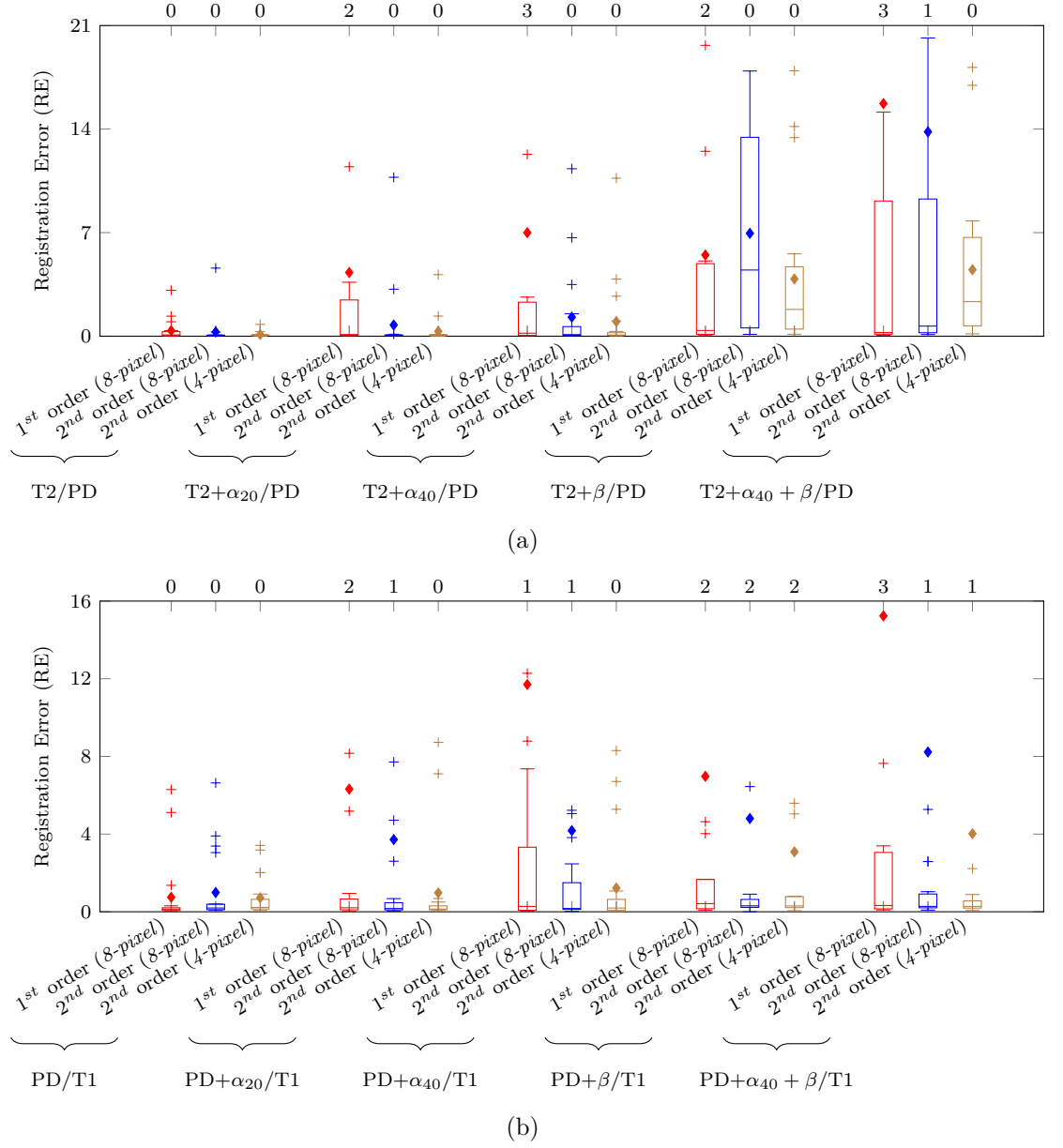


Figure E.2: RE summary boxplot of multimodal (a) T2/PD and (b) PD/T1 pairs using 1st order (8-pixel), 2nd order (8-pixel) and 2nd order (4-pixel) neighbourhood region connectivity in EMPCA-MI framework for all 20 initial misregistration scenarios. The *mean* and *outliers* are denoted by ♦ and + shapes. The numbers on top of the plots refer to the number of *out-of-range* outliers with RE higher than 21 and 16 pixels respectively.

Appendix F

Supplementary Results for

Chapter 7

This Appendix includes supplementary results for *Chapter 7*. Figures F.1 and F.2 show the RE summary boxplot of mono (T2/T2 and PD/PD) and multimodal (T2/PD and PD/T1) pairs respectively using the EMPCA-MI $\{1\}$ and *adaptive* EMPCA-MI $\{P\}$ for all 20 initial misregistration scenarios (having five INU and noise levels).

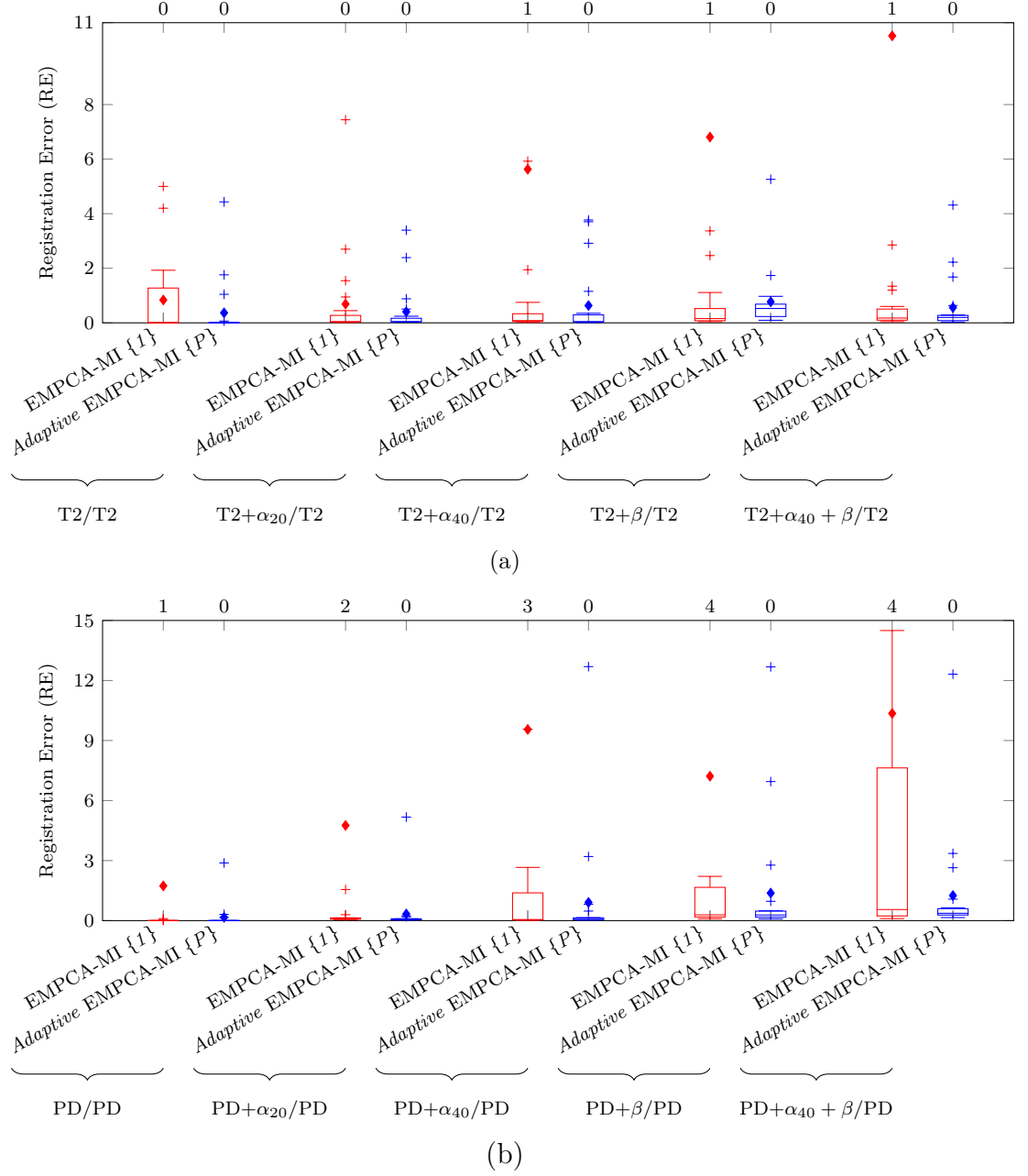


Figure F.1: RE summary boxplot of monomodal (a) T2/T2 and (b) PD/PD pairs using the EMPCA-MI $\{1\}$ and *adaptive* EMPCA-MI $\{P\}$ for all 20 initial misregistration scenarios. The *mean* and *outliers* are denoted by \blacklozenge and $+$ shapes. The numbers on top of the plots refer to the number of *out-of-range* outliers with RE higher than 11 and 15 pixels respectively.

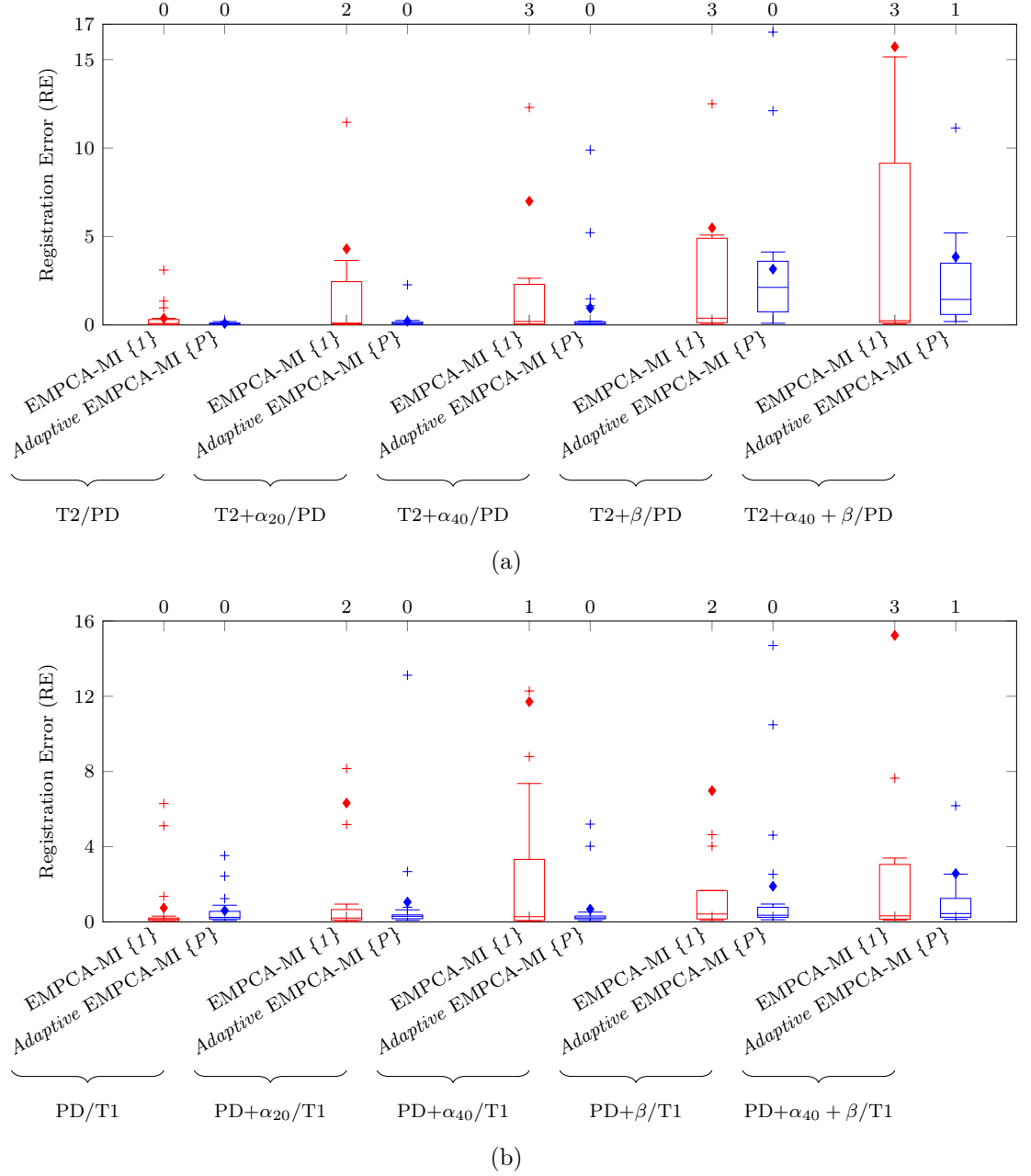


Figure F.2: RE summary boxplot of multimodal (a) T2/PD and (b) PD/T1 pairs using the EMPCA-MI $\{1\}$ and *adaptive* EMPCA-MI $\{P\}$ for all 20 initial misregistration scenarios. The *mean* and *outliers* are denoted by \blacklozenge and $+$ shapes. The numbers on top of the plots refer to the number of *out-of-range* outliers with RE higher than 17 and 16 pixels respectively.